Fall 11-16-2022

Single-crystal elasticity of Earth's mantle transition zone minerals and High pressure-temperature phase equilibrium experiments on Martian basalts

Wenyi Zhou

Wenyi Zhou

Candidate

Department of Earth and Planetary Sciences

Department

This dissertation is approved, and it is acceptable in quality and form for publication:

Approved by the Dissertation Committee:

Brandon Schmandt , Chairperson

Jin Zhang (co-chair)

Charles Shearer

Carl Agee

Bin Chen

Single-crystal elasticity of Earth's mantle transition zone minerals and High pressure-temperature phase equilibrium experiments on Martian basalts

BY

Wenyi Zhou

B.S., Geology, China University of Geosciences, 2014

M.S., Geology, China University of Geosciences, 2017

DISSERTATION

Submitted in Partial Fulfillment of the

Requirements for the Degree of

Doctor of Philosophy

Earth and Planetary Sciences

The University of New Mexico

Albuquerque, New Mexico

December, 2022

ACKNOWLEDGMENTS

I would like to express my deepest gratitude to my Ph.D. advisor Dr. Jin Zhang for her guidance. Thank Jin for her time, patience, and opportunities in ensuring me getting the best training she could give. Not only did she teach me a lot of things, but also support me to attend meetings and workshops. Without Jin, I could not gain so much knowledge about Earth and Mars. It is also a great pleasure to work with Jin who is knowledgeable and generous. Her positive attitude towards both work and life have inspired me to be a better person. I'm very lucky to have Jin as my advisor.

I am also grateful to all my committee members: Dr. Brandon Schmandt, Dr. Chip Shearer, Dr. Carl Agee, and Dr. Bin Chen. Dr. Many thanks to Dr. Brandon Schmandt for his guidance and great contributions towards the Mantle Transition Zone projects. Special thanks to Dr. Chip Shearer for his detailed guidance and support with the Martian basalt project during the 4-year long journey. Many thanks to Dr. Carl Agee for helping and providing resources to make the phase equilibrium experiments successful. Special thanks to Dr. Bin Chen who helped me to synthesize precious wadsleyite and ringwoodite samples as well as provided insightful suggestions about manuscripts.

Sincere thanks should also go to Dr. Przemek Dera, Dr. Dongzhou Zhang, Dr. Esen E. Alpg, Dr. Barbara Lavinag, Dr. Rostislav Hrubiak, Dr. Curtis Kenney-Benson, Dr. Sergey Tkachev, and Dr. Vitali Prakapenka for their generous help in all the XRD and gas-loading experiments. Special thanks to Dr. Peter Olson for his generous help in the modeling and writing of the Martian basalt paper. Many thanks to Mike Spilde, Dr. Ruijia Wang, Sibo Chen,

Dr. Xiaojing Lai, and Dr. Man Xu for offering their professional help in experiments and coding.

I would like to thank all the faculties, staffs, and friends in and out of the department and institute. It’s a pleasure to work with Ming Hao, Roselyn Hurlow, Mingqiang Hou, Wade Mans, Zhiyuan Ren, Soisiri Charin, Arlacee Luu and Margaret Glasgow. I also would like to thank my TA advisor Dr. Aurora Pun for her support and guidance. Special thanks to Paula Pascetti and Cecilia Arias for their generous help during my Ph.D. journey. Many thanks to Chris Anderson for installing and fixing experimental tools in the lab.

To conclude, I cannot forget to thank my parents for all the unconditional love in these years. I am also grateful to Ming Hao, who is both my important science collaborator and fiancé. I would be remiss in not mentioning my cat Mimi who has brought happiness to my daily life.

Single-crystal elasticity of Earth's mantle transition zone minerals and High pressure-temperature phase equilibrium experiments on Martian basalts

by

Wenyi Zhou

B.S., Geology, China University of Geosciences, 2014

M.S., Geology, China University of Geosciences, 2017

Ph.D., Earth and Planetary Sciences, the University of New Mexico, 2022

ABSTRACT

Wadsleyite and ringwoodite are major minerals in the Earth's Mantle Transition Zone. Global and local seismic studies have detected strong lateral variations in seismic velocity and anisotropy in the Mantle Transition Zone, reflecting temperature and possible composition variations. Interpretation of these seismic observations requires knowledge of thermoelastic properties of wadsleyite and ringwoodite with different compositions (water and Fe contents) under high pressure-temperature conditions. In this dissertation, we have measured single-crystal elastic properties of wadsleyite and ringwoodite under high pressure-temperature conditions by Brillouin spectroscopy. Based on our measurements and previous experimental results, we further model the effects of water and Fe on elasticity of wadsleyite and ringwoodite, respectively. Finally, we combine experiments-obtained mineral physics elasticity data with global and local seismic observations to understand temperature and composition variations in the Mantle Transition Zone,

We have also conducted phase equilibrium experiments on 3 different Martian basalts (Yamato 980459, GUSEV basalt (Humphrey), NWA 8159) along a typical Martian areotherm to understand their composition and density changes as functions of depth. We then compare their densities with those of the ambient Martian mantle to understand the likelihood of Earth-like plate tectonics in Martian history.

TABLE OF CONTENTS

LIST OF FIGURES

LIST OF TABLES

Chapter I

Introduction

1. Single-crystal elastic properties of wadsleyite and ringwoodite

Wadsleyite and ringwoodite ($(Mg,Fe)_2SiO_4$), the high-pressure polymorphs of olivine, are major minerals in the Earth's Mantle Transition Zone (MTZ). In a pyrolite model, the upper MTZ (~410-520 km depth) is composed of ~53 vol% wadsleyite, 37-47 vol% garnet, and 0-10 vol% clinopyroxene; the lower MTZ (~520-660 km depth) is composed of ~53 vol% ringwoodite, 42-47 vol% garnet, and 0-5 vol% Davemaoite (Ishii et al., 2018). The olivine to wadsleyite phase transition at ~410 km depth can cause large seismic velocity (compressional wave velocity (Vp) and shear wave velocity (Vs)) jumps, resulting in the 410-km seismic discontinuity (410). Similarly, the wadsleyite to ringwoodite phase transition is very likely to be the main cause for the 520-km seismic discontinuity (520) with a potential contribution from the exsolution of Davemaoite. The decomposition of ringwoodite to perovskite and ferropericlase largely contributes to the sharp 660-km seismic discontinuity (660) at the bottom of the MTZ (Frost, 2008; Ishii et al., 2018).

Global and local seismic tomography models found that Vp and Vs varies laterally across the MTZ. For example, the MTZ beneath subductions zones (e.g., circum-Pacific subduction zones) almost uniformly show positive Vp and Vs anomalies, suggesting a strong correlation with slabs in the MTZ (e.g., Ritsema et al., 2011; Fukao and Obayashi, 2013). The high velocities of slabs in the MTZ originate from their low temperatures and possibly harzburgitic compositions with higher amount of wadsleyite/ringwoodite than the pyrolitic ambient mantle. In addition, fast and cold slabs could also transport water into the MTZ and

make the MTZ a potential water reservoir considering high water solubility in wadsleyite and ringwoodite (1-3 wt% water, Inoue et al., 1995; Fei and Katsura, 2020). The lateral variations in seismic velocities in the MTZ may not only reflect lateral temperature and mineral fraction variations but also have implications in volatile storage and transport in the MTZ. Interpretations of these seismic velocity observations require knowledge of sound velocities of the major MTZ minerals. However, the high pressure-temperature sound velocities of wadsleyite and ringwoodite up to the MTZ pressures under high temperatures are poorly constrained.

In addition to seismic velocity observations, many lines of evidence suggested that the seismic anisotropy of the MTZ can be strong in localized regions adjacent to slabs (e.g., ~2-3% beath the circum-Pacific subducting slabs) but weak on the global scale (~1%) (Chang and Ferreira, 2019; Huang et al., 2019; Moulik and Ekstrom, 2014, Yuan and Beghein, 2013). Interpretation of these global and local anisotropic seismic observations requires knowledge of the single-crystal elastic properties of wadsleyite and ringwoodite and lattice preferred orientations of them under different environments.

In my dissertation, we have conducted high pressure-temperature Brillouin single-crystal elasticity measurements for hydrous Fe-bearing wadsleyite up to 16 GPa and 700K and anhydrous Fe-bearing ringwoodite up to 32 GPa and 700K. Combing our results with all previous single-crystal elasticity data, we model the effects of water and Fe# on elasticity (V_P, V_S, anisotropy) of wadsleyite and ringwoodite. Finally, these results are used to interpret global or local seismic observations to understand composition and temperature variations in the MTZ.

2. High pressure-temperature phase equilibrium experiments on Martian basalts

Present-day Earth operates with mobile plate tectonics mainly driven by dense oceanic lithospheric slabs. The high densities of slabs are caused by not only their low temperatures but also the high-density eclogite transformed from the Mid-Ocean Ridge Basalt (MORB, major component of oceanic crust) (Coltice et al., 2019). On the contrary, present-day Mars is dominated by stagnant lid convection, with an intact and immobile lithosphere lid covering the mantle (Tosi and Padovan, 2021). It remains controversial why Earth-like plate tectonics fail to operate with Mars.

Martian crust and mantle compositions are different from Earth's. Martian basaltic crust is depleted in Al compared with Earth's basaltic crust (MORB), therefore Martian eclogite transformed from Martian basaltic crust would contain less garnet and thus possibly less dense than the terrestrial eclogite transformed from MORB. On the other hand, the Martian ambient mantle is Fe enriched compared with the Earth's ambient mantle (pyrolite), resulting in a much denser Martian mantle (Bertka and Fei, 1997). Therefore, the buoyancy relationship between the slab crust and the mantle on Mars may be different from Earth. Slab subduction inside Mars may be hindered if the density of Martian eclogite is smaller than the ambient Martian mantle.

To evaluate this hypothesis, we have carried out high *P*-*T* phase equilibrium experiments for 3 different Martian basalts with the compositions of Yamato 980459, GUSEV basalt (Humphrey), and NWA 8159 along a typical Martian areotherm (Longhi et al., 1992). Yamato 980459, a nearly primitive Martian basalt with a bulk composition similar to the average composition of all Ol-phyric shergottites (White et al., 2006), may be representative of Martian crust considering the limited magmatic differentiation on Mars (Collinet et al., 2021;

Filiberto and Dasgupta, 2011; McSween et al., 2009). NWA 8159 (~2370 Ma), one of the oldest Martian meteorites, is significantly Fe-enriched (~21 wt% FeO) and may represent an evolved part of the crust formed early in Mars history (Herd et al., 2017). The GUSEV basalt (Humphrey), the least weathered picritic basalt in the GUSEV crater on the Martian surface, has been analyzed by the Spirit Rover (McSween et al., 2006). Based on our experimental results on Yamato 980459 and Bertka and Fei (1997)'s experimental results on the ambient Martina mantle, we further compare density and seismic velocities of Yamato 980459 and the ambient Martian. Finally, we model the Martian slab sinking torques in different evolution stages of Martian geological history to further evaluate effects of slab temperatures and structures in driving subduction.

References

Frost, D. J. (2008). The upper mantle and transition zone. Elements, 4(3), 171-176.

Ishii, T., Kojitani, H. & Akaogi, M. Phase relations and mineral chemistry in pyrolitic mantle at 1600–2200 °C under pressures up to the uppermost lower mantle: Phase transitions around the 660-km discontinuity and dynamics of upwelling hot plumes. Physics of the Earth and Planetary Interiors 274, 127-137, doi:10.1016/j.pepi.2017.10.005 (2018).

Ritsema, J., Deuss, a. A., Van Heijst, H. & Woodhouse, J. S40RTS: a degree-40 shear-velocity model for the mantle from new Rayleigh wave dispersion, teleseismic traveltime and normal-mode splitting function measurements. Geophysical Journal International 184, 1223-1236 (2011).

Fukao, Y. & Obayashi, M. Subducted slabs stagnant above, penetrating through, and trapped below the 660 km discontinuity. Journal of Geophysical Research: Solid Earth 118, 5920-5938 (2013).

Inoue, T., Yurimoto, H., & Kudoh, Y. (1995). Hydrous modified spinel, Mg1. 75SiH0. 5O4: a new water reservoir in the mantle transition region. Geophysical Research Letters, 22(2), 117-120.

Fei, H. & Katsura, T. High water solubility of ringwoodite at mantle transition zone temperature. Earth and Planetary Science Letters 531, 115987 (2020).

Chang, S. J., & Ferreira, A. M. (2019). Inference on water content in the mantle transition zone near subducted slabs from anisotropy tomography. Geochemistry, Geophysics, Geosystems, 20(2), 1189-1201.

Huang, Q., Schmerr, N., Waszek, L., & Beghein, C. (2019). Constraints on seismic anisotropy in the mantle transition zone from long‐period SS precursors. Journal of Geophysical Research: Solid Earth, 124(7), 6779-6800.

Moulik, P., & Ekström, G. (2014). An anisotropic shear velocity model of the Earth's mantle using normal modes, body waves, surface waves and long-period waveforms. Geophysical Journal International, 199(3), 1713-1738.

Yuan, K., & Beghein, C. (2013). Seismic anisotropy changes across upper mantle phase transitions. Earth and Planetary Science Letters, 374, 132-144.

Coltice, N., Husson, L., Faccenna, C., Arnould, M., 2019. What drives tectonic plates? Science advances 5, eaax4295.

Tosi, N., Padovan, S., 2021. Mercury, Moon, Mars: Surface Expressions of Mantle Convection and Interior Evolution of Stagnant‐Lid Bodies. Mantle convection and surface expressions, 455-489.

Bertka, C.M., Fei, Y., 1997. Mineralogy of the Martian interior up to core-mantle boundary pressures. Journal of Geophysical Research: Solid Earth 102, 5251-5264.

Longhi, J., Knittle, E., Holloway, J.R., Waenke, H., 1992. The bulk composition, mineralogy and internal structure of Mars. Mars, 184-208.

White, D.S.M., Dalton, H.A., Kiefer, W.S., Treiman, A.H., 2006. Experimental petrology of the basaltic shergottite Yamato‐980459: Implications for the thermal structure of the Martian mantle. Meteoritics & Planetary Science 41, 1271-1290.

Collinet, M., Plesa, A.C., Grove, T.L., Schwinger, S., Ruedas, T., Breuer, D., 2021. MAGMARS: A Melting Model for the Martian Mantle and FeO-Rich Peridotite. Journal of Geophysical Research: Planets 126, e2021JE006985.

Filiberto, J., Dasgupta, R., 2011. Fe2+–Mg partitioning between olivine and basaltic melts: Applications to genesis of olivine-phyric shergottites and conditions of melting in the Martian interior. Earth and Planetary Science Letters 304, 527-537.

McSween, H.Y., Taylor, G.J., Wyatt, M.B., 2009. Elemental composition of the Martian crust. Science 324, 736-739.

Chapter II

The Water-Fe-Pressure dependent single-crystal elastic properties of wadsleyite: Implications for the seismic anisotropy in the upper Mantle Transition Zone

Abstract

Recent seismic studies suggested an anisotropic Mantle Transition Zone (MTZ) in areas adjacent to subducted slabs. Wadsleyite is the main anisotropy contributor in the upper MTZ, therefore the interpretation of these seismic observations requires the knowledge of single-crystal elastic moduli (C_{ij}s) and the deformation-induced lattice preferred orientation (LPO) of wadsleyite. Wadsleyite can host up to 3 wt% water in its crystal structure as point defects in the form of hydroxyl groups, however, the combined effect of water content, Fe content, and pressure on the C_{ij}s of wadsleyite remains unclear. In this study, we measured the high-pressure single-crystal elasticity of a synthetic hydrous Fe-bearing wadsleyite (0.14 (4) wt% water, Fe#=9.4, $Fe^{3+}/\Sigma Fe$=0.3) up to 18.2 (2) GPa. In combination with previous experimental data, we separated the effects of pressure, water, and Fe contents on the C_{ij}s and intrinsic elastic anisotropy of wadsleyite. Our results suggest that the intrinsic elastic anisotropy of wadsleyite decreases with pressure, water, and Fe contents. At 15 GPa, increasing the water content by 0.1 wt% or Fe# by 1 decreases the V_P and V_S anisotropy of wadsleyite by ~1.1-1.3%, and ~0.8-1.3% in average, respectively. Combined with the LPO determined in previous deformation experiments, we modeled the seismic anisotropy in the upper MTZ generated by a sub-vertical mantle flow near cold subducted slabs and a sub-horizontal mantle flow in the ambient mantle. In both scenarios, the LPO of wadsleyite leads to V_{SV} (vertically polarized shear wave velocity) > V_{SH} (horizontally polarized shear wave velocity). Our results suggest that wadsleyite may account for a weak anisotropic MTZ (<1%)

on the global scale. Considering the fact that water decreases the elastic anisotropy but promotes LPO of wadsleyite, seismic anisotropy may not be a good water sensor in the upper MTZ.

1. Introduction

The existence and magnitude of radial and azimuthal anisotropy in the Mantle Transition Zone (MTZ, ~410-660 km depth) on the global scale is highly controversial. A study using long-period surface wave overtones by Yuan and Beghein (2013) suggested that ~1% anisotropy is common throughout the MTZ, whereas other path integrated shear-wave splitting data are more consistent with the seismic anisotropy restricted to the upper mantle down to ~300 km (Savage, 1999). Many lines of evidence suggested that the seismic anisotropy of MTZ can be strong in the localized regions adjacent to some subducting slabs (Foley and Long, 2011; Chang and Ferreira, 2019; Huang et al., 2019). Interpretation of these global and local anisotropic seismic observations requires knowledge of the anisotropic elastic properties of relevant MTZ minerals.

Compared with other MTZ minerals, wadsleyite, which constitutes 50-60 vol% in pyrolite, is the major anisotropy contributor in the upper MTZ (~410-520 km depth). Garnet is nearly elastically isotropic (Jiang et al., 2004), and elastically anisotropic clinopyroxene only constitutes <10 vol.% at ~410 km depth and may completely dissolve into the garnet structure at ~500 km (Frost, 2008). As a result, lattice preferred orientation (LPO) of anisotropic wadsleyite under high pressure-temperature conditions is the most viable explanation for the seismic anisotropy observed in the upper MTZ.

Wadsleyite can host up to 3 wt% water (exists as hydroxyl in crystal structure instead of molecular water, Inoue et al., 1995) and its single-crystal elastic properties at high-pressure conditions have been determined in several previous studies. Hydrous Fe-bearing wadsleyite with different Fe and water contents were measured up to ~12 GPa and ~20 GPa by Mao et al. (2011) and Buchen et al. (2018), respectively (Fig. II.1), whereas anhydrous Fe-bearing wadsleyite was measured up to ~18 GPa by Wang et al. (2014) (Fig. II.2). Buchen et al. (2018) modeled the combined effects of Fe# ($100*Fe_{mol}/(Fe_{mol}+Mg_{mol})$) and water on the isotropic aggregate sound wave velocities of wadsleyite based on experimental data. First-principal calculation has also been employed to study the effect of Fe# on the single-crystal elastic properties of wadsleyite (Núñez-Valdez et al. 2011). However, the combined influences of water content, Fe#, and pressure on the single-crystal elastic properties and thus elastic anisotropy of wadsleyite remain poorly constrained. The strong softening of C_{44} and C_{12} inferred from the finite strain equation of state derived in Mao et al. (2011) was not observed by Buchen et al. (2018). As pointed out in Zhang et al. (2018), the softening of C_{44} and C_{12}, if true, would result in a strong increase of elastic anisotropy of wadsleyite at the MTZ depth range and potentially create detectable seismic signatures of anisotropy. Therefore, new measurements on hydrous Fe-bearing wadsleyite, in particular, the modeling of water-Fe-pressure effects using all the available single-crystal experimental data is needed to clarify this issue.

Wadsleyite can develop several different deformation-induced LPOs at 15-17 GPa under relatively low stress (<1 GPa), and the exact type depends on both the water content and temperature: Under normal upper MTZ temperatures, type I [0 0 1] (0 1 0) and type II [0 0 1]

(1 0 0) dominate when water contents are <0.05 wt% and >0.05 wt%, respectively; Under cold conditions (1550-1720 K), type III [1 0 0] (0 0 1) LPO develops (Ohuchi et al., 2014).

In this study, we determined the single-crystal elasticity of a new hydrous Fe-bearing wadsleyite sample up to 18.2 (2) GPa by Brillouin spectroscopy, and then performed systematic analysis based on all the available experimental data to separate the effects of water, Fe, and pressure on the single-crystal elasticity of wadsleyite. Finally, we combined the water-Fe-pressure dependent single-crystal elastic moduli ($C_{ij}s$) of wadsleyite with different deformation-induced LPOs determined in Ohuchi et al. (2014) to estimate the seismic anisotropy under different flow fields in the MTZ and compared it with seismic observations.

2. Methods

2.1. Sample synthesis and characterization

The hydrous Fe-bearing wadsleyite crystals were synthesized using the COMPRES 10/5 assembly in a 1000-ton Multi-Anvil Press at the University of Hawai‘i at Mānoa (UHM). We packed and sealed the small San Carlos olivine crystals with deionized water into a gold capsule. The crystals were synthesized at 1673 K and 16 GPa with a duration of 24 hours. The sizes of wadsleyite crystals in the run product range from 50 μm to 100 μm.

We measured the water weight content (wt%) of 9 wadsleyite platelets using the Thermal Fisher Nicolet Nexus 670 Fourier Transformed Infrared Spectrometer (FTIR) at the University of New Mexico (UNM). The narrow-band mercury-cadmium-telluride detector was cooled by liquid nitrogen before starting measurements. The unpolarized spectra with wavenumber ranging from 1500 to 4800 cm^{-1} were acquired by an IR light source and a CaF_2 beam splitter. The average water content for the synthetic wadsleyite is 0.14 (4) wt.% (see

Supplementary Information, Fig. II.S1 for details). We obtained the chemical composition of the synthetic wadsleyite sample by the Electron Probe Micro-Analysis (EPMA) using the JEOL 8200 Electron Microprobe facility at UNM (Table II.S1). The accelerating voltage is 15 kV and the beam current is 20 nA. The main element standards were Forsterite for Mg and Si, and Almandine for Fe. We also measured the $Fe^{3+}/\Sigma Fe$ of the synthetic wadsleyite samples using the Mössbauer spectrometer at the offline Mössbauer spectroscopy laboratory at sector 3, Advanced Photon Source (APS) in the Argonne National Laboratory (ANL). The data was obtained using constant acceleration mode, with a ^{57}Co/Pd source of approximately 5 mCi strength. Vortex silicon drift detector with an energy resolution of 150 eV at 14.4 keV was used to reduce the background. The data was analyzed using WinNormos (WISSEL Co.) program. The transmission Mössbauer spectrum of our sample is shown in Fig. II.S2. A two-site model corresponding to Fe^{2+} and Fe^{3+} hyperfine parameter values was used. Fe^{2+} site has an isomer shift of 1.04 mm/s, and quadrupole splitting of 2.6 mm/s. The Fe^{3+} site, on the other hand, has an isomer shift value of 0.36 mm/s and quadrupole splitting of 0.88 mm/s. These valence assignments are consistent with the literature values for 6-fold coordinated Fe (Dyar et al., 2006). The final chemical formula of the sample is determined as $Mg_{1.788}Fe^{2+}_{0.131}Fe^{3+}_{0.056}Al_{0.003}Mn_{0.003}Ni_{0.007}H_{0.022}Si_{0.986}O_4$ (Fe#=9.4(2)).

We polished 6 wadsleyite single crystals into thin platelets with size ~50 μm × 50 μm × 12 μm for single-crystal X-ray Diffraction experiments. These platelets are without scratches and inclusions after examination under a high magnification petrographic microscope. The unit cell parameters and orientations of the 6 polished wadsleyite crystals were determined by the single-crystal XRD experiments at 1) the GeoSoilEnviroCars (GSECARS) experimental station 13-BM-C at APS in ANL and 2) the X-ray Atlas Diffraction Lab at UHM. At 13-BM-

C, the X-ray beam was monochromated to 28.6 keV (0.434 Å) with 1 eV bandwidth. A Kirkpatrick-Baez mirror system was used to obtain a vertical × horizontal focus spot size of 12 μm × 18 μm, measured as full width at half maximum (FWHM). The MAR165 detector (Rayonix) was placed about 175 mm away from the sample, and LaB_6 powder at ambient conditions was used to calibrate the distance and tilting of the detector. The crystals were placed on a glass slide, we found that the tilting of the samples and glass slide was minimal by examining the laser beam reflected at the polished crystal surfaces and glass slide with 0º incident angle. The diffraction patterns were collected in the φ-scan geometry for a φ angle range of ± 23º with 1º step and 1 second exposure per frame. ATREX software package was used to extract the unit cell parameters and the orientation of each crystal. At the X-ray Atlas Lab, diffraction measurements were carried out on a customized Bruker D8 Venture diffractometer with a Phonon II detector, fixed-chi goniometer and Incoatec IμS 3.0 Ag Kα microfocus source with Helios focusing optics. Similar φ-scan geometry was used for the diffraction and the exposure time was 20 seconds per frame, and the Bruker APEX3 software was used to extract the lattice parameters. The ambient density (ρ_0) was calculated as 3.595(6) g/cm^3 based on the unit cell parameters of a=5.711(2) Å, b=11.453(6) Å, c=8.268(7) Å. To better constrain the 9 independent C_{ij}s, we performed a sensitivity test (see Supplementary Information) to choose the best combination of crystal orientations for Brillouin measurements. The plane normals of the 3 crystals we selected are (-0.3420 0.8718 0.3506), (-0.1013 -0.4397 0.8924), and (0.5341 0.0953 -0.8401) in the Cartesian coordinates. The angular uncertainties of the measured plane normals are within 0.5°, propagating to a velocity measurement uncertainty of <15 m/s, which is well under the Brillouin measurement precision of 30 m/s.

2.2 High-pressure Brillouin spectroscopy experiments and data analysis procedure

We used BX90 Diamond Anvil Cells (DAC) to generate high-pressure conditions. The slow directions of the two diamonds were pre-oriented to match each other. Rhenium gaskets were indented using the 350 μm-culet diamonds and 250 μm-diameter holes were drilled to create the sample chambers. The sample was loaded with two ruby spheres which acted as the pressure standards. A neon pressure-transmitting medium was gas-loaded into the sample chamber at GSECARS, APS, ANL. As part of the alignment process, we examined the tilting and non-parallelism of the sample and the diamonds in the DAC using the laser beam reflected at the polished crystal surfaces and diamond tables with 0˚ incident angle. The reflected laser beams match each other nicely, suggesting that the tilting and non-parallelism were minimal. The Brillouin spectroscopy experiments were performed at the Laser Spectroscopy Lab at UNM. A 532 nm single-mode diode-pumped solid-state laser was used as the light source for the Brillouin experiments. We used a 50° symmetric forward scattering geometry. Before the experiment, the scattering angle of the system was calibrated to be 50.47(8)° using a standard silica glass Corning 7980. A 6-pass tandem Fabry-Pérot interferometer was used to measure the Brillouin frequency shift. At each pressure condition, we measured the compressional wave (P-Wave) velocity (V_P) and shear wave (S-Wave) velocities (V_S) of the crystals every 15º along the 360° azimuth (Chi angles at 0, 15, 30, 45, 60, 75, 90, 105, 120, 135, 150, 165, 180, 195, 210, 225, 240, 255, 270, 285, 300, 315, 330, 345). The typical spectrums are shown in Fig. II.S4.

Given a starting $C_{ij}s$ model of wadsleyite, we calculated a set of phonon directions of each Brillouin measurement after fixing the plane normals for the selected three crystals. Based on the calculated phonon direction–measured V_P, V_S data set, we then calculated the best-fit

C_{ij}s model through a least-square inversion of the Christoffel equation (Speziale and Duffy, 2002). Afterwards, we recalculated the phonon directions of each measurement based on this newly obtained best-fit C_{ij}s model. The recalculated phonon directions and the velocities were used as the input again to calculate an updated C_{ij}s model for another round. This process was repeated2-3 times until the difference in root-mean-square (RMS) residuals of two successive runs is smaller than 0.1 m/s. We assigned an assumed density (ρ) in the starting C_{ij}s model to fit the high-pressure phonon direction–measured V_P, V_S data set, thus the inverted high-pressure C_{ij}s at this step are not the best-fit values and will need to be updated with the best-fit high-pressure ρ in a later step. However, based on these obtained high-pressure C_{ij}s with assumed ρ, we can calculate the best-fit K_S/ρ, G/ρ, thus V_P and V_S of wadsleyite aggregates under Voigt-Reuss-Hill (VRH) averaging scheme (Hill, 1963). The aggregate velocities are independent of the assumed high-pressure ρ and only depend on the experimentally measured velocities along different crystallographic directions (Zhang and Bass, 2016). We can then utilize the 4th order finite strain equation of state (EOS) (Equations S3-S20) to fit the lab-measured pressure-V_P-V_S data to derive K_{S0}' ($\partial K_{S0}/\partial P$), K_{S0}'' ($\partial^2 K_{S0}/\partial P^2$), G_0' ($\partial G_0/\partial P$), and G_0''($\partial^2 G_0/\partial P^2$) with fixed lab-measured ρ_0, K_{S0}, and G_0 (0 in the subscript represents ambient-condition) (Davies and Dziewonski, 1975), as well as the best-fit high-pressure ρ. Finally, we updated the C_{ij}s, K_S, and G at each high pressure with the obtained best-fit high-pressure ρ.

2.3. Water-Fe-Pressure-elasticity modeling and anisotropy indices

To systematically study the effects of water, Fe, and pressure on the elasticity of wadsleyite, we compiled the water content, Fe#, ρ, and single-crystal elasticity data (K_S, G, C_{ij}s, V_P, and V_S) of 8 different wadsleyite samples under different pressure conditions (Sawamoto et al., 1984; Zha et al., 1997; Mao et al., 2008a, b; Mao et al., 2011; Wang et al.,

2014; Buchen et al., 2018; this study; Table II.S2). The 8 wadsleyite samples cover a wide range of water content (0-2.9 wt%) and Fe# (0-11.2), and 6 wadsleyite samples have been measured at high-pressure conditions including this study.

We adopted the following procedures to separate the effects of water, Fe, and pressure on the single-crystal elastic properties of wadsleyite:

(1) To reduce the number of fitting parameters, we firstly fit the ρ_0, K_{S0}, G_0, and each $C_{ij,0}$ of wadsleyite with respect to water contents (wt%) and Fe#, which was sufficiently simple to be described by an empirical linear relationship of $\boldsymbol{B} = \boldsymbol{B_0} + \boldsymbol{B_1} \times$ water (wt%) $+ \boldsymbol{B_2} \times$ Fe#;

(2) Given the ρ_0, K_{S0}, G_0, and $C_{ij,0}$ as well as their compositional dependence derived in step (1), the ambient thermoelastic properties of the 6 samples that have been measured at high-pressure conditions were fixed in the subsequent inversion process. After extensive testing (see Supplementary Information), we chose to fit the K_{S0}' and G_0' as compositional dependent with respect to water content or Fe#, and fix the K_{S0}'' and G_0'' to the values determined for the hydrous Fe-bearing wadsleyite measured in this study. We utilized 4th order finite strain EOS, and subsequently calculated the compositional dependence of each $C_{ij,0}'$ ($\partial C_{ij,0}/\partial P$) and $C_{ij,0}''$ ($\partial^2 C_{ij,0}/\partial P^2$). The equations utilized are shown in the Supplementary Information as equations S3-S20.

To further verify the reliability of our inverted water-Fe-pressure dependent single-crystal elasticity model of wadsleyite, we compared the model-predicted values of C_{ij}s, K_S, G, V_P, and V_S at different pressures for all 8 wadsleyite samples with the experimentally determined values we compiled from previous studies (Table II.S3). The differences are mostly within 2% and 5% for aggregate elastic properties and C_{ij}s, respectively (**Fig. II.3**). The

pressure derivatives of the K_S, G, and $C_{ij}s$ calculated from our model are also consistent with the individually inverted values from our Brillouin experiments within uncertainty (Table II.S4). It is important to note that extrapolation to the composition and pressure range far beyond what has been experimentally investigated might lead to unreliable predictions. The accuracy of our modeling results can be improved with more high-pressure experimental data on wadsleyite in the future, especially those with water content higher than 2 wt%.

Buchen et al. (2017) has pointed out the possible effect of Fe^{3+} on the single-crystal elastic properties of wadsleyite. In this study, we chose to not separate the effect of Fe^{3+} from Fe^{2+} primarily due to the following 2 reasons: 1) Only 3 single-crystal sound velocity measurements exist for Fe-bearing wadsleyite with known $Fe^{3+}/\Sigma Fe$ (Mao et al., 2011, Buchen et al., 2018, this study). With limited experimental data, it is difficult for us to separate the effects of Fe^{2+}, Fe^{3+}, pressure, and water together. 2) The calculated effects of $Fe^{3+}/\Sigma Fe$ =0.3 in our sample on its isothermal bulk modulus (1 GPa) and linear elastic moduli (3-5 GPa) at ambient condition are significantly smaller than the estimated uncertainties of the isothermal bulk modulus (2-49 GPa), and linear elastic moduli (7-464 GPa) for the 4-end members of wadsleyite given in Buchen et al. (2017). Although quantitative analysis on the effect of Fe^{3+} is challenging based on the currently available experimental data, future studies on Fe-rich wadsleyite with higher Fe^{3+} concentration can help to further clarify this issue.

We subsequently derived the $C_{ij}s$, K_S, G, V_P, and V_S as well as several anisotropy indices in the parameter space spanned by typical water contents (0-3 wt% H_2O), Fe contents (Fe# 0-15), and relevant pressures (0-18 GPa) using the 4^{th} order finite strain EOS.

The anisotropy indices we used are: Universal Anisotropy (A^U), which refers to the overall elastic anisotropy of minerals (Ranganathan and Ostoja-Starzewski, 2008). The

superscripts R and V denote the Reuss and Voigt bounds of the homogeneous isotropic aggregate (Hill, 1963).

$$A^{\mathrm{U}} = (5\frac{G^{\mathrm{V}}}{G^{\mathrm{R}}} + \frac{{K_S}^{\mathrm{V}}}{{K_S}^{\mathrm{R}}} - 6) * 100\ (\%)$$

V_{P} azimuthal anisotropy (A^{Vp}), which represents the maximum velocity difference of all Vp propagating along all directions, is defined as

$$A^{\mathrm{Vp}} = \frac{V\mathrm{p}_{max} - V\mathrm{p}_{min}}{V\mathrm{p}_{max} + V\mathrm{p}_{min}} * 200\ (\%)$$

V_{S} azimuthal anisotropy (A^{Vs}), which represents the maximum difference of all Vs propagating along all directions, is defined as

$$A^{\mathrm{Vs}} = \frac{V\mathrm{s}_{max} - V\mathrm{s}_{min}}{V\mathrm{s}_{max} + V\mathrm{s}_{min}} * 200\ (\%)$$

V_{S} radial anisotropy (D^{Vs}), which represents the maximum velocity difference between V_{S1} and V_{S2}, V_{S1} represents speed of fast S-Wave and V_{S2} represents speed of slow S-Wave propagating along the same direction but with different polarizations.

$$D^{\mathrm{Vs}} = (\frac{|V\mathrm{s}_1 - V\mathrm{s}_2|}{V\mathrm{s}_1 + V\mathrm{s}_2})_{max} * 200\ (\%)$$

3. Results

3.1. Single-crystal elasticity of the hydrous Fe-bearing wadsleyite measured in this study

For the synthetic wadsleyite sample (0.14 wt% water, Fe#=9.4, $Fe^{3+}/\Sigma Fe$=0.3) measured in this study, using the data analysis procedure outlined in Section 2.2, we determined its K_{S0}, G_0, K_{S0}', K_{S0}'', G_0' and G_0'' as 165 (2) GPa, 104 (2) GPa, 5.2 (5), -0.16

(11) GPa^{-1}, 1.9 (2), and -0.076 (28) GPa^{-1}, respectively. The calculated aggregate elastic properties using the 4th order finite strain EOS based on these parameters match well with our experimentally determined values (Fig. II.1, II.2, II.3). The values of $C_{ij}s$ at each pressure in this study are listed in Table II.1 and can be fit well using the 3rd or 4th order finite strain EOS (Fig. II.1). The velocities predicted by the best-fit $C_{ij}s$ at high-pressure conditions match the experimentally measured velocities of the 3 wadsleyite crystals with RMS error less than 45 m/s (Fig. II.S5).

The softening of C_{44} and C_{12} starting at ~8 GPa inferred by the finite strain EOS reported in Mao et al. (2011) is not observed in our data (Fig. II.1). In this study, $C_{44,0}$ is obtained as 106 (2) GPa with $\partial C_{44,0}/\partial P$ = 0.89 (5); $C_{12,0}$ is derived as 75 (1) GPa with $\partial C_{12,0}/\partial P$ = 4.8 (2) and $\partial C_{12,0}^2/\partial^2 P$ = -0.15 (2) GPa^{-1}.

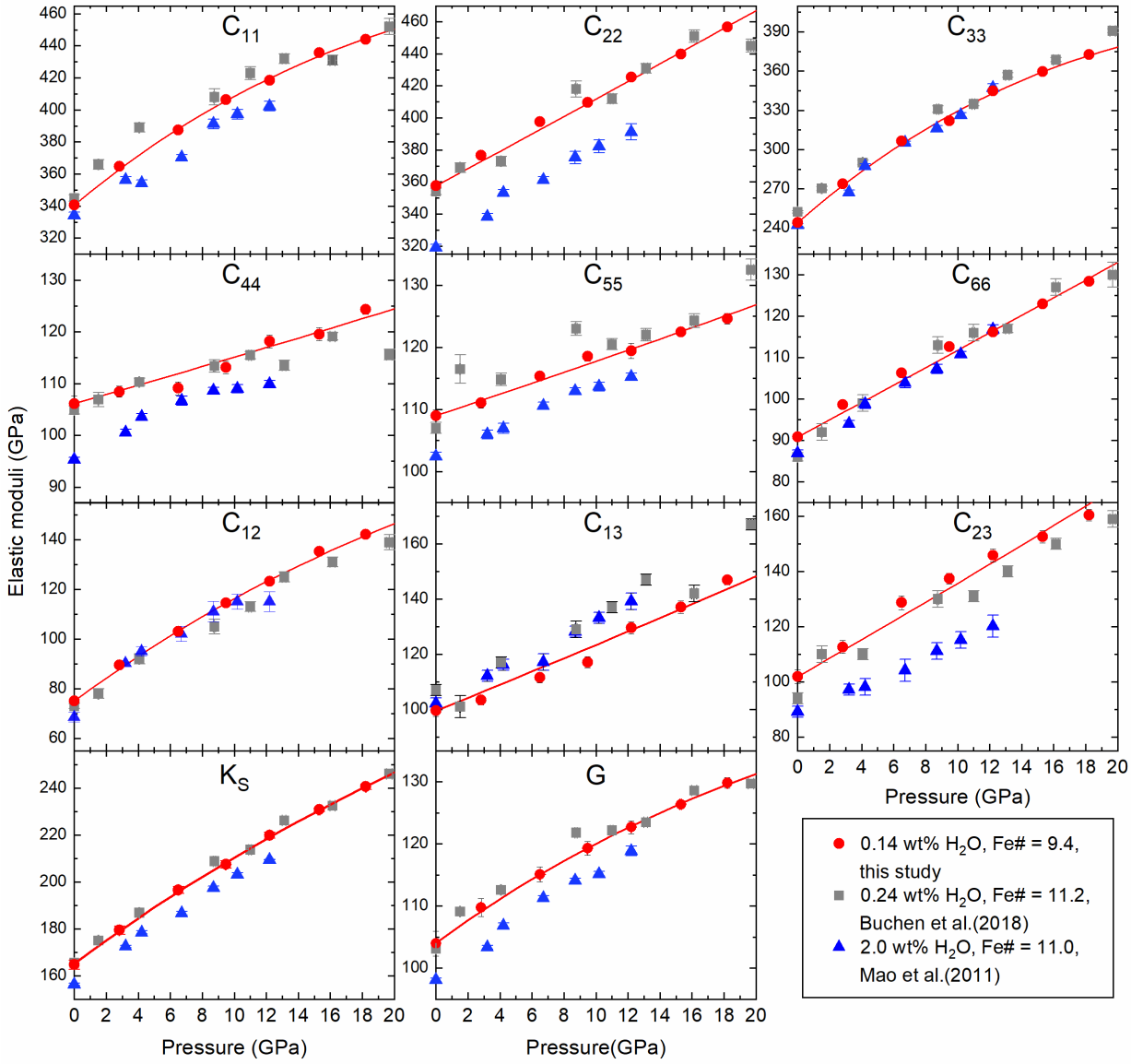

Fig. II.1. *C_{ij}s, K_S, and G of three different hydrous Fe-bearing wadsleyite samples as a function of pressure. Solid lines represent 3rd or 4th order finite strain EOS fitting results for the wadsleyite sample measured in this study. VRH averaging scheme is used to calculate the Ks and G of isotropic polycrystalline aggregates in this study.*

Table II.1. *C_{ij}s, K_S, G, V_P, and V_S for the hydrous Fe-bearing wadsleyite sample (0.14 wt% water, Fe#=9.4, $Fe^{3+}/\Sigma Fe$=0.3) measured in this study.*

Pressure	**1.0 atm**	**2.9(1) GPa**	**6.6(1) GPa**	**9.5(1) GPa**	**12.2(1) GPa**	**15.4(1) GPa**	**18.2(2) GPa**
ρ(g/cm3)	3.595(6)	3.656	3.729	3.783	3.831	3.886	3.933
C_{11}(GPa)	341(1)	364(1)	387(1)	406(1)	418(1)	436(1)	444(1)
C_{22}(GPa)	358(1)	376(1)	397(1)	410(1)	425(2)	440(1)	457(1)
C_{33}(GPa)	244(2)	273(2)	307(2)	322(2)	345(2)	360(2)	373(2)
C_{44}(GPa)	106(2)	108(1)	109(1)	113(1)	118(1)	120(1)	124.3(9)
C_{55}(GPa)	109(1)	111(1)	115(1)	119(1)	119(1)	122.5(7)	124.6(9)
C_{66}(GPa)	90.8(7)	98.5(6)	106.3(7)	112.6(6)	116.1(8)	123.0(7)	128.4(5)
C_{12}(GPa)	75(1)	89(1)	103(1)	114(1)	123(1)	135(1)	142(1)
C_{13}(GPa)	99(2)	103(2)	112(2)	117(2)	129(2)	137(2)	147(2)
C_{23}(GPa)	102(3)	112(2)	129(2)	137(2)	146(2)	153(2)	160(2)
K_S^{VRH}(GPa)	165(2)	179(2)	197(1)	207(1)	220(1)	231(1)	241(1)
G^{VRH}(GPa)	104(2)	110(1)	115(1)	119(1)	123(1)	126(1)	130(1)
V_P(km/s)	9.19(3)	9.43(2)	9.69(2)	9.84(1)	10.00(1)	10.14(1)	10.26(1)
V_S(km/s)	5.38(3)	5.47(2)	5.56(2)	5.62(1)	5.66(1)	5.70(1)	5.75(1)

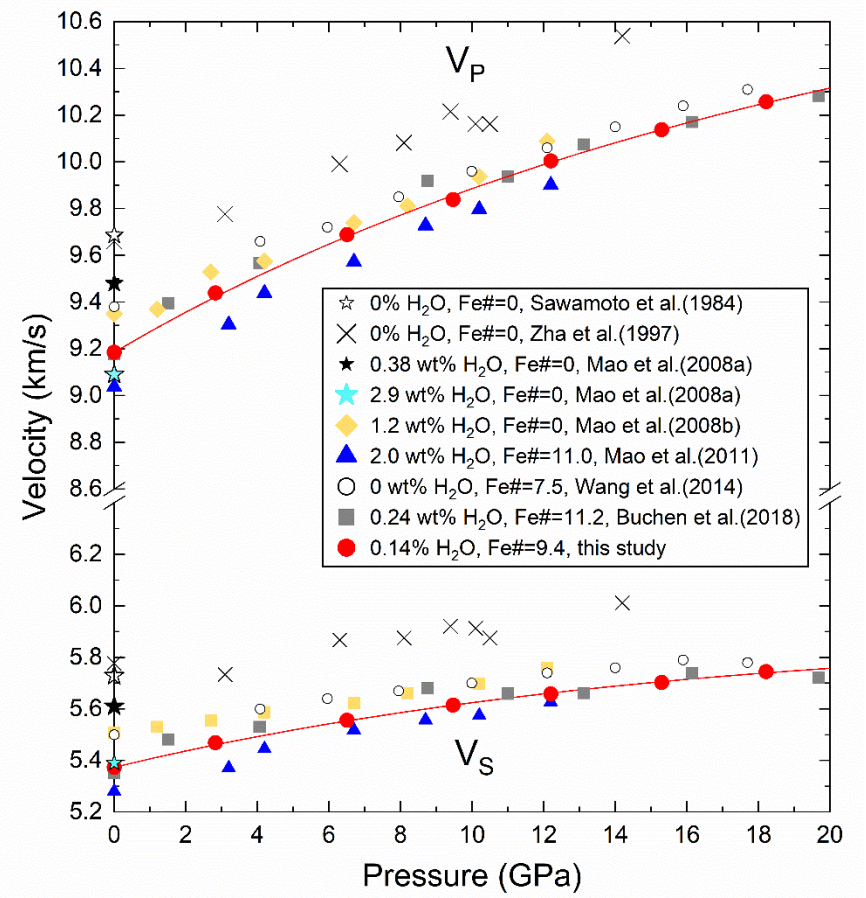

Fig. II.2. *Experimentally determined V_P and V_S of isotropic polycrystalline wadsleyite aggregates from single-crystal Brillouin spectroscopy experiments compiled and utilized in this study. The water contents of wadsleyite samples in Mao et al. (2008a, b) and Mao et al. (2011) were updated to values re-examined by Chang et al. (2015). Solid lines represent the 4^{th} order finite strain EOS fitting results for the wadsleyite sample measured in this study calculated from the best-fit C_{ij}s model under VRH averaging scheme.*

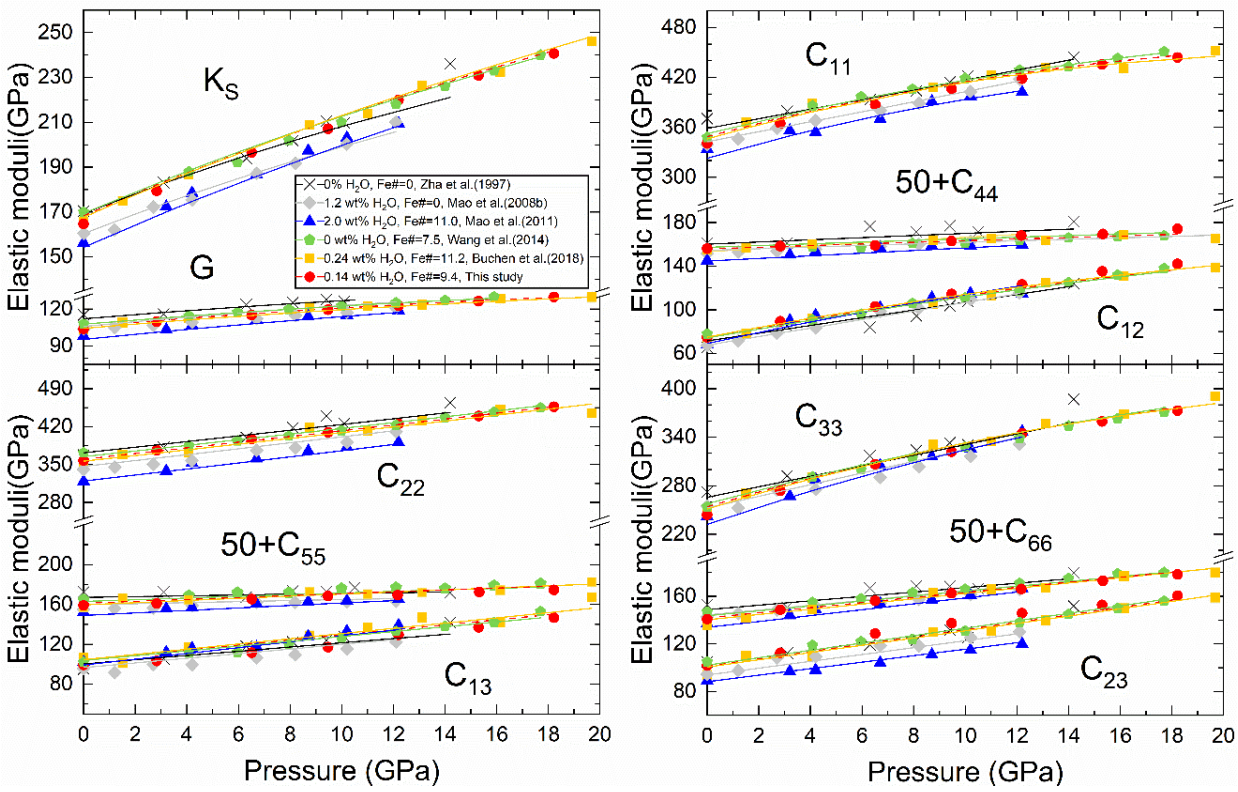

Fig. II.3. *Comparison between input Ks, G, C_{ij}s of wadsleyite (symbols) and model-predicted values (lines).*

3.2. The water-Fe-pressure dependent single-crystal elasticity model of wadsleyite

Based on the modeling method described in section 2.3, the compositional dependence of the ρ, K_{S0}, G_0, $C_{ij,0}$, and their pressure derivatives are listed in Table II.S5 and Table II.2.

3.2.1 The effects of water, Fe, and pressure on C_{ij}s

Similar to olivine, water decreases all $C_{ij,0}$ in wadsleyite (Fig. II.S6, Table II.2). The addition of 1 wt% water to Fe-free wadsleyite reduces its $C_{ij,0}$ by ~3-7%, whereas the reduction of $C_{ij,0}$ caused by the same amount of water for Fe-free olivine is only ~1-4% (Jacobsen et al., 2008). Among all the C_{ij}s of wadsleyite at ambient condition, C_{22} and C_{23} are most sensitive

to the water, whereas C_{12} and C_{13} are the least sensitive ones (Table II.2). In comparison, increasing Fe# of wadsleyite by 10 only decreases diagonal $C_{ij,0}$ by ~2-7% (Table II.2).

Table II.2. *Effects of adding 1 wt% water or increasing Fe# by 10 on the elastic properties of the dry Mg-endmember wadsleyite at 0 GPa and 300 K (one can calculate the effects of water or Fe for different wadsleyite samples based on the parameters listed in Table II.S5). "\" denotes that the influence is negligible.*

	Add 1 wt% water	**Increase Fe# by 10**
$\boldsymbol{C_{11,0}}$	↓ by 4%	↓ by 3%
$\boldsymbol{C_{22,0}}$	↓ by 6%	↓ by 2%
$\boldsymbol{C_{33,0}}$	↓ by 4%	↓ by 4%
$\boldsymbol{C_{44,0}}$	↓ by 5%	↓ by 3%
$\boldsymbol{C_{55,0}}$	↓ by 5%	↓ by 4%
$\boldsymbol{C_{66,0}}$	↓ by 4%	↓ by 7%
$\boldsymbol{C_{12,0}}$	↓ by 4%	↑ by 6%
$\boldsymbol{C_{13,0}}$	↓ by 3%	↑ by 5%
$\boldsymbol{C_{23,0}}$	↓ by 7%	\
$\boldsymbol{K_{S0}}$	↓ by 4%	\
$\boldsymbol{K_{S0}'}$	\	↑ by 13%
$\boldsymbol{K_{S0}''}$	\	\
$\boldsymbol{G_0}$	↓ by 5%	↓ by 5%
$\boldsymbol{G_0'}$	↑ by 10%	\
$\boldsymbol{G_0''}$	\	\

Water in wadsleyite increases all $C_{ij,0}'$ except $C_{23,0}'$, Fe increases all $C_{ij,0}'$ except $C_{44,0}'$ and $C_{23,0}'$ (Table II.S5). Therefore, the high-pressure C_{ij} is determined by the two competing factors: Increasing water and Fe contents reduces $C_{ij,0}$ yet elevates $C_{ij,0}'$. Under the high-

pressure condition of the upper MTZ (14-18 GPa, Fig. II.S6), water reduces C_{11}, C_{22}, C_{55} yet increases C_{23}; Fe reduces C_{11}, C_{44} yet increases C_{55}, C_{12}, C_{13}. Both C_{33} and C_{66} are relatively insensitive to the water and Fe contents. The modeling of the water and Fe effects on C_{44} and C_{12} further suggests that the strong softening of C_{44} and C_{12} at MTZ pressures, implied from the finite strain EOS derived in Mao et al. (2011), might be a fitting artifact, since the set of EOS in this study without showing such softening could fit the experimental data in Mao et al. (2011) reasonably well.

3.2.3 The effects of water, Fe, and pressure on K_S, G, V_P, and V_S

The incorporation of water in wadsleyite decreases both K_{S0} and $G_{0,}$ whereas increasing Fe# only decreases G_0 (Fig. II.4, Table II.2), which is consistent with previous studies (Mao et al., 2008a; Wang et al., 2014; Hazen et al., 2000).

Chang et al. (2015) found that water has no resolvable effect on pressure derivative of isothermal bulk modulus by performing high-pressure X-ray diffraction experiments on different hydrous wadsleyite crystals loaded in the same DAC. However, Buchen et al. (2018) suggested water increases K_{S0}' after comparing the K_{S0}' for their less hydrated wadsleyite with the K_{S0}' for a more hydrated sample measured in Mao et al. (2011). In this study, after removing the effect of Fe, our modeling results suggest that the increase of K_{S0}' caused by hydration is minimal. However, water in wadsleyite does increase G_0', so the softening effect of water on G is smaller at higher pressures while the effect of water on K_S persists to high pressure. On the other hand, increasing Fe# of wadsleyite would only increase K_{S0}' whereas it has no distinguishable effect on G_0', so the effect of Fe on G remains at high-pressure conditions. Interestingly, adding Fe increases K_S of wadsleyite at high-pressure conditions, possibly related to a stronger Fe-O bond than Mg-O bond, or stronger geometrical constraints

after replacing Mg with Fe in the wadsleyite crystal structure under high pressure (Hazen et al., 2000; Buchen et al, 2017). In addition, the existence of Fe^{3+}

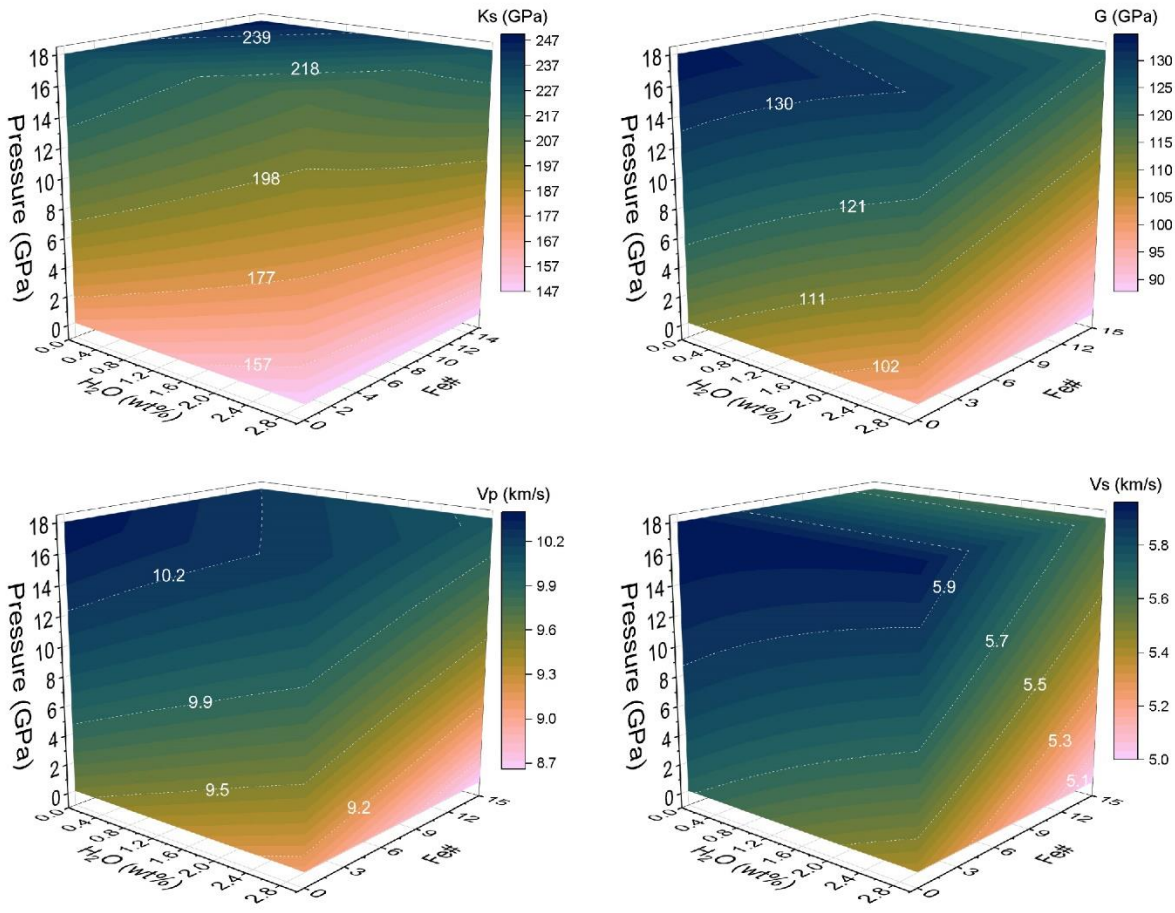

Fig. II.4. *The water, Fe, and pressure–dependent Ks, G, V_P, and V_S of isotropic polycrystalline wadsleyite aggregates under VRH averaging scheme (the batlow color scale is from Crameri, 2020).*

rather than Fe^{2+} may soften the structure of wadsleyite along a axis under ambient condition (Buchen et al., 2017), although the modeling in the present study did not take the effect of valance state of Fe into account.

To summarize, at 14-18 GPa, water decreases the K_S, G, ρ, V_P, and V_S, whereas Fe decreases G, V_P, Vs but increases the K_S and ρ (Fig. II.4).

3.2.4 The effects of water, Fe, and pressure on intrinsic anisotropy of wadsleyite

Our data suggest that the incorporation of water in wadsleyite reduces its intrinsic anisotropy monotonically (Fig. II.5, Table II.3). However, increasing Fe# of wadsleyite decreases A^U, A^{Vp}, and D^{Vs} monotonically but its effect on A^{Vs} depends on the water content and pressure (Fig. II.5). For example, A^{Vs} for dry wadsleyite at 15 GPa decreases with Fe# from 0 to ~3, then increases with Fe# from ~3 to 15. Pressure decreases the anisotropy of wadsleyite significantly through most of the investigated pressure range (Fig. II.5). Increasing pressure from ambient condition to 15 GPa would reduce A^{Vp}, A^{Vs}, and D^{Vs} of wadsleyite by 40-50% (Table II.3).

Table II.3. *Average decrease of the elastic anisotropy caused by 1) increasing pressure from 0 to 15 GPa 2) adding 1 wt% water at 15 GPa and 300 K 3) increasing Fe# by 10 at 15 GPa and 300 K.*

	1) Increase Pressure from 0 GPa to 15 GPa	**2) Add 1 wt% water (at 15 GPa, 300K)**	**3) Increase Fe# by 10 (at 15 GPa, 300K)**
$\boldsymbol{A^U}$	↓ by ~72%	↓ by ~25%	↓ by ~19%
$\boldsymbol{A^{Vp}}$	↓ by ~50%	↓ by ~13%	↓ by ~8%
$\boldsymbol{A^{Vs}}$	↓ by ~49%	↓ by ~13%	↓ by ~13%
$\boldsymbol{D^{Vs}}$	↓ by ~40%	↓ by ~11%	↓ by ~11%

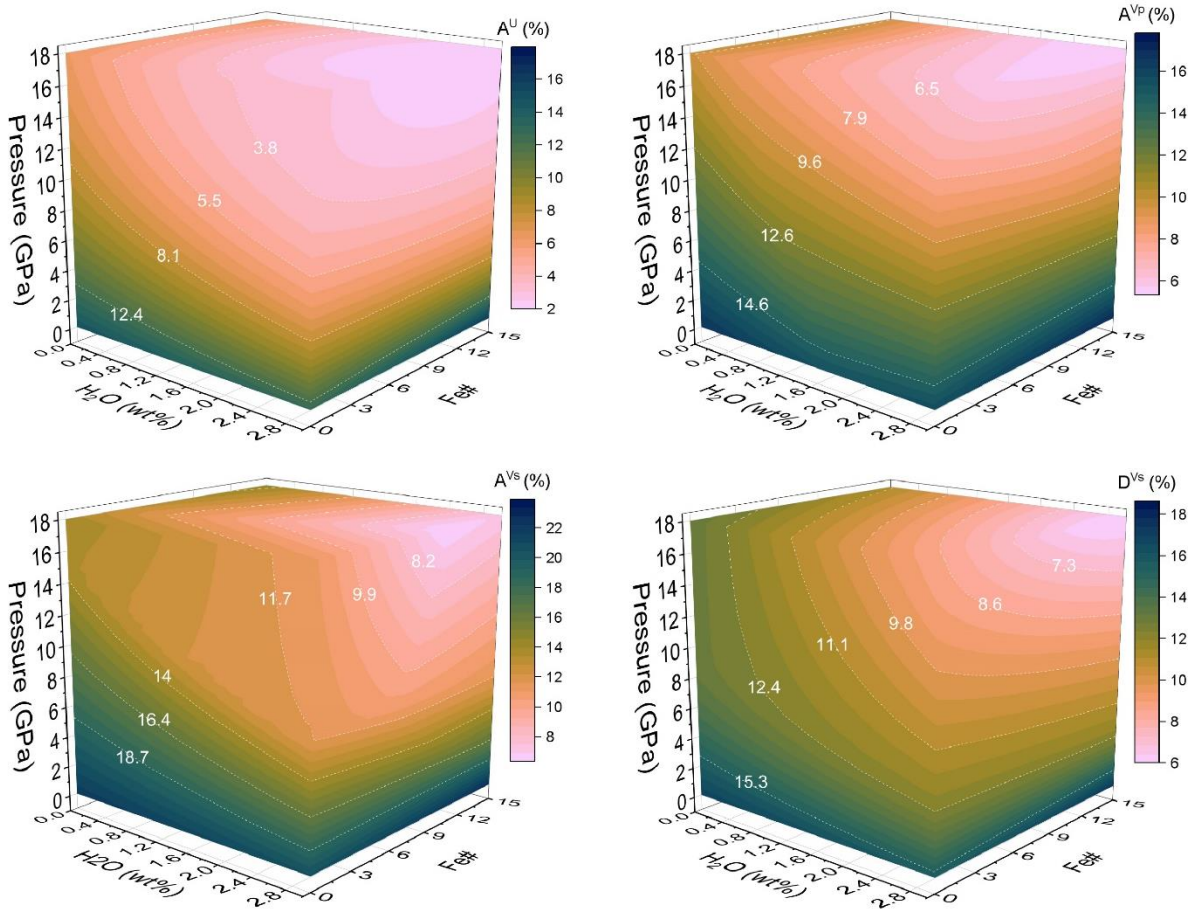

Fig. II.5. *The water, Fe, and pressure–dependent intrinsic anisotropy of single-crystal wadsleyite.* A^U *is universal anisotropy,* A^{Vp} *is Vp azimuthal anisotropy,* A^{Vs} *is Vs azimuthal anisotropy,* D^{Vs} *is radial anisotropy.*

4. Discussion

4.1 Compositional dependent elastic properties of single-crystal wadsleyite

To understand how water, Fe, and pressure influence acoustic velocities along different crystallographic directions of wadsleyite, we plotted the acoustic velocity surfaces for different single-crystal wadsleyite compositions derived from our water-Fe-pressure dependent single-crystal elasticity model using the MTEX software package (Mainprice, 2011).

For Fe-free dry wadsleyite at ambient condition (Fig. II.6a), the fastest V_P is along [0 1 0] direction whereas the slowest V_P is along [0 0 1], because $C_{22}>C_{11}>C_{33}$. The fastest and slowest Vs propagation directions are along [0.6930 0.7199 0.0372] and [-0.5439 -0.4842 -0.6853] directions, which are close to [1 1 0] and [1 1 1] direction, respectively. The maximum V_S splitting direction is along [-0.5690 -0.6175 -0.5431], close to the direction of the slowest V_S propagation direction [1 1 1]. The velocity maximum and minimum directions for both V_P and V_S are insensitive to pressure (Fig. II.6a and II.6b).

After incorporating 1.5 wt% water to the Fe-free wadsleyite at 15 GPa (Fig. II.6b and II.6c), the fastest direction changes from [0 1 0] to [1 0 0] and the maximum V_P value drops from 10.9 km/s to 10.8 km/s. This is caused by the greater reduction of C_{22} than C_{11} caused by water. On the contrary, the slowest V_P value (9.9 km/s) and direction ([0 0 1]) remain almost the same after adding water in the crystal structure because C_{33} is relatively insensitive to water. Therefore, adding water decreases A^{Vp}. The higher sensitivity of C_{22} to water content compared with C_{33} is consistent with the fact that the unit cell parameters b and c are the most and least sensitive parameters to the water content, respectively (Holl et al., 2008; Buchen et al, 2017). On the other

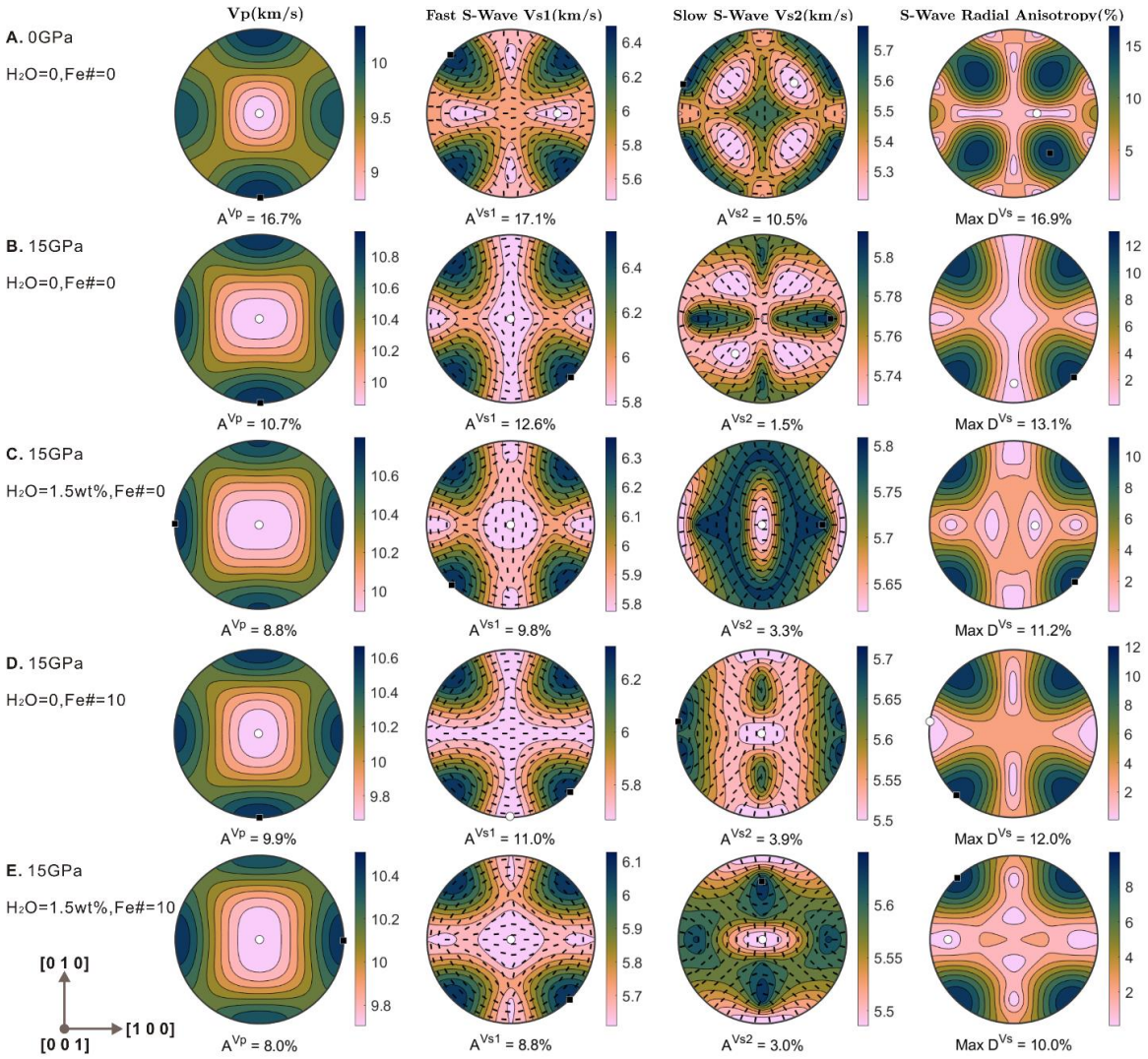

Fig. II.6. *Acoustic velocities along different crystallographic directions in stereographic projections for (A) dry wadsleyite with Fe#=0 at 0 GPa, (B) dry wadsleyite with Fe#=0 at 15 GPa, (C) hydrous wadsleyite with Fe#=0 at 15 GPa, (D) dry wadsleyite with Fe#=10 at 15 GPa, (E) hydrous wadsleyite with Fe#=10 at 15 GPa. Black and white dots represent the positions of the maximum and minimum velocities, respectively; The black short lines in fast S-wave* V_{S1} *and slow S-wave* V_{S2} *plots indicate the polarization directions. The crystallographic axes are shown in the bottom left corner.* A^{Vp}, A^{Vs1} *and* A^{Vs2} *refer to the maximum anisotropy values.*

hand, the fastest V_S direction remains unchanged with higher water content, and the slowest V_S direction changes to [0 0 1] for hydrous wadsleyite (Fig. II.6b and II.6c).

With Fe# of wadsleyite changing from 0 to 10, the fastest and slowest V_P directions as well as the fastest Vs direction remain almost unchanged (Fig. II.6b and II.6d). However, the slowest V_S direction changes from [1 1 1] to [0 0 1]. Fe decreases the A^{Vp} because Fe affects C_{22} more than C_{33} (Fig. II.S6).

4.2 Seismic properties of deformed wadsleyite aggregates

Combining our modeled water-Fe-pressure dependent $C_{ij}s$ with the experimentally determined deformation-induced LPOs of wadsleyite aggregates from Ohuchi et al. (2014), we calculated the anisotropic seismic properties of deformed wadsleyite aggregates utilizing the MTEX software package (Fig. II.7). The $C_{ij}s$ of wadsleyite used here are calculated at 15 GPa 300 K due to the lack of high pressure-temperature single-crystal elasticity measurements of wadsleyite. The deformation-induced LPOs of wadsleyite aggregates are measured by Electron Back Scattering Diffraction in Ohuchi et al., 2014, including sample M0327 for the type I [0 0 1] (0 1 0) fabric, sample M0310 for the type II [0 0 1] (1 0 0) fabric, samples Y0313 and M0308 for the type III fabric [1 0 0] (0 0 1). The type-II and type-III LPOs presented in Ohuchi et al. (2014) are based on deformation experiments on hydrous wadsleyite aggregates with water content limited to 0.3 wt%. The updated anisotropy modeling results using the $C_{ij}s$ model in this study for wadsleyite with 0.3 wt% water are shown in Fig. II.S8. However, in a hydrated mantle near subduction zones, the water content in wadsleyite might be higher than that considering the relatively large amount of water supply and the low-temperature condition in the subduction zones (Bercovici and Karato, 2003). Therefore, as an extreme end member case, we performed the anisotropy modeling on hydrous wadsleyite aggregates containing ~1.5 wt%

water, under the assumption that they would develop the same fabrics as the less hydrated wadsleyite aggregates used in Ohuchi et al. (2014) (Fig. II.7).

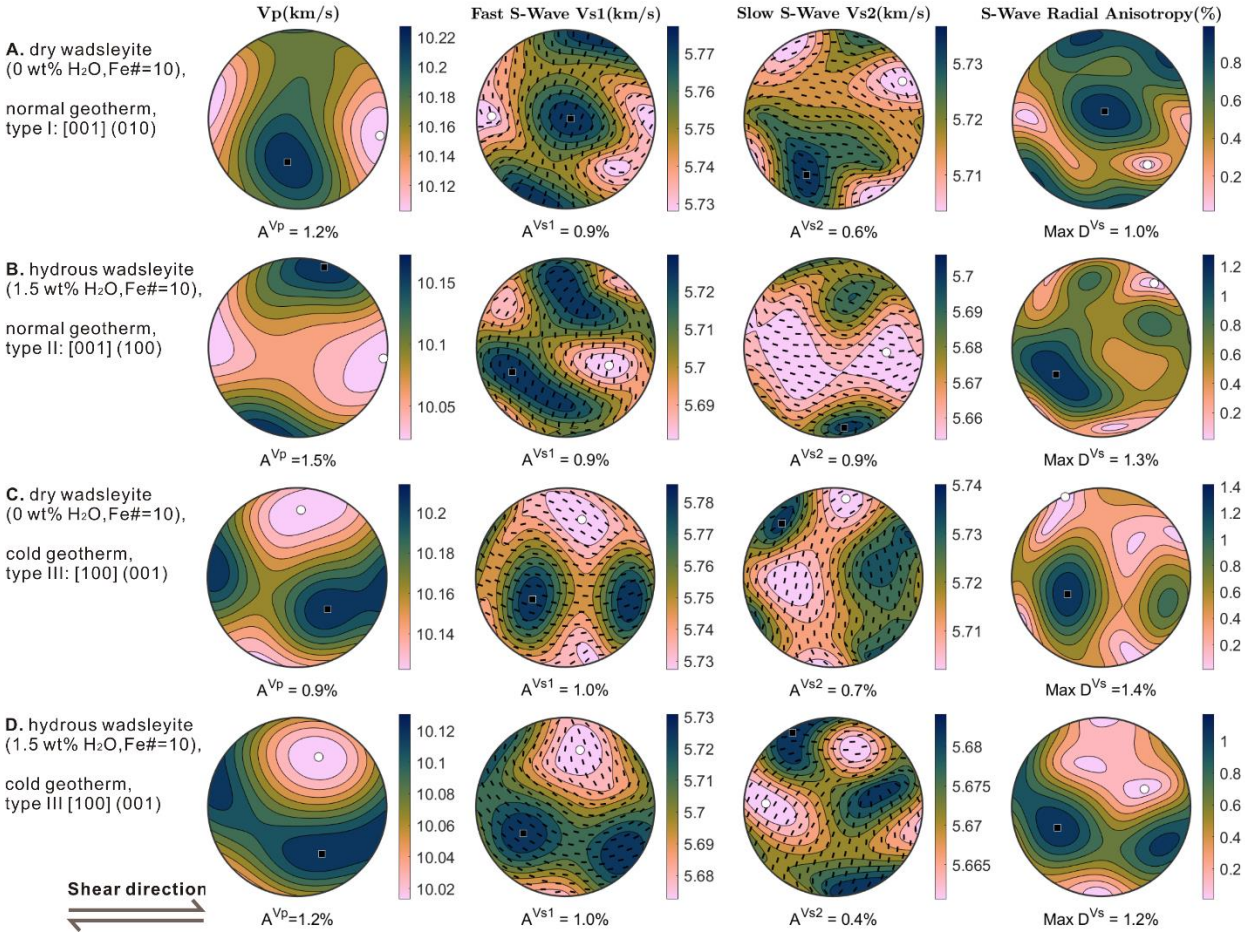

Fig. II.7. *The calculated acoustic velocities in stereographic projections for (A) dry wadsleyite aggregate with type I LPO (M0327), (B) hydrous wadsleyite aggregate with type II LPO (M0310), (C) dry wadsleyite aggregate with type III LPO (Y0313), (D) hydrous wadsleyite aggregate with type III LPO (M0308). The LPO data are from Ohuchi et al. (2014). The shear plane normal is north-south. The geometrical relationship between* V_{SV} *and* V_{SH} *is shown in Fig. II.S7.* A^{Vp}, A^{Vs1} *and* A^{Vs2} *refer to the maximum anisotropy values.*

Under the normal upper MTZ temperatures (~1800 K), type-I and type-II fabrics of wadsleyite are more likely to develop with [0 0 1] axis of wadsleyite sub-parallel to the shear direction (Ohuchi et al., 2014). As discussed in section 4.1, [0 0 1] is always the slowest V_P direction of wadsleyite which is unlikely to be influenced by the water or Fe contents, so both the dry wadsleyite aggregate with type-I fabric and hydrous wadsleyite aggregate with type-II fabric show the slowest V_P direction along the shear direction (Fig. II.7). Under lower temperatures (1473-1713 K), type III fabric is developed with [1 0 0] axis of wadsleyite parallel to the shear direction (Ohuchi et al., 2014). [1 0 0] is a fast V_P direction for dry wadsleyite and the fastest one for hydrous wadsleyite, so both dry wadsleyite aggregate and hydrous wadsleyite aggregate with type-III fabric show the fastest V_P direction sub-parallel to the shear direction.

Constraining V_{SH} (horizontally polarized shear wave velocity)/V_{SV} (vertically polarized shear wave velocity) for wadsleyite aggregates under a vertical flow or a horizontal flow can help us understand the mantle flow field based on seismic observations. Higher mode surface waves have been used by seismic studies to constrain the V_{SH}/V_{SV} in the MTZ (Panning and Romanowicz, 2006; Visser et al., 2008). The polarization of V_{SV} is sub-perpendicular to the Earth's surface and the polarization of V_{SH} is sub-parallel to the Earth's surface (Fig. II.S7). In this study, we assumed V_{S1} is the fast V_S and V_{S2} is the slow V_S propagating along the same direction. For wadsleyite aggregates developing type-I and -II fabrics under normal MTZ temperatures (Fig. II.7a, II.7b), V_{S1} is V_{SV} assuming a horizontal mantle flow field while V_{S1} is V_{SH} in a vertical mantle flow field (Fig. II.S7). Therefore, wadsleyite aggregate with type-I and -II fabrics results in $V_{SV} > V_{SH}$ in a horizontal flow field, whereas $V_{SV} < V_{SH}$ is expected in a vertical flow field. Visser et al. (2008) and French and Romanowicz (2014) both suggested

$V_{SV} > V_{SH}$ as a global feature in the MTZ, which is consistent with the Type-I and -II fabrics of wadsleyite developed under the normal MTZ temperatures in a horizontal flow field. Therefore, the flow field in the MTZ on the global scale is likely to be dominated by a horizontal flow (Ohuchi et al., 2014). This conclusion also coincides with the eastward horizontal mantle flow down to 700 km depth suggested by the observed global subduction asymmetry (steep westward subduction angle ~65 º versus gentle eastward subduction angle ~27º, Ficini et al., 2017).

For wadsleyite aggregates with type-III fabric under cold conditions (Fig. II.7c, II.7d), we expect $V_{SV} < V_{SH}$ in a horizontal flow field and $V_{SV} > V_{SH}$ in a vertical flow field. $V_{SV} > V_{SH}$ has been reported to be associated with subducted slabs in the MTZ in locations such as the Western Pacific (Panning and Romanowicz, 2006; Chang and Ferreira, 2019), Central America (Panning and Romanowicz, 2006), and South America (Moulik and Ekstrom, 2014). This is consistent with the primarily vertical flow fields in the MTZ induced by subducted slabs suggested by the present study. However, some caution is warranted regarding the association of seismically imaged slabs in the MTZ and radial anisotropy given that actual flow directions can deviate from an exactly vertical orientation and not all hypothesized slabs in the MTZ exhibit $V_{SV} > V_{SH}$.

5. Implications

5.1 Anisotropy features in the MTZ

The magnitude of the azimuthal shear wave anisotropy A^{Vs} in the MTZ is controversial. It is constrained to be 0.8-1.1% by Yuan and Beghein (2013, 2018), 0.3-0.4% by Schaeffer et al. (2016), and 0.7-0.8% by Debayle et al. (2016). As suggested by Huang et al. (2019), the

amplitude of azimuthal shear wave anisotropy A^{Vs} in the global upper mantle above the 410-km discontinuity is constrained to be ~1-2 %, but this value in the MTZ drops to less than 1%, which is consistent with the significantly smaller intrinsic anisotropy of wadsleyite compared with olivine (Zhang et al., 2018). As shown in section 4.2, the A^{Vs} of wadsleyite aggregates with type I and type II fabrics is calculated to be only 0.6-0.9% under ambient MTZ conditions (Fig. II.7). Considering that wadsleyite may make up ~60 vol% of the ambient mantle (Frost, 2008), the resulting anisotropy in the MTZ would be at the level of only ~0.4-0.5%, which is more consistent with the estimates of Schaeffer et al. (2016), Debayle et al. (2016) and Huang et al. (2019).

The amplitude for the radial anisotropy D^{Vs} above the 410-km discontinuity is about 2%, but this value drops to ~1% below the 410-km discontinuity (Visser et al., 2008). In a pyrolitic mantle, the D^{Vs} caused by deformed wadsleyite with type-I and -II fabrics is only ~0.6-0.8%. A pyrolitic layer of 100 km thickness in the upper MTZ (~410-520 km) produces very short delay time (S-wave splitting time < 0.1 s) regardless of the types of LPO fabrics or water content in wadsleyite assumed. This is consistent with the negligible depth dependence of shear-wave splitting delay times obtained from deep earthquakes (Mohiuddin et al., 2015). The weak radial anisotropy in the global MTZ is well-explained by the weak radial anisotropy of deformed wadsleyite aggregates.

Near subducted slabs in the MTZ, the A^{Vs} and D^{Vs} can reach 2-3% locally beneath the circum-Pacific Ocean subduction zones (Huang et al., 2019; Moulik and Ekstrom, 2014). However, for wadsleyite developing type-III fabric along cold subduction geotherm, the pure wadsleyite aggregate shows a maximum A^{Vs} and D^{Vs} on the order of only 1-1.4% (Fig. II.7). It is possible that the total strain in the MTZ induced by the subduction of cold slabs is

significantly higher than strain achieved in the laboratory deformation experiment (0.6-1.1) by Ohuchi et al. (2014). Stronger LPO of wadsleyite may lead to the higher seismic anisotropy suggested by these local seismic studies. Some other studies have attributed the marked anisotropy underneath the subducted zones to the LPO of highly anisotropic hydrous alphabet phases (Nowacki et al., 2015) or K-hollandite (Mookherjee and Steinle-Neumann, 2009) in the subducted slabs. However, the stability and abundance of alphabet phases in the subducting slabs remain controversial and K-hollandite may only be present within subducted continental materials (Hao et al., 2020). Kawakatsu and Yoshioka (2011) identified a wedge-shape low-velocity layer in the subducting Pacific slab up to 450 km depth beneath SE Japan and explained it as the metastable olivine wedge. Tono et al. (2009) also reported a uniform anisotropy signal of the Pacific slab beneath Japan likely at depths beyond the 410-discontinuity. Considering the relatively high elastic anisotropy of olivine at 410 km (~19–25%, Zhang et al., 2018), the existence of metastable olivine in MTZ can explain the ~3% anisotropy associated with some cold subduction zones. Other possibilities include the highly anisotropic akimotoite (Shiraishi et al., 2008) and stishovite (Xu et al., 2020) accumulated in the stagnant slabs in the MTZ or shape-preferred orientation (SPO) of rheologically/elastically weak minerals/melts (Li et al. 2018). Deformed pure akimotoite aggregates show 3-4.3 % A^{Vp} under the strain of 0.09-0.61 (Shiraishi et al., 2008), much higher than the deformed pure wadsleyite aggregates (~1%) and pure ringwoodite aggregates (~0.2%) under similar strain condition (Ohuchi et al., 2014). Foley and Long (2011) suggested that the main anisotropy contribution to splitting from deep earthquakes may come from stagnant slabs at the boundary between the MTZ and the Lower Mantle, in which stishovite is likely to be locally enriched. A recent seismic study suggested that the non-double-couple deep earthquakes are probably

originated in regions that are highly anisotropic (up to 25%) within the subducting slabs (Li et al., 2018), such high seismic anisotropy is difficult to be caused by LPO of elastically anisotropic mantle minerals, thus SPO seems a more viable explanation.

5.2 Is the seismic anisotropy in the upper MTZ a good water sensor?

A recent seismic study by Chang and Ferreira (2019) proposed a nearly dry upper MTZ (< ~0.02 wt% water) near subducting slabs under the western Pacific due to the observed high radial anisotropy (~l.5%), and suggested that the high seismic anisotropy of the upper MTZ may indicate a low water content. It is interesting to reevaluate this conclusion based on our results that separate the pressure, Fe and water content effects and take various types of wadsleyite fabrics into account.

As shown in Fig. II.5, water indeed reduces the intrinsic anisotropy of wadsleyite, for example, the A^{Vp} and D^{Vs} of hydrous wadsleyite (1.5 wt% water, Fe#=10) are lower than dry wadsleyite (Fe#=10) by 18% and 15%, respectively (Fig. II.6d, II.6e). However, the deformed hydrous wadsleyite aggregate usually shows type II fabric, whereas the deformed dry wadsleyite aggregate primarily displays type I fabric (Ohuchi et al., 2014). After taking the different types of fabrics into account, the hydrous wadsleyite actually shows higher A^{Vp} and D^{Vs} than the dry wadsleyite aggregate by 25% and 30%, respectively (Fig. II.7a, II.7b). A possible reason is that the incorporation of water results in more structural defects and assists the formation of stronger LPO of high-pressure olivine polymorphs such as wadsleyite and ringwoodite. As shown in Ohuchi et al. (2014), hydrous wadsleyite aggregate with type II fabric shows almost 2 times higher strain rate (~$1.3*10^{-4}$) than the almost dry wadsleyite aggregate (~$7.4*10^{-5}$) with type I fabric, thus the hydrous wadsleyite aggregate is rheologically weaker. Similarly, Kavner (2003) also reported that the presence of water in the crystal

structure of ringwoodite increases the ductile strain rate, and thus, promotes the development of LPO of ringwoodite. Although the hydrous wadsleyite aggregate tends to show higher seismic anisotropy than the dry aggregate after taking the single-crystal elasticity and fabrics into account, whether this anisotropy difference can be resolved seismically will likely depend on the actual strain thus the strength of the flow field in the MTZ. Therefore, the seismic anisotropy in the upper MTZ may not necessarily reflect the degree of hydration in the MTZ.

6. Conclusions

(1) We determined the single-crystal elastic properties of a synthetic hydrous Fe-bearing wadsleyite (0.14 (4) wt% water, Fe#=9.4, $Fe^{3+}/\Sigma Fe$=0.3) up to 18.2 (2) GPa. The experimental results are: K_{S0} = 165 (2) GPa, G_0 = 104 (2) GPa, K_{S0}' = 5.2 (5), K_{S0}'' = -0.16 (11) GPa^{-1}, G_0' = 1.9 (2), and G_0'' = -0.076 (28) GPa^{-1}. Strong softening of C_{44} and C_{12} at pressures higher than 8 GPa is not observed in this study.

(2) We quantitively constrained the influence of water, Fe, and pressure on single-crystal elastic properties and intrinsic anisotropy of wadsleyite. In average, adding 1 wt% water into wadsleyite crystal structure at 15 GPa decreases intrinsic anisotropy by ~11-13%, adding 10 mol% Fe at 15 GPa decreases intrinsic anisotropy by ~8-11%, increasing pressure from 0 to 15 GPa decreases intrinsic anisotropy by ~40-50 %.

(3) Utilizing the water-Fe-pressure dependent C_{ij} models of wadsleyite in the present study and 3 different types of fabrics measured by deformation experiments in Ohuchi et al. (2014), we modeled the seismic anisotropy of wadsleyite aggregates. Comparisons between our results and seismic observations in the MTZ are consistent with sub-horizontal flow in the ambient mantle and sub-vertical flow near subducted slabs. Our results are consistent with a weak

anisotropic MTZ (<1%) on the global scale. The observed local high seismic anisotropy up to 3% near subducted slabs requires either high strain caused by strong flow fields, or the LPO of other strongly anisotropic minerals such as akimotoite, stishovite, and metastable olivine near the slabs.

(4) Water in wadsleyite's crystal structure decreases its intrinsic anisotropy but promotes the development of LPO. Depending on the total accumulated strain in the MTZ, the seismic anisotropy in the upper MTZ may not necessarily reflect the degree of hydration in the MTZ.

Acknowledgement

We thank Mike Spilde for his general help in the EMPA analysis, Dr. Ruijia Wang for discussion of seismic ray paths, and Sibo Chen for the advice in the FTIR measurement. This project is funded by NSF-EAR-1664471 (JSZ). B.C. acknowledges the support from NSF-EAR-1555388 and NSF-EAR-1829273. LM acknowledges the support from NSF-EAR-1654687. Use of 13-BM-C was supported by COMPRES under NSF Cooperative Agreement EAR -1661511 and by GSECARS through NSF grant EAR-1634415 and DOE grant DE-FG02-94ER14466. Use of the APS was supported by the US Department of Energy, Office of Science, Office of Basic Energy Sciences, under Contract No.DE-AC02-06CH11357.

References:

Bercovici, D., & Karato, S. I. (2003). Whole-mantle convection and the transition-zone water filter. Nature, 425(6953), 39-44.

Buchen, J., Marquardt, H., Ballaran, T. B., Kawazoe, T., & McCammon, C. (2017). The equation of state of wadsleyite solid solutions: Constraining the effects of anisotropy and crystal chemistry. American Mineralogist, 102(12), 2494-2504.

Buchen, J., Marquardt, H., Speziale, S., Kawazoe, T., Ballaran, T. B., & Kurnosov, A. (2018). High-pressure single-crystal elasticity of wadsleyite and the seismic signature of water in the shallow transition zone. Earth and Planetary Science Letters, 498, 77-87.

Chang, S. J., & Ferreira, A. M. (2019). Inference on water content in the mantle transition zone near subducted slabs from anisotropy tomography. *Geochemistry, Geophysics, Geosystems*, *20*(2), 1189-1201.

Chang, Y. Y., Jacobsen, S. D., Bina, C. R., Thomas, S. M., Smyth, J. R., Frost, D. J., ... & Dera, P. (2015). Comparative compressibility of hydrous wadsleyite and ringwoodite: Effect of H2O and implications for detecting water in the transition zone. Journal of Geophysical Research: Solid Earth, 120(12), 8259-8280.

Crameri, F. Scientific Colour Maps, http://www.fabiocrameri.ch/colourmaps(2020).

Davies, G. F., & Dziewonski, A. M. (1975). Homogeneity and constitution of the Earth's lower mantle and outer core. Physics of the Earth and Planetary Interiors, 10(4), 336–343.

Debayle, E., Dubuffet, F., & Durand, S. (2016). An automatically updated S-wave model of the upper mantle and the depth extent of azimuthal anisotropy. *Geophysical Research Letters*, *43*(2), 674-682.

Dyar, M. D., Agresti, D. G., Schaefer, M. W., Grant, C. A., & Sklute, E. C. (2006). Mössbauer spectroscopy of earth and planetary materials. Annu. Rev. Earth Planet. Sci., 34, 83-125.

Ficini, E., Dal Zilio, L., Doglioni, C., & Gerya, T. V. (2017). Horizontal mantle flow controls subduction dynamics. Scientific reports, 7(1), 1-7.

French, S. W., & Romanowicz, B. A. (2014). Whole-mantle radially anisotropic shear velocity structure from spectral-element waveform tomography. Geophysical Journal International, 199(3), 1303-1327.

Frost, D. J. (2008). The upper mantle and transition zone. Elements, 4(3), 171-176.

Foley, B. J., & Long, M. D. (2011). Upper and mid-mantle anisotropy beneath the Tonga slab. *Geophysical Research Letters*, *38*(2).

Hazen, R. M., Weinberger, M. B., Yang, H., & Prewitt, C. T. (2000). Comparative high-pressure crystal chemistry of wadsleyite, β-(Mg1–x Fe x) 2SiO4, with x= 0 and 0.25. American Mineralogist, 85(5-6), 770-777.

Hao, M., Zhang, J. S., Pierotti, C. E., Zhou, W. Y., Zhang, D., & Dera, P. (2020). The seismically fastest chemical heterogeneity in the Earth's deep upper mantle—implications from the single-crystal thermoelastic properties of jadeite. Earth and Planetary Science Letters, 543, 116345.

Hill, R. (1963). Elastic properties of reinforced solids: some theoretical principles. *Journal of the Mechanics and Physics of Solids*, *11*(5), 357-372.

Holl, C. M., Smyth, J. R., Jacobsen, S. D., & Frost, D. J. (2008). Effects of hydration on the structure and compressibility of wadsleyite, β-(Mg2SiO4). *American Mineralogist*, *93*(4), 598-607.

Huang, Q., Schmerr, N., Waszek, L., & Beghein, C. (2019). Constraints on seismic anisotropy in the mantle transition zone from long-period SS precursors. *Journal of Geophysical Research: Solid Earth*, *124*(7), 6779-6800.

Inoue, T., Yurimoto, H., & Kudoh, Y. (1995). Hydrous modified spinel, Mg1. 75SiH0. 5O4: a new water reservoir in the mantle transition region. Geophysical Research Letters, 22(2), 117-120.

Jacobsen, S. D., Jiang, F., Mao, Z., Duffy, T. S., Smyth, J. R., Holl, C. M., & Frost, D. J. (2008). Effects of hydration on the elastic properties of olivine. Geophysical Research Letters, 35(14).

Jiang, F., Speziale, S., & Duffy, T. S. (2004). Single-crystal elasticity of grossular-and almandine-rich garnets to 11 GPa by Brillouin scattering. Journal of Geophysical Research: Solid Earth, 109(B10).

Kavner, A. (2003). Elasticity and strength of hydrous ringwoodite at high pressure. Earth and Planetary Science Letters, 214(3-4), 645-654.

Kawakatsu, H., & Yoshioka, S. (2011). Metastable olivine wedge and deep dry cold slab beneath southwest Japan. Earth and Planetary Science Letters, 303(1-2), 1-10.

Li, J., Zheng, Y., Thomsen, L., Lapen, T. J., & Fang, X. (2018). Deep earthquakes in subducting slabs hosted in highly anisotropic rock fabric. Nature Geoscience, 11(9), 696-700.

Mainprice, D., Hielscher, R., & Schaeben, H. (2011). Calculating anisotropic physical properties from texture data using the MTEX open-source package. *Geological Society, London, Special Publications*, *360*(1), 175-192.

Mao, Z., Jacobsen, S. D., Frost, D. J., McCammon, C. A., Hauri, E. H., & Duffy, T. S. (2011). Effect of hydration on the single-crystal elasticity of Fe-bearing wadsleyite to 12 GPa. American Mineralogist, 96(10), 1606-1612.

Mao, Z., Jacobsen, S. D., Jiang, F., Smyth, J. R., Holl, C. M., Frost, D. J., & Duffy, T. S. (2008a). Single-crystal elasticity of wadsleyites, β-Mg2SiO4, containing 0.37–1.66 wt.% H2O. Earth and Planetary Science Letters, 266(1-2), 78-89.

Mao, Z., Jacobsen, S. D., Jiang, F., Smyth, J. R., Holl, C. M., & Duffy, T. S. (2008b). Elasticity of hydrous wadsleyite to 12 GPa: implications for Earth's transition zone. Geophysical Research Letters, 35(21).

Mohiuddin, A., Long, M. D., & Lynner, C. (2015). Mid-mantle seismic anisotropy beneath southwestern Pacific subduction systems and implications for mid-mantle deformation. *Physics of the Earth and Planetary Interiors*, *245*, 1-14.

Mookherjee, M., & Steinle-Neumann, G. (2009). Detecting deeply subducted crust from the elasticity of hollandite. Earth and Planetary Science Letters, 288(3-4), 349-358.

Moulik, P., & Ekström, G. (2014). An anisotropic shear velocity model of the Earth's mantle using normal modes, body waves, surface waves and long-period waveforms. Geophysical Journal International, 199(3), 1713-1738.

Nowacki, A., Kendall, J. M., Wookey, J., & Pemberton, A. (2015). Mid-mantle anisotropy in subduction zones and deep water transport. Geochemistry, Geophysics, Geosystems, 16(3), 764-784.

Núñez-Valdez, M., Da Silveira, P., & Wentzcovitch, R. M. (2011). Influence of iron on the elastic properties of wadsleyite and ringwoodite. Journal of Geophysical Research: Solid Earth, 116(B12).

Ohuchi, T., Fujino, K., Kawazoe, T., & Irifune, T. (2014). Crystallographic preferred orientation of wadsleyite and ringwoodite: Effects of phase transformation and water on seismic anisotropy in the mantle transition zone. Earth and Planetary Science Letters, 397, 133-144.

Panning, M., & Romanowicz, B. (2006). A three-dimensional radially anisotropic model of shear velocity in the whole mantle. Geophysical Journal International, 167(1), 361-379.

Ranganathan, S. I., & Ostoja-Starzewski, M. (2008). Universal elastic anisotropy index. *Physical Review Letters*, *101*(5), 055504.

Savage, M. K. (1999). Seismic anisotropy and mantle deformation: what have we learned from shear wave splitting?. Reviews of Geophysics, 37(1), 65-106.

Sawamoto, H., Weidner, D. J., Sasaki, S., & Kumazawa, M. (1984). Single-crystal elastic properties of the modified spinel (beta) phase of magnesium orthosilicate. Science, 224(4650), 749-751. 10.

Schaeffer, A. J., Lebedev, S., & Becker, T. W. (2016). Azimuthal seismic anisotropy in the Earth's upper mantle and the thickness of tectonic plates. *Geophysical Supplements to the Monthly Notices of the Royal Astronomical Society*, *207*(2), 901-933.

Shiraishi, R., Ohtani, E., Kanagawa, K., Shimojuku, A., & Zhao, D. (2008). Crystallographic preferred orientation of akimotoite and seismic anisotropy of Tonga slab. Nature, 455(7213), 657-660.

Speziale, S., & Duffy, T. S. (2002). Single-crystal elastic constants of fluorite (CaF 2) to 9.3 GPa. Physics and Chemistry of Minerals, 29(7), 465-472.

Tono, Y., Fukao, Y., Kunugi, T., & Tsuboi, S. (2009). Seismic anisotropy of the Pacific slab and mantle wedge beneath the Japanese islands. Journal of Geophysical Research: Solid Earth, 114(B7).

Visser, K., Trampert, J., Lebedev, S., & Kennett, B. L. N. (2008). Probability of radial anisotropy in the deep mantle. *Earth and Planetary Science Letters*, *270*(3-4), 241-250.

Wang, J., Bass, J. D., & Kastura, T. (2014). Elastic properties of iron-bearing wadsleyite to 17.7 GPa: Implications for mantle mineral models. Physics of the Earth and Planetary Interiors, 228, 92-96.

Xu, F., Yamazaki, D., Tsujino, N., & Guan, L. (2020). Lattice preferred orientation of stishovite deformed at high pressure and high temperature. Physics of the Earth and Planetary Interiors, 306, 106546.

Yuan, K., & Beghein, C. (2013). Seismic anisotropy changes across upper mantle phase transitions. Earth and Planetary Science Letters, 374, 132-144.

Yuan, K., & Beghein, C. (2018). A Bayesian method to quantify azimuthal anisotropy model uncertainties: application to global azimuthal anisotropy in the upper mantle and transition zone. *Geophysical Journal International*, *213*(1), 603-622.

Zha, C. S., Duffy, T. S., Mao, H. K., Downs, R. T., Hemley, R. J., & Weidner, D. J. (1997). Single-crystal elasticity of β-Mg2SiO4 to the pressure of the 410 km seismic discontinuity in the earth's mantle. Earth and Planetary Science Letters, 147(1-4), E9-E15.

Zhang, J. S., & Bass, J. D. (2016). Sound velocities of olivine at high pressures and temperatures and the composition of Earth's upper mantle. Geophysical Research Letters, 43(18), 9611-9618.

Zhang, J. S., Bass, J. D., & Schmandt, B. (2018). The elastic anisotropy change near the 410-km discontinuity: Predictions from single-crystal elasticity measurements of olivine and wadsleyite. Journal of Geophysical Research: Solid Earth, 123(4), 2674-2684.

Supporting Information

II.1. EPMA results

Table II.S1. EPMA results for randomly chosen synthetic wadsleyite single crystals.

	Na_2O wt(%)	MgO wt(%)	Al_2O_3 wt(%)	SiO_2 wt(%)	CaO wt(%)	TiO_2 wt(%)	Cr_2O_3 wt(%)	MnO wt(%)	FeO wt(%)	NiO wt(%)	TOTAL wt(%)
	0.03	49.67	0.15	39.58	0.02	0.00	0.02	0.12	9.15	0.39	99.13
	0.04	49.94	0.14	39.59	0.03	0.01	0.01	0.14	8.99	0.34	99.22
	0.02	49.20	0.07	40.82	0.03	0.00	0.00	0.12	9.02	0.41	99.70
	0.03	49.06	0.10	40.84	0.02	0.02	0.02	0.15	9.09	0.32	99.63
	0.00	48.70	0.11	40.72	0.02	0.01	0.01	0.13	9.59	0.34	99.64
	0.02	49.15	0.10	40.32	0.02	0.00	0.01	0.12	9.06	0.34	99.13
	0.02	49.19	0.13	40.26	0.03	0.01	0.01	0.15	9.13	0.37	99.29
	0.02	49.15	0.10	40.38	0.03	0.02	0.02	0.12	9.14	0.36	99.35
	0.03	49.07	0.15	40.04	0.00	0.00	0.01	0.14	9.30	0.37	99.11
	0.03	49.10	0.14	40.13	0.01	0.01	0.02	0.13	9.16	0.39	99.12
	0.03	48.75	0.11	41.03	0.03	0.01	0.02	0.00	8.91	0.33	99.21
	0.02	48.75	0.12	40.70	0.00	0.00	0.00	0.16	8.96	0.37	99.10
	0.03	48.78	0.11	40.41	0.01	0.01	0.01	0.13	9.19	0.39	99.06
Average	0.02	49.12	0.12	40.37	0.02	0.01	0.01	0.12	9.13	0.36	99.28

II.2. Fourier Transformed Infrared Spectroscopy (FTIR)

We carried out unpolarized FTIR measurements on 9 double-polished wadsleyite samples with random orientations. The water content was determined as the average of all measured values (Fig. I.S1). The water content was calculated from the following equation (Libowitzky and Rossman, 1997):

$$c(H_2O) = \frac{1.8}{\gamma D \varepsilon_i} \int \frac{K(\nu)}{t} d\nu \quad \text{(S1)}$$

with ε_i=246.6(3753-ν_m) where ε_i (cm^{-2} per mol H_2O/L) is the integrated molar absorption coefficient. ν_m is the mean wavenumber of the stretching band in cm^{-1}. c(H_2O) is the water concentration by wt%. K (ν) is the band intensity height and ν is the wavenumber (cm^{-1}), t is the thickness of the sample in cm, and D is the density in g/cm^3. The FTIR spectra we obtained are shown in Fig. II.S1. The difference in terms of relative peak intensity compared with the spectra in Bolfan-Casanova et al. (2018) can be explained by the high $Fe^{3+}/\Sigma Fe$ of wadsleyite samples (Smyth et al., 2014). Using equation S1, the synthetic wadsleyite in this study has an average water content of 0.14 (4) wt%.

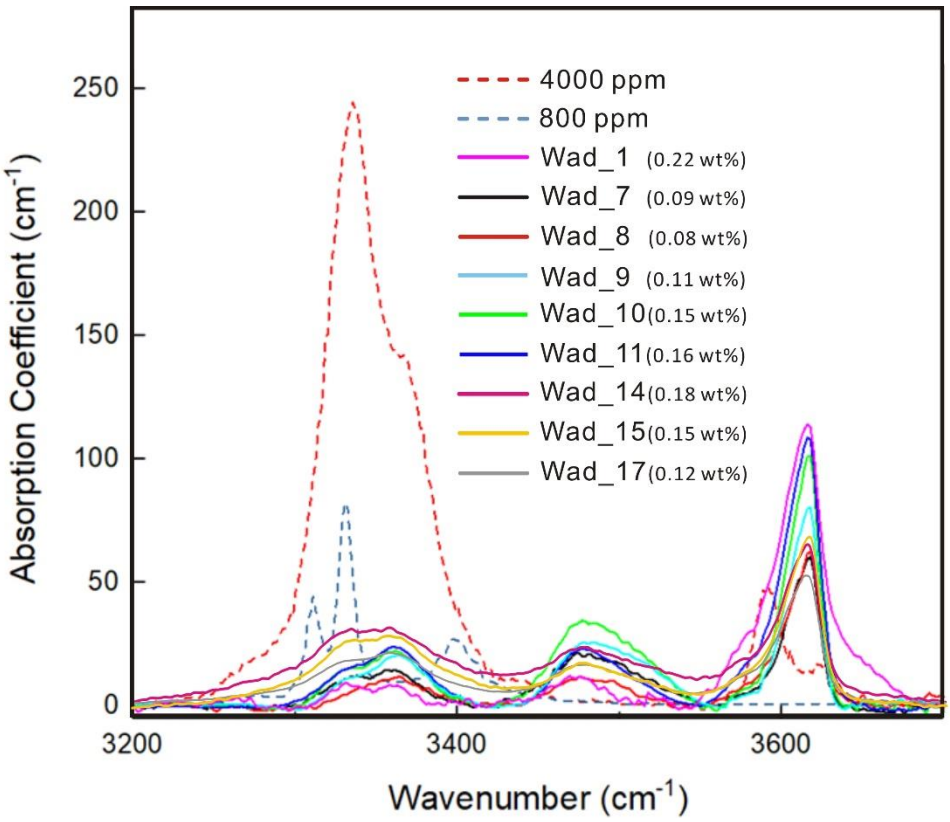

Fig. II.S1. *Absorption coefficient as a function of wavenumber measured by unpolarized FTIR spectroscopy. Dashed lines: wadsleyite with 4000 ppm and 800 ppm water measured by unpolarized FTIR method (Bolfan-Casanova et al., 2018). Solid lines: this study.*

II.3. Mössbauer Spectroscopy Experiment

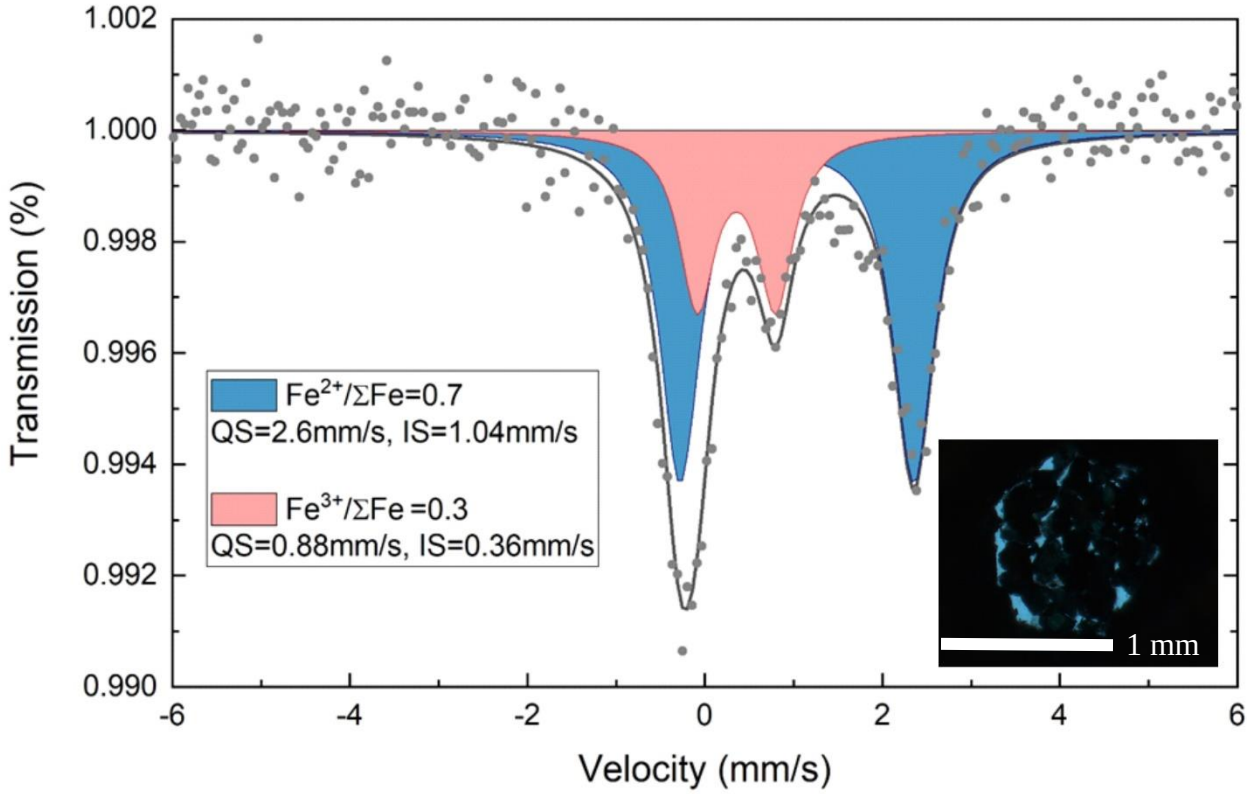

Fig. II.S2. *Mössbauer spectrum of our wadsleyite crystals in a Re gasket. The data is consistent with two separate sites for Fe with +2 and +3 valence, based on the combined values of hyperfine interaction parameters of quadrupole splitting (QS) and isomer shift (IS) (Dyar et al., 2006).*

II.4. Sensitivity Test

Sensitivity test is a way to evaluate whether the combination of crystallographic orientations of single-crystal minerals for Brillouin experiments can provide reliable constraints to the single-crystal elastic moduli (C_{ij}s) (Lin et al., 2018; Fu et al., 2019; Hao et al., 2020). We utilized the sensitivity testing code from Hao et al. (2020) to choose the best combination of crystallographic orientations of wadsleyite crystals for our Brillouin experiments. The sensitivity value, representing the maximum change of sound velocities along the 39 different crystallographic directions with 0.1% change of each C_{ij}, is defined as.

$$S_x = \left[\frac{\partial V_x / V_x}{\partial C_{ij} / C_{ij}} \right]_{maximum} \quad \text{(S2)}$$

where V_x refers to V_P, V_{S1}, and V_{S2}, respectively. The final chosen orientations are (-0.342 0.8718 0.3506), (-0.1013 -0.4397 0.8924), and (0.5341 0.0953 -0.8401) and their sensitivity testing results are shown in Fig. II.S2. All C_{ij}s can be inverted with high enough sensitivity based on the velocity measurements on the 3 selected wadsleyite crystals.

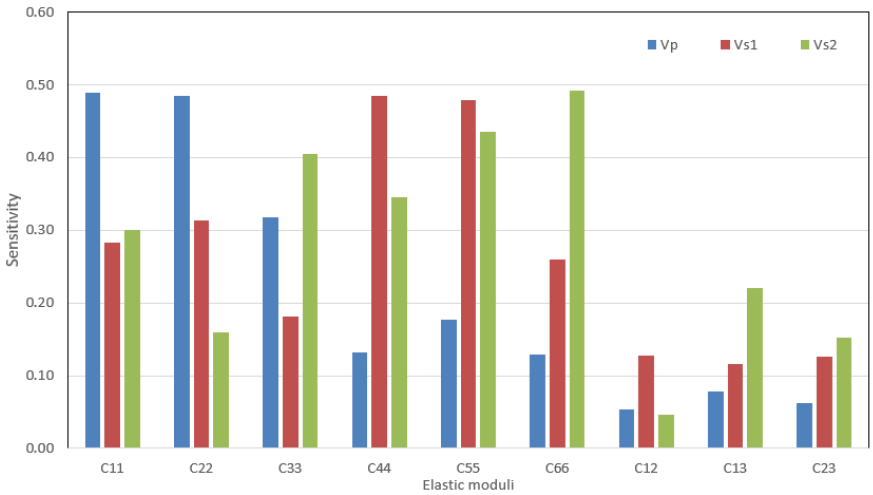

Fig. II.S3*. The sensitivity test results for the orientation combination in this study.*

II.5. Brillouin Spectroscopy Experimental Results

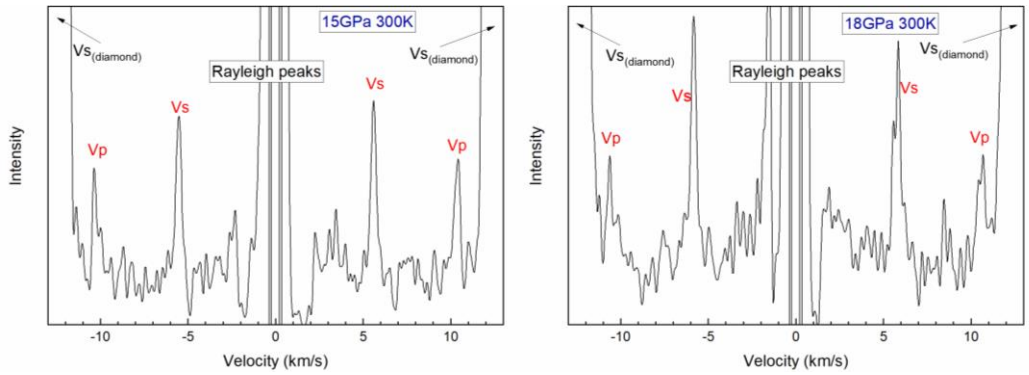

Fig. II.S4. *Left: A typical Brillouin spectrum at 15 GPa for wadsleyite with orientation of (0.5341 0.0953 0.8401); Right: A typical Brillouin spectrum at 18 GPa for wadsleyite with orientation of (-0.342 0.8718 0.3506); the collection time is 30 min. The Neon peak is invisible in both spectra.*

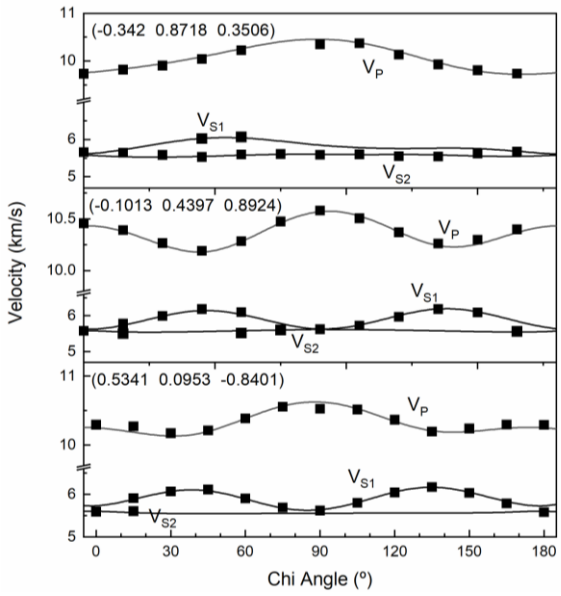

Fig. II.S5. *Measured acoustic velocities of wadsleyite as a function of laboratory chi angles for 3 wadsleyite crystals. Solid lines are the acoustic velocities calculated from the best-fit single-crystal elasticity model; squares are the experimentally determined velocities. Errors are within the size of the symbols.*

II.6. Modeling of Water-Fe-Pressure dependent single-crystal elastic properties

6.1 The use of 3rd order versus 4th order finite strain equation of state (EOS)

We have tried to use only 3rd order finite strain EOS to obtain the water and Fe# dependent K_{S0}' and G_0'. The results are K_{S0}' = 4.2 (3) and G_0'=1.2 (3) + 0.3 (1) × water (wt%) + 0.02 (2) × Fe#. However, the Ks and G of wadsleyite aggregate predicted from this model are of relatively large difference from experimental values at high pressures. For example, this model-predicted Ks and G of Fe-bearing wadsleyite can be up to 3% higher than experimental values from Wang et al. (2014), Buchen et al. (2018), and this study. In particular, for the experimental data in this study, using 3rd order finite strain EOS fitting would result in a more than 5-fold increase of root-mean-square (RMS) error for Ks and G (RMS=37.5) than using 4th order (RMS=6.2). Considering that 4th order finite strain EOS gives better constraints on Ks and G, Vp, and Vs at 14-18 GPa, which is the pressure range that wadsleyite is stable at in the mantle, 4th order finite strain EOS was thus chosen in our modeling. However, we would also like to point out that, although it seems that 3rd order EOS does not work for our modeling which covers a wide compositional and pressure range, it may be sufficient to model the experimental data set measured for a given wadsleyite sample with a fixed composition.

6.2. Choice of compositional dependent elasticity parameters

When performing the modeling using the 4th order finite strain EOS, more elastic parameters are involved. To reduce the number of fitting parameters, we have pre-fitted and obtained the compositional dependance of K_{S0}, G_0 and ρ_0, leaving only the K_{S0}', G_0', K_{S0}'', and G_0'' involved. We firstly treated K_{S0}', G_0', K_{S0}'', and G_0'' all as compositional dependent, the fitting results we obtained are always with uncertainties greater than 100%. We have also tried to fit the K_{S0}', G_0' as compositional dependent and K_{S0}'' and G_0'' as compositional independent, the results improved yet still gives us uncertainties greater than 100%. These tests

indicate that the current data we have compiled so far do not provide enough constraints and we are overfitting the data. Eventually, we figured out that if we fixed the K_{S0}''and G_0'' to the values we determined for the hydrous Fe-bearing wadsleyite measured in this study, the modeling using 4th order finite strain EOS could give us satisfactory results for the compositional dependance of the K_{S0}', G_0', $C_{ij,0}$' ($\partial C_{ij,0}/\partial P$) and $C_{ij,0}$'' ($\partial^2 C_{ij,0}/\partial P^2$) as shown in Table II.S4.

4.3. 4th order finite EOS

The 4th order finite EOS we utilized in this study are shown as S3-S20 (Davies, 1974; Davies and Dzieonski, 1975):

$$\rho \cdot Vs^2 = (1-2\varepsilon)^{5/2}(M_1 + M_2 \cdot \varepsilon + \frac{1}{2} M_3 \cdot \varepsilon^2) \quad (S3)$$

$$\rho \cdot Vp^2 = (1-2\varepsilon)^{5/2}(L_1 + L_2 \cdot \varepsilon + \frac{1}{2} L_3 \cdot \varepsilon^2) \quad (S4)$$

$$P = -(1-2\varepsilon)^{5/2}(C_1 \cdot \varepsilon + \frac{1}{2} C_2 \cdot \varepsilon^2 + \frac{1}{6} C_3 \cdot \varepsilon^3) \quad (S5)$$

$$\varepsilon = \frac{1}{2}[1-(\rho/\rho_0)^{2/3}] \quad (S6)$$

where P represents pressure, ε represents strain, M_1, M_2, M_3, L_1, L_2, L_3, C_1, C_2, and C_3 are defined as:

$$M_1 = G_0 \quad (S7)$$

$$M_2 = 5M_1 - 3K_{S0} \cdot G_0' \quad (S8)$$

$$M_3 = 9G_0'' \cdot K_{S0}^2 - 3(K_{S0}' - 4)M_2 + 5(3K_{S0}' - 5)M_1 \quad (S9)$$

$$L_1 = K_0 + \frac{4}{3} M_1 \quad (S10)$$

$$L_2 = 5L_1 - 3K_{S0}(K_{S0}' + \frac{4}{3} G_0') \quad (S11)$$

$$L_3 = 9K_{S0}'' \cdot K_{S0}^2 + 12 \cdot G_0'' \cdot K_{S0}^2 - 3(K_{S0}' - 4)L_2 + 5(3K_{S0}' - 5)L_1 \quad (S12)$$

$$C_1 = 3\,L_1 - 4\,M_1 \tag{S13}$$

$$C_2 = 3\,L_2 - 4\,M_2 + 7\,C_1 \tag{S14}$$

$$C_3 = 3\,L_3 - 4\,M_3 + 9\,C_2 \tag{S15}$$

$$G = \rho \cdot Vs^2 \tag{S16}$$

$$K_S = \rho \cdot Vp^2 - \frac{4}{3} G \tag{S17}$$

$$a_1 = -3\,K_{S0} \cdot (C_{ij,0}' + a_3) + 7\,C_{ij0} \tag{S18}$$

$$a_2 = 9\,K_{S0}^2 \cdot C_{ij,0}'' - 3K_{S0}' (a_1 - 7\,C_{ij,0}) + 16\,a_1 - 49\,C_{ij,0} \tag{S19}$$

$$C_{ij} = (1-2\,\varepsilon)^{7/2} (C_{ij,0} + a_1 \cdot \varepsilon + \frac{1}{2}\,a_2 \cdot \varepsilon^2 + \cdots\cdots) - P \cdot a_3 \tag{S20}$$

where a_3 is -3 for C_{11}, C_{22}, and C_{33}, a_3 is -1 for C_{44}, C_{55}, C_{66}, C_{12}, C_{13}, and C_{23}.

Table II.S2. *Single-crystal elasticity data of different wadsleyite samples we complied for the modeling in this study.*

References	P	Fe#	$Fe^{3+}/\Sigma Fe$	H_2O	ρ	Ks	G	Vp	Vs	C_{11}	C_{22}	C_{33}	C_{44}	C_{55}	C_{66}	C_{12}	C_{13}	C_{23}
	GPa			wt%	g/cm^3	GPa	GPa	km/s	km/s	GPa	GPa	GPa	GPa	GPa	GPa	GPa	GPa	GPa
Sawamoto et al., 1984	0	0	0	0	3.474	174	114	9.69	5.73	360	383	273	112	118	98	75	110	105
Zha et al., 1997	0	0	0	0	3.488	170	115	9.66	5.78	371	368	272	111	123	103	66	95	105
	3.1	0	0	0	3.550	183	116	9.78	5.73	379	382	292	111	123	101	85	106	112
	6.3	0	0	0	3.610	194	124	9.99	5.87	393	400	317	127	118	117	84	118	119
	8.1	0	0	0	3.643	202	125	10.08	5.88	404	418	324	121	124	119	94	122	123
	9.4	0	0	0	3.666	211	128	10.22	5.92	414	440	333	127	123	118	104	124	132
	10.5	0	0	0	3.685	210	126	10.16	5.88	422	426	331	122	127	116	108	128	125
	14.2	0	0	0	3.747	236	134	10.54	6.01	445	465	387	131	122	130	124	142	152
Mao et al., 2008a	0	0	0	0.38	3.455	165	109	9.48	5.61	357	358	256	107	112	96	69	97	98
	0	0	0	1.2	3.418	160	105	9.36	5.54	336	344	251	103	110	94	71	99	91
	0	0	0	2.9	3.339	147	97	9.09	5.39	317	316	228	94	99	88	62	89	84
Mao et al., 2008b	0	0	0	1.2	3.418	161	104	9.35	5.51	339	341	255	101	105	93	68	96	95
	1.2	0	0	1.2	3.443	162	105	9.37	5.53	346	345	253	103	106	96	72	92	98
	2.7	0	0	1.2	3.474	172	107	9.53	5.56	359	350	275	104	107	99	79	100	108
	4.2	0	0	1.2	3.503	175	109	9.58	5.59	368	357	276	105	109	101	84	100	109
	6.7	0	0	1.2	3.551	187	112	9.74	5.62	380	376	291	108	112	104	99	106	118
	8.2	0	0	1.2	3.580	192	115	9.81	5.66	389	381	303	110	112	107	101	109	118
	10.2	0	0	1.2	3.615	200	117	9.94	5.70	403	391	316	113	113	111	109	115	125
	12.1	0	0	1.2	3.648	210	121	10.09	5.76	418	411	331	116	113	116	115	122	130

Table II.S2. (Continue)

Mao et al., 2011	0	11.0	0.1	2.0	3.515	156	98	9.04	5.28	334	319	242	95	102	87	69	102	89
	3.2	11.0	0.1	2.0	3.584	172	103	9.30	5.37	356	338	267	101	106	94	90	112	97
	4.2	11.0	0.1	2.0	3.605	179	107	9.44	5.45	354	353	287	104	107	99	95	116	98
	6.7	11.0	0.1	2.0	3.655	187	111	9.57	5.52	370	361	305	107	111	104	102	117	104
	8.7	11.0	0.1	2.0	3.693	197	114	9.73	5.56	391	375	316	109	113	107	111	128	111
	10.2	11.0	0.1	2.0	3.721	203	115	9.80	5.58	397	382	326	109	114	111	115	133	115
	12.2	11.0	0.1	2.0	3.757	210	119	9.90	5.63	402	391	347	110	115	117	115	139	120
Wang et al., 2014	0	7.5	unknown	0	3.570	170	108	9.38	5.50	348	372	254	106	115	97	78	102	105
Wang, 2008	4.1	7.5	unknown	0	3.653	188	115	9.66	5.60	386	385	291	108	119	105	91	111	119
	6.0	7.5	unknown	0	3.690	192	117	9.72	5.64	397	394	300	107	122	108	96	112	122
	8.0	7.5	unknown	0	3.727	202	120	9.85	5.67	406	403	314	111	122	113	106	120	124
	10.0	7.5	unknown	0	3.765	210	123	9.96	5.70	419	413	328	111	126	116	111	126	131
	12.1	7.5	unknown	0	3.802	218	125	10.06	5.74	429	423	339	114	127	121	117	133	138
	14	7.5	unknown	0	3.835	226	127	10.15	5.76	433	437	354	116	126	125	125	138	145
	15.9	7.5	unknown	0	3.867	233	130	10.24	5.79	443	447	363	117	129	129	132	142	150
	17.7	7.5	unknown	0	3.897	240	130	10.31	5.78	451	455	371	118	131	130	138	153	156
Buchen et al., 2018	0	11.2	0.15	0.24	3.598	166	103	9.18	5.35	345	354	252	105	107	86	73	107	94
	1.5	11.2	0.15	0.24	3.630	175	109	9.40	5.48	366	369	270	107	117	92	78	101	110
	4.1	11.2	0.15	0.24	3.683	187	113	9.57	5.53	389	373	290	110	115	99	92	117	110
	8.8	11.2	0.15	0.24	3.774	209	122	9.92	5.68	408	418	331	113	123	113	105	129	130
	11.0	11.2	0.15	0.24	3.815	214	122	9.94	5.66	423	412	335	116	121	116	113	137	131

Table II.S2. (Continue)

	13.1	11.2	0.15	0.24	3.853	226	124	10.07	5.66	432	431	357	114	122	117	125	147	140
	16.1	11.2	0.15	0.24	3.905	233	129	10.17	5.74	431	451	369	119	124	127	131	142	150
	19.7	11.2	0.15	0.24	3.964	246	130	10.28	5.72	452	445	391	116	133	130	139	167	159
This study	0	9.4	0.3	0.14	3.595	165	104	9.19	5.38	341	358	244	106	109	91	75	99	102
	2.9	9.4	0.3	0.14	3.656	179	110	9.43	5.47	364	376	274	108	111	99	89	103	112
	6.6	9.4	0.3	0.14	3.729	197	115	9.69	5.56	387	397	307	109	115	106	103	112	129
	9.5	9.4	0.3	0.14	3.783	207	119	9.84	5.62	406	410	322	113	119	113	114	117	137
	12.2	9.4	0.3	0.14	3.831	220	123	10.00	5.66	418	425	345	118	119	116	123	129	146
	15.4	9.4	0.3	0.14	3.886	231	126	10.14	5.70	436	440	360	120	123	123	135	137	153
	18.2	9.4	0.3	0.14	3.933	241	130	10.26	5.75	444	457	373	124	125	128	142	147	160

2

Table II.S3. *Difference between model-predicted values and experiment-determined values (Table II.S2) of Vp, Vs, K_S, G, and C_{ij}s for all 8 wadsleyite samples at different pressure conditions ($(X_{model}-X_{exp.})/X_{exp.}$). Most of the experimental data are within 5% difference compared with the modeling result, with only a few disperse data points, which are mostly off-diagonal C_{ij}s. Off-diagonal C_{ij}s are typically less well constrained compared with diagonal C_{ij}s.*

	Pressure	Fe #	$Fe^{3+}/\Sigma Fe$	H_2O wt%	Vp	Vs	Ks	G	C_{11}	C_{22}	C_{33}	C_{44}	C_{55}	C_{66}	C_{12}	C_{13}	C_{23}
Sawamoto et al., 1984	0	0.0	0	0	-1%	-1%	-3%	-2%	0%	-3%	-3%	-2%	-1%	1%	-5%	-9%	-3%
Zha et al., 1997	0	0.0	0	0	-1%	-2%	-1%	-3%	-3%	1%	-2%	-1%	-4%	-4%	9%	5%	-3%
	3.1	0.0	0	0	0%	0%	0%	1%	-1%	2%	-2%	2%	-4%	4%	-3%	1%	-1%
	6.3	0.0	0	0	0%	-1%	1%	-1%	0%	1%	-3%	-8%	2%	-6%	12%	-4%	2%
	8.1	0.0	0	0	0%	0%	0%	-1%	0%	-1%	-2%	-3%	-3%	-4%	6%	-4%	3%
	9.4	0.0	0	0	-1%	-1%	-2%	-1%	0%	-4%	-2%	-6%	-2%	-2%	1%	-3%	0%
	10.5	0.0	0	0	0%	0%	0%	1%	0%	0%	1%	-1%	-5%	2%	1%	-4%	7%
	14.2	0.0	0	0	-2%	-1%	-6%	-2%	-1%	-4%	-7%	-5%	1%	-4%	-2%	-8%	-4%
Mao et al., 2008a	0	0.0	0	0.38	0%	1%	1%	1%	-1%	2%	2%	1%	2%	1%	2%	2%	2%
	0	0.0	0	1.2	0%	0%	1%	1%	2%	1%	1%	0%	-1%	1%	-4%	-2%	4%
	0	0.0	0	2.9	0%	0%	0%	0%	1%	-1%	3%	-1%	0%	1%	1%	2%	-2%

Table II.S3. (Continue)

Mao et al., 2008b	0	0.0	0	1.2	0%	1%	0%	2%	1%	2%	-1%	2%	4%	2%	0%	1%	-1%		
	1.2	0.0	0	1.2	1%	1%	2%	3%	1%	2%	3%	2%	4%	1%	1%	9%	0%		
	2.7	0.0	0	1.2	1%	2%	0%	4%	0%	3%	-1%	3%	4%	1%	0%	3%	-6%		
	4.2	0.0	0	1.2	1%	2%	2%	4%	0%	3%	3%	3%	3%	1%	1%	7%	-3%		
	6.7	0.0	0	1.2	1%	2%	0%	5%	1%	2%	4%	4%	1%	3%	-5%	5%	-4%		
	8.2	0.0	0	1.2	1%	2%	1%	5%	1%	3%	3%	4%	2%	3%	-2%	6%	-1%		
	10.2	0.0	0	1.2	1%	2%	0%	5%	0%	3%	3%	3%	2%	3%	-2%	4%	-2%		
	12.1	0.0	0	1.2	0%	2%	-2%	4%	-1%	1%	3%	3%	2%	3%	0%	2%	-1%		
Mao et al., 2011	0	11.0	0.1	2.0	-1%	-1%	-1%	-3%	-3%	0%	-4%	0%	-3%	-4%	1%	-3%	-1%		
	3.2	11.0	0.1	2.0	-1%	-1%	-1%	-1%	-2%	0%	-1%	-2%	-3%	-2%	-6%	-3%	0%		
	4.2	11.0	0.1	2.0	-1%	-1%	-2%	-3%	1%	-3%	-4%	-4%	-2%	-5%	-6%	-4%	2%		
	6.7	11.0	0.1	2.0	-1%	-1%	0%	-3%	1%	-1%	-2%	-4%	-3%	-3%	-1%	1%	2%		
	8.7	11.0	0.1	2.0	-1%	-1%	-2%	-2%	-1%	-2%	-1%	-3%	-3%	-2%	-2%	-3%	1%		
	10.2	11.0	0.1	2.0	-1%	-1%	-1%	-1%	-1%	-1%	0%	-2%	-2%	-1%	0%	-3%	1%		
	12.2	11.0	0.1	2.0	-1%	-1%	-1%	-1%	1%	-1%	-2%	0%	-1%	-2%	6%	-3%	1%		

Table II.S3. (Continue)

Wang et al., 2014	0	7.5	unknown	0	0%	0%	0%	0%	1%	-2%	1%	1%	-2%	-3%	-5%	2%	-3%	
	4.1	7.5	unknown	0	0%	0%	0%	0%	-1%	0%	0%	2%	-2%	-3%	0%	2%	-3%	
	6.0	7.5	unknown	0	1%	0%	2%	0%	-1%	0%	2%	5%	-3%	-2%	2%	6%	-1%	
	8.0	7.5	unknown	0	0%	0%	1%	0%	0%	1%	2%	2%	-2%	-3%	-1%	2%	2%	
	10.0	7.5	unknown	0	0%	0%	1%	0%	-1%	1%	2%	4%	-4%	-1%	1%	2%	2%	
	12.1	7.5	unknown	0	0%	0%	1%	0%	0%	1%	2%	2%	-3%	-2%	1%	0%	1%	
	14	7.5	unknown	0	0%	0%	0%	0%	1%	0%	1%	2%	-1%	-2%	0%	0%	0%	
	15.9	7.5	unknown	0	0%	0%	0%	-1%	0%	0%	1%	2%	-2%	-2%	-2%	0%	1%	
	17.7	7.5	unknown	0	0%	0%	0%	0%	0%	1%	1%	2%	-3%	0%	-2%	-4%	1%	
Buchen et al., 2018	0	11.2	0.15	0.24	1%	1%	1%	1%	0%	1%	0%	0%	3%	5%	3%	-2%	7%	
	1.5	11.2	0.15	0.24	0%	-1%	0%	-2%	-2%	-1%	-2%	-1%	-4%	2%	5%	8%	-4%	
	4.1	11.2	0.15	0.24	0%	-1%	0%	-1%	-3%	1%	0%	-2%	-1%	0%	1%	-1%	3%	
	8.8	11.2	0.15	0.24	-1%	-2%	0%	-3%	0%	-4%	-2%	-2%	-3%	-3%	5%	-1%	-2%	
	11	11.2	0.15	0.24	0%	-1%	2%	-1%	-1%	1%	1%	-2%	1%	-1%	4%	-3%	2%	
	13.1	11.2	0.15	0.24	0%	0%	0%	0%	-1%	-1%	-1%	1%	1%	2%	-1%	-5%	0%	

	16.1	11.2	0.15	0.24	0%	-1%	2%	-2%	2%	-2%	0%	-2%	2%	-1%	1%	3%	0%
	19.7	11.2	0.15	0.24	0%	0%	1%	0%	-1%	4%	-2%	2%	-2%	3%	1%	-6%	1%
This study	0	9.4	0.3	0.14	1%	1%	2%	2%	2%	1%	4%	0%	2%	1%	0%	5%	-1%
	2.9	9.4	0.3	0.14	1%	1%	2%	1%	2%	0%	2%	0%	3%	-1%	-3%	8%	-2%
	6.6	9.4	0.3	0.14	1%	1%	1%	1%	2%	-1%	1%	2%	2%	0%	-2%	8%	-6%
	9.5	9.4	0.3	0.14	1%	1%	2%	1%	2%	0%	2%	0%	2%	0%	-3%	9%	-5%
	12.2	9.4	0.3	0.14	0%	0%	0%	1%	2%	0%	0%	-3%	3%	2%	-3%	4%	-5%
	15.4	9.4	0.3	0.14	0%	0%	1%	0%	0%	0%	1%	-2%	3%	1%	-4%	4%	-3%
	18.2	9.4	0.3	0.14	0%	0%	1%	0%	1%	0%	1%	-4%	3%	2%	-4%	2%	-2%

7

Table II.S4. *Comparison between experiment-determined and model-predicted $C_{ij,0}$, K_{S0}, G_0, and their pressure derivatives for our synthetic wadsleyite sample (Fe#=9.4, 0.14 wt% water, $Fe^{3+}/\Sigma Fe=0.3$) in this study.*

	Experimental results			Model-predicted results		
	M_0(GPa)	$\partial M/\partial P$	$\partial^2 M/\partial P^2$(GPa^{-1})	M_0(GPa)	$\partial M/\partial P$	$\partial^2 M/\partial P^2$(GPa^{-1})
C_{11}	341(1)	8.4(2)	-0.37(3)	349(9)	8.5(6)	-0.41(6)
C_{22}	358(1)	5.4(1)	0	361(7)	5.2(1)	0
C_{33}	244(2)	10.7(3)	-0.50(5)	254(9)	9.6(8)	-0.38(9)
C_{44}	106(2)	0.89(5)	0	106(2)	0.8(2)	0
C_{55}	109(1)	0.87(2)	0	111(4)	1.0(2)	0
C_{66}	90.8(7)	2.09(5)	0	92(4)	1.9(1)	0
C_{12}	75(1)	4.8(2)	-0.15(2)	75(4)	4.4(4)	-0.14(4)
C_{13}	99(2)	2.4(1)	0	104(5)	2.5(4)	0
C_{23}	102(3)	3.4 (1)	0	102(2)	3.06(7)	0
Ks^{VRH}	165(2)	5.2(5)	-0.16(11)	168(1)	5.1(7)	-0.16(fix)
G^{VRH}	104(2)	1.9(2)	-0.076(28)	106(2)	1.8(1)	-0.076(fix)

Table II.S5. *The water-Fe-pressure dependent elastic properties of single-crystal wadsleyite described by the empirical relationship of* $\boldsymbol{B = B_0 + B_1 \times}$ *water (wt%)* $\boldsymbol{+ B_2 \times}$ *Fe#.*

B	**B_0**	**B1**	**B_2**	**B**	**B_0**	**B_1**	**B_2**
ρ_0 (g/cm^3)	3.479(3)	-0.049(2)	0.0122(4)	**$C_{11,0}$'**	5.8(2)	0.2(1)	0.28(4)
K_{S0}(GPa)	169(1)	-7.6(8)	0	**$C_{11,0}$''(GPa$^-$**	0	0	-0.044(6)
G_0(GPa)	112(1)	-5.2(7)	-0.6(1)	**$C_{22,0}$'**	5.2(1)	0.2(2)	0
$C_{11,0}$(GPa)	359(4)	-13(3)	-0.9(5)	**$C_{33,0}$'**	6.5(2)	0.6(2)	0.32(6)
$C_{22,0}$(GPa)	372(3)	-21(2)	-0.9(4)	**$C_{33,0}$''(GPa$^-$**	0	0	-0.040(9)
$C_{33,0}$(GPa)	266(4)	-11(2)	-1.1(5)	**$C_{44,0}$'**	1.0(1)	0.26(8)	-0.03(1)
$C_{44,0}$(GPa)	110.2(7)	-5.6(4)	-0.38(8)	**$C_{55,0}$'**	0.4(1)	0.10(8)	0.06(1)
$C_{55,0}$(GPa)	117(2)	-6(1)	-0.5(2)	**$C_{66,0}$'**	1.85(9)	0.16(7)	0.003(1)
$C_{66,0}$(GPa)	99(2)	-4(1)	-0.7(2)	**$C_{12,0}$'**	3.5(1)	0.30(9)	0.09(3)
$C_{12,0}$(GPa)	72(2)	-3(1)	0.4(2)	**$C_{12,0}$''(GPa$^-$**	0	0	-0.015(4)
$C_{13,0}$(GPa)	100(2)	-3(2)	0.5(3)	**$C_{13,0}$'**	2.1(2)	0.2(1)	0.04(2)
$C_{23,0}$(GPa)	103(2)	-7(1)	0	**$C_{23,0}$'**	3.09(6)	-0.19(9)	0
K_{S0}'	4.5(4)	0	0.06(3)	**G_0'**	1.8(1)	0.18(9)	0
K_{S0}''(GPa$^-$	-0.16	0	0	**G_0'' (GPa^{-1})**	-0.076	0	0

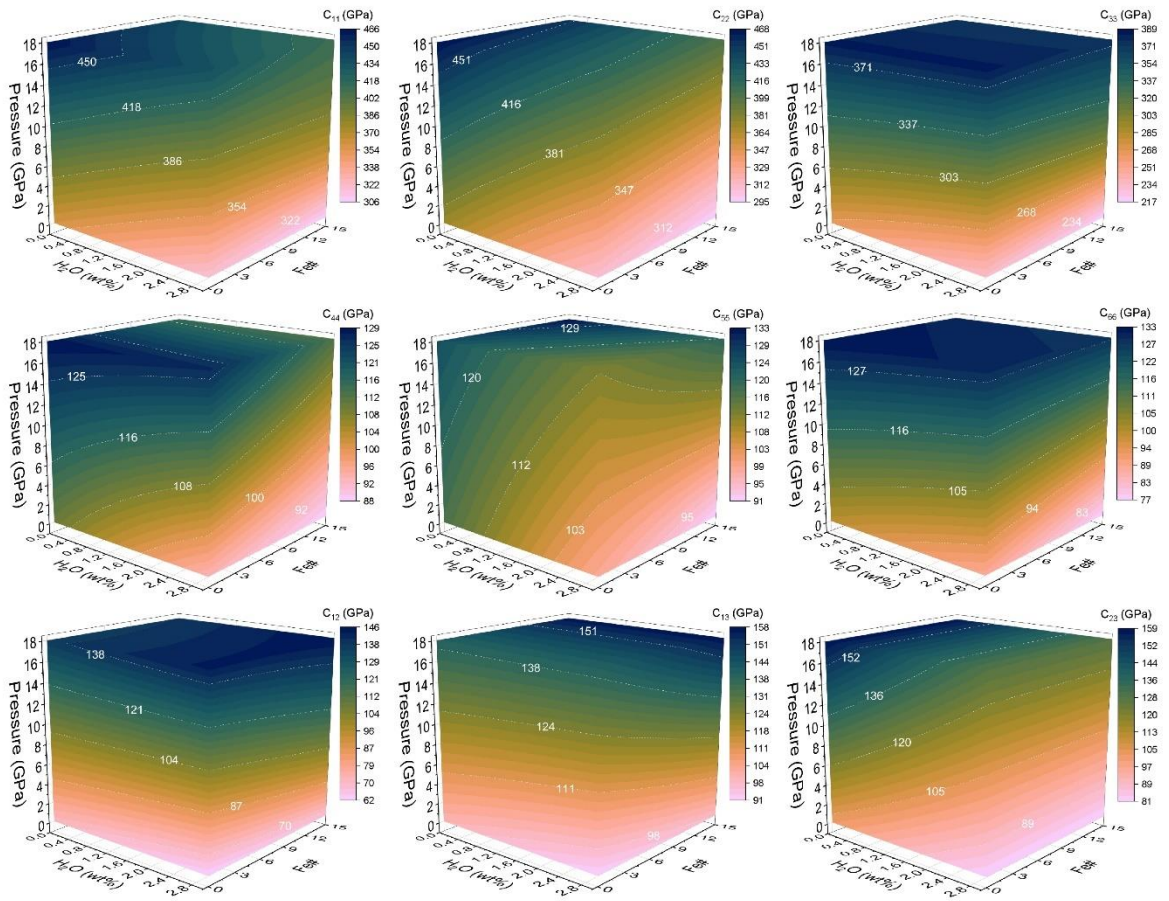

Fig. II.S6. *The water, Fe, and pressure–dependent C_{ij}s of single-crystal wadsleyite (the batlow color scale is from Crameri, 2020).*

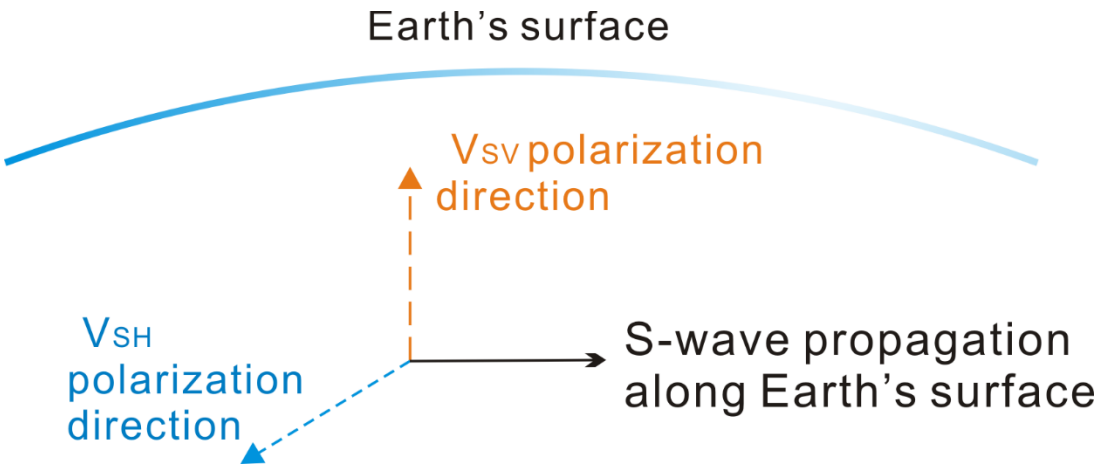

Fig. II.S7. *The geometrical relationship between V_{SV} and V_{SH} from surface waves.*

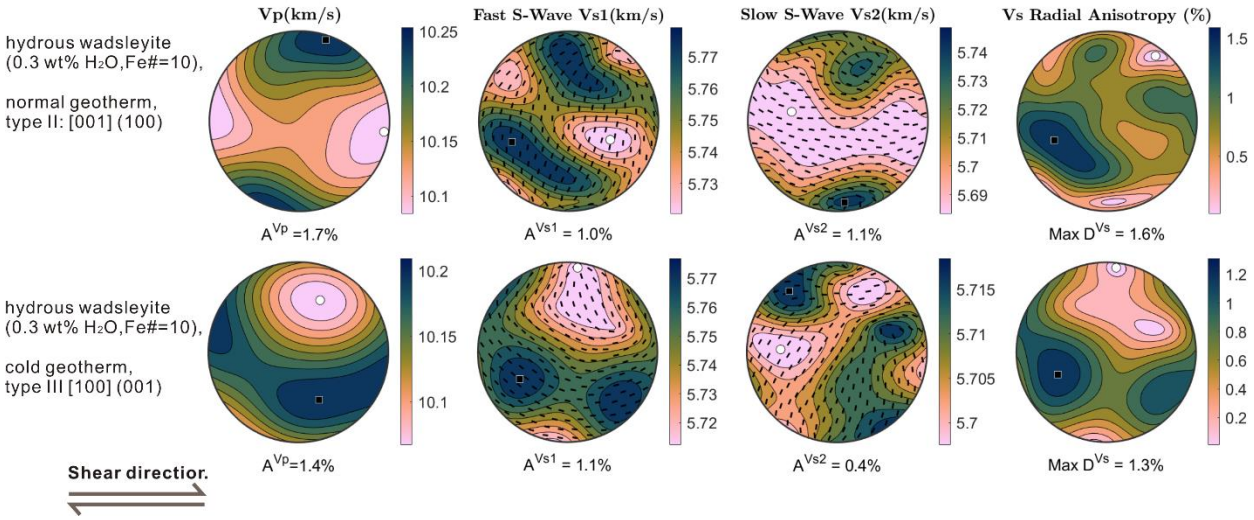

Fig. II.S8. *The calculated acoustic velocities in stereographic projections for hydrous wadsleyite aggregates (0.3 wt% water) with type II LPO (M0310) and type III LPO (M0308), respectively. The LPO data are from Ohuchi et al. (2014). The shear plane normal is north-south. The anisotropy of hydrous wadsleyite aggregates with 0.3 wt% water is slightly higher than the anisotropy of hydrous wadsleyite aggregates with 1.5 wt% water, because water decreases the intrinsic anisotropy of wadsleyite.* A^{Vp}*,* A^{Vs1} *and* A^{Vs2} *refer to the maximum anisotropy values.*

Supplementary References

Buchen, J., Marquardt, H., Speziale, S., Kawazoe, T., Ballaran, T. B., & Kurnosov, A. (2018). High-pressure single-crystal elasticity of wadsleyite and the seismic signature of water in the shallow transition zone. Earth and Planetary Science Letters, 498, 77-87.

Bolfan-Casanova, N., Schiavi, F., Novella, D., Bureau, H., Raepsaet, C., Khodja, H., & Demouchy, S. (2018). Examination of water quantification and incorporation in Transition Zone Minerals: wadsleyite, ringwoodite and phase D using ERDA (Elastic recoil detection Analysis). Frontiers in Earth Science, 6, 75.

Crameri, F. Scientific Colour Maps,

Davies, G. F. (1974). Effective elastic moduli under hydrostatic stress—I. Quasi-harmonic theory. Journal of Physics and Chemistry of Solids, 35(11), 1513–1520.

Davies, G. F., & Dziewonski, A. M. (1975). Homogeneity and constitution of the Earth's lower mantle and outer core. Physics of the Earth and Planetary Interiors, 10(4), 336–343.

Dyar, M. D., Agresti, D. G., Schaefer, M. W., Grant, C. A., & Sklute, E. C. (2006). Mössbauer spectroscopy of earth and planetary materials. Annu. Rev. Earth Planet. Sci., 34, 83-125.

Fu, S., Yang, J., Tsujino, N., Okuchi, T., Purevjav, N., & Lin, J. F. (2019). Single-crystal elasticity of (Al, Fe)-bearing bridgmanite and seismic shear wave radial anisotropy at the topmost lower mantle. Earth and Planetary Science Letters, *518*, 116-12.

Hill, R. (1963). Elastic properties of reinforced solids: some theoretical principles. *Journal of the Mechanics and Physics of Solids*, *11*(5), 357-372.

Jacobsen, S. D., Demouchy, S., Frost, D. J., Ballaran, T. B., & Kung, J. (2005). A systematic study of OH in hydrous wadsleyite from polarized FTIR spectroscopy and single-crystal X-ray diffraction: Oxygen sites for hydrogen storage in Earth's interior. American Mineralogist, 90(1), 61-70.

Libowitzky, E., & Rossman, G. R. (1997). An IR absorption calibration for water in minerals. American Mineralogist, 82(11-12), 1111-1115.

Lin, J. F., Mao, Z., Yang, J., & Fu, S. (2018). Elasticity of lower-mantle bridgmanite. *Nature*, *564*(7736), E18-E26.

Mao, Z., Jacobsen, S. D., Frost, D. J., McCammon, C. A., Hauri, E. H., & Duffy, T. S. (2011). Effect of hydration on the single-crystal elasticity of Fe-bearing wadsleyite to 12 GPa. American Mineralogist, 96(10), 1606-1612.

Mao, Z., Jacobsen, S. D., Jiang, F., Smyth, J. R., Holl, C. M., Frost, D. J., & Duffy, T. S. (2008a). Single-crystal elasticity of wadsleyites, β-Mg2SiO4, containing 0.37–1.66 wt.% H2O. Earth and Planetary Science Letters, 266(1-2), 78-89.

Mao, Z., Jacobsen, S. D., Jiang, F., Smyth, J. R., Holl, C. M., & Duffy, T. S. (2008b). Elasticity of hydrous wadsleyite to 12 GPa: implications for Earth's transition zone. Geophysical Research Letters, 35(21).

Ohuchi, T., Fujino, K., Kawazoe, T., & Irifune, T. (2014). Crystallographic preferred orientation of wadsleyite and ringwoodite: Effects of phase transformation and water on seismic anisotropy in the mantle transition zone. Earth and Planetary Science Letters, 397, 133-144.

Sawamoto, H., Weidner, D. J., Sasaki, S., & Kumazawa, M. (1984). Single-crystal elastic properties of the modified spinel (beta) phase of magnesium orthosilicate. Science, 224(4650), 749-751.

Smyth, J. R., Bolfan-Casanova, N., Avignant, D., El-Ghozzi, M., & Hirner, S. M. (2014). Tetrahedral ferric iron in oxidized hydrous wadsleyite. American Mineralogist, 99(2-3), 458-466.

Wang, J. (2008). The effect of hydration state, Fe, and spin state of Fe on the elasticity of mantle minerals at high pressure (Doctoral dissertation, University of Illinois at Urbana-Champaign).

Wang, J., Bass, J. D., & Kastura, T. (2014). Elastic properties of iron-bearing wadsleyite to 17.7 GPa: Implications for mantle mineral models. Physics of the Earth and Planetary Interiors, 228, 92-96.

Zha, C. S., Duffy, T. S., Mao, H. K., Downs, R. T., Hemley, R. J., & Weidner, D. J. (1997). Single-crystal elasticity of β-Mg2SiO4 to the pressure of the 410 km seismic discontinuity in the earth's mantle. Earth and Planetary Science Letters, 147(1-4), E9-E15.

Chapter III

Constraining Composition and Temperature Variations in the Mantle Transition Zone

Abstract

The Mantle Transition Zone connects 2 major layers of Earth's interior that may be compositionally distinct: the upper mantle and the lower mantle. Wadsleyite is a major mineral in the upper Mantle Transition Zone. Here, we measure the single-crystal elastic properties of hydrous Fe-bearing wadsleyite at high pressure-temperature conditions by Brillouin spectroscopy. Our results are then used to model the global distribution of wadsleyite proportion, temperature, and water content in the upper Mantle Transition Zone by integrating mineral physics data with global seismic observations. Our models show that the upper Mantle Transition Zone near subducted slabs is relatively cold, enriched in wadsleyite, and slightly more hydrated compared to regions where plumes are expected. This study provides direct evidence for the thermochemical heterogeneities in the upper Mantle Transition Zone which is important for understanding the material exchange processes between the upper and lower mantle.

1. Introduction

The chemical composition of bulk silicate Earth is highly controversial, ranging from the Si-poor pyrolite (olivine content 53-65%) to the Si-rich chondritic or perovskitic composition (olivine content 30-45%) (Anderson and Bass, 1986; Irifune et al., 2008a; Kaminsky, 2012; Murakami et al., 2012). Although the pyrolitic upper mantle is less debated, growing evidence suggests that the lower mantle can be chemically more enriched in Si, that is bridgmanite(Mashino et al., 2020; Mattern et al., 2005; Murakami et al., 2012; Ricolleau et al., 2009; Xie et al., 2020). As a result, the silicate Earth is likely to be compositionally layered. This view, however, has been challenged by the widely observed material exchange between the upper and lower mantle suggested by seismic tomography, such as slabs penetrating into the lower mantle (Fukao and Obayashi, 2013), and possible plumes rising beneath hotspots (Courtillot et al., 2003). It is possible that such wide-range material exchange did not happen until recently in Earth's history and the time is too short to completely homogenize the lower mantle (Goes et al., 2008; Korenaga, 2013). As the Mantle Transition Zone (MTZ) connects the upper and lower mantle, mapping the thermochemical heterogeneities in MTZ is critical for understanding the material exchange between the upper and lower mantle, as well as volatile storage and transport in the deep Earth.

Unlike the low water solubility of the major upper and lower mantle minerals, the most abundant mineral phases in the MTZ, wadsleyite, and ringwoodite, can store up to 2-3 wt% water as hydroxyl groups in their crystal structures (Inoue et al., 1995). Although later studies suggested that the upper limit of water concentration in wadsleyite and ringwoodite is ~1 wt% under normal mantle geotherm (Fei and Katsura, 2020), the MTZ is still a giant potential water reservoir in the deep Earth. The possible enrichment of water in the MTZ can affect not only the seismic wave speeds of minerals (Mao et al., 2008b; Wang et al., 2019; Wang et al., 2021), but also the phase

transition boundary and binary phase loop width of relevant phase transitions in the MTZ pressure-temperature (*P*-*T*) space (Frost and Dolejš, 2007; Katsura et al., 2010).

The depth, width, and magnitude of the 410 km, 520 km, and 660 km seismic discontinuities (hereinafter referred to as the 410, 520, and 660), which are mainly caused by the olivine to wadsleyite, wadsleyite to ringwoodite, and ringwoodite to bridgmanite+ferropericlase transitions, are functions of not only *T* (Katsura et al., 2004), but also chemical composition, such as water (Frost and Dolejš, 2007) and Fe# (Katsura et al., 2004). Prior attempts have been made utilizing mineral physics data to better understand the seismic observations of these discontinuities. For example, Houser (Houser, 2016) used the 410 and 660 depth and *V*s anomaly in the lower MTZ to map the global water distribution assuming a pyrolitic MTZ. Wang et al. (2021) took one step further by taking the ΔT which is temperature anomaly into account, using both the 660 depth and *V*s anomaly in the lower MTZ to map the water distribution again assuming a pyrolitic MTZ, although at least 20% of the lower MTZ cannot be explained by the pyrolitic composition within the reasonable water content and ΔT range assumed in Wang et al. (2021). As suggested Zhang and Bass (2016), it is possible that chemical composition in the MTZ, at least locally, can significantly deviate from the idealized pyrolite model and influence seismic observations of discontinuities. Therefore, modeling the water content, ΔT, and the bulk mineralogical composition together is needed to quantify thermochemical heterogeneities in the MTZ.

The most important physical properties needed for such modeling work are the high *P*-*T* elastic properties of wadsleyite and majoritic garnet in the MTZ. Garnet (pyrope-grossular-almandine-majorite solid solution) is among the most intensively studied mantle minerals with numerous high *P*-*T* sound velocity measurements available (Arimoto et al., 2015; Li and Liebermann, 2014). For example, the sound velocities of a synthetic garnet with “pyrolite minus

olivine" composition were determined up to 18 GPa and 1673 K (Irifune et al., 2008a) and a polycrystalline almandine sample has also been measured up to 19 GPa and 1700 K (Arimoto et al., 2015). Previous sound velocity measurements on wadsleyite have covered a wide range of Fe# (0-11.2) and water content (0-2.9wt%) at high-*P* ambient-*T* or ambient *P*-*T* conditions (Buchen et al., 2018; Mao et al., 2011; Mao et al., 2008a; Mao et al., 2008b; Wang et al., 2014; Zha et al., 1997; Zhou et al., 2021). In particular, Zhou et al. (2021) has established a Fe# and water content dependent single-crystal elasticity model of wadsleyite based on their own experimental data and all previous measurements (Buchen et al., 2018; Mao et al., 2011; Mao et al., 2008a; Mao et al., 2008b; Wang et al., 2014; Zha et al., 1997; Zhou et al., 2021). However, the velocities of hydrous Fe-bearing wadsleyite samples have never been measured at simultaneously high *P*-*T* conditions, and previous ultrasound interferometry experiments on polycrystalline wadsleyite were conducted outside the stability field of wadsleyite (Gwanmesia et al., 2020; Li et al., 2001; Liu et al., 2009b). Moreover, the single-crystal elastic moduli (C_{ij}s) of wadsleyite have never been determined at simultaneously high *P*-*T* conditions. Fe# and water content both have moderate effects on the *P* dependence of the C_{ij}s, bulk modulus (*K*s), and shear modulus (*G*) at 300 K (Zhou et al., 2021) and references cited in Zhou et al. (2021); however, whether these effects are still significant at high *T* remains unknown. First-principles calculations have provided useful insights toward the *P* and *T* dependence of the C_{ij}s of wadsleyite (Wang et al., 2019). Given the large discrepancy between the computationally and experimentally determined elasticity data of ringwoodite (Wang et al., 2021), it is worthwhile to examine the single-crystal elasticity of wadsleyite experimentally in the high *P*-*T* space. Therefore, in this study, we measured the sound velocities of the hydrous Fe-bearing wadsleyite single crystals (Fe# = 9.4 (2), 0.15 (4) wt% water) up to 16 GPa and 700 K using Brillouin spectroscopy (Fig. III.1, Figs. III. S1-S3).

Compared with the more complicated 520 and 660 discontinuities, which may be affected by other phase transitions nearby (e.g., exsolution of Ca silicate perovskite, majoritic garnet-bridgmanite transition), the 410 is solely related to the olivine to wadsleyite phase transition.

In this study, we exploit the petrological simplicity of the 410. By integrating the experimental constraints on the high *P*-*T* elasticity of wadsleyite and majoritic garnet along with previously published mineral physics and global seismic imaging results, we map the global distributions of wadsleyite proportion, ΔT, and water content in the upper MTZ, and statistically analyze their associations with different geographic and tectonic settings.

2.Methods

Sample characterization

The samples used in this study are the same as the ones used in Zhou et al. (2021) for ambient-*T* high-*P* sound velocity measurements. Hydrous wadsleyite single crystals were synthesized from San Carlos olivine powder at 1673 K and 16 GPa for 24 hours in the 1000-ton Multi-Anvil Press at the University of Hawai‘i at Mānoa. We used the JEOL 8200 Electron Microprobe (beam current =20 nA; accelerating voltage =15 kV) to determine the composition of the wadsleyite samples at the University of New Mexico (UNM). The electron microprobe analysis on 5 single-crystal grains yielded an average Fe# of 9.4 (2). The Mössbauer spectroscopy experiment was performed on ~80 randomly oriented wadsleyite grains in the offline Mössbauer spectroscopy lab at sector 3, Advanced Photon Source, Argonne National Laboratory. The $Fe^{3+}/\Sigma Fe$ of synthetic wadsleyite is determined to be 0.3. The Nicolet Nexus 670 Fourier Transformed Infrared Spectrometer (FTIR) at UNM was used to determine the water content using the calibration presented in Libowitzky and Rossman (Libowitzky and Rossman, 1997). Using the calibration procedure outlined in Deon et al. (2010) yielded a similar water content as shown in

Table III.S5. The technical details and results of the Electron microscope analysis, Mössbauer spectroscopy, and part of the FTIR experimental results were all presented in Zhou et al. (2021). In this study, for more precise water content determination, we polished another 8 randomly selected wadsleyite single crystals for additional unpolarized FTIR measurements. The results are shown in Fig. III. S5 and Table III. S5. The updated water content is 0.15 (4) wt% by averaging the unpolarized IR absorption spectra on 17 crystals. 9 crystals have been measured and shown in Zhou et al. (2021) and the rest are the new measurements conducted in this study. The new water content of 0.15 (4) wt% is about 0.01 wt% higher than the water content determined from 9 crystals (0.14 (4) wt%) in Zhou et al. (2021), which is within the water content uncertainty of 400 ppm (Table III.S5). The small change of water content has a negligible effect on the composition dependent single-crystal elasticity model presented in Zhou et al. (2021).

High *P*-*T* Brillouin spectroscopy experiments

We performed high *P*-*T* Brillouin spectroscopy experiments on 3 wadsleyite single-crystal platelets with orientations: (-0.3420 0.8718 0.3506), (0.0748 0.3154 -0.9460), and (0.5341 0.0953 -0.8401). Each crystal (~50 μm × 50 μm × 12 μm) was loaded into a high-*T* BX90 diamond anvil cell (DAC) along with 2 ruby spheres for *P* determination. The pair of diamond anvils (350 μm culet) was oriented before experiments so that the slow directions of the top and bottom diamonds matched each other. A 250 μm hole was drilled in a pre-indented Rhenium gasket. Neon was gas-loaded into the sample chamber as *P*-transmitting medium at GeoSoilEnviroCARS, Advanced Photon Source. High *T* was generated by Platinum resistive heaters located at the center of the DAC (Lai et al., 2020). We attached 2 K-type thermocouples to the diamond surface as close as possible to the diamond culet for *T* measurement. The *T* difference given by 2 thermocouples is < 15 K throughout all experiments.

We performed Brillouin spectroscopy experiments at the Laser Spectroscopy Laboratory at UNM using a 532 nm single-mode diode-pumped solid-state laser as the light source. We used 50° symmetric forward scattering geometry and a standard silica glass Corning 7980 was employed to calibrate the scattering angle every 2 months (Zhang et al., 2015). The high *P*-*T* Brillouin measurements of wadsleyite crystals lasted for 8 months, and the calibrated scattering angles used for data analysis are: 50.42 (5)°, 50.60 (8)°, 50.68 (6)°, and 50.77 (6)°. The Brillouin frequency shift was measured using a 6-pass tandem Fabry-Pérot interferometer. At each *P*-*T* condition, *V*p and *V*s of each single crystal were measured from 0º to 360º with a step of 15º (24 different Chi angles). Typical Brillouin spectra are shown in Fig. III.S1. Brillouin experiments under high *P*-*T* conditions along 400 K, 500 K, and 700 K isotherms were conducted for all 3 wadsleyite platelets.

Using the Christoffel equations, we inverted the best-fit C_{ij}s of wadsleyite based on the high *P*-*T* phonon direction-*V*p-*V*s dataset on the 3 wadsleyite single crystals (Fig. III. S2) with initial estimated high *P*-*T* densities. The RMS error at each *P*-*T* condition is less than 60 m/s. We then utilized Voigt-Reuss-Hill averaging scheme (Hill, 1963) to calculate the aggregate V_P and *V*s at each high *P*-*T* condition. It is worth noting that although the density is based on an initial guess, the V_P and *V*s derived here are actually true values. With fixed ambient *P*-*T* K_{S0}, G_0, and ρ_0 from Zhou et al. (2021), thermal expansivity (Katsura et al., 2009) α as $2.31(3) \times 10^{-5} + 1.18(3) \times 10^{-8}$ $(T - 300)$ K^{-1}, we fitted the new high *P*-*T* velocity data collected in this study together with the room-*T* high-*P* elasticity data presented in Zhou et al.[29] using *T* dependent 4th order finite strain equation of state (Davies and Dziewonski, 1975; Duffy and Anderson, 1989), and derived the best-fit $(\partial K_S/\partial P)_{T0}$, $(\partial^2 K_S/\partial P^2)_{T0}$, $(\partial G/\partial P)_{T0}$, $(\partial^2 G/\partial P^2)_{T0}$, $(\partial K_S/\partial T)_{P0}$, $(\partial G/\partial T)_{P0}$, and densities. Then, we updated the C_{ij}s, *K*s, *G* at each high *P*-*T* condition with the derived true densities (Table III.S1).

Finally, using the aggregate thermoelastic parameters obtained above, we fitted *P*-*T*-C_{ij}s data to the *T*-dependent 3rd order or 4th order finite strain equation of state (Davies, 1974) to obtain the best-fit $(\partial C_{ij}/\partial P)_{T0}$, $(\partial^2 C_{ij}/\partial P^2)_{T0,}$ $(\partial C_{ij}/\partial T)_{P0}$, which were shown in Table III.S3.

Evaluation of water loss during the high *P*-*T* experiments

We conducted the following 3 experiments to confirm that the wadsleyite crystals remained hydrated after the completion of the high *P*-*T* experiments: 1. We collected additional FTIR spectra on Wad34 at 300 K before heating, and at 300 K after it was heated to 400K, 500K, and 700K (Fig. III.S6). The water content is determined to be 1800 ppm before heating, and it remains the same after multiple heating and cooling cycles. There is no resolvable water loss. 2. We conducted additional Brillouin spectroscopy measurements on sample Wad9 (0.0748 0.3154 -0.9460) at 400 K and 0 GPa after the completion of high *P*-*T* experiments on this sample. If significant water loss has taken place, the newly collected sound velocity data would be faster than the C_{ij} model-predicted *V*p and *V*s values (Fig. III.S7), which is not the case. 3. After we completed the 700 K and 9.4 GPa Brillouin spectroscopy experiments of wadsleyite sample Wad6 (-0.3420, 0.8718, 0.3506) and cooled it down to 300 K, we collected 5 additional Brillouin spectra of this sample at 300 K and 9 GPa along 5 additional different crystallographic directions. Due to the short collection time, the spectrum quality only allows reliable determination of *V*s at these 5 different directions. The obtained *V*s values nicely matched the C_{ij} model-predicted *V*s values at 300 K and 9 GPa, as well as the *V*s at 300 K and 9.5 GPa measured before the sample was heated (Fig. III.S8). Thus, the crystals are unlikely dehydrated during the high *P*-*T* experiments.

Grid search modeling

Based on the experimentally determined mineral physics data, we calculated the predicted *V*p and *V*s anomaly at 450 km depth and the 410 depth at each location by varying the wadsleyite content (13-93 vol % in 2 vol% steps), ΔT (-300-300 K in 15 K steps), water content in wadsleyite (0-2 wt% in 0.05 wt% steps), resulting in ~70000 predicted models.

The *V*p anomaly compared with a dry pyrolite model at 450 km are estimated using the following equation:

$$\Delta V\text{p\_pred} = (a * P_{\text{Wad}} + b * (100 - P_{\text{Wad}})) * 0.01 * \Delta T + c * (P_{\text{Wad}} - 53) - d * W * P_{\text{Wad}} * 0.01 \quad (1)$$

where P_{Wad} (vol%) is the wadsleyite content, ΔT (K) is the T anomaly compared with 1870 K (Katsura et al., 2010), and W (wt%) is the water content in wadsleyite. a (-0.0027) and b (-0.0028) are the influence of ΔT = 1 K on ΔVp_pred (%) of wadsleyite and majoritic garnet in the upper MTZ, respectively. c (0.0397) refers to the influence of increasing wadsleyite proportion by 1% on ΔVp_pred. The reference pyrolite model and harzburgite model we used in this study have 53 vol% and 73 vol% wadsleyite at ~15 GPa 1870 K, according to the most recent experimental study by Ishii et al. (2018, 2019). The chemical compositions of relevant mineral phases in pyrolite and harzburgite were also adopted from Ishii et al. (2018, 2019). d (0.9750) describes the relative change of ΔVp_pred of wadsleyite caused by adding 1wt% water in wadsleyite (this study, Zhou et al., 2021) at the upper MTZ P-T conditions. The parameters used to determine these coefficients (a, b, c, d) are reported in Table III.S2, and III.S4.

Similarly, the *V*s anomaly change as a function of P_{Wad} (vol%), ΔT (K), and W (wt%) is calculated as:

$$\Delta V\text{s\_pred} = (A * P_{\text{Wad}} + B * (100 - P_{Wad})) * 0.01 * \Delta T + C * (P_{\text{Wad}} - 53) - W * P_{\text{Wad}} * 0.01 * D \quad (2)$$

with A = -0.0040 (this study), B = -0.0045, C = 0.0868, D=0.4850. The parameters used to determine these coefficients (A, B, C, D) are reported in Table III.S2 and III.S4. Both equation 1 and 2 used volume-weighted velocities instead of the volume-weighted elastic moduli and density for calculating the velocities of garnet/wadsleyite mixtures due to the following 2 reasons: 1) Velocities of pyrolite calculated using these 2 approaches are very similar (difference is < 0.1%), as shown in Table III.S6; 2) Avoid additional parameters related to T and composition dependent density in the modeling and reduce the total number of parameters.

The 410 depth is affected by both ΔT (K) and W (wt%), and it is modeled as:

$$d410\_\text{pred} = \Delta T * e + \Delta T * \frac{W}{f} \ (\Delta T < 0) \quad (3)$$

$$d410\_\text{pred} = \Delta T * e \ \ (\Delta T \geq 0) \quad (4)$$

The effect of ΔT on the 410 depth is represented by e, which is determined to be 0.107 km K^{-1} by Katsura et al. (2004). As suggested by Frost and Dolejš (2007), increasing the water concentration of wadsleyite elevates the 410 discontinuity when T is low, however, such effect vanishes at higher T. In this study, we assume a linear decrease of the 410 depth ($\frac{-\Delta T}{f}$; f = 20) as a function of ΔT by adding 1 wt% water in wadsleyite when the T is lower than the reference T of 1870 K.

We compared the values predicted from the grid search process in the P_{Wad} - ΔT (K) -W (wt%) data space with global seismic models (the 410 depths (d410_obs) from Huang et al. (2019); Vp and Vs anomaly (ΔVp_obs, ΔVs_obs) at 450 km depth from Koelemeijer et al. (2015) at each location. The goodness of the model at each location is evaluated based on all 3 seismic observations:

$$\text{Misfit} = \sqrt{\frac{(d410\_\text{pred} - d410\_\text{obs})^2}{(d410\_\text{obs\_error})^2} + \frac{(\Delta V\text{p\_pred} - \Delta V\text{p\_obs})^2}{(\Delta V\text{p\_obs\_error})^2} + \frac{(\Delta V\text{s\_pred} - \Delta V\text{s\_obs})^2}{(\Delta V\text{s\_obs\_error})^2}} \quad (5)$$

with d410_obs_error = 1.3 % (Huang et al., 2019); ΔVp_obs_error = 0.5 %; ΔVs_obs_error = 0.85 % (Burdick and Lekić, 2017). We also conducted additional tests to verify the robustness of our modeling results given the uncertainties of the mineral physics predictions involved in the modeling. Details can be found in the Supplementary Discussion 1, Fig. III.S9, and Table III.S7.

We then picked the best-fit model with misfit <1 at each location, and then averaged the wadsleyite proportion, ΔT, and water content in wadsleyite of the chosen best-fit models (Fig. III.3). The standard deviation of these parameters in the chosen best-fit models would be the uncertainties for each parameter. We also averaged the best-fit models with misfit <1.5 at each location and the results are shown in Fig. III.S4. Due to the similar density of wadsleyite and majoritic garnet at the condition of the upper MTZ, the difference between wadsleyite vol% and wt% is less than 1% in the upper MTZ. Therefore, the water content in the upper MTZ at each location is derived by multiplying the wadsleyite proportion (vol%) and water content in wadsleyite (wt%). All the modeling codes are written in Python. All figures are plotted with PyGMT (Wessel et al., 2019).

Regional features of the upper MTZ

To statistically analyze the features in the upper MTZ under different geographic and tectonic settings, we selected four regional groups in this study: ocean, continents, subducting slabs, and deeply sourced hotspots (plumes), and calculated their average wadsleyite proportion, ΔT, and water content in the upper MTZ. Slab locations near the upper MTZ are defined by software Slab2 and shown in Fig. III.S10. The land and ocean locations are downloaded from the GMT database and shown in Fig. III.S11. The locations for deeply sourced hotspots (plumes) used in this study meet ≥ 2 requirements for deeply sourced hotspots given by Courtillot et al. (2003) and are shown in Fig. III.3.

3. Results and Discussion

High *P-T* single-crystal elasticity of wadsleyite

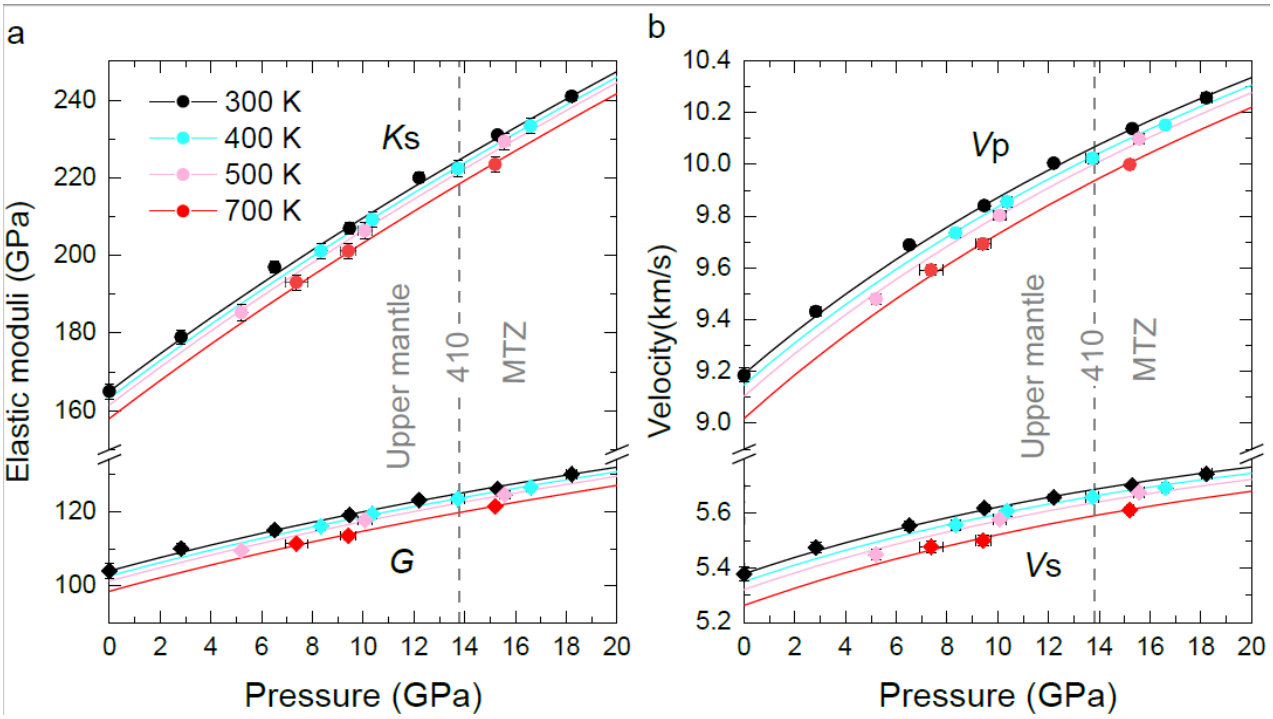

Fig. III.1. High P-T elastic properties of the hydrous Fe-bearing wadsleyite sample used in this study. a *Bulk modulus Ks and shear modulus G of the isotropic polycrystalline wadsleyite as a function of P and T.* ***b*** *Vp and Vs of the isotropic polycrystalline wadsleyite as a function of P and T. Solid lines represent 4th order finite strain equation of state fitting results. Voigt-Reuss-Hill averaging scheme is used to calculate the Ks, G, Vp, and Vs of the isotropic polycrystalline wadsleyite at 300 K, 400 K, 500 K, 700 K, respectively. Data along the 300 K isotherm are adopted from Zhou et al. (2021). Error bars smaller than the symbols are not shown.*

Using high *P-T* diamond anvil cell combined with Brillouin spectroscopy method, we measured sound velocitie on 3 wadsleyite platelets (Fe# = 9.4 (2), 0.15 (4) wt% water) with different orientations up to 16 GPa and 700 K (Fig. III.1). We then obtained the best-fit *P* and *T* dependence of *K*s, *G*, and C_{ij}s using *T* dependent finite strain equations of state (see Methods). The

aggregate elastic properties of the wadsleyite used in this study are: density ρ_0 = 3.595 (6) g cm^{-3}, Ks_0 = 165 (2) GPa (Zhou et al., 2021), G_0 = 104 (2) GPa (Zhou et al., 2021), $(\partial Ks/\partial P)_{T0}$ = 5.1 (1), $(\partial^2 Ks/\partial P^2)_{T0}$ = − 0.14 (2) GPa^{-1}, $(\partial G/\partial P)_{T0}$ = 1.9 (1), $(\partial^2 G/\partial P^2)_{T0}$ = − 0.07 (1) GPa^{-1}, $(\partial Ks/\partial T)_{P0}$ = − 0.018 (2) GPa K^{-1}, and $(\partial G/\partial T)_{P0}$ = − 0.014 (1) GPa K^{-1} (Table III.S1). As shown in Table III.S2, the $(\partial Ks/\partial T)_{P0}$ and $(\partial G/\partial T)_{P0}$ of wadsleyite measured in this study agree with what were given in Gwanmesia et al. (2020) and Isaak et al. (2007a), suggesting that the effects of water and Fe on the T derivatives of the elastic moduli are negligible. The $(\partial C_{ij}s/\partial T)_{P0}$ for our wadsleyite sample are shown in Table III.S3. The 6 diagonal C_{ij}s are more sensitive to T compared with the off-diagonal C_{ij}s (Fig. III.S3). T also has a more pronounced effect on Vs than Vp.

Mineral physics constraints on the upper MTZ seismic observations

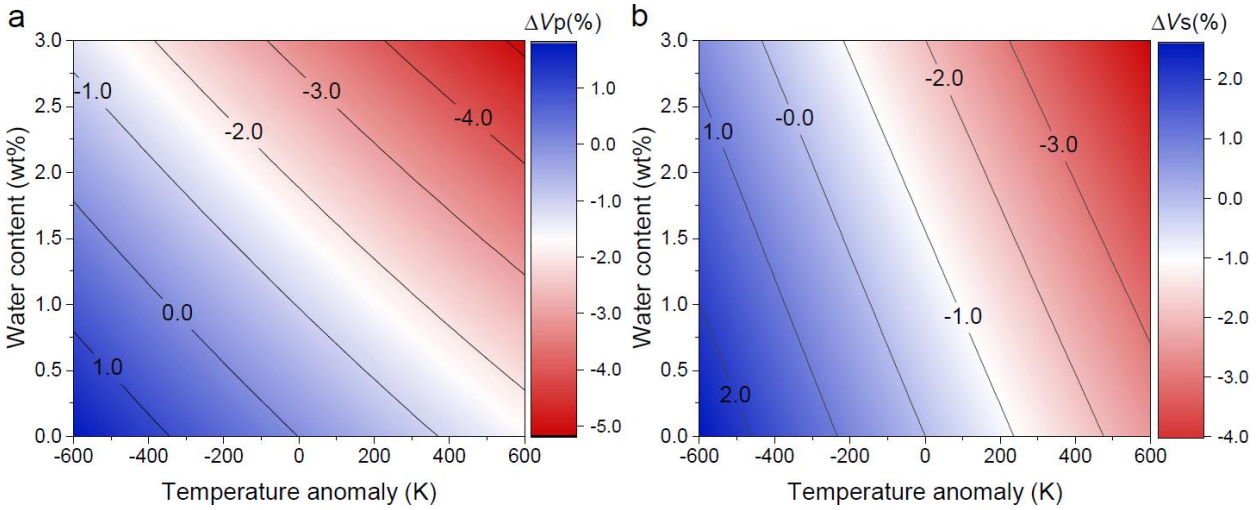

Fig. III.2. *Effects of water content in wadsleyite and temperature anomaly ΔT on the sound velocities of wadsleyite. a Relative variation, in percent, of wadsleyite Vp (ΔVp) as a consequence of water content and ΔT at the P-T conditions near the 410.* ***b*** *Relative variation, in percent, of wadsleyite Vs (ΔVs) as a consequence of water content and ΔT at the P-T conditions near the 410.*

Based on the $(\partial Ks/\partial T)_{P0}$ and $(\partial G/\partial T)_{P0}$ determined in this study and the relationship between water content and Ks_0, G_0, $(\partial Ks/\partial P)_{T0}$, and $(\partial G/\partial P)_{T0}$ derived in Zhou et al. (2021), we

found that the hydration effect diminishes with *P* but slightly enhances with *T*. Under high *P*-*T* conditions of the upper MTZ, adding 1wt% water in wadsleyite decreases its *V*p by ~1% and *V*s by ~0.5 % (Fig. III.2). In addition, the *V*p and *V*s decrease caused by adding 1 wt% water in wadsleyite is comparable to the velocity reduction resulted from *T* increase of 300 K and 100 K, respectively (Fig. III.2).

In addition to *T* and water content, wadsleyite proportion also affects the *V*p and *V*s of upper MTZ. Pyroxenes completely dissolve into majoritic garnet at depths shallower than 450 km (Ishii et al., 2018). As suggested by previous phase equilibrium experiments (e.g., Ishii et al., 2018, 2019), wadsleyite and majoritic garnet are the only major minerals at depths greater than 450 km in the upper MTZ. Therefore, the upper MTZ can be viewed as a simplified binary mineral mixture of wadsleyite and majoritic garnet, although it does not cover the full range of possible compositional variations in the MTZ since we ignored the possible existence of other minor mineral phases (e.g., clinopyroxene between 410 and 450 km depth). The lateral variations of wadsleyite and majoritic garnet contents in the upper MTZ are directly linked to the change of major element distributions in the MTZ, including Fe, Al, Ca, Si etc. For example, a wadsleyite-poor region in the upper MTZ is expected to be Fe, Al, Ca and Si-rich, but Mg-poor (Ishii et al., 2018, 2019).

Wadsleyite is ~4% faster than majoritic garnet in both pyrolite and harzburgite bulk compositions under MTZ *P*-*T* conditions (the thermoelastic parameters of wadsleyite and garnet used for calculating the high *P*-*T* velocities are shown in Table III.S2, and III.S4), therefore increased wadsleyite proportion would result in higher *V*p and *V*s in the upper MTZ.

Seismically fast and slow anomalies have been widely identified in the upper MTZ, e.g., positive anomalies beneath the western Pacific subduction zone, negative anomalies under the

central Pacific plate (Koelemeijer et al., 2015). The 410 depth, influenced by both ΔT and water content (see Methods), also varies globally (Huang et al., 2019). The effect of Fe^{3+} content on the 410 depth is expected to be very small considering the small Fe# range near 410 km depth (Katsura et al., 2004). The existence of Fe^{3+} may broaden the 410 (Frost and Dolejš, 2007), while accurate quantification suffers from the limited experimental data as well as the unknown redox state near 410 km depth in the Earth's interior. Therefore, we did not consider the effect of Fe^{3+}, only water content and wadsleyite proportion were considered as the compositional factors in our modeling.

Modeling the composition and *T* variations in the upper MTZ

We attempt to constrain the global variations of wadsleyite proportion, water concentration and ΔT in the upper MTZ from the seismically determined *V*p and *V*s at 450 km from the SP12RTS model (Koelemeijer et al., 2015), and the 410 depths from Huang et al. (2019).The SP12RTS tomography models used inversion framework of the S40RTS (Ritsema et al., 2011) *V*s tomography model. The most recent global MTZ discontinuity topography model by Huang et al. (2019) also used S40RTS tomography model to correct for the lateral seismic heterogeneities in the upper mantle. Therefore, the seismic data products we chose in this study are internally consistent.

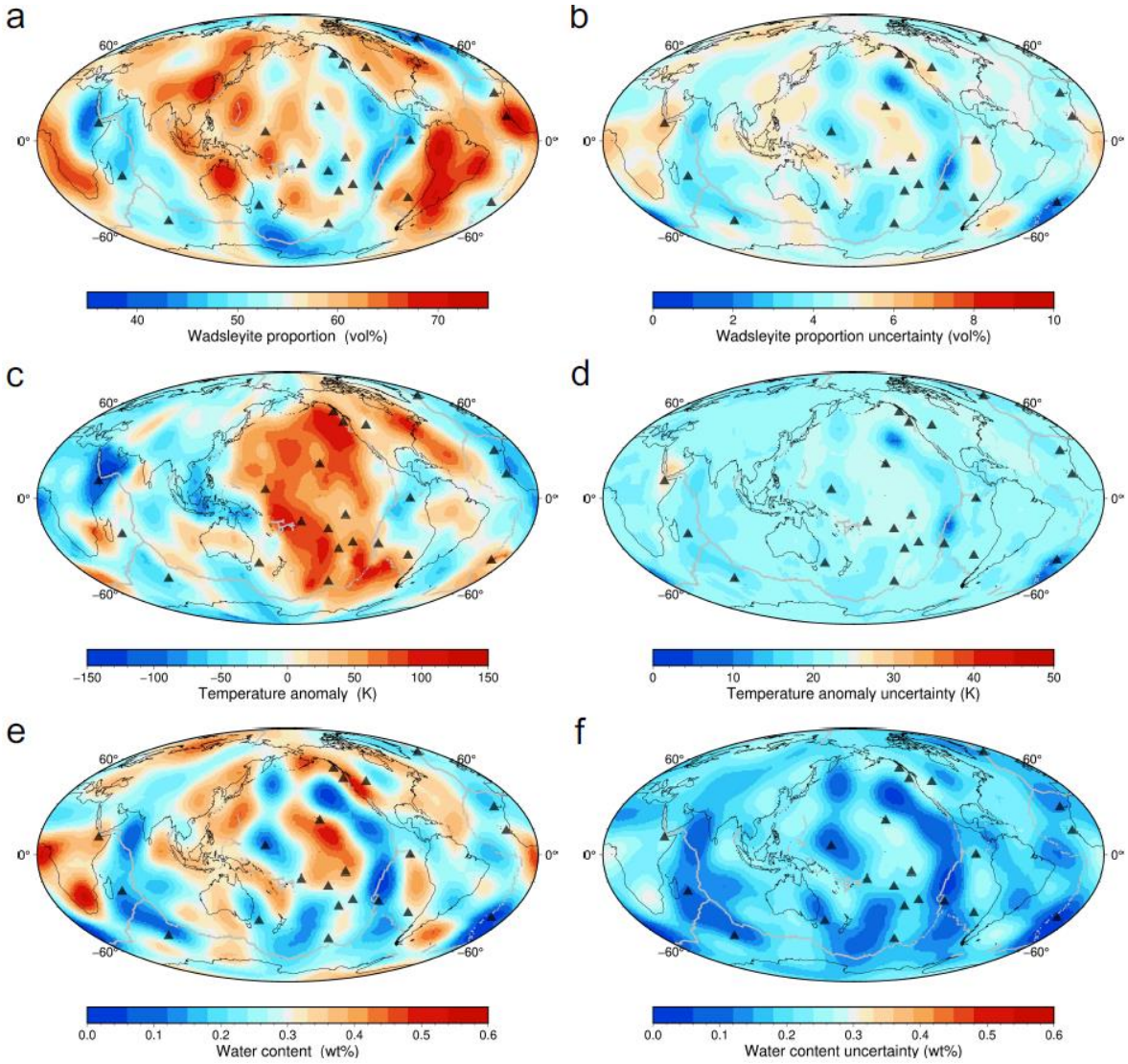

Fig. III.3. Wadsleyite proportion, temperature anomaly ΔT, and water content in the upper MTZ constrained from the depth variation of the 410, Vp and Vs anomaly. a *global distribution of wadsleyite proportion.* ***b*** *global distribution of the uncertainty of wadsleyite proportion.* ***c*** *global distribution of ΔT.* ***d*** *global distribution of the uncertainty of ΔT.* ***e*** *global distribution of water content.* ***f*** *global distribution of the uncertainty of water content. Deeply sourced hotspots (Courtillot et al., 2003) are plotted as black triangles.*

A grid search method was employed to calculate the predicted *V*p and *V*s anomaly at 450 km depth and the 410 depth by allowing the wadsleyite proportion, Δ*T*, and water content to vary

between 13 to 93 vol%, -300 to 300 K, 0 to 2 wt%, respectively, based on the mineral physics data in this and previous studies (Table III.S2 and III.S4) (Equations 1-4 in Methods). We then compared the mineral physics predicted values with the internally consistent global seismic models presented in Huang et al. (2019) and Koelemeijer et al. (2015) to search for the mineral physics models with misfit less than 1.0 and 1.5 defined by Equation 5 in Methods. The best-fit wadsleyite proportion, ΔT, and water content models were calculated by averaging those selected mineral physics models with misfit less than 1.0 and 1.5 (Fig. III.3, III.S4). Uncertainties involved in the modeling are considered and evaluated (See Methods and Supplementary Discussion 1).

The average of the best-fit models with misfit < 1.0 yields an estimated global average wadsleyite content of 56 ± 6 vol%, T of 1866 ± 42 K, and water content of 0.28 ± 0.08 wt%. The results we obtained from the best-fit models with misfit < 1.5 yield slightly higher average water content (0.40 ± 0.07 wt%). However, the lateral variations for water content, ΔT, and wadsleyite proportion in the upper MTZ remain consistent and the spatial distribution is stable as shown in Fig. III.3 (misfit < 1) and Fig. III.S4 (misfit < 1.5).

In the maps derived from best-fit models (Figs. III.3, III.S4), the maximum wadsleyite proportion, T, and water content differences for the upper MTZ are ~35 vol%, ~270 K, and ~0.5 wt%, respectively. To statistically analyze their associations with different geographic and tectonic settings, we selected four regional groups: ocean, continents, subducting slabs, and hotspots (plumes).

The wadsleyite content distribution map is shown in Fig. III.3a. The most prominent feature is the strong correlation between the high wadsleyite content and the places where slabs are expected, e.g., beneath the circum-Pacific subduction zones (Figs. III.3a, III.4). A possible explanation can be the olivine-rich harzburgitic lithospheric mantle of the slabs penetrating or

accumulating in the MTZ (Fukao and Obayashi, 2013). For example, seismic tomography has revealed possible slab stagnation in the MTZ under northeastern China (Ye et al., 2011), Bonin arc (Fukao and Obayashi, 2013), eastern Java subduction zone (Fukao and Obayashi, 2013), southern Chile (Li et al., 2019), etc. Some locations where slabs penetrate through the MTZ also coincide with the regions with high wadsleyite content, such as beneath northern New Zealand (Fukao and Obayashi, 2013). In addition, due to the existence of subducting slabs under most continents with active continental margins (e.g., western South and North America, East Asia), higher wadsleyite content was found beneath continents compared with oceans (Fig. III.4).

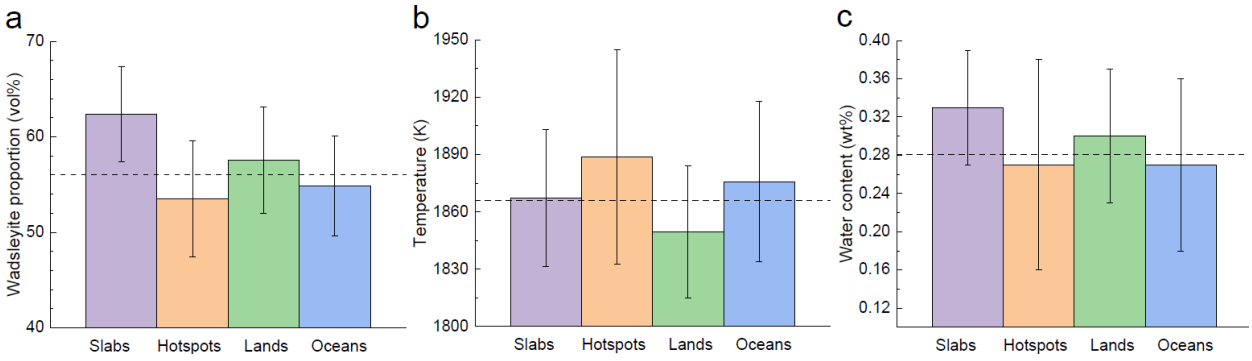

Fig. III.4. Wadsleyite proportion, temperature T, water content in the upper MTZ near slabs, beneath deeply sourced hotspots, lands, and oceans. ***a*** *The wadsleyite proportion difference between slabs and hotspots is greater than 1 standard deviation.* ***b*** *The ~30 K T differences between slabs and hotspots as well as lands and oceans are both slightly smaller than 1 standard deviation largely due to the different thermal states of the grouped individual locations used in this study.* ***c*** *The subtle difference in estimated water content is much smaller than the 1 standard deviation and the absolute values of the water content are only weakly constrained. The dashed lines represent the global average.*

Another interesting correlation is found between the regions depleted in wadsleyite content and the deeply sourced hotspots (Courtillot et al., 2003) (Fig. III.3a). Under 18 out of 22 deeply

sourced hotspots, the wadsleyite content is lower than what is expected in a pyrolite model (Fig. III.3a). As shown in Fig. III.4a, the average upper MTZ beneath all deeply sourced hotspots has ~ 2 vol% less wadsleyite than the global average MTZ (~56 vol%), and ~10 vol% less wadsleyite than the average upper MTZ near slabs. This observation could be explained by the upwelling of the possible Si-rich, thus "olivine-poor" material from the lower mantle associated with the plumes. Although still controversial, recent sound velocity, density, and viscosity experiments on lower mantle minerals support a Si-rich bridgmanite-dominated lower mantle (Mashino et al., 2020; Mattern et al., 2005; Murakami et al., 2012; Ricolleau et al., 2009; Xie et al., 2020). After being transported to the upper MTZ by the rising plumes, the bridgmanite-rich lower mantle materials would transform into a relatively wadsleyite-poor aggregate, and eventually result in the low wadsleyite content under these deeply sourced hotspots. Our observation is also consistent with recent geodynamical modeling results, which suggest the compositionally "garnet"-rich, therefore "olivine"-depleted plumes can better reproduce the expected plume features such as tail size, stability, and buoyancy (Dannberg and Sobolev, 2015).

ΔT distribution in the upper MTZ is shown in Fig. III.3c. The most pronounced feature in this figure is the unusually high T beneath the Pacific Ocean (Fig. III.3c), consistent with a previous T model derived from Vs only at 300 km (Hwang et al., 2011). The high T beneath the Pacific Ocean in the MTZ and upper mantle may be related to the relatively large number (~60%) of the deeply originated hotspots found in this region (Courtillot et al., 2003) (Fig. III.4).

On the other hand, the upper MTZ under continents is the coldest among the 4 regional groups (Fig. III.4), which may be expected due to the existence of the thick and cold lithosphere under continents (Jordan, 1988). Lower T is also observed beneath some subduction zones, e.g., beneath southeastern Asia (Fig. III.3c). Interestingly, the T under the Cascadia subduction zone is

actually high, which can be explained by the slow subduction (~3 cm/year) of the young (<10 Ma) Juan De Fuca slab with a thick sediment cover (Canales et al., 2017), as well as by the nearby Yellowstone hotspot in the Western U.S. (Fig. III.3c). Due to the different thermal states of different subducting slabs, the *T* under subduction zones is highly variable (Fig. III.4b).

One mysterious feature shown in Fig. III.3c is the low *T* beneath the Red Sea near where a plume is expected to its southeast. The global topography model of the 410 adopted in this study suggested an uplifted 410 beneath the Red Sea (Huang et al., 2019), likely associated with a negative ΔT. On the contrary, a local seismic study near the Red Sea reported a depressed 410 up to 30 km (Mohamed et al., 2014), suggesting the MTZ beneath the Red Sea is hotter than the ambient mantle by up to 280 K. More seismic studies with denser ray coverage are needed to clarify the 410 depth variation in this region.

Although the absolute water content in the MTZ is not well resolved, the lateral variation of water content in the upper MTZ is stable for different ensemble sizes from the grid search as shown in Fig. III.3e (misfit < 1) and Fig. III.S4e (misfit < 1.5).

The circum-Pacific regions show a slightly elevated water content, consistent with the existence of subduction slabs. Pore fluids or hydrous minerals (e.g., antigorite, Ice VII, phase A) carried by fast-subducting cold slabs could supply water to the MTZ (Ivanov and Litasov, 2014). The MTZ beneath the Western Pacific subduction zone is suggested to be hydrated by seismic observations (Zhao et al., 2009), electrical conductivity studies (Karato, 2011; Kelbert et al., 2009), and basalt geochemistry (Kuritani et al., 2019). Higher water content in the upper MTZ under the Western U.S. seen in Fig. III.3e is also supported by the observed low-velocity layer atop the 410 (Schmandt et al., 2011; Song et al., 2004) and high seismic attenuation (Tian et al., 2011). It can

be caused by the dehydration of the old stagnant Farallon slab (Song et al., 2004) or the sediments atop the Juan de Fuca slab, which is the north remnant of the Farallon slab (Canales et al., 2017).

Recent studies suggested that the large low-shear-velocity provinces (LLSVPs) in the lower mantle may be locally hydrated by fluids released from the phase δ-H solid solution (AlO_2H-$MgSiO_4H_2$) (Ohira et al., 2021) and pyrite FeO_2H_x (Liu et al., 2017). Upwelling plumes originating from the hydrated regions in LLSVPs may hydrate the upper MTZ locally, as seen under Hawaii and South Africa. On the other hand, the Archean and Paleoproterozoic cratons in southern Africa were formed and welded by processes similar to modern-day subduction (Parman et al., 2001), so the MTZ under southern Africa may also have been hydrated by ancient subducting slabs (Blum and Shen, 2004).

Other hydrous or anhydrous areas are interspersed in the upper MTZ, possibly due to three-dimensional mantle convection (Price et al., 2019). The correlations between high (or low) water concentration and surface properties (i.e. lands, oceans, hotspots, or slabs) may be complicated by three-dimensional mantle convection that offsets deep thermal or compositional anomalies from their past or present surface expressions (Fig. III.4c).

4. Summary

We found that the upper MTZ near subducted slabs is relatively cold, enriched in wadsleyite, and slightly more hydrated compared to regions where plumes are expected. It is very likely that both the subduction of Si-poor oceanic mantle lithosphere and upwelling of the possibly Si-rich lower mantle materials contribute to the large composition and *T* heterogeneities in the upper MTZ. We would also like to point out that the results presented in this study are restricted by the mineral physics constraints and seismic resolution. As a result, some other factors, such as the presence of minor phases, fluids, or anelastic effects were not taken into account.

Extensive collaborations between seismologists and mineral physicists are needed to address these technical challenges in order to quantitatively understand the multi-dimensional thermochemical heterogeneities in the petrologically more complicated regions inside the Earth.

References

Anderson, D.L., Bass, J.D., 1986. Transition region of the Earth's upper mantle. Nature 320, 321-328.

Arimoto, T., Gréaux, S., Irifune, T., Zhou, C., Higo, Y., 2015. Sound velocities of Fe3Al2Si3O12 almandine up to 19 GPa and 1700 K. Physics of the Earth and Planetary Interiors 246, 1-8.

Blum, J., Shen, Y., 2004. Thermal, hydrous, and mechanical states of the mantle transition zone beneath southern Africa. Earth and Planetary Science Letters 217, 367-378.

Buchen, J., Marquardt, H., Speziale, S., Kawazoe, T., Boffa Ballaran, T., Kurnosov, A., 2018. High-pressure single-crystal elasticity of wadsleyite and the seismic signature of water in the shallow transition zone. Earth and Planetary Science Letters 498, 77-87.

Burdick, S., Lekić, V., 2017. Velocity variations and uncertainty from transdimensional P-wave tomography of North America. Geophysical Journal International 209, 1337-1351.

Canales, J.P., Carbotte, S.M., Nedimović, M., Carton, H., 2017. Dry Juan de Fuca slab revealed by quantification of water entering Cascadia subduction zone. Nature Geoscience 10, 864-870.

Courtillot, V., Davaille, A., Besse, J., Stock, J., 2003. Three distinct types of hotspots in the Earth’s mantle. Earth and Planetary Science Letters 205, 295-308.

Dannberg, J., Sobolev, S.V., 2015. Low-buoyancy thermochemical plumes resolve controversy of classical mantle plume concept. Nat Commun 6, 6960.

Davies, G., 1974. Effective elastic moduli under hydrostatic stress—I. quasi-harmonic theory. Journal of Physics and Chemistry of Solids 35, 1513-1520.

Davies, G., Dziewonski, A., 1975. Homogeneity and constitution of the Earth's lower mantle and outer core. Physics of the Earth and Planetary Interiors 10, 336-343.

Deon, F., Koch-Müller, M., Rhede, D., Wirth, R., 2010. Water and Iron effect on the P-T-x coordinates of the 410-km discontinuity in the Earth upper mantle. Contributions to Mineralogy and Petrology 161, 653-666.

Duffy, T.S., Anderson, D.L., 1989. Seismic velocities in mantle minerals and the mineralogy of the upper mantle. Journal of Geophysical Research: Solid Earth 94, 1895-1912.

Fei, H., Katsura, T., 2020. High water solubility of ringwoodite at mantle transition zone temperature. Earth and Planetary Science Letters 531, 115987.

Frost, D.J., Dolejš, D., 2007. Experimental determination of the effect of H2O on the 410-km seismic discontinuity. Earth and Planetary Science Letters 256, 182-195.

Fukao, Y., Obayashi, M., 2013. Subducted slabs stagnant above, penetrating through, and trapped below the 660 km discontinuity. Journal of Geophysical Research: Solid Earth 118, 5920-5938.

Goes, S., Capitanio, F.A., Morra, G., 2008. Evidence of lower-mantle slab penetration phases in plate motions. Nature 451, 981-984.

Gwanmesia, G.D., Whitaker, M.L., Dai, L., James, A., Chen, H., Triplett, R.S., Cai, N., 2020. The Elastic Properties of β-Mg2SiO4 Containing 0.73 wt.% of H2O to 10 GPa and 600 K by Ultrasonic Interferometry with Synchrotron X-Radiation. Minerals 10, 209.

Hill, R., 1963. Elastic properties of reinforced solids: some theoretical principles. Journal of the Mechanics and Physics of Solids 11, 357-372.

Houser, C., 2016. Global seismic data reveal little water in the mantle transition zone. Earth and Planetary Science Letters 448, 94-101.

Huang, Q., Schmerr, N., Waszek, L., Beghein, C., 2019. Constraints on Seismic Anisotropy in the Mantle Transition Zone From Long-Period SS Precursors. Journal of Geophysical Research: Solid Earth 124, 6779-6800.

Hwang, Y.K., Ritsema, J., Goes, S., 2011. Global variation of body-wave attenuation in the upper mantle from teleseismic P wave and S wave spectra. Geophysical research letters 38.

Inoue, T., Yurimoto, H., Kudoh, Y., 1995. Hydrous modified spinel, Mg1. 75SiH0. 5O4: a new water reservoir in the mantle transition region. Geophysical Research Letters 22, 117-120.

Irifune, T., Higo, Y., Inoue, T., Kono, Y., Ohfuji, H., Funakoshi, K., 2008. Sound velocities of majorite garnet and the composition of the mantle transition region. Nature 451, 814-817.

Isaak, D.G., Gwanmesia, G.D., Falde, D., Davis, M.G., Triplett, R.S., Wang, L., 2007. The elastic properties of β-Mg2SiO4 from 295 to 660 K and implications on the composition of Earth's upper mantle. Physics of the Earth and Planetary Interiors 162, 22-31.

Ishii, T., Kojitani, H., Akaogi, M., 2018. Phase relations and mineral chemistry in pyrolitic mantle at 1600–2200 °C under pressures up to the uppermost lower mantle: Phase transitions around the 660-km discontinuity and dynamics of upwelling hot plumes. Physics of the Earth and Planetary Interiors 274, 127-137.

Ishii, T., Kojitani, H., Akaogi, M., 2019. Phase Relations of Harzburgite and MORB up to the Uppermost Lower Mantle Conditions: Precise Comparison With Pyrolite by Multisample Cell High-Pressure Experiments With Implication to Dynamics of Subducted Slabs. Journal of Geophysical Research: Solid Earth 124, 3491-3507.

Ivanov, A.V., Litasov, K.D., 2014. The deep water cycle and flood basalt volcanism. International Geology Review 56, 1-14.

Jordan, T.H., 1988. Structure and formation of the continental tectosphere. Journal of Petrology, 11-37.

Kaminsky, F., 2012. Mineralogy of the lower mantle: A review of 'super-deep'mineral inclusions in diamond. Earth-Science Reviews 110, 127-147.

Karato, S.-i., 2011. Water distribution across the mantle transition zone and its implications for global material circulation. Earth and Planetary Science Letters 301, 413-423.

Katsura, T., Shatskiy, A., Manthilake, M.A.G.M., Zhai, S., Yamazaki, D., Matsuzaki, T., Yoshino, T., Yoneda, A., Ito, E., Sugita, M., Tomioka, N., Nozawa, A., Funakoshi, K.-i., 2009. P-V-Trelations of wadsleyite determined by in situ X-ray diffraction in a large-volume high-pressure apparatus. Geophysical Research Letters 36.

Katsura, T., Yamada, H., Nishikawa, O., Song, M., Kubo, A., Shinmei, T., Yokoshi, S., Aizawa, Y., Yoshino, T., Walter, M.J., Ito, E., Funakoshi, K.-i., 2004. Olivine-wadsleyite transition in the system (Mg,Fe)2SiO4. Journal of Geophysical Research: Solid Earth 109.

Katsura, T., Yoneda, A., Yamazaki, D., Yoshino, T., Ito, E., 2010. Adiabatic temperature profile in the mantle. Physics of the Earth and Planetary Interiors 183, 212-218.

Kelbert, A., Schultz, A., Egbert, G., 2009. Global electromagnetic induction constraints on transition-zone water content variations. Nature 460, 1003-1006.

Koelemeijer, P., Ritsema, J., Deuss, A., van Heijst, H.J., 2015. SP12RTS: a degree-12 model of shear- and compressional-wave velocity for Earth's mantle. Geophysical Journal International 204, 1024-1039.

Korenaga, J., 2013. Initiation and Evolution of Plate Tectonics on Earth: Theories and Observations. Annual Review of Earth and Planetary Sciences 41, 117-151.

Kuritani, T., Xia, Q.-K., Kimura, J.-I., Liu, J., Shimizu, K., Ushikubo, T., Zhao, D., Nakagawa, M., Yoshimura, S., 2019. Buoyant hydrous mantle plume from the mantle transition zone. Scientific reports 9, 1-7.

Lai, X., Zhu, F., Zhang, J.S., Zhang, D., Tkachev, S., Prakapenka, V.B., Chen, B., 2020. An Externally-Heated Diamond Anvil Cell for Synthesis and Single-Crystal Elasticity Determination of Ice-VII at High Pressure-Temperature Conditions. JoVE (Journal of Visualized Experiments), e61389.

Li, B., Liebermann, R.C., 2014. Study of the Earth's interior using measurements of sound velocities in minerals by ultrasonic interferometry. Physics of the Earth and Planetary Interiors 233, 135-153.

Li, B., Liebermann, R.C., Weidner, D.J., 2001. P-V-Vp-Vs-T measurements on wadsleyite to 7 GPa and 873 K: Implications for the 410-km seismic discontinuity. Journal of Geophysical Research: Solid Earth 106, 30579-30591.

Li, Z.-H., Gerya, T., Connolly, J.A., 2019. Variability of subducting slab morphologies in the mantle transition zone: Insight from petrological-thermomechanical modeling. Earth-Science Reviews 196, 102874.

Libowitzky, E., Rossman, G.R., 1997. An IR absorption calibration for water in minerals. American Mineralogist 82, 1111-1115.

Liu, J., Hu, Q., Kim, D.Y., Wu, Z., Wang, W., Xiao, Y., Chow, P., Meng, Y., Prakapenka, V.B., Mao, H.-K., 2017. Hydrogen-bearing iron peroxide and the origin of ultralow-velocity zones. Nature 551, 494-497.

Liu, W., Kung, J., Li, B., Nishiyama, N., Wang, Y., 2009. Elasticity of (Mg0. 87Fe0. 13) 2SiO4 wadsleyite to 12 GPa and 1073 K. Physics of the Earth and Planetary Interiors 174, 98-104.

Mao, Z., Jacobsen, S.D., Frost, D.J., McCammon, C.A., Hauri, E.H., Duffy, T.S., 2011. Effect of hydration on the single-crystal elasticity of Fe-bearing wadsleyite to 12 GPa. American Mineralogist 96, 1606-1612.

Mao, Z., Jacobsen, S.D., Jiang, F., Smyth, J.R., Holl, C.M., Duffy, T.S., 2008a. Elasticity of hydrous wadsleyite to 12 GPa: Implications for Earth's transition zone. Geophysical Research Letters 35.

Mao, Z., Jacobsen, S.D., Jiang, F.M., Smyth, J.R., Holl, C.M., Frost, D.J., Duffy, T.S., 2008b. Single-crystal elasticity of wadsleyites, β-Mg2SiO4, containing 0.37–1.66 wt.% H2O. Earth and Planetary Science Letters 268, 540-549.

Mashino, I., Murakami, M., Miyajima, N., Petitgirard, S., 2020. Experimental evidence for silica-enriched Earth’s lower mantle with ferrous iron dominant bridgmanite. Proceedings of the National Academy of Sciences 117, 27899-27905.

Mattern, E., Matas, J., Ricard, Y., Bass, J., 2005. Lower mantle composition and temperature from mineral physics and thermodynamic modelling. Geophysical Journal International 160, 973-990.

Mohamed, A., Gao, S.S., Elsheikh, A., Liu, K.H., Yu, Y., Fat-Helbary, R., 2014. Seismic imaging of mantle transition zone discontinuities beneath the northern Red Sea and adjacent areas. Geophysical Journal International 199, 648-657.

Murakami, M., Ohishi, Y., Hirao, N., Hirose, K., 2012. A perovskitic lower mantle inferred from high-pressure, high-temperature sound velocity data. Nature 485, 90-94.

Ohira, I., Jackson, J.M., Sturhahn, W., Finkelstein, G.J., Kawazoe, T., Toellner, T.S., Suzuki, A., Ohtani, E., 2021. The influence of δ-(Al, Fe) OOH on seismic heterogeneities in Earth’s lower mantle. Scientific reports 11, 1-9.

Parman, S., Grove, T., Dann, J., 2001. The production of Barberton komatiites in an Archean subduction zone. Geophysical Research Letters 28, 2513-2516.

Price, M.G., Davies, J., Panton, J., 2019. Controls on the Deep-Water Cycle Within Three-Dimensional Mantle Convection Models. Geochemistry, Geophysics, Geosystems 20, 2199-2213.

Ricolleau, A., Fei, Y., Cottrell, E., Watson, H., Deng, L., Zhang, L., Fiquet, G., Auzende, A.L., Roskosz, M., Morard, G., 2009. Density profile of pyrolite under the lower mantle conditions. Geophysical Research Letters 36.

Ritsema, J., Deuss, a.A., Van Heijst, H., Woodhouse, J., 2011. S40RTS: a degree-40 shear-velocity model for the mantle from new Rayleigh wave dispersion, teleseismic traveltime and normal-mode splitting function measurements. Geophysical Journal International 184, 1223-1236.

Schmandt, B., Dueker, K., Hansen, S., Jasbinsek, J.J., Zhang, Z., 2011. A sporadic low-velocity layer atop the western US mantle transition zone and short-wavelength variations in transition zone discontinuities. Geochemistry, Geophysics, Geosystems 12.

Song, T.-R.A., Helmberger, D.V., Grand, S.P., 2004. Low-velocity zone atop the 410-km seismic discontinuity in the northwestern United States. Nature 427, 530-533.

Tian, Y., Zhou, Y., Sigloch, K., Nolet, G., Laske, G., 2011. Structure of North American mantle constrained by simultaneous inversion of multiple-frequency SH, SS, and Love waves. Journal of Geophysical Research: Solid Earth 116.

Wang, J., Bass, J.D., Kastura, T., 2014. Elastic properties of iron-bearing wadsleyite to 17.7GPa: Implications for mantle mineral models. Physics of the Earth and Planetary Interiors 228, 92-96.

Wang, W., Walter, M.J., Peng, Y., Redfern, S., Wu, Z., 2019. Constraining olivine abundance and water content of the mantle at the 410-km discontinuity from the elasticity of olivine and wadsleyite. Earth and Planetary Science Letters 519, 1-11.

Wang, W., Zhang, H., Brodholt, J.P., Wu, Z., 2021. Elasticity of hydrous ringwoodite at mantle conditions: Implication for water distribution in the lowermost mantle transition zone. Earth and Planetary Science Letters 554, 116626.

Wessel, P., Luis, J., Uieda, L., Scharroo, R., Wobbe, F., Smith, W., Tian, D., 2019. The generic mapping tools version 6. Geochemistry, Geophysics, Geosystems 20, 5556-5564.

Xie, L., Yoneda, A., Yamazaki, D., Manthilake, G., Higo, Y., Tange, Y., Guignot, N., King, A., Scheel, M., Andrault, D., 2020. Formation of bridgmanite-enriched layer at the top lower-mantle during magma ocean solidification. Nature communications 11, 1-10.

Ye, L., Li, J., Tseng, T.-L., Yao, Z., 2011. A stagnant slab in a water-bearing mantle transition zone beneath northeast China: implications from regional SH waveform modelling. Geophysical Journal International 186, 706-710.

Zha, C.-s., Duffy, T.S., Mao, H.-k., Downs, R.T., Hemley, R.J., Weidner, D.J., 1997. Single-crystal elasticity of β-Mg2SiO4 to the pressure of the 410 km seismic discontinuity in the earth's mantle. Earth and Planetary Science Letters 147, E9-E15.

Zhang, J.S., Bass, J.D., 2016. Sound velocities of olivine at high pressures and temperatures and the composition of Earth's upper mantle. Geophysical Research Letters 43, 9611-9618.

Zhang, J.S., Bass, J.D., Zhu, G., 2015. Single-crystal Brillouin spectroscopy with CO2 laser heating and variable q. Review of Scientific Instruments 86, 063905.

Zhao, D., Tian, Y., Lei, J., Liu, L., Zheng, S., 2009. Seismic image and origin of the Changbai intraplate volcano in East Asia: role of big mantle wedge above the stagnant Pacific slab. Physics of the Earth and Planetary Interiors 173, 197-206.

Zhou, W.-Y., Ren, Z., Zhang, J.S., Chen, B., Hao, M., Ohuchi, T., Miyagi, L., Zhang, D., Alp, E.E., Lavina, B., 2021. The Water-Fe-Pressure dependent single-crystal elastic properties of wadsleyite: Implications for the seismic anisotropy in the upper Mantle Transition Zone. Earth and Planetary Science Letters 565, 116955.

Supplementary Information

Supplementary Discussion 1. Testing the robustness of the wadsleyite proportion, temperature anomaly, and water content models given uncertainties of the mineral physics models used in this study

In terms of the Fe and water effects on the *V*p and *V*s of wadsleyite, the average difference between model-predicted values and the experimental data from previous studies is 0.7%(Zhou et al., 2021). In terms of the *T* effect, as shown in Fig. III.1 in the main text, the average difference between the model-predicted values and the experimental data is even less and on the level of 0.1%. However, given the limited *T* range we experimentally explored, in the parameter space used in this study (ΔT from -150K to 150 K compared with 1870 K(Katsura et al., 2010), water content from 0 to 1 wt%), the calculated *V*p and *V*s uncertainties of our wadsleyite sample at 1870 K and 14 GPa are higher than 0.1%, and on the level of 1% without considering the composition effect-induced uncertainties. Therefore, as a conservative estimate, we assigned an assumed 1 standard deviation of 10% for each of the parameters (*a*, *b*, *c*, *d*, *A*, *B*, *C*, *D*, *e*, and *f* in Equation 1-5 in Methods) used in our modeling work, and then took the following procedures to evaluate the possible influence of these uncertainties on the robustness of our calculation:

1) Instead of fixing the *a*, *b*, *c*, *d*, *A*, *B*, *C*, *D*, *e*, and *f* parameters to the best-fit values, we randomly sampled the value of each parameter from a normal (Gaussian) distribution based on the best-fit value and the assumed 10% standard deviation.

2) We then re-calculated the global wadsleyite proportion, ΔT, and water content maps in the upper MTZ.

3) We repeated setup 1) and 2) a few times, and found that they yielded nearly identical results compared to those shown in the manuscript, which suggests that these uncertainties are unlikely

to affect the robustness of this study. The simple explanation is that the influence of the global variance in seismic structure is large compared to the uncertainties in the experimentally derived model parameters. Two typical test results are shown in Fig. III.S9 and Table III.7.

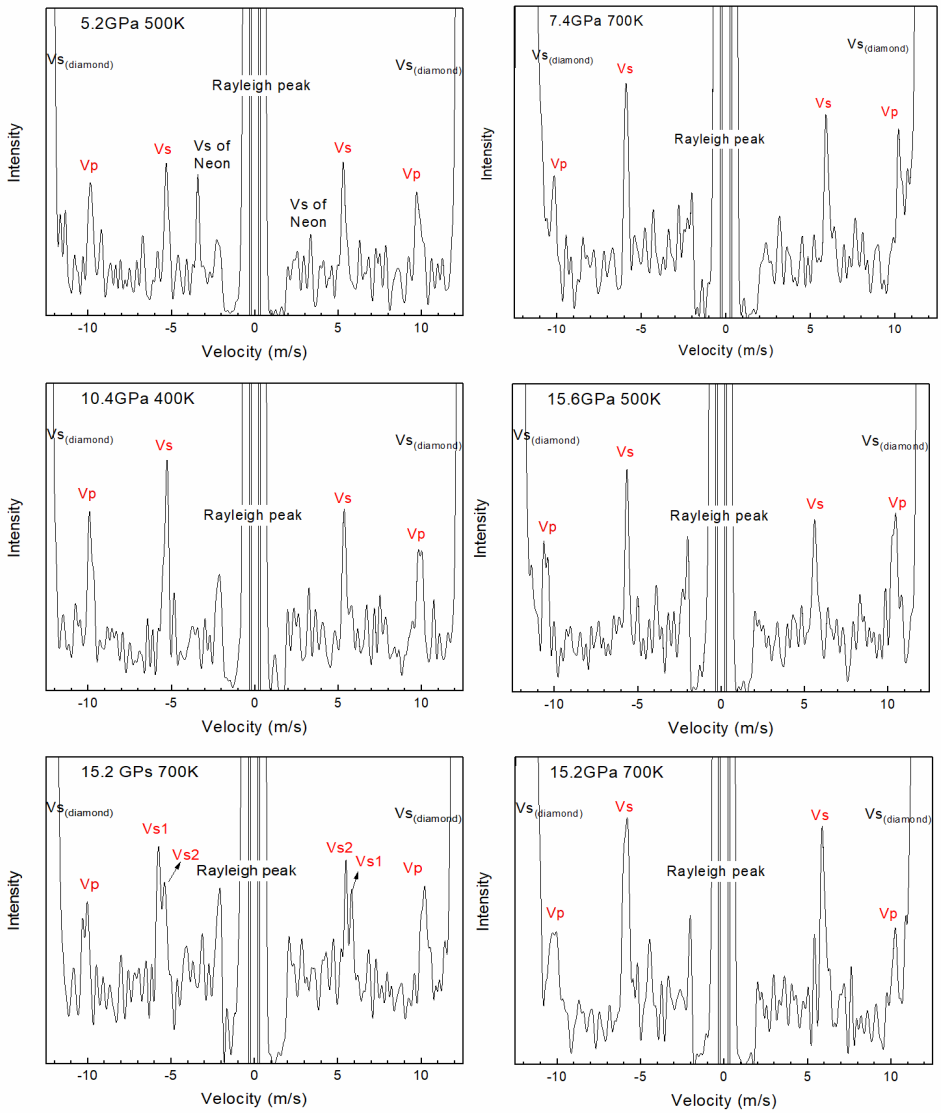

Fig. III.S1. *Representative Brillouin spectra of single-crystal wadsleyite at different high P-T conditions. The spectra have been processed with a low pass filter. The collection time is approximately 20 minutes for each spectrum.*

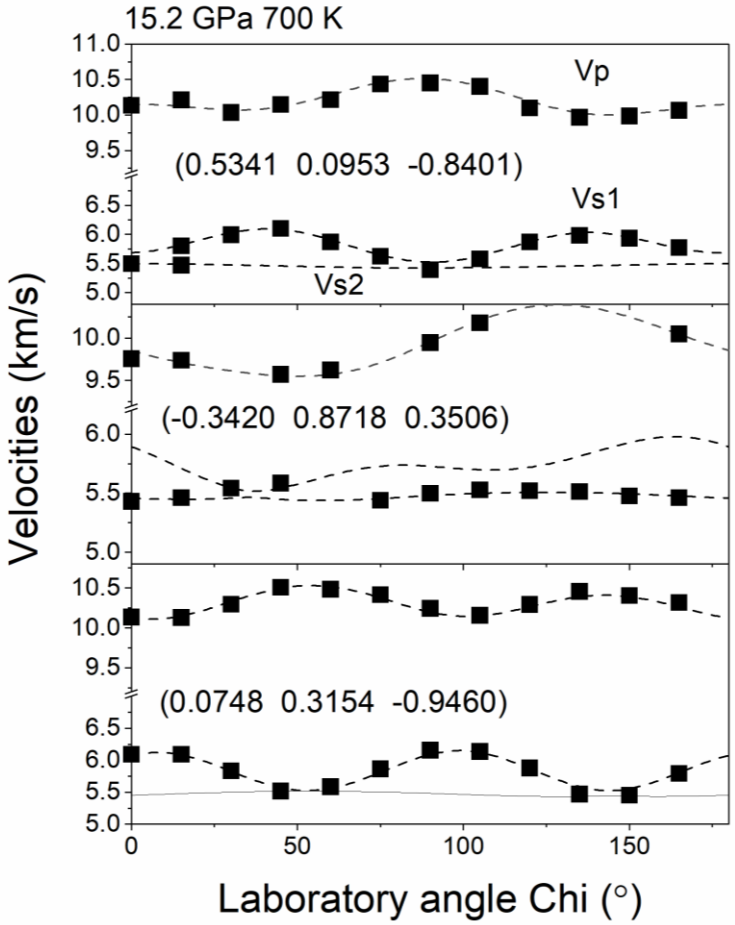

Fig. III.S2. *Change of velocities as a function of laboratory measurement angle Chi at 15.2 GPa and 700 K. Dashed lines: the velocities predicted by the best-fit C_{ij} model; Solid squares: experiment data. Error bars smaller than the symbols are not shown.*

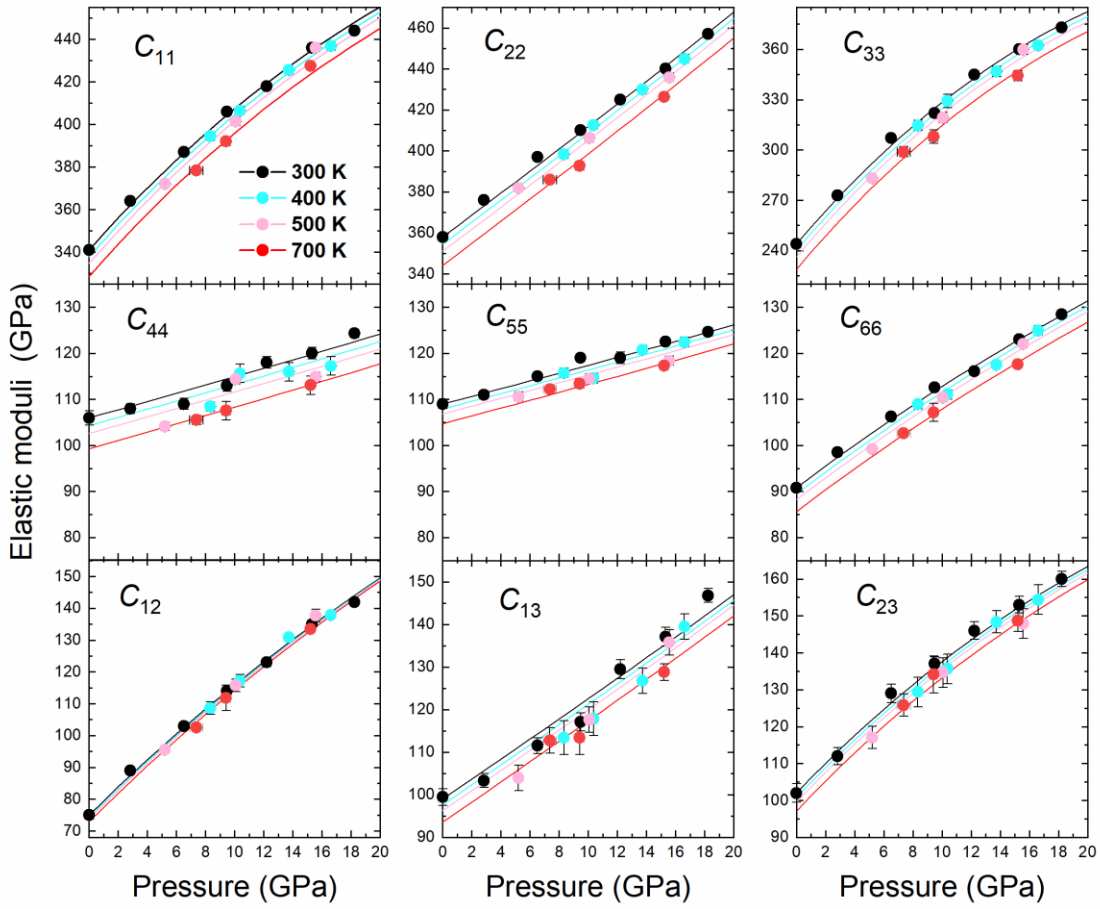

Fig. III.S3. *Change of the C_{ij}s of the hydrous Fe-bearing wadsleyite sample used in this study as a function of P along 300 K, 400 K, 500 K, and 700 K isotherms. Solid lines represent T-dependent 3rd or 4th order finite strain EOS fitting results. Data along the 300 K isotherm are adopted from Zhou et al.(Zhou et al., 2021). Error bars smaller than the symbols are not shown.*

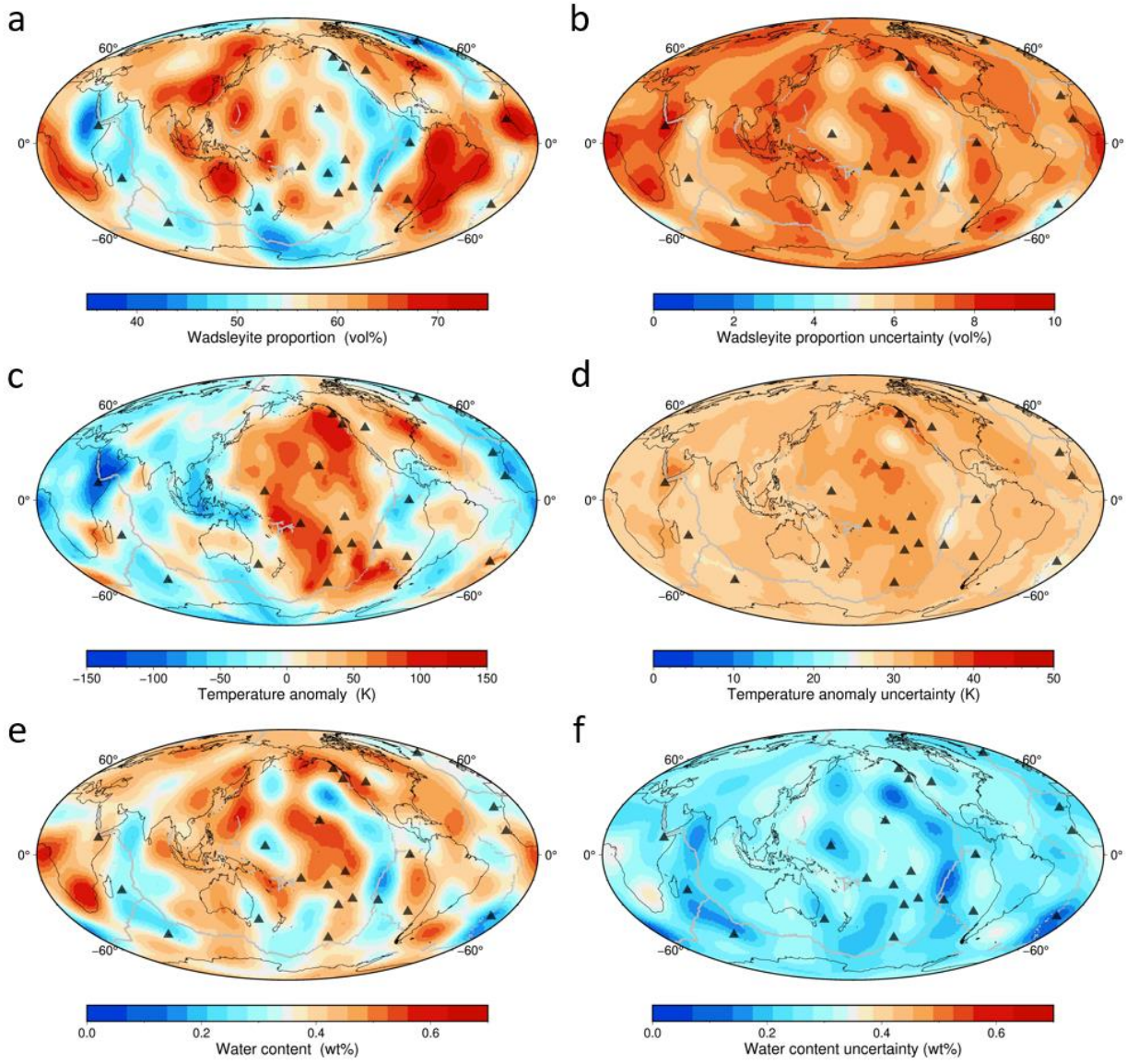

Fig. III.S4. Global wadsleyite proportion, temperature anomaly ΔT, and water content maps in the upper MTZ with final misfit <1.5, constrained from depth variation of the 410, Vp and Vs anomaly at 450 km depth. ***a*** *global distribution of wadsleyite proportion;* ***b*** *global distribution of the uncertainty of wadsleyite proportion;* ***c*** *global distribution of ΔT;* ***d*** *global distribution of the uncertainty of ΔT;* ***e*** *global distribution of water content;* ***f*** *global distribution of the uncertainty of water content. Deeply sourced hotspots(Courtillot et al., 2003) are plotted as black triangles.*

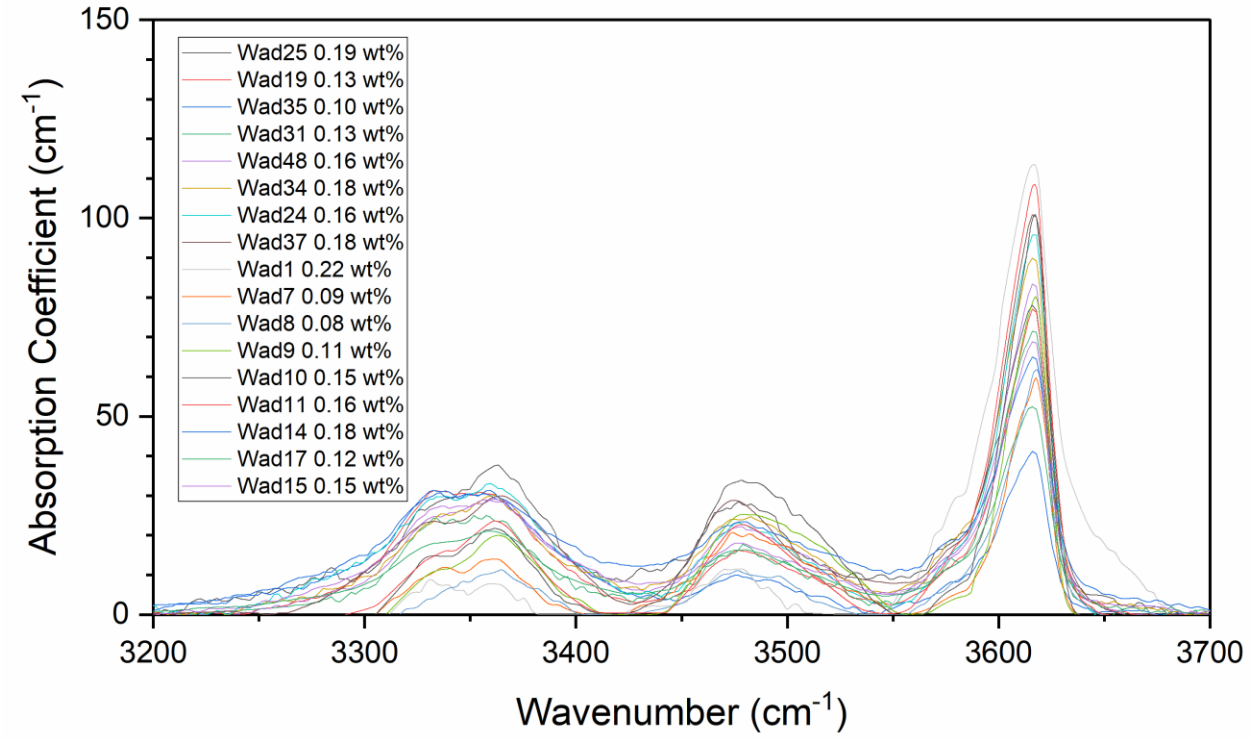

Fig. III.S5. *Unpolarized FTIR spectra of 17 randomly oriented wadsleyite platelets. The water contents shown in the legend were calculated using the calibration procedure outlined in Libowitzky and Rossman(Libowitzky and Rossman, 1997).*

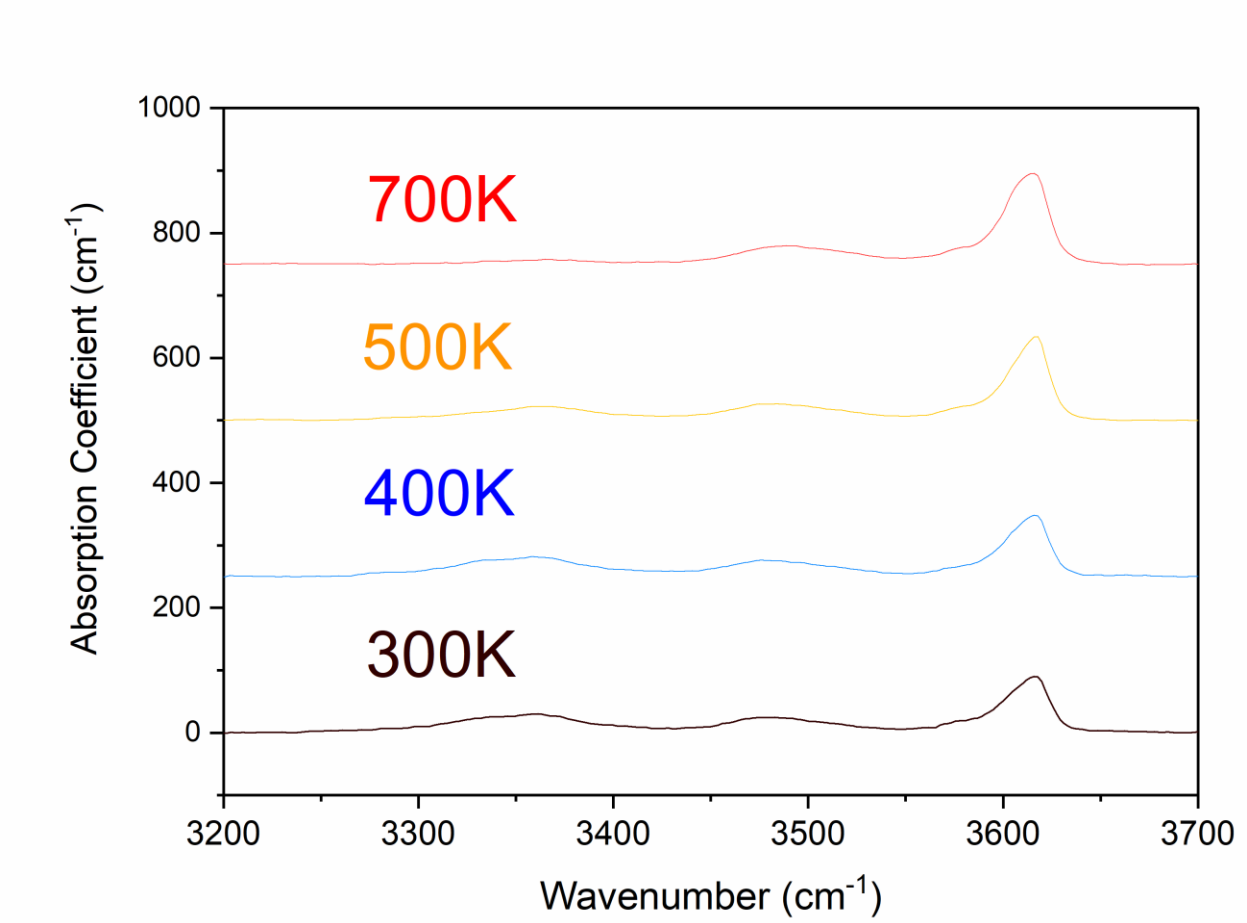

Fig. III.S6. *FTIR spectra of wadsleyite crystal Wad34 after several heating and cooling cycles. Black line: FTIR spectrum collected before heating; Blue line: FTIR spectrum collected after the sample had been heated at 400 K and then cooled down to 300 K. Yellow line: FTIR spectrum collected after the sample had been heated at 500 K and then cooled down to 300 K. Red line: FTIR spectrum collected after the sample had been heated at 700 K and then cooled down to 300 K.*

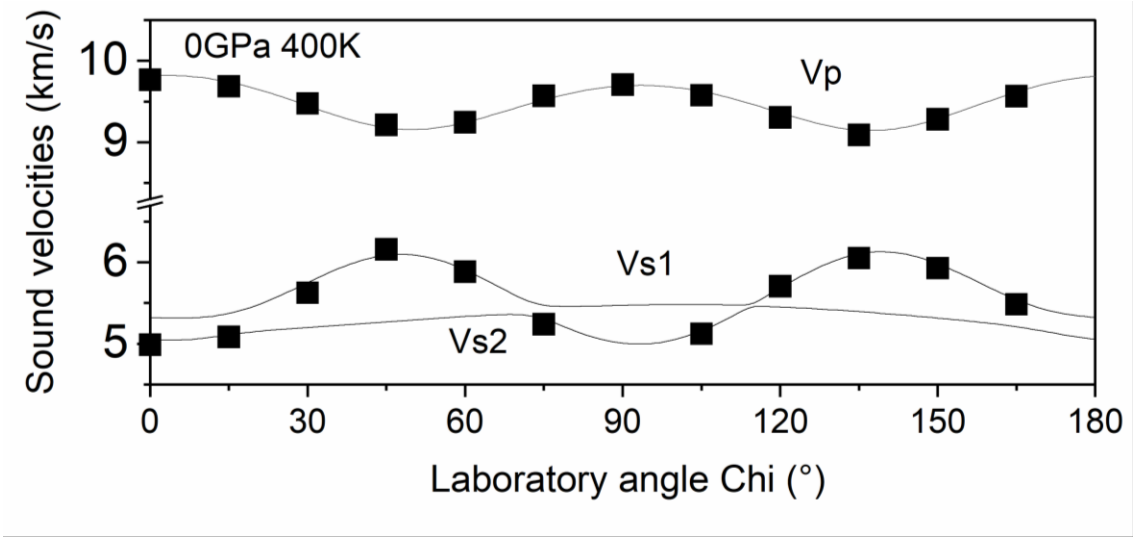

Fig. III.S7. *Change of velocities for wadsleyite sample Wad9 (0.0748 0.3154 -0.9460) as a function of laboratory angle Chi at 400 K and 0 GPa. Solid lines: the velocities predicted by the best-fit C_{ij} model at 400 K and 0 GPa based on high P-T experiments in this study; Squares: velocities collected at 400 K and 0 GPa after the completion of the high P-T experiments. Note, the Vp and Vs measurements at 400 K and 0 GPa (squares in this figure) are not utilized to derive the high P-T C_{ij} model of wadsleyite, which are shown in Fig. III.S3.*

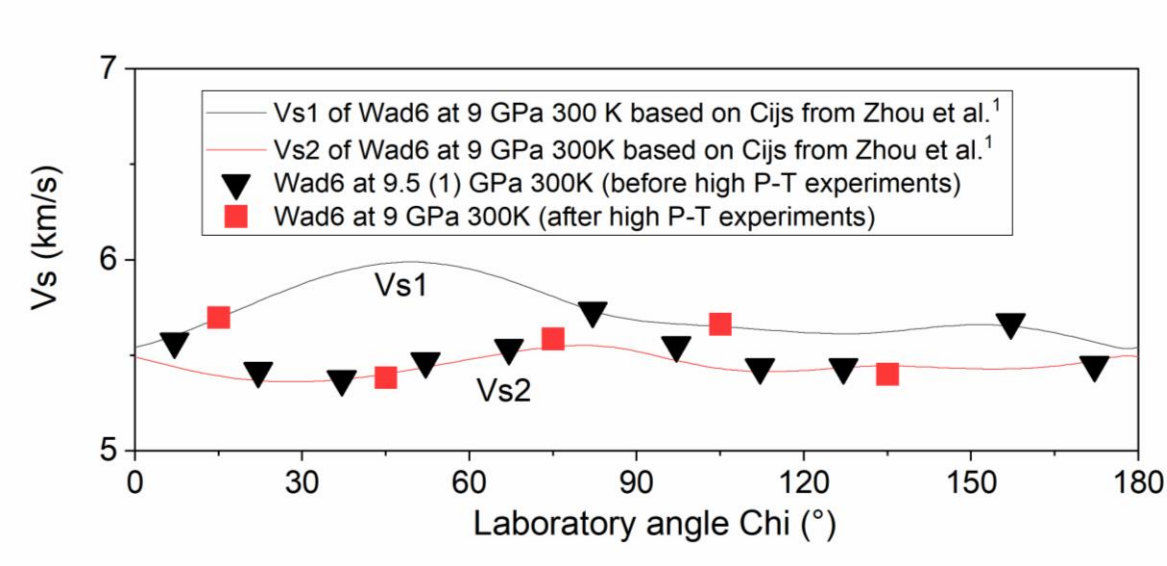

Fig. III.S8. *Change of Vs as a function of laboratory angle Chi for wadsleyite sample Wad6 (-0.3420, 0.8718, 0.3506). Solid lines: the velocities predicted by the best-fit C_{ij} model at 300 K and 9 GPa from ambient-T high-P experiments in Zhou et al.(Zhou et al., 2021) (before high P-T experiments in this study); Triangles: velocities measured at 300 K and 9.5 (2) GPa in Zhou et al.(Zhou et al., 2021) (before high P-T experiments in this study); Red squares: velocities measured at 300 K and 9 GPa after the sample has been heated to 700 K and 9.4 GPa in this study.*

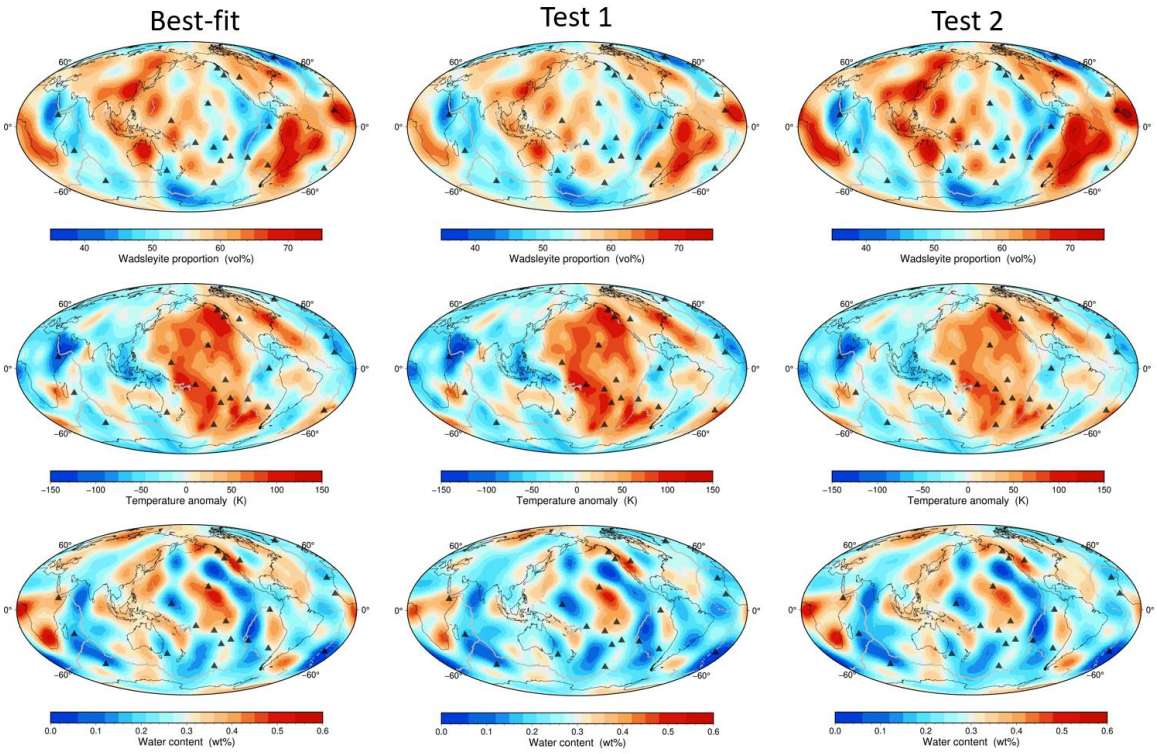

Fig. III.S9. *Global wadsleyite proportion, ΔT, and water content maps of the upper MTZ based on the 3 different sets of mineral physics parameters shown in Table III.S7.*

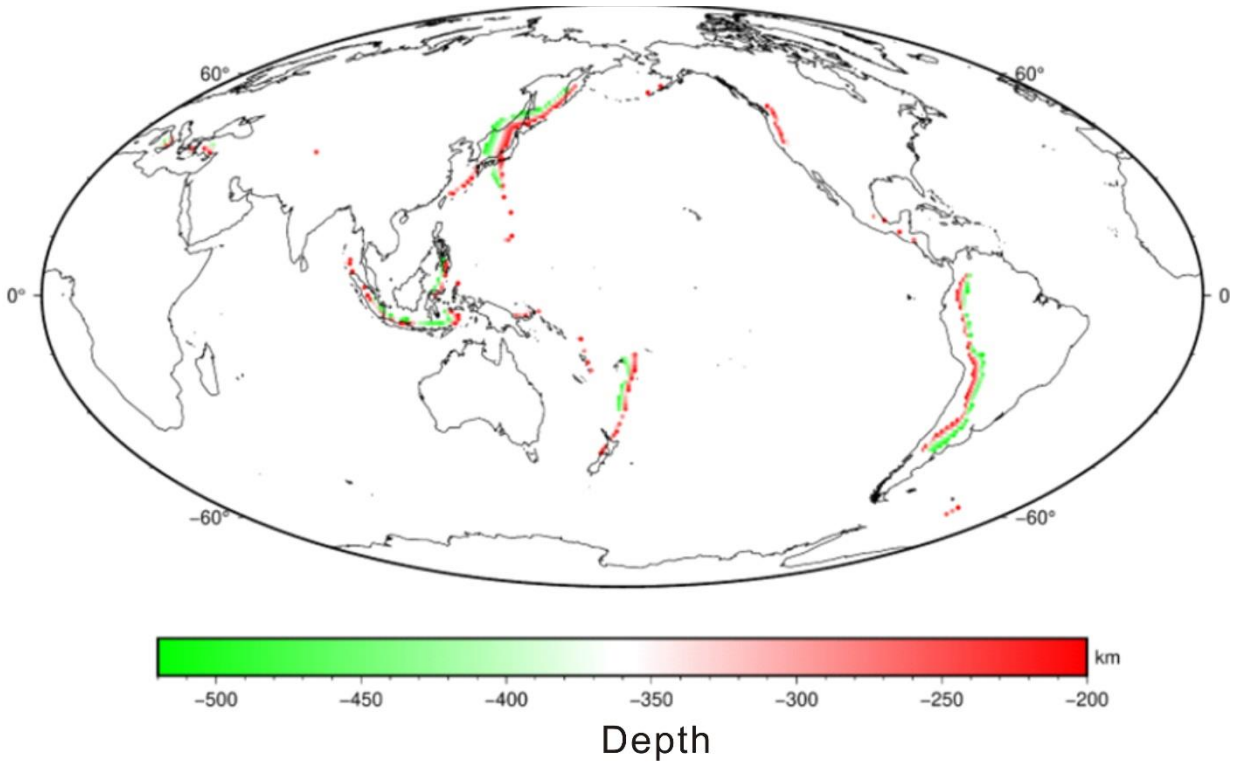

Fig. III.S10. *Slab locations near the upper MTZ constrained by Slab 2(Hayes et al., 2018). We used slab locations between 200 and 520 km to ensure the complete coverage of the slabs in the upper MTZ, especially for subduction zones with few earthquakes or sparse sampling in tomography. We also averaged structures within a wide area near each slab (~500 km) since the resolution is relatively low in the upper MTZ.*

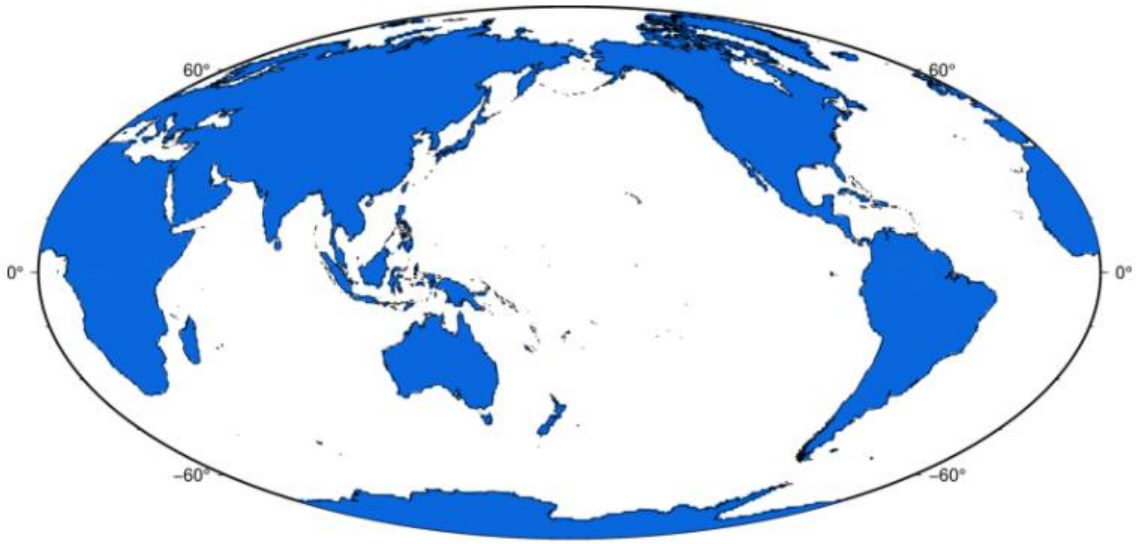

Fig. III.S11. *Land (blue) and ocean (white) locations downloaded from GMT(Wessel et al., 2019) based on Global Self-consistent, Hierarchical, High-resolution Geography database(Wessel and Smith, 1996).*

Table III.S1. *C_{ij}s, Ks, G, Vp, and Vs for the hydrous Fe-bearing wadsleyite sample measured in this study.*

T	(K)	400	400	400	400	500	500	500	700	700	700
P	(GPa)	8.3(2)	10.4(2)	13.7(2)	16.6(1)	5.2(1)	10.1(3)	15.6(2)	7.4(5)	9.4(3)	15.2(1)
ρ	g cm^{-3}	3.754	3.792	3.851	3.900	3.686	3.780	3.876	3.712	3.750	3.855
C_{11}	(GPa)	394(2)	407(2)	426(1)	437(2)	372(1)	401(2)	436(2)	379(1)	392(2)	428(1)
C_{22}	(GPa)	398(2)	413(2)	430(1)	445(2)	382(1)	406(2)	436(2)	386(1)	393(2)	427(1)
C_{33}	(GPa)	314(3)	329(4)	347(3)	362(2)	283(2)	320(3)	360(3)	299(3)	308(4)	344(3)
C_{44}	(GPa)	109(2)	116(2)	116(1)	117(2)	104(1)	114(1)	115(1)	106(2)	108(2)	113.1(9)
C_{55}	(GPa)	116(1)	115(1)	120.7(9)	122(1)	111(1)	115(1)	118(1)	112.2(8)	113(1)	117.3(7)
C_{66}	(GPa)	109(1)	111(1)	117.5(7)	125(1)	99.3(7)	110.4(9)	122.1(8)	102.7(7)	107(2)	117.6(7)
C_{12}	(GPa)	109(2)	117(2)	131(1)	138(1)	96(1)	116(2)	138(2)	103(1)	112(4)	134(1)
C_{13}	(GPa)	113(4)	118(4)	127(3)	140(3)	104(3)	118(3)	136(3)	113(3)	113(4)	129(2)
C_{23}	(GPa)	129(4)	136(4)	148(3)	154(4)	117(3)	135(4)	148(4)	126(3)	134(5)	149(3)
Ks^{VRH}	(GPa)	201(2)	209(2)	222(2)	233(2)	185(2)	206(2)	229(2)	193(2)	201(2)	224(2)
G^{VRH}	(GPa)	116(1)	119(1)	123(1)	126(1)	110(1)	118(1)	125(1)	111(1)	113(1)	121(1)
Vp	(km s^{-1})	9.74(2)	9.86(2)	10.02(2)	10.15(1)	9.48(2)	9.80(2)	10.10(2)	9.59(2)	9.69(2)	10.00(1)
Vs	(km s^{-1})	5.56(2)	5.61(2)	5.66(1)	5.70(1)	5.45(2)	5.58(1)	5.68(1)	5.48(2)	5.50(2)	5.61(1)

Note: VRH refers to Voigt-Reuss-Hill averaging scheme(Hill, 1963).

Table III.S2. *Summary of previous high-T velocity measurements on different wadsleyite samples, and the experimental result at 300K(Zhou et al., 2021) on the same samples used in this study.*

water	Fe#	Ks_0	G_0	$(\partial Ks/\partial P)_{T0}$	$(\partial Ks^2/\partial P^2)_{T0}$	$(\partial G/\partial P)_{T0}$	$(\partial G^2/\partial P^2)_{T0}$	$(\partial Ks/\partial T)_{P0}$	$(\partial G/\partial T)_{P0}$	Experiments	References
wt%		GPa	GPa		GPa^{-1}		GPa^{-1}	GPa K^{-1}	GPa K^{-1}		
0	0	170.7(11)	111.6(5)	4.56(23)	\	1.75(9)	\	−0.013(2)	−0.016(1)	7GPa,873K, UI	Li et al. (2001); (Liu et al., 2005)
0	0	170.2(19)	113.9(7)	\	\	\	\	−0.0171(5)	−0.0157(3)	1bar,660K, RUS	(Isaak et al., 2007b)
0	9	165.7(1)	105.66(3)	\	\	\	\	−0.016(3)	−0.012(1)	1bar,318K, RUS	(Katsura et al., 2001)
0	9	165.72(1)	105.43(2)	\	\	\	\	−0.0175(3)	−0.0159(1)	1bar,470K, RUS	(Mayama et al., 2004)
0	13	171.3	108.7	4.74(8)	\	1.52(4)	\	−0.013(1)	−0.0144(8)	12GPa,1073K, UI	(Liu et al., 2009a)
0.73	0	161.5(2)	101.6(1)	4.84(4)	\	1.68(2)	\	-0.013(2)	-0.015(4)	10GPa,600K, UI	(Gwanmesia et al., 2020)
0.15	9.4	165(2)	104(2)	5.2(1)	-0.16(2)	1.9(1)	-0.07(1)	\	\	18GPa, 300K, BS	(Zhou et al., 2021)
0.15	9.4	165(2)	104(2)	5.1(1)	-0.14(2)	1.9(1)	-0.07(1)	−0.018(2)	−0.014(1)	16GPa,700K, BS	This study

UI: Ultrasonic Interferometry

RUS: Resonant Ultrasound Spectroscopy

BS: Brillouin Spectroscopy

Note: The entries at row 7 (reference 1) have been compared with an existing literature focusing on the pressure dependence of the elastic properties of wadsleyite at ambient temperature. The references to those studies can be found in reference 1. The errors shown in this study represent 1 standard deviation.

Table III.S3. *Single-crystal elastic moduli for the hydrous Fe-bearing wadsleyite samples measured in this study.*

	C_{ij0} (GPa)	$(\partial C_{ij}/\partial P)_{T0}$	$(\partial^2 C_{ij}/\partial P^2)_{T0}$ (GPa^{-1})	$(\partial C_{ij}/\partial T)_{P0}$ ($GPa\ K^{-1}$)
C_{11}	341(1)	7.8(3)	-0.26(4)	-0.029(4)
C_{22}	358(1)	5.37(5)	0	-0.036(3)
C_{33}	244(2)	10.5(2)	-0.46(3)	-0.040(4)
C_{44}	106(2)	0.87(5)	0	-0.018(3)
C_{55}	109(1)	0.84(3)	0	-0.011(2)
C_{66}	90.8(7)	2.43(4)	-0.053(6)	-0.013(1)
C_{12}	75(1)	4.6(2)	-0.11(2)	-0.006(2)
C_{13}	99(2)	2.33(8)	0	-0.019(5)
C_{23}	102(3)	4.2(2)	-0.14(3)	-0.012(3)

Table III.S4. *Thermoelastic properties of garnet.*

Mineral	**Endmember**	K_{S_0}	G_0	ρ_0	$(\partial K_S/\partial P)_{T0}$	$(\partial K_S/\partial T)_{P0}$	$(\partial G/\partial P)_{T0}$	$(\partial G/\partial T)_{P0}$	a_0	a_1	a_2
		GPa	GPa	g cm^{-3}		(GPa K^{-1})		(GPa K^{-1})	(10^{-4} K^{-1})	(10^{-8} K^{-1})	(K^{-1})
Garnet	Pyrope (Fei, 1995; Irifune et al., 2008a; Liu et al., 2000; Sinogeikin, 2002; SUZUKI and ANDERSON, 1983)	171.0(5)	94.9(2)	3.560(2)	4.4(1)	-0.014(3)	1.15(6)	-0.011(2)	0.288	0.2787	-0.5521
	Almandine (Arimoto et al., 2015; Fei, 1995)	174.2(12)	94.9(7)	4.319(2)	4.61(14)	-0.0267(7)	1.06(6)	-0.0131(8)	0.26(5)	2.3(14)	0
	Grossular (Fei, 1995; Gwanmesia et al., 2014)	171.2(8)	107.4(2)	3.605(2)	4.47(2)	-0.0138(3)	1.29(5)	-0.0128(2)	0.1951	0.8089	-0.4972
	Mg-majorite (Fei, 1995; Hao et al., 2020; Irifune et al., 2008a; Liu et al., 2000; Sinogeikin, 2002; SUZUKI and ANDERSON, 1983)	162.0(5)	86.2(2)	3.560(2)	4.4(1)	-0.014 (3)	1.15(6)	-0.011(2)	0.288	0.2787	-0.5521

Note: In terms of our choice of the source data for calculating the sound velocities of Fe-Ca bearing majoritic garnet in the upper MTZ, our preference was given to the most recent direct sound velocity measurements at simultaneously high P-T conditions. For end member majorite and pyrope, their ambient-condition K_{S_0} and G_0 are calculated using the elasticity data of $Maj_{38}Py_{62}$ (Liu et al., 2000), $Maj_{50}Py_{50}$(Sinogeikin, 2002; Sinogeikin and Bass, 2002), $En_{80}Py_{20}$(Sinogeikin and Bass, 2002). As suggested by Liu et al. (2019), both the velocities and elastic moduli of the garnet within the majorite-pyrope solid solution increase linearly with Al content within analytical uncertainties. Their *P* and *T* derivatives of *K*s and *G* are based on the sound velocity data collected on a pyrolitic garnet ($Maj_{50}Py_{18}Gro_{25}Alm_6$) by Irifune et al. (2008b) up to ~18 GPa and 1673 K, which are close to the *P*-*T* conditions we explored in this study. The thermoelastic properties of the almandine end member are adopted from the most recent high *P*-*T* sound velocity measurements up to 19 GPa and 1700 K by Arimoto et al. (2015). For the grossular end member, the values presented in this table are from the most recent high *P*-*T* elasticity measurements up to 10 GPa and 1000 K by Gwanmesia et al. (2020)

Table III.S5. *Water contents of the 17 different wadsleyite crystals determined using unpolarized FTIR with two different calibration methods. The water contents of sample Wad1-Wad17 have been determined and reported in Zhou et al.[1]. We reported the values calculated based on the Libowitzky and Rossman(Libowitzky and Rossman, 1997) calibration in the main text to be consistent with previous studies(Buchen et al., 2018; Mao et al., 2008b).*

Sample Name	Water content (wt %)	
	Libowitzky and Rossman (1997) calibration	Deon et al. (2010) calibration
Wad25	0.19	0.17
Wad19	0.13	0.13
Wad35	0.10	0.11
Wad31	0.13	0.11
Wad48	0.16	0.14
Wad 34	0.18	0.15
Wad24	0.16	0.15
Wad37	0.18	0.16
Wad1(Zhou et al., 2021)	0.22	0.12
Wad7(Zhou et al., 2021)	0.09	0.08
Wad8(Zhou et al., 2021)	0.08	0.06
Wad9(Zhou et al., 2021)	0.11	0.10
Wad10(Zhou et al., 2021)	0.15	0.12
Wad11(Zhou et al., 2021)	0.16	0.12
Wad14(Zhou et al., 2021)	0.18	0.17
Wad15(Zhou et al., 2021)	0.15	0.14
Wad17(Zhou et al., 2021)	0.12	0.11
Average	0.15 (4)	0.13 (3)

Table III.S6. *Sound velocities of pyrolite at 15.2 GPa and 1870 K (Ishii et al., 2018) calculated using 2 different methods. The thermoelastic parameters used to determine these values are reported in Tables III.S2, S4.*

Pyrolite	Velocities by volume-weighted elastic moduli (km s^{-1})	Direct volume-weighted velocities (km s^{-1})	Difference
*V*p	9.521	9.527	6 m s^{-1}, 0.1%
*V*s	5.147	5.153	6 m s^{-1}, 0.1%

Table III.S7. *Two different sets of mineral physics parameters used in the modeling tests described in Supplementary Discussion 1, and their differences from the best-fit parameters.*

Parameters	**a**	**b**	**c**	**d**	**A**	**B**	**C**	**D**	**e**	**f**
Best-fit	-0.0027	-0.0028	0.0397	0.9750	-0.0040	-0.0045	0.0868	0.4850	0.107	20
Test 1	-0.0026	-0.0029	0.0358	0.9439	-0.0036	-0.0054	0.0957	0.4266	0.102	19
difference	-4%	5%	-10%	-3%	-11%	18%	10%	-12%	-4%	-5%
Test 2	-0.0028	-0.0027	0.0341	1.0444	-0.0036	-0.0049	0.0741	0.5405	0.122	25
difference	3%	-3%	-14%	7%	-11%	9%	-15%	11%	14%	25%

Supplementary References

Arimoto, T., Gréaux, S., Irifune, T., Zhou, C., Higo, Y., 2015. Sound velocities of Fe3Al2Si3O12 almandine up to 19 GPa and 1700 K. Physics of the Earth and Planetary Interiors 246, 1-8.

Buchen, J., Marquardt, H., Speziale, S., Kawazoe, T., Boffa Ballaran, T., Kurnosov, A., 2018. High-pressure single-crystal elasticity of wadsleyite and the seismic signature of water in the shallow transition zone. Earth and Planetary Science Letters 498, 77-87.

Courtillot, V., Davaille, A., Besse, J., Stock, J., 2003. Three distinct types of hotspots in the Earth's mantle. Earth and Planetary Science Letters 205, 295-308.

Deon, F., Koch-Müller, M., Rhede, D., Wirth, R., 2010. Water and Iron effect on the P-T-x coordinates of the 410-km discontinuity in the Earth upper mantle. Contributions to Mineralogy and Petrology 161, 653-666.

Fei, Y., 1995. Thermal expansion. Mineral physics and crystallography: a handbook of physical constants 2, 29-44.

Gwanmesia, G.D., Wang, L., Heady, A., Liebermann, R.C., 2014. Elasticity and sound velocities of polycrystalline grossular garnet (Ca3Al2Si3O12) at simultaneous high pressures and high temperatures. Physics of the Earth and Planetary Interiors 228, 80-87.

Gwanmesia, G.D., Whitaker, M.L., Dai, L., James, A., Chen, H., Triplett, R.S., Cai, N., 2020. The Elastic Properties of β-Mg2SiO4 Containing 0.73 wt.% of H2O to 10 GPa and 600 K by Ultrasonic Interferometry with Synchrotron X-Radiation. Minerals 10, 209.

Hao, M., Zhang, J.S., Pierotti, C.E., Zhou, W.-Y., Zhang, D., Dera, P., 2020. The seismically fastest chemical heterogeneity in the Earth's deep upper mantle—implications from the single-crystal thermoelastic properties of jadeite. Earth and Planetary Science Letters 543, 116345.

Hayes, G.P., Moore, G.L., Portner, D.E., Hearne, M., Flamme, H., Furtney, M., Smoczyk, G.M., 2018. Slab2, a comprehensive subduction zone geometry model. Science 362, 58-61.

Hill, R., 1963. Elastic properties of reinforced solids: some theoretical principles. Journal of the Mechanics and Physics of Solids 11, 357-372.

Irifune, T., Higo, Y., Inoue, T., Kono, Y., Ohfuji, H., Funakoshi, K., 2008a. Sound velocities of majorite garnet and the composition of the mantle transition region. Nature 451, 814-817.

Irifune, T., Higo, Y., Inoue, T., Kono, Y., Ohfuji, H., Funakoshi, K., 2008b. Sound velocities of majorite garnet and the composition of the mantle transition region. Nature 451, 814-817.

Isaak, D.G., Gwanmesia, G.D., Falde, D., Davis, M.G., Triplett, R.S., Wang, L., 2007. The elastic properties of β-Mg2SiO4 from 295 to 660K and implications on the composition of Earth's upper mantle. Physics of the Earth and Planetary Interiors 162, 22-31.

Ishii, T., Kojitani, H., Akaogi, M., 2018. Phase relations and mineral chemistry in pyrolitic mantle at 1600–2200 °C under pressures up to the uppermost lower mantle: Phase transitions around the 660-km discontinuity and dynamics of upwelling hot plumes. Physics of the Earth and Planetary Interiors 274, 127-137.

Katsura, T., Mayama, N., Shouno, K., Sakai, M., Yoneda, A., Suzuki, I., 2001. Temperature derivatives of elastic moduli of (Mg0. 91Fe0. 09) 2SiO4 modified spinel. Physics of the Earth and Planetary Interiors 124, 163-166.

Katsura, T., Yoneda, A., Yamazaki, D., Yoshino, T., Ito, E., 2010. Adiabatic temperature profile in the mantle. Physics of the Earth and Planetary Interiors 183, 212-218.

Li, B., Liebermann, R.C., Weidner, D.J., 2001. P-V-Vp-Vs-T measurements on wadsleyite to 7 GPa and 873 K: Implications for the 410-km seismic discontinuity. Journal of Geophysical Research: Solid Earth 106, 30579-30591.

Libowitzky, E., Rossman, G.R., 1997. An IR absorption calibration for water in minerals. American Mineralogist 82, 1111-1115.

Liu, J., Chen, G., Gwanmesia, G.D., Liebermann, R.C., 2000. Elastic wave velocities of pyrope–majorite garnets (Py62Mj38 and Py50Mj50) to 9 GPa. Physics of the Earth and Planetary Interiors 120, 153-163.

Liu, W., Kung, J., Li, B., 2005. Elasticity of San Carlos olivine to 8 GPa and 1073 K. Geophysical Research Letters 32.

Liu, W., Kung, J., Li, B., Nishiyama, N., Wang, Y., 2009. Elasticity of (Mg0.87Fe0.13)2SiO4 wadsleyite to 12GPa and 1073K. Physics of the Earth and Planetary Interiors 174, 98-104.

Liu, Z., Gréaux, S., Cai, N., Siersch, N., Ballaran, T.B., Irifune, T., Frost, D.J., 2019. Influence of aluminum on the elasticity of majorite-pyrope garnets. American Mineralogist: Journal of Earth and Planetary Materials 104, 929-935.

Mao, Z., Jacobsen, S.D., Jiang, F.M., Smyth, J.R., Holl, C.M., Frost, D.J., Duffy, T.S., 2008. Single-crystal elasticity of wadsleyites, β-Mg2SiO4, containing 0.37–1.66 wt.% H2O. Earth and Planetary Science Letters 268, 540-549.

Mayama, N., Suzuki, I., Saito, T., Ohno, I., Katsura, T., Yoneda, A., 2004. Temperature dependence of elastic moduli of β-(Mg, Fe) 2SiO4. Geophysical research letters 31.

Sinogeikin, S.V., 2002. Elasticity of Majorite and a Majorite-Pyrope solid solution to high pressure: Implications for the Transition Zone. Geophysical Research Letters 29.

Sinogeikin, S.V., Bass, J.D., 2002. Elasticity of pyrope and majorite–pyrope solid solutions to high temperatures. Earth and Planetary Science Letters 203, 549-555.

SUZUKI, I., ANDERSON, O.L., 1983. ELASTICITY AND THERMAL EXPANSION OF A NATURAL GARNET UP TO 1, 000K. Journal of Physics of the Earth 31, 125-138.

Wessel, P., Luis, J., Uieda, L., Scharroo, R., Wobbe, F., Smith, W., Tian, D., 2019. The generic mapping tools version 6. Geochemistry, Geophysics, Geosystems 20, 5556-5564.

Wessel, P., Smith, W.H., 1996. A global, self-consistent, hierarchical, high-resolution shoreline database. Journal of Geophysical Research: Solid Earth 101, 8741-8743.

Zhou, W.-Y., Ren, Z., Zhang, J.S., Chen, B., Hao, M., Ohuchi, T., Miyagi, L., Zhang, D., Alp, E.E., Lavina, B., 2021. The Water-Fe-Pressure dependent single-crystal elastic properties of wadsleyite: Implications for the seismic anisotropy in the upper Mantle Transition Zone. Earth and Planetary Science Letters 565, 116955.

Chapter IV

High pressure-temperature single-crystal elasticity of ringwoodite: Implications for detecting the 520 discontinuity and metastable ringwoodite at depths greater than 660 km

Abstract

The 520 km discontinuity (the 520) and the 660 km discontinuity (the 660) are primarily caused by the wadsleyite to ringwoodite and ringwoodite to bridgmanite + ferropericlase phase transitions, respectively. Global seismic studies show significant regional variations of the 520, which are likely due to chemical and thermal heterogeneities in the Mantle Transition Zone (MTZ). However, the effects of chemical composition and temperature on the detectability of the 520 are unclear. Additionally, it remains unknown whether the possibly existing metastable ringwoodite in the core of the cold and fast subducting slabs could create a detectable seismic signature near the top of the lower mantle. Our understanding of both issues is hindered by the lack of single-crystal elasticity measurements of ringwoodite at simultaneous high pressure-temperature (*P*-*T*) conditions. In this study, we measured the single-crystal elasticity of an anhydrous Fe-bearing ringwoodite up to 32 GPa and 700 K by Brillouin spectroscopy, and then modeled the composition-dependent elastic properties of ringwoodite to calculate the compositional effects on the velocity jumps at the 520. We found that opposite to the effect of Fe, water enhances the *V*p (P-wave velocity) jump, yet decreases the *V*s (S-wave velocity) jump of the 520 across the wadsleyite to ringwoodite transition. Higher temperature increases both *V*p and *V*s contrasts across the 520. At depths between 660-700 km in the lower mantle, the existence of metastable ringwoodite may only result in ~1-2% low velocity anomaly, which is seismically difficult to

resolve. The low velocity anomaly caused by metastable ringwoodite increases to 5-7% at 750 km depth due to the weak pressure dependence of *V*s in ringwoodite at lower mantle conditions, but whether it is seismically detectable depends on the extension of the regions in subducted slabs that are sufficiently cold to host metastable ringwoodite.

1. Introduction

The high pressure-temperature (*P-T*) phase transformations of olivine ($(Mg, Fe)_2SiO_4$) are largely responsible for 3 major seismic discontinuities in the Earth's ambient (normal) mantle: the 410 km seismic discontinuity (the 410), which separates the upper mantle and the mantle transition zone (MTZ), is linked to the olivine to wadsleyite transition; the wadsleyite to ringwoodite transformation corresponds to the 520 km seismic discontinuity (the 520); and finally the breakdown of ringwoodite to bridgmanite + ferropericlase marks the 660-km seismic discontinuity (the 660), which is the boundary between the MTZ and the lower mantle (Ringwood, 1991). While the 520 is believed to be a global feature (Tian et al., 2020), it is a less prominent discontinuity compared to the 410 and the 660. The depth and magnitude of the 520 (476-543 km, 1.2-4.8% velocity jump) vary significantly on a global scale, which is likely caused by chemical and thermal heterogeneities in the MTZ (Tian et al., 2020; Sinogeikin et al., 2003). The MTZ is a potential water reservoir due to the high water solubility in the structures of wadsleyite and ringwoodite as hydroxyl groups, but the water distribution in the MTZ is suggested to be highly variable based on global magnetotelluric and seismic studies (0-1 wt% water, e.g., Kelbert et al., 2009; Wang et al., 2021). However, the effect of water on the magnitude of the 520 (velocity and impedance contrasts) remains poorly constrained, particularly in the more realistic Fe-bearing system. A prior study by first-principles calculations modeled the effect of water in the Fe-free system and suggested that water reduces *V*p and *V*s impedance contrasts at the 520 (Panero, 2010). Sinogeikin et al. (2003) suggested that Fe enhances *V*p and *V*s velocity contrasts across the wadsleyite-ringwoodite

transition, which was later contradicted by a first-principals computational study (Núñez-Valdez et al., 2011). Jacobsen and Smyth (2006) found that *V*p of hydrous and anhydrous ringwoodite is indistinguishable under lower MTZ pressures at 300 K, while Mao et al. (2012) found that adding 1 wt% water into ringwoodite structure would significantly decrease both *V*p and *V*s by ~2.5% under similar *P*-*T* conditions. In addition, large discrepancies in terms of the high *P*-*T* single-crystal elastic properties of ringwoodite exist between the first-principles computational results and different experimental measurements (e.g., Mao et al. 2012; Schulze et al., 2018; Wang et al., 2021). The lack of benchmark high *P*-*T* single-crystal elasticity measurements on Fe-bearing ringwoodite has hindered quantitative efforts to resolve these existing discrepancies, as well as the further evaluation of the compositional and thermal effects on the detectability of the 520.

It is worth noting that the transition pressures between olivine polymorphs in the Earth's interior, which largely control the 410, 520, and 660 depths, depend on the temperatures and Clapeyron slopes of these phase transitions. For example, the positive Clapeyron slope of the olivine-wadsleyite-ringwoodite transition would result in shallower 410 and 520 under cold subduction zones, and a shallower 660 is expected under the deeply sourced hotspots due to the negative Clapeyron slope of ringwoodite to bridgmanite + ferropericlase transition (Lebedev et al., 2003). Compared with wadsleyite, olivine and ringwoodite have much larger thermodynamic stability fields in the composition-*P*-*T* space. Moreover, considering the transition kinetics, for cold and fast subducting slabs, when the descending rate of the slab is faster than the phase transition rate, low-pressure polymorphs may metastably exist at greater depth exceeding their pressure stability fields (Hosoya et al., 2005). Seismic studies have identified low-velocity metastable olivine wedges in the core of the slabs subducting underneath Japan and Marianas at 410-560 km and 410-630 km depth ranges, respectively (Jiang et al., 2008; Kawakatsu and

Yoshioka, 2011; Kaneshima et al., 2007). Ringwoodite may also metastably exist in the coldest part of the fast subducting slabs at depths greater than 660 km (Liu et al., 2018). However, due to the lack of knowledge on the sound velocities of metastable ringwoodite at relevant *P-T* conditions, whether metastable ringwoodite can be seismically detected remains unknown.

To overcome the aforementioned limitations, in this study, we measured single-crystal elasticity of an anhydrous Fe-bearing ringwoodite sample up to 32 GPa and 700 K by Brillouin spectroscopy. We then modeled the thermal and chemical effects on the magnitude of the 520 based on this study and literature data. We finally calculated the seismic properties of metastable ringwoodite near the 660 and discussed whether it might be detected in cold and fast subducting slabs.

2. Methods

2.1. Sample synthesis and characterization

San Carlos olivine was ground into powder and then packed in a boron nitride capsule without water in a 10/5 multi-anvil assembly to synthesize anhydrous Fe-bearing ringwoodite single crystals. The synthesis experiment was conducted at 1673K and 18 GPa for 6.5 hours in a 1000-ton Multi-Anvil Press at the University of Hawai‘i at Mānoa (UHM). The typical sizes of ringwoodite single crystals in the run product range from 30 μm to 90 μm. A few crystals ~70-90 μm in size were hand-picked and double-side polished into platelets with ~30-50 μm thickness and then examined using the Thermo Fisher Nicolet Nexus 670 Fourier Transformed Infrared Spectrometer (FTIR) with an infrared light source, a CaF_2 beam splitter, and a narrow-band mercury-cadmium-telluride detector at the University of New Mexico (UNM). We could not identify any visible peaks between 2400-3800 cm^{-1} in the collected unpolarized FTIR spectra related with O-H in ringwoodite, suggesting that the synthetic ringwoodite crystals were nearly anhydrous. Typical FTIR spectra are shown in Fig. IV.S1. We also determined the chemical

composition of the synthetic ringwoodite crystals to be $(Mg_{0.904}Fe_{0.096})_2SiO_4$ (Fe# = 9.60(3)) using the JEOL 8200 Electron Microprobe operated at 15 kV and 20nA at UNM (Table IV.S1). The major element standards were forsterite for Mg and Si, almandine for Fe and Al, and diopside for Ca.

We further polished 1 ringwoodite platelet down to ~10 μm thickness for single-crystal X-ray diffraction (XRD) and Brillouin spectroscopy experiments. The single-crystal XRD experiments were conducted under room *P-T* conditions at the X-ray Atlas Diffraction Lab using the Incoatec IμS 3.0 AgKα microfocus source and a customized Bruker D8 Venture diffractometer at UHM. The diffraction images were collected in the φ-scan geometry for a φ angle range of ± 23° with 1° step and 20-second exposure per frame. The unit cell parameters and crystal orientation were calculated using the Bruker APEX3 software. The density (ρ_0) at room *P-T* conditions was determined to be 3.709 (1) g/cm^3 with the cubic unit cell parameter a = 8.0704 (6) Å. The plane normal of the ringwoodite platelet is determined to be (-0.8729, -0.4364, 0.2182).

2.2. High *P-T* Brillouin spectroscopy experiments and data analysis

We used a resistively heated BX90 diamond anvil cell (DAC) with 350 μm-culet diamond anvils to generate high *P-T* conditions for the Brillouin spectroscopy experiments (Kantor et al., 2012). The acoustically fast and slow directions of both diamond anvils were pre-determined using Brillouin spectroscopy based on the frequency shifts in the collected Brillouin spectra. The two diamond anvils were then manually rotated within the diamond anvil cell to ensure that their slow directions matched each other before experiments. A 250 μm thick Rhenium gasket was indented to ~49 μm thickness, and a 250 μm hole was drilled at the center of the gasket to form the sample chamber. The polished ringwoodite platelet and 2 ruby spheres (pressure marker, Shen et al., 2020; Datchi et al., 2007) were loaded into the sample chamber. Neon was gas-loaded as the pressure-transmitting medium in the sample chamber at the GeoSoilEnviroCARS, Advanced Photon Source,

Argonne National Laboratory. High temperature up to 700 K was generated by a platinum resistive heater placed around the diamond anvils in the BX90 DAC (Lai et al., 2020). We attached 2 K-type thermocouples near the diamond culet to determine the temperatures. The temperature differences given by the 2 thermocouples were always less than 15 K up to the maximum temperature reached during the experiments.

We conducted Brillouin spectroscopy experiments using 50° symmetric forward scattering geometry at the Laser Spectroscopy Laboratory at UNM. The light source is a single-mode 532 nm solid-state laser. A 6-pass tandem Fabry-Pérot interferometer was used to measure the Brillouin frequency shift. The scattering angle of the Brillouin spectroscopy system was routinely calibrated using a standard silica glass Corning 7980 (Zhang et al., 2015). The scattering angles were calibrated twice during the 4-month experiments: 50.77º and 50.51º. We collected Brillouin spectra of ringwoodite with a step of 15º from *Chi* angle 0º to 360º at each *P-T* condition. Fig. IV.S2 shows a typical Brillouin spectrum. Fewer velocity data were obtained at pressures higher than ~18 GPa (Fig. IV.S3), because the ringwoodite v_p peaks start to overlap with the diamond v_s peaks along the acoustically slowest directions of diamonds. In addition, the externally connected electric wires of the heater sometimes blocked the scattered light path. At higher *P-T* conditions, bending the fragile heating wires back and forth can easily result in heater failure. Thus, we skipped the Brillouin measurements at *Chi* angles of 135º and 150º (Fig. IV.S3). Fortunately, due to the high symmetry of ringwoodite, v_p and v_s along 8-10 different crystallographic directions are enough to constrain the 3 independent C_{ij}s of ringwoodite. All the high *P-T* data are collected along the isotherms, respectively (Fig. IV.1). Typical collection time for a Brillouin spectrum with similar quality as the one shown in Fig. IV.S2 is about 15-20 min at 300 K, and that reduces to about 10-15 min under high temperatures. The temperature averaged from the two thermocouple

readings was stabilized at the target temperature of 400 K, 500K, or 700 K during the high *P-T* experiments through adjustment of the heater power. The temperature fluctuations in each experimental run are less than 10 K.

With the initially estimated high *P-T* densities (Nishihara et al., 2004) and the measured phonon direction-v_p-v_s data set for ringwoodite, we inverted the best-fit C_{ij}s (C_{11}, C_{44}, C_{12}) under each *P-T* condition using Christoffel equation. The RMS errors are always less than 40 m/s, suggesting an excellent fit between the C_{ij}s model and the measured velocities (Fig. IV.S3). Voigt-Reuss-Hill (VRH) averaging scheme is used to calculate bulk modulus (Ks), shear modulus (G), Vp, and Vs for isotropic polycrystalline ringwoodite (Hill, 1963). Note the Vp and Vs are independent of the assumed densities, thus they are the true values at high *P-T* conditions. After fixing the K_{S0}, G_0, ρ_0, and thermal expansivity (Inoue et al., 2004), we fitted the *P-T-V*p-*V*s data set collected in this study using temperature-dependent 4th order finite strain equation of state (EOS) (Equations S1-S15, S19-S21) and derived the aggregate thermoelastic parameters: $(\partial K_S/\partial P)_{T0}$, $(\partial^2 K_S/\partial P^2)_{T0}$, $(\partial G/\partial P)_{T0}$, $(\partial^2 G/\partial P^2)_{T0}$, $(\partial K_S/\partial T)_{P0}$, $(\partial G/\partial T)_{P0}$, and best-fit high *P-T* densities (Davies and Dziewonski, 1975; Duffy and Anderson, 1989). We chose 4th order finite strain EOS here for fitting the aggregate elastic properties of ringwoodite instead of 3rd order finite strain EOS due to the significantly reduced RMS error (12 m/s versus 44 m/s). As shown in Fig. IV.S4, the use of 3rd order finite strain EOS underestimates the Vp and Vs at lower pressures while overestimates them at higher pressures (23-32 GPa, Fig. IV.1). C_{ij}s, K_S, and G at each high *P-T* condition were then updated with the newly derived best-fit densities (Table IV.1). Finally, using temperature-dependent 3rd order or 4th order finite strain EOS (Equations S16-S18) (Davies, 1974; Duffy and Anderson, 1989), we fitted the *P-T-*C_{ij}s data set to derive the pressure and temperature derivatives of the C_{ij}s: $(\partial C_{ij0}/\partial P)_{T0}$, $(\partial^2 C_{ij0}/\partial P^2)_{T0}$, $(\partial C_{ij0}/\partial T)_{P0}$ (Fig. IV.1; Table IV.S2).

Table IV.1. *C_{ij}s, Ks, G, Vp, and Vs for the ringwoodite sample measured in this study.*

Temperature	***Pressure***	**density**	C_{11}	C_{44}	C_{12}	***K*s**	***G***	***V*p**	***V*s**
K	GPa	g/cm^3	GPa	GPa	GPa	GPa	GPa	km/s	km/s
300	0	3.709(1)	330(1)	128.5(6)	117(1)	188(1)	119 (1)	9.67(1)	5.67(1)
300	2.9(1)	3.765	350(1)	132.2(5)	126(1)	200.6(5)	123.9(7)	9.86(1)	5.74(1)
300	5.9(1)	3.820	369(1)	135.7(6)	131(1)	209.9(6)	128.7(6)	9.99(1)	5.81(1)
300	8.4(2)	3.865	384(1)	136.7(6)	139(1)	220.0(6)	130.6(5)	10.10(1)	5.81(1)
300	9.8(1)	3.889	393.6(9)	137.5(5)	141.2(9)	225.3(5)	132.9(4)	10.17(1)	5.84(1)
300	16.1(1)	3.994	426.0(7)	142.6(4)	159.6(6)	248.4(3)	138.8(3)	10.42(1)	5.89(1)
300	19.3(4)	4.044	441(1)	146.3(7)	172(1)	261.6(6)	141.5(5)	10.55(1)	5.92(1)
300	23.2(2)	4.104	463(1)	146.9(8)	179(1)	273.5(7)	145.0(4)	10.67(1)	5.95(1)
300	24.9(3)	4.129	472.3(1)	147.0(5)	187(1)	282.1(6)	145.2(3)	10.73(1)	5.93(1)
300	28.8(2)	4.186	497(1)	145.4(6)	194(1)	294.6(6)	147.9(4)	10.84(1)	5.94(1)
300	31.8(3)	4.228	508(1)	148.1(9)	203(1)	304.3(7)	149.9(5)	10.92(1)	5.95(1)
400	6.9(1)	3.828	370.3(9)	135.0(5)	134.0(9)	212.8(5)	128.0(5)	10.01(1)	5.78(1)
400	9.1(1)	3.867	385(1)	135.9(5)	141.6(9)	222.7(5)	130.0(5)	10.12(1)	5.80(1)
400	15.7(4)	3.977	420(1)	139.6(7)	159(1)	245.9(6)	136.0(4)	10.36(1)	5.85(1)
400	18.5(5)	4.022	436(1)	142.6(6)	168(1)	257.6(6)	139.0(4)	10.50(1)	5.88(1)
400	28.4(4)	4.170	492(2)	145.2(6)	192(2)	292.0(8)	147.0(4)	10.82(1)	5.94(1)
500	6.4(2)	3.808	365(1)	132.9(5)	132.2(9)	209.9(5)	126.1(5)	9.96(1)	5.76(1)
500	11.4(2)	3.895	394(1)	137.5(5)	143.9(9)	227.3(5)	132.4(4)	10.18(1)	5.83(1)
500	17.3(1)	3.993	430(1)	140.9(8)	161.5(1)	250.9(7)	138.1(5)	10.44(1)	5.88(1)
500	21.5(3)	4.058	449(1)	144.5(6)	176(1)	267.1(7)	141.3(4)	10.59(1)	5.90(1)
500	28.6(2)	4.164	488(1)	144.7(7)	188(1)	288.1(6)	146.6(4)	10.78(1)	5.93(1)
700	9.2(3)	3.837	378(1)	131.9(6)	140(1)	219.1(6)	126.8(5)	10.06(1)	5.75(1)
700	15.4(5)	3.942	411.5(9)	137.8(5)	156.9(8)	241.8(4)	133.5(4)	10.32(1)	5.82(1)
700	18.4(5)	3.991	425(1)	142.1(4)	161(1)	249.1(6)	138.0(3)	10.42(1)	5.88(1)
700	20.7(3)	4.027	440.9(9)	141.3(9)	171(1)	261.1(6)	138.7(5)	10.52(1)	5.87(1)
700	28.7(4)	4.146	485(1)	142.7(5)	189(1)	287.9(6)	144.8(4)	10.77(1)	5.91(1)

2.3. Modeling of effects of Fe# and water on the velocity jumps across the wadsleyite-ringwoodite transition

We adopted a similar procedure as what has been used in Zhou et al. (2021) to model the effects of Fe# ($\frac{100\ \mathrm{Fe}_{mol}}{Mg_{mol}+Fe_{mol}}$) and water on the *V*p and *V*s of ringwoodite under high *P*-*T* conditions:

(1) We compiled the water content, Fe#, density, *K*s, *G*, *V*p, and *V*s of 8 different ringwoodite samples used in previous Brillouin spectroscopy studies (Jackson et al., 2000; Sinogeikin et al., 2003; Wang et al., 2006; Schulze et al., 2018, this study) to avoid any possible

discrepancies resulting from the use of different experimental techniques, such as ultrasound interferometry. These ringwoodite samples cover a wide range of water content (0-2.34 wt %) and Fe# (0-11.5) (Fig. IV.S5).

(2) We fitted the ρ_0, K_{S0}, G_0 of ringwoodite with respect to water contents (in wt%) and Fe# for these 8 different samples assuming an empirical linear relationship as shown in Table IV.S3.

(3) After adopting the results derived in step (2) under room *P*-*T* conditions, we fitted the parameters of the 4th order finite strain EOS to the entire Fe#, water and pressure-dependent V_P and V_S data set for the 8 ringwoodite samples to get water content and Fe# dependent $(\partial K_S/\partial P)_{T0}$, $(\partial^2 K_S/\partial P^2)_{T0,}$ $(\partial G/\partial P)_{T0}$, and $(\partial^2 G/\partial P^2)_{T0}$ (Equations S1-S15, Table IV.S3).

To evaluate the goodness of the fit of the obtained composition dependent high-pressure elasticity model, we compared the model-predicted values of V_P and V_S for all 8 ringwoodite samples with the experimentally determined values under high-pressure conditions. The differences are all within 1% for both V_P and V_S (Fig. IV.S5A), suggesting our model is robust within the investigated range of water content and Fe# of ringwoodite in the Earth's mantle.

(4) Water content and Fe# in ringwoodite are suggested to have negligible effects on the temperature derivatives of K_S and G of ringwoodite (Schulze et al., 2018; Jackson et al., 2000; Sinogeikin et al., 2003). Therefore, we adopted $(\partial K_S/\partial T)_{P0}$ and $(\partial G/\partial T)_{P0}$ determined for the anhydrous Fe-bearing ringwoodite sample in this study in our model to calculate the high *P*-*T* elasticity of ringwoodite.

Combined with the composition-dependent high *P*-*T* elasticity model of wadsleyite in Zhou et al. (2020, 2021), we calculated the effects of water and Fe# on the velocity (V_P, V_S) as well as impedance contrasts across the wadsleyite-ringwoodite transition at 18 GPa along a 1600

K adiabat (Katsura et al., 2010). The impedance refers to density*velocity, the velocity and impedance jumps at the 520 for wadsleyite-ringwoodite phase transition are calculated as:

$$\frac{\mathrm{A(ringwoodite)-A(wadsleyite)}}{\mathrm{A(ringwoodite)+A(wadsleyite)}} * 200\% \quad (1)$$

where A is velocity or impedance. The water partitioning coefficient between wadsleyite and ringwoodite adopted in our modeling is 2:1 (Inoue et al., 2010). The Fe partitioning coefficient between wadsleyite and ringwoodite used in our modeling is 0.6 (Tsujino et al., 2019).

We would like to point out that in our model, we have included all previous single-crystal Brillouin spectroscopy studies of ringwoodite after 2000 except Mao et al. (2012). We excluded the experimental data in Mao et al. (2012) in our modeling based on the following reasons:

(1) We have computed another composition-dependent elasticity model of ringwoodite without excluding the data presented in Mao et al. (2012), as shown in Fig. IV.S5B. However, the final best-fit model we obtained this way still shows large deviations from the data in Mao et al. (2012), while at the same time it fits the rest of the data in all the other studies well.

(2) Although the ringwoodite samples used in Schulze et al. (2018) and Mao et al. (2012) are compositionally very similar, the *V*p and *V*s obtained in Schulze et al. (2018) are ~2% and ~3% higher than what were presented in Mao et al. (2012), respectively. Our model is in excellent agreement with all the other experimental studies, including Schulze et al. (2018). As suggested by Schulze et al. (2018), the ringwoodite sample used in Mao et al. (2012) was possibly hydrated through a mechanism that is different from all the other studies. While we could not rule out the possibility that both potential hydration mechanisms may take place in nature, due to the lack of experimental data on the ringwoodite crystals hydrated through similar mechanisms as the sample used in Mao et al. (2012), we could only conduct the modeling work in this study based on all the

other Brillouin spectroscopy studies. More sophisticated modeling work could be done with more experimental data available in the future.

3. Results

3.1. Elasticity of the anhydrous Fe-bearing ringwoodite sample measured in this study

The single-crystal elasticity measurements conducted in this study suggest that the 3 C_{ij}s (C_{11}, C_{44}, C_{12}) of ringwoodite behave differently with temperature and pressure (Fig. IV.1). C_{11} of ringwoodite is most sensitive to temperature while C_{12} is least sensitive (Fig. IV.1; Table IV.S2). C_{11} is also most sensitive to pressure while C_{44} is least sensitive (Fig. IV.1), consistent with all previous studies for ringwoodite (Fig. IV.S6, e.g., Sinogeikin et al., 2003; Wang et al., 2006; Mao et al., 2012; Schulze et al., 2018; Wang et al., 2021). C_{11} and C_{12} increase almost linearly with pressure throughout the entire pressure range we investigated. In comparison, C_{44} increases nonlinearly only up to ~23 GPa in this study, consistent with Schulze et al. (2018) as shown in Fig. IV.S6. At pressures between 23 GPa and 32 GPa, C_{44} remains almost constant, which has not been reported before due to the limited pressure range explored in previous studies. The weak pressure dependence of C_{44} possibly reflects the coupling between shear strains and atomic displacements in minerals with spinel-type structure (Caracas and Banigan, 2009).

The elastic properties of an isotropic polycrystalline aggregate of ringwoodite are calculated under the VRH averaging scheme (Table IV.1). Vp increases with P from 0 GPa to 32 GPa, while the Vs increase becomes negligible when P exceeds ~23 GPa, mainly due to the minimal increase of C_{44} in the relevant pressure range (Fig. IV.1). The best-fit aggregate elastic properties for the anhydrous Fe-bearing ringwoodite sample used in this study are: $K\mathrm{s}_0$ = 188 (1) GPa, G_0 = 119 (1) GPa, $(\partial K\mathrm{s}/\partial P)_{T0}$ = 4.0 (2), $(\partial^2 K\mathrm{s}/\partial P^2)_{T0}$ = − 0.03 (2) GPa^{-1}, $(\partial G/\partial P)_{T0}$ = 1.56 (7), $(\partial^2 G/\partial P^2)_{T0}$ = − 0.049 (6) GPa^{-1}, $(\partial K\mathrm{s}/\partial T)_{P0}$ = − 0.017 (3) GPa/K, and $(\partial G/\partial T)_{P0}$ = − 0.011 (2) GPa/K. Fixing the $(\partial^2 K\mathrm{s}/\partial P^2)_{T0}$ to 0 GPa^{-1} as what was done in previous studies (Mao et al., 2012;

Schulze et al., 2018) yields slightly smaller $(\partial Ks/\partial T)_{P0}$ (-0.014 (3) GPa/K) and $(\partial G/\partial T)_{P0}$ (-0.012 (2) GPa/K). The values of $(\partial Ks/\partial T)_{P0}$ and $(\partial G/\partial T)_{P0}$ obtained in this study are in between the previous high *P-T* ultrasonic experiments on polycrystalline ringwoodite up to 18 GPa 1600K ($(\partial Ks/\partial T)_{P0} = -0.0181$ (8) GPa/K and $(\partial G/\partial T)_{P0} = -0.0150$ (4) GPa/K) by Higo et al. (2008), and previous high *P-T* XRD experiments up to 21 GPa 1273 K ($(\partial Ks/\partial T)_{P0} = -0.008$ (5) GPa/K calculated from $(\partial K_T/\partial T)_{P0} = -0.015$ (5) GPa/K using Equation S24) by Nishihara et al. (2004) (Table IV.S4).

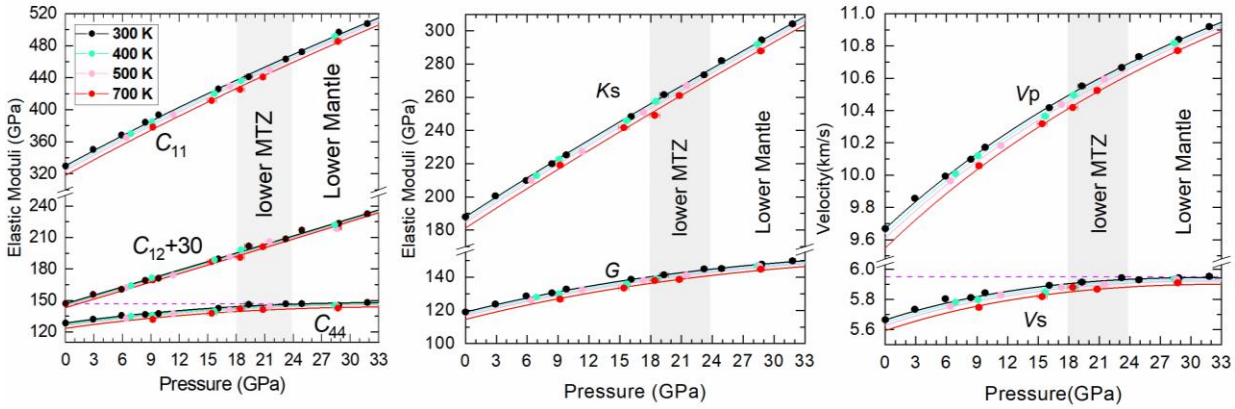

Fig. IV.1. *C_{11}, C_{12}, C_{44}, Ks, G, Vp, and Vs of the Fe-bearing anhydrous ringwoodite measured in this study as a function of P along 300 K, 400 K, 500 K, 700 K isotherms (error bars are behind symbols). VRH averaging scheme is used to calculate the Ks, G, Vp, and Vs of the isotropic polycrystalline ringwoodite. Solid lines represent 4^{th} order finite strain EOS fitting results. The dashed, horizontal purple lines indicate that the P-induced increases of C_{44} and Vs are negligible above 23 GPa.*

3.2. Intrinsic anisotropy of ringwoodite

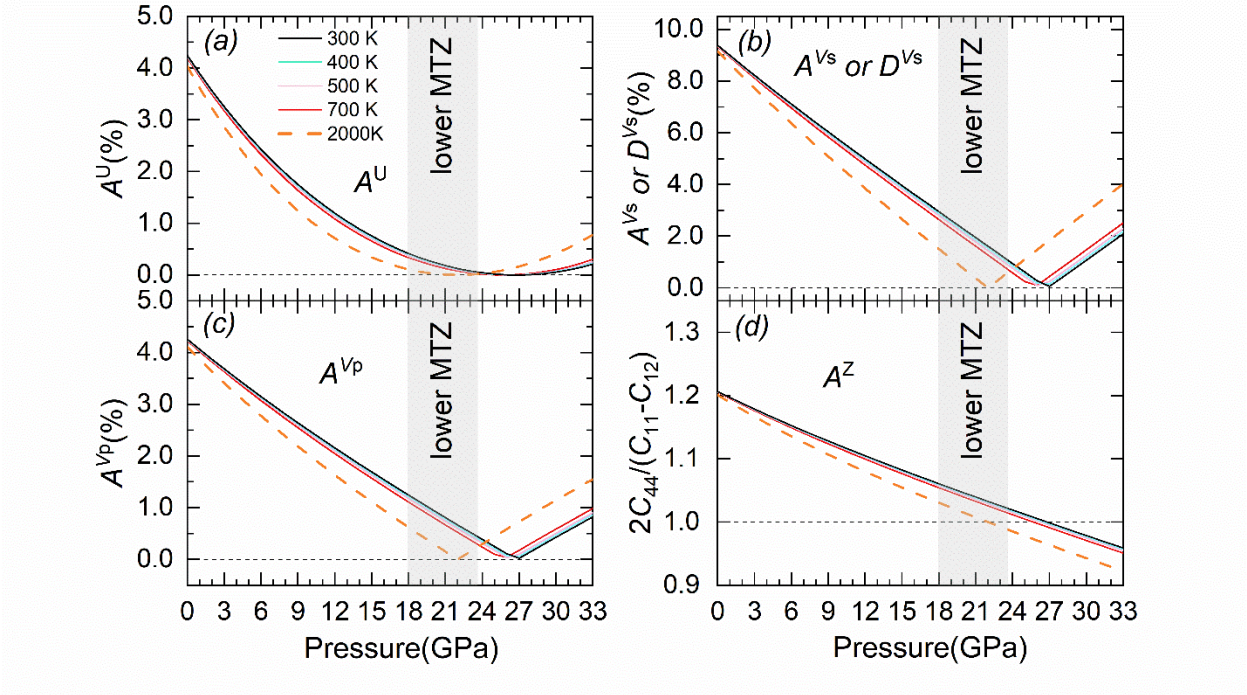

Fig. IV.2. Universal anisotropy (a), acoustic velocity anisotropy (b, c), and Zener anisotropy (d) of the Fe-bearing ringwoodite measured in this study as a function of pressure along different temperature isotherms.

Based on the *P-T* dependence of the C_{ij}s measured in this study (Table IV.S2), we calculated ringwoodite's intrinsic anisotropy indices under high *P-T* conditions (Fig. IV.2). A total of 5 elastic anisotropy indices are used: universal anisotropy (A^U), Zener anisotropy (A^Z), *V*p azimuthal anisotropy (A^{Vp}), *V*s azimuthal anisotropy (A^{Vs}), and *V*s radial anisotropy (D^{Vs}) (see Equations S25-S29 and references in the Supplementary Information). For ringwoodite, due to its cubic symmetry, its A^{Vs} is equal to D^{Vs} (Fig. IV.2b).

The most prominent feature in Fig. IV.2 is that the intrinsic anisotropy of ringwoodite decreases significantly with pressure down to the bottom of the MTZ and then increases with pressure again. The increases of A^U, A^{Vp}, A^{Vs} and D^{Vs} above a certain threshold (e.g., ~27 GPa at 300 K) are the consequence of the switch between the acoustically fastest and the slowest

crystallographic directions in ringwoodite, which is characterized by the decrease of A^Z below 1 (Fig. IV.2d, Table IV.S5). Temperature also decreases the intrinsic anisotropy of Fe-bearing ringwoodite at the MTZ pressures, similar to Fe-free ringwoodite as suggested by previous first-principles calculations (Li et al., 2006). Previous studies suggested that the intrinsic elastic anisotropy of ringwoodite is small (e.g., Wang et al., 2006; Schulze et al., 2018). At lower MTZ conditions, our study suggests that Fe-bearing ringwoodite is elastically almost isotropic with all 4 elastic anisotropy indices approaching 0. Note, these values represent the maximum possible seismic anisotropy that can be induced by the lattice preferred orientations (LPO) of ringwoodite. The realistic seismic anisotropy induced by LPO of ringwoodite would be significantly less, thus any observed seismic anisotropy in the lower MTZ (e.g., Zhang et al., 2021) is unlikely to be caused by the presence of ringwoodite. Minerals with significantly higher elastic anisotropy (e.g., akimotoite, stishovite, metastable olivine) or shape-preferred orientation of rheologically/elastically weak minerals melts are the more possible explanations for the observed seismic anisotropy in the MTZ (Zhou et al., 2021 and references in Zhou et al., 2021).

4. Discussion and Implications

4.1. Effects of Fe#, water, and temperature on velocity and impedance jumps of the 520

Based on the experimental data of ringwoodite measured in this study and previous studies (Fig. IV.S5A), we modeled the effects of water content and Fe# on the elasticity of ringwoodite under high *P-T* conditions (Table IV.S3). Combined with a previous composition-dependent elasticity model of wadsleyite under high *P-T* conditions (Zhou et al., 2020; 2021), we evaluated the effects of Fe#, water, and temperature on the velocity and impedance jumps across the wadsleyite to ringwoodite transition in pure $(Mg,Fe)_2SiO_4$ system (Figs. 3, 4). In the Earth's mantle, these jumps would be smaller considering the dilution effect due to the coexistence of garnet. Assuming the Earth's mantle is pyrolitic with ~53 vol% olivine, based on the phase equilibrium

experiments by Ishii et al. (2018), the 520 for a pyrolitic MTZ is characterized by ~2% *V*p and *V*s velocity jumps as well as ~3% *V*p and *V*s impedance jumps with a theoretical thickness of 0 km. Our results agree with the globally estimated ~3% *V*p and *V*s impedance contrasts across the 520 of using SS precursors by Shearer et al. (1990). It is worth noting that, for SS precursors studies, a strong trade-off exists between the impedance contrast and sharpness of the 520. As pointed by Tian et al. (2020), a 0-km thick 520 with *V*s impedance contrast of 2.4% can result in the same waveform as a 30-km wide 520 with 4.4% *V*s impedance contrast.

4.1.1. Effects of Fe# and water on Vp and Vs jumps at the 520

The effects of Fe# and water on the velocity jumps across wadsleyite-ringwoodite transition are shown in Fig. IV.3. Increasing Fe# reduces the *V*p jump. Fe increases the $(\partial K_S/\partial P)_{T0}$ of wadsleyite (Buchen et al., 2017; Zhou et al., 2021), whereas the $(\partial K_S/\partial P)_{T0}$ of ringwoodite is not sensitive to Fe# (Higo et al., 2006). The *K*s of wadsleyite approaches that of ringwoodite with increasing Fe# in both wadsleyite and ringwoodite. Interestingly, the *V*s jump is less sensitive to Fe (Fig. IV.3), because the effect of Fe on *V*s jump is controlled by 2 competing factors. On the one hand, wadsleyite's V_S and *G* are more sensitive to Fe compared with ringwoodite (e.g., adding 1 mol% of Fe decreases wadsleyite's G_0 by 0.5% and ringwoodite's G_0 by only 0.2%), and thus, adding the same amount of Fe in wadsleyite and ringwoodite could enhance the *V*s jump. On the other hand, Fe# of ringwoodite is larger than Fe# of wadsleyite under equilibrated mantle condition considering Fe preferentially partitions into ringwoodite (e.g. 2 mol% of Fe in ringwoodite corresponds to ~1.2 mol% Fe in wadsleyite) (Tsujino et al., 2019), increasing Fe# in the MTZ could reduce the *V*s jump across the wadsleyite-ringwoodite transition.

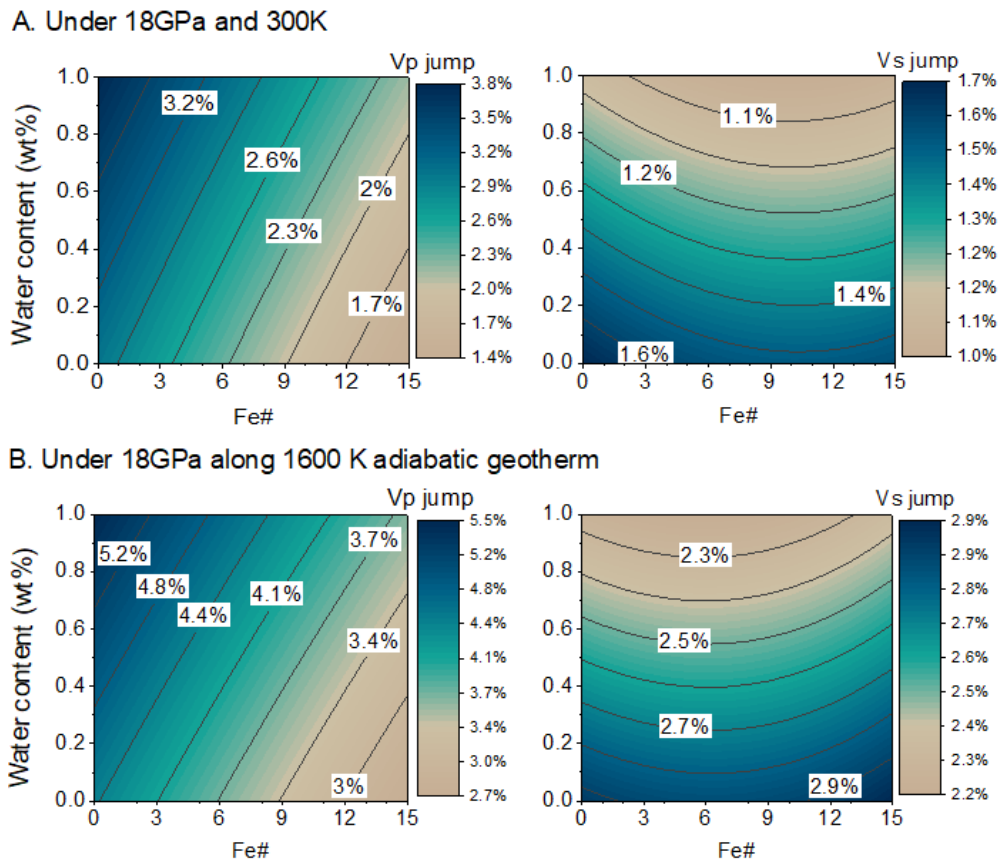

Fig. IV.3. *Effects of Fe# and water on the Vp and Vs jumps (Equation 1) across the wadsleyite-ringwoodite transition in pure* $(Mg, Fe)_2SiO_4$ *system. The horizontal axis is the Fe# in ringwoodite* ($Fe\#_{ring}$), *the corresponding Fe# in wadsleyite is* $\frac{60Fe\#_{ring}}{(100-0.4Fe\#_{ring})}$ *according to the Fe partitioning coefficient of 0.6 between wadsleyite and ringwoodite (Tsujino et al., 2019). The vertical axis is the water content in ringwoodite, 1 wt% of water in ringwoodite corresponds to 2 wt% of water in wadsleyite based on the water partitioning coefficient of 2 between wadsleyite and ringwoodite (Inoue et al., 2010).*

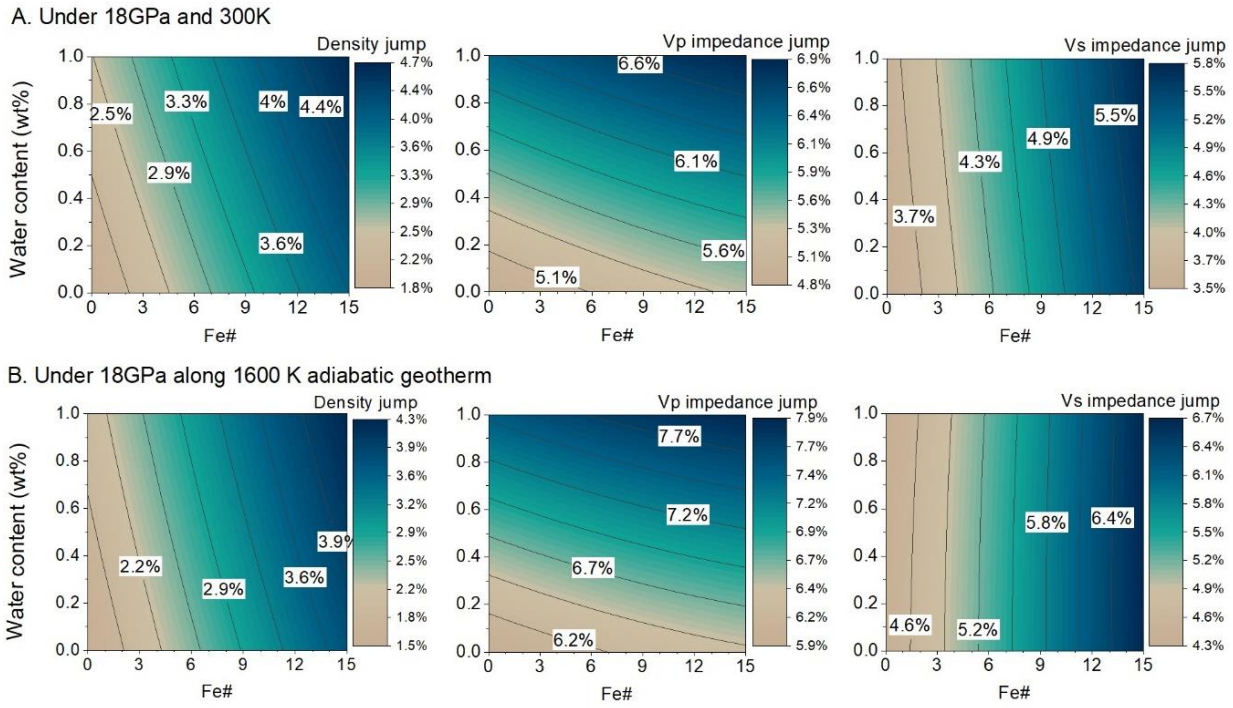

Fig. IV.4. *Effects of Fe# and water on density, Vp impedance contrast and Vs impedance contrast (Equation 1) across wadsleyite-ringwoodite transition in pure (Mg, Fe)$_2$SiO$_4$ system. The horizontal axis is the Fe# in ringwoodite ($Fe\#_{ring}$), the corresponding Fe# in wadsleyite is:* $Fe\#_{wad} = \frac{60Fe\#_{ring}}{(100-0.4Fe\#_{ring})}$ *based on the average Fe partitioning coefficient of 0.6 between wadsleyite and ringwoodite (Tsujino et al., 2019). The vertical axis is the water content in ringwoodite. 1 wt% of water in ringwoodite corresponds to 2 wt% of water in wadsleyite based on the water partitioning coefficient of 2 between wadsleyite and ringwoodite (Inoue et al., 2010).*

Sinogeikin et al. (2003) suggested that higher Fe content will increase both the *V*p and *V*s jumps across the 520 primarily based on the elasticity measurements at ambient condition, whereas Núñez-Valdez et al. (2011) suggested the opposite based on first-principles calculations. Our results (the *V*p jump is reduced by Fe whereas the *V*s jump is almost insensitive to Fe) are in partial agreement with both studies. Sinogeikin et al. (2003) assumed that Fe does not affect $(\partial Ks/\partial P)_{T0}$ of wadsleyite while our calculation adopted the relationship that was determined in Zhou et al.

(2021), which suggested that adding 1 mol% Fe increases the $(\partial Ks/\partial P)_{T0}$ of wadsleyite by 1.3%. This relationship is in agreement with Buchen et al. (2017) which also found that Fe increases the $(\partial K_T/\partial P)_{T0}$ of wadsleyite. On the other hand, Núñez-Valdez et al. (2011) suggested Fe of ringwoodite decreases its $(\partial G/\partial P)_{T0}$ and finally decreases *V*s jump at the 520, while our result (Table IV.2) shows that Fe has no resolvable effect on $(\partial G/\partial P)_{T0}$ of ringwoodite. Our result, in terms of the Fe effect on the $(\partial G/\partial P)_{T0}$ and $(\partial K_T/\partial P)_{T0}$ of ringwoodite, is consistent with Higo et al. (2006).

Table IV.2. *Comparison of the effects of water content and Fe# on the elastic properties of wadsleyite (Zhou et al., 2020; 2021) and ringwoodite (this study).*

	Wadsleyite		**Ringwoodite**	
	Increase Fe# by 1	**Add 1 wt% water**	**Increase Fe# by 1**	**Add 1 wt% water**
K_{S0}	\	↓ by 4%	↑ by 0.1%	↓ by 5%
$(\partial K_S/\partial P)_{T0}$	↑ by 1.3%	\	\	↑ by 5%
$(\partial K_S/\partial T)_{P0}$	\	\	\	\
G_0	↓ by 0.5%	↓ by 5%	↓ by 0.1%	↓ by 5%
$(\partial G/\partial P)_{T0}$	\	↑ by 10%	\	↑ by 7%
$(\partial^2 G/\partial P^2)_{T0}$	\	\	\	\
$(\partial G/\partial T)_{P0}$	\	\	\	\

In contrast to the effect of Fe, higher water content increases *V*p jump across the wadsleyite to ringwoodite transition at the 520. Higher water content increases $(\partial K\text{s}/\partial P)_{T0}$ of ringwoodite (Jacobsen and Smyth, 2006), whereas $(\partial K\text{s}/\partial P)_{T0}$ of wadsleyite is not sensitive to water content (Table IV.2). Thus, the difference between the *V*p of ringwoodite and wadsleyite increases with water content (Fig. IV.3). On the other hand, water reduces the *V*s jump across the wadsleyite to ringwoodite transition. Adding 1 wt% water into the crystal structures increases $(\partial G/\partial P)_{T0}$ of wadsleyite and ringwoodite by 10% and 7%, respectively (Table IV.2). Moreover, considering the water preferably partitions into wadsleyite than ringwoodite (Inoue et al., 2010), incorporating twice as much water in wadsleyite than ringwoodite would results in an even higher $(\partial G/\partial P)_{T0}$ of the hydrous wadsleyite coexisting with the hydrous ringwoodite near the 520. As a result, wadsleyite's *G* or *V*s approaches those of ringwoodite at 18 GPa with increasing water content in the MTZ.

4.1.2. Effects of Fe# and water on Vp and Vs impedance jumps at the 520

The density and impedance jumps across the wadsleyite-ringwoodite transition at the 520 are shown in Fig. IV.4. Fe increases the densities of both ringwoodite and wadsleyite, but the density of ringwoodite is more sensitive to Fe. Moreover, Fe preferentially partitions into ringwoodite compared with wadsleyite (Tsujino et al., 2019). Thus, increasing Fe# of the MTZ increases the density jump across the wadsleyite to ringwoodite transition (Fig. IV.4). Similarly, increasing water content in the MTZ would result in an increase of the density jump at the 520, because water preferentially partitions into wadsleyite rather than ringwoodite and water decreases densities of both ringwoodite and wadsleyite (Inoue et al., 2010). Due to the influence of density, *V*p impedance contrast is more sensitive to water and less sensitive to Fe compared with *V*p jump, whereas *V*s impedance contrast is much more sensitive to Fe and less sensitive to water compared with *V*s jump (Figs. 3, 4).

4.1.3. Effect of temperature on the 520

To understand the influence of temperature on the 520, we calculated the velocity jumps and impedance contrasts across the wadsleyite to ringwoodite transition at 18 GPa along a 1600 K adiabat (Katsura et al., 2010) and compared with the results at 18 GPa and 300 K (Figs. 3, 4). Temperature strongly enhances all velocity jumps while it decreases density jump, and thus, temperature only weakly enhances the impedance (density*velocity) contrasts across the wadsleyite to ringwoodite. Our results are different from the first-principles calculation studies in the Fe-free system (Yonggang et al., 2008; Panero et al., 2010). Yonggang et al. (2008) suggested that temperature has a negligible effect on the 520 impedance contrasts, whereas Panero (2010) suggests that temperature decreases the 520 impedance contrasts for Fe-free olivine polymorphs.

In summary, Fe, water, and temperature have different effects on *V*p and *V*s jumps across the wadsleyite-ringwoodite transformation at the 520. Fe decreases the *V*p jump and is insensitive to the *V*s jump. Water increases the *V*p jump yet decreases the *V*s jump. Temperature increases both *V*p and *V*s jumps. The mineral physics modeling in this study suggests that lateral changes in chemical composition and temperature in the MTZ can help explain the global variations of the 520. In addition, our findings have potential applications in estimating water content in the MTZ. For example, in a hydrated MTZ, we would expect a slightly higher *V*p jump with a reduced *V*s jump across the 520. However, the hydration effect needs to be used with caution, since local variation of Fe# could also influence the observed magnitude of the 520.

4.2. Metastable olivine and metastable ringwoodite

Due to the transition kinetics, metastable olivine and ringwoodite may survive at depths greater than 410 km and 660 km, respectively, under *P-T* conditions in cold subduction zones (Hosoya et al., 2005). A metastable olivine wedge has been reported beneath the Japan Sea at ~410-560 km depth range based on waveform modeling of the P-wave coda (e.g., Kaneshima et

al., 2007), forward travel time modeling (e.g., Jiang et al., 2008), receiver functions (Kawakatsu and Yoshioka, 2011), and inter-source interferometry (Shen and Zhan, 2020). Kaneshima et al. (2007), Jiang et al. (2008), and Shen and Zhan (2020) all suggested that *V*p of the metastable olivine wedge beneath the Japan Sea is ~3% slower than the ambient mantle and ~5% slower than the surrounding slabs at 410-560 km. If this subducting slab remains relatively cold at the bottom of the MTZ (e.g., < 973 K, Inoue et al., 2004; Bina et al., 2000), metastable ringwoodite may exist in the form of a low velocity wedge near the slab core extending from ~660 km to greater depth in the lower mantle (Liu et al., 2018), similar to the metastable olivine wedge in the MTZ. However, whether these wedge-shape slow anomaly caused by ringwoodite can be observed seismically remains unknown.

In this study, we modeled the seismic anomalies that are induced by metastable olivine and possibly metastable ringwoodite in the Pacific slab subducting underneath the Japan Sea and the eastern China using the mineral physics data in this study and previous study (Zhang and Bass, 2016). The velocity structure of an ambient mantle is represented by the global seismic model AK135 (Kennett et al., 1995). The Pacific subducting slab reaches the MTZ depths under the Japan Sea, and penetrates through the 660 beneath the eastern China (Tao et al., 2008). Therefore, the velocity structure of the Pacific subducting slab at 410-560 km depth is illustrated by the local seismic model under the Japan Sea (36°-42° latitude and 130°-140° longitude), whereas the local seismic model under the eastern China was used to show the slab's velocity structure at 660-800 km depth (30°-40° latitude and 115°-125°). We calculated *V*p and *V*s of anhydrous olivine (Fe#=9.5, Zhang and Bass, 2016) along an 873 K isotherm as well as the *V*p and *V*s of anhydrous ringwoodite (Fe#=9.6, this study) along a 973 K isotherm (Fig. IV.5). The metastable olivine and ringwoodite are assumed to be anhydrous. Ishii et al. (2021) suggested that water strongly

partitions into the high-pressure hydrous minerals (such as hydrous phase A) in wet subducting slabs, thus the nominally anhydrous olivine and its high-pressure polymorphs are nearly dry. We choose the 873 K isotherm for metastable olivine and the 973 K isotherm for metastable ringwoodite for the following reasons. Hosoya et al. (2005) suggested that at 873K, nearly dry olivine (500 ppm water) could metastably exist down to the depth of ~ 650 km in the Earth's interior based on in-situ XRD DAC experiments. At 1 atm, anhydrous ringwoodite would not transform back to olivine until the temperature reaches 973 K (Inoue et al., 2004). At much higher pressures in the Earth's interior, the decomposition of ringwoodite into bridgmanite + ferropericlase is thus unlikely to take place as long as the temperature remains lower than 973 K. It is possible that olivine and ringwoodite can metastably survive at even higher temperature inside the Earth, thus 873 K and 973 K are conservative estimates of the temperatures that metastable olivine and ringwoodite can exist at depths greater than 410 km and 660 km, respectively. In addition, 873 K and 973 K are consistent with the modeled core temperature of the western Pacific subducting slabs in the MTZ (700-973 K) (Bina et al., 2000; Kawakatsu and Yoshioka, 2011; Ishii and Ohtani, 2021).

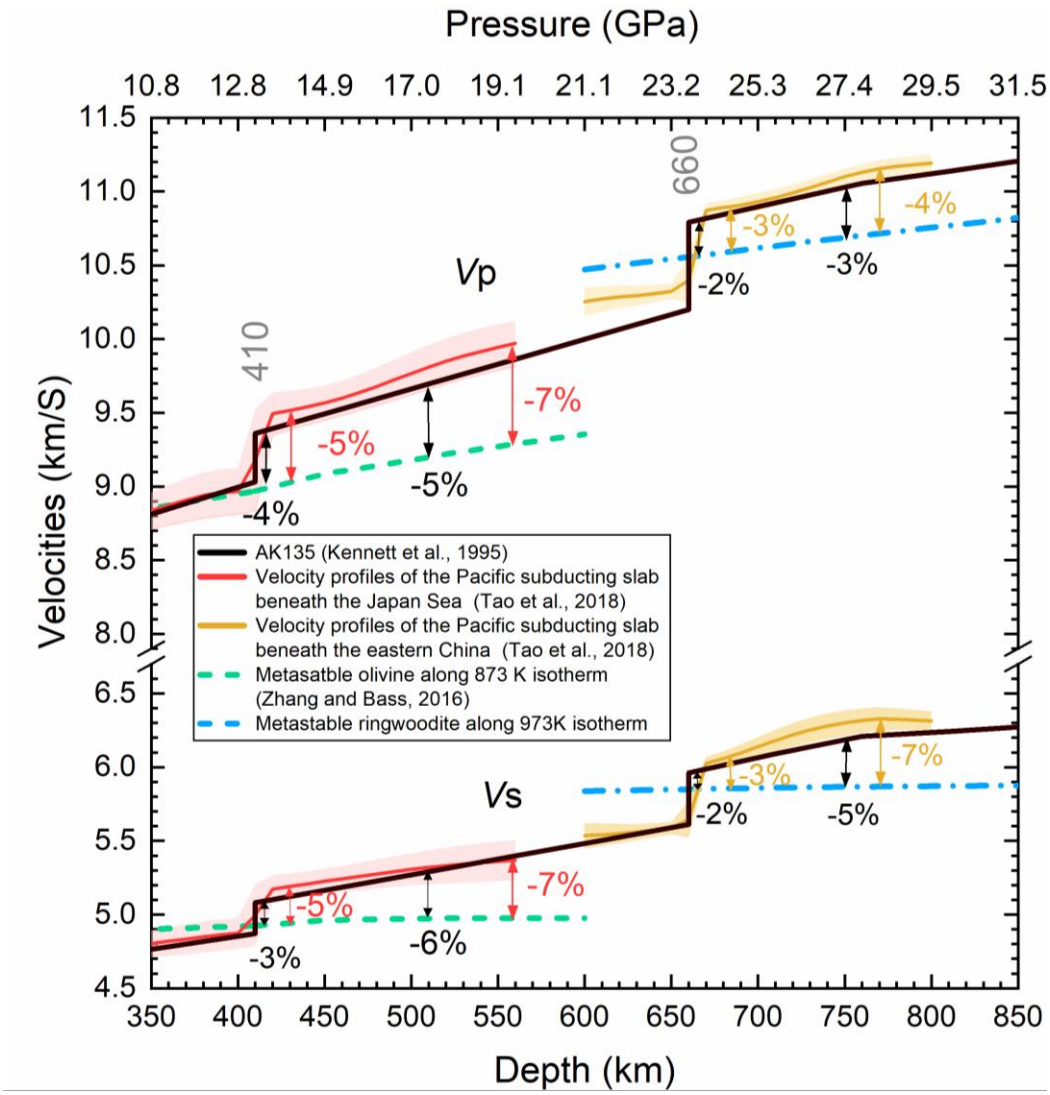

Figure IV.5. *Negative velocity anomaly caused by metastable olivine and ringwoodite compared with an ambient mantle (AK135) and the Pacific subducting slab beneath the Japan Sea and the eastern China, respectively. The shaded areas denote the standard deviations of Vp and Vs from the averaged velocities of the Pacific subducting slab under the Japan Sea and the eastern China. The velocity profiles of the Pacific subducting slab as a function of depth are based on the tomography study by Tao et al. (2018). They only represent the averaged velocity profiles of the slab, the thin metastable olivine or ringwoodite wedges inside the slab could not be resolved by seismic tomography in Tao et al. (2018).*

As shown in Fig. IV.5, the *V*p of olivine is about 5% lower than the ambient mantle (AK135) and 5-7% lower than the surrounding slabs under the Japan Sea at 410-560 km depths. These values are consistent with the observed *V*p anomalies of the metastable olivine wedge (~3% lower than the ambient mantle, ~5% lower than the nearby slabs) beneath the Japan Sea at 410-560 km depths considering that the lithospheric mantle of the subducting slabs contains ~60-80 vol % olivine (Shen and Zhan, 2020).

Whether metastable ringwoodite could cause seismically detectable low velocity regions at 660-700 km depends on both the volume of metastable ringwoodite in slabs and the velocity contrast between the metastable ringwoodite and mantle nearby. At the depth between 660-700 km, metastable ringwoodite is only ~2-3% slower than the ambient mantle (AK135) and the Pacific subducting slab beneath the eastern China. Considering the dilution effect caused by the coexistence of majoritic garnet (20-40 vol% garnet) in the subducted lithosphere, metastable ringwoodite wedge would only result in ~1-2% low velocity anomaly at the depth of 660-700 km, which may not be detectable.

However, metastable ringwoodite, if it exists, could produce a stronger negative *V*s anomaly at greater depth due to the minimal increase of *V*s with pressure at lower mantle conditions. For example, *V*s of metastable ringwoodite would be ~5% slower than the ambient mantle (AK135) and ~7% slower than the Pacific subducting slab if it can reach ~750 km depth. Whether it is detectable also depends on the volume of metastable ringwoodite wedge in the subducting slabs. Kawakatsu and Yoshioka (2011) modeled the temperature distributions of the Pacific subducting slab stagnant at the 660 under Japan Sea. They found that the layer with $T <$ 973 K near the core of the slab is <5 km thick at the 660. This layer might get thinner after it reaches even greater depth, making metastable ringwoodite wedge too thin to be resolved

seismically although it carries a strong negative *V*s anomaly at ~750 km. In comparison, the metastable olivine wedge in the subducting slab beneath the Japan Sea is observed to be ~30-50 km wide at 410 km depth, making it easier to resolve with seismic imaging (Jiang et al., 2008; Kawakatsu and Yoshioka, 2011; Shen and Zhan, 2020). If ringwoodite can metastably exist at slightly higher temperature at depths greater than 660 km, for example, 1173 K, then the thickness of the metastable ringwoodite wedge could reach ~25-30 km, making it more likely to be detected. Alternatively, if the slab folds and buckles near the 660, and thus has a thick cold core (e.g., Marianas region, Li et al., 2019), the layer enriched in metastable ringwoodite might also become seismically detectable as the low velocity layers near the top of the lower mantle.

In summary, different from a metastable olivine wedge, which carries a stronger seismic velocity anomaly, a metastable ringwoodite wedge, if it exists, is more likely to become seismically detectable with stronger *V*s anomaly at depths greater than ~750 km if the cold core of the slab is sufficiently thick. Future studies on the metastability field of ringwoodite under subduction zone *P-T* conditions are needed to better understand the detectability of metastable ringwoodite.

5. Conclusions

(1) We determined the elasticity of anhydrous Fe-bearing single-crystal ringwoodite (Fe# = 9.6) up to 32 GPa and 700K by Brillouin Spectroscopy. The coefficients of the 4th order finite Eulerian strains equations describing the isotropic aggregate bulk and shear moduli of anhydrous ringwoodite (Fe# = 9.6) at high *P-T* conditions are: K_{S0} = 188 (1) GPa, G_0 = 119 (1) GPa, $(\partial K_S/\partial P)_{T0}$ = 4.0 (2), $(\partial^2 K_S/\partial P^2)_{T0}$ = − 0.03 (2) GPa^{-1}, $(\partial G/\partial P)_{T0}$ = 1.56 (7), $(\partial^2 G/\partial P^2)_{T0}$ = − 0.049 (6) GPa^{-1}, $(\partial K_S/\partial T)_{P0}$ = − 0.017 (3) GPa/K, and $(\partial G/\partial T)_{P0}$ = − 0.011 (2) GPa/K.

(2) The intrinsic elastic anisotropy of ringwoodite is approaching 0 at the bottom of the MTZ. Lattice preferred orientation of ringwoodite could not account for the seismic anisotropy observed in the lower MTZ.

(3) Fe, water, and temperature have different effects on *V*p and *V*s jumps across the wadsleyite-ringwoodite transformation. Fe decreases the *V*p jump and is insensitive to the *V*s jump. Water increases the *V*p jump yet decreases the *V*s jump. Temperature increases both *V*p and *V*s jumps. Lateral changes in chemical composition and temperature in the MTZ could help explain the strong global variations of the 520.

(4) We calculated the sound velocity of metastable ringwoodite at depths greater than 660 km. Compared with a metastable olivine wedge in cold subducting slabs, seismic detection of a metastable ringwoodite wedge is challenging due to its smaller velocity contrast and lesser thickness. Future studies on the metastability field of ringwoodite under subduction zone *P*-*T* conditions are needed.

Acknowledgment

We thank Mingqiang Hou for help in sample preparation and Mike Splide for help in Electron Microprobe Analysis experiments at UNM. We thank Ruijia Wang for help in data analysis. We also thank Sergey Tkachev for the gas loading of the DACs at GSECARS, APS, ANL. The use of the gas-loading system is supported by COMPRES, the Consortium for Materials Properties Research in Earth Sciences under NSF Co-operative Agreement EAR 1661511, and GSECARS is funded by NSF (EAR -1634415) and Department of Energy (DOE) – GeoSciences (DE-FG02-94ER14466). This project is supported by NSF-EAR1664471 (J.S.Z and B.S).

References

Bina, C. R., & Navrotsky, A. (2000). Possible presence of high-pressure ice in cold subducting slabs. Nature, 408(6814), 844-847.

Buchen, J., Marquardt, H., Boffa Ballaran, T., Kawazoe, T., & McCammon, C. (2017). The equation of state of wadsleyite solid solutions: Constraining the effects of anisotropy and crystal chemistry. American Mineralogist: Journal of Earth and Planetary Materials, 102(12), 2494-2504.

Caracas, R., & Banigan, E. J. (2009). Elasticity and Raman and infrared spectra of MgAl2O4 spinel from density functional perturbation theory. Physics of the Earth and Planetary Interiors, 174(1-4), 113-121.

Datchi, F., Dewaele, A., Loubeyre, P., Letoullec, R., Le Godec, Y., & Canny, B. (2007). Optical pressure sensors for high-pressure–high-temperature studies in a diamond anvil cell. High Pressure Research, 27(4), 447-463.

Davies, G. Effective elastic moduli under hydrostatic stress—I. quasi-harmonic theory. Journal of Physics and Chemistry of Solids 35, 1513-1520 (1974).

Davies, G. & Dziewonski, A. Homogeneity and constitution of the Earth's lower mantle and outer core. Physics of the Earth and Planetary Interiors 10, 336-343 (1975).

Duffy, T. S. & Anderson, D. L. Seismic velocities in mantle minerals and the mineralogy of the upper mantle. Journal of Geophysical Research: Solid Earth 94, 1895-1912 (1989).

Higo, Y., Inoue, T., Irifune, T., Funakoshi, K. I., & Li, B. (2008). Elastic wave velocities of (Mg0. 91Fe0. 09) 2SiO4 ringwoodite under P–T conditions of the mantle transition region. *Physics of the Earth and Planetary Interiors*, *166*(3-4), 167-174.

Higo, Y., Inoue, T., Li, B., Irifune, T., & Liebermann, R. C. (2006). The effect of iron on the elastic properties of ringwoodite at high pressure. Physics of the Earth and Planetary Interiors, 159(3-4), 276-285.

Hill, R. Elastic properties of reinforced solids: some theoretical principles. Journal of the Mechanics and Physics of Solids 11, 357-372 (1963).

Hosoya, T., Kubo, T., Ohtani, E., Sano, A., & Funakoshi, K. I. (2005). Water controls the fields of metastable olivine in cold subducting slabs. *Geophysical Research Letters*, *32*(17).

Inoue, T., Tanimoto, Y., Irifune, T., Suzuki, T., Fukui, H., & Ohtaka, O. (2004). Thermal expansion of wadsleyite, ringwoodite, hydrous wadsleyite and hydrous ringwoodite. *Physics of the Earth and Planetary Interiors*, *143*, 279-290.

Inoue, T., Wada, T., Sasaki, R., & Yurimoto, H. (2010). Water partitioning in the Earth's mantle. *Physics of the Earth and Planetary Interiors*, *183*(1-2), 245-251.

Ishii, T., Kojitani, H., & Akaogi, M. (2018). Phase relations and mineral chemistry in pyrolitic mantle at 1600–2200° C under pressures up to the uppermost lower mantle: Phase transitions around the 660-km discontinuity and dynamics of upwelling hot plumes. Physics of the Earth and Planetary Interiors, 274, 127-137.

Ishii, T., & Ohtani, E. (2021). Dry metastable olivine and slab deformation in a wet subducting slab. Nature Geoscience, 1-5.

Jackson, J. M., Sinogeikin, S. V., & Bass, J. D. (2000). Sound velocities and elastic properties of γ-Mg2SiO4 to 873 K by Brillouin spectroscopy. *American Mineralogist*, *85*(2), 296-303.

Jacobsen, S.D., & Smyth, J.R., 2006. Effect of water on the sound velocities of ringwoodite in the transition zone. In: Jacobsen, S.D., Lee, S.V.D. (Eds.), Earth's Deep Water Cycle. American Geophysical Union, pp.131–145.

Jiang, G., Zhao, D., & Zhang, G. (2008). Seismic evidence for a metastable olivine wedge in the subducting Pacific slab under Japan Sea. *Earth and Planetary Science Letters*, *270*(3-4), 300-307.

Kantor, I., Prakapenka, V., Kantor, A., Dera, P., Kurnosov, A., Sinogeikin, S., Dubrovinskaia, N., & Dubrovinsky, L., 2012. BX90: A new diamond anvil cell design for X-ray diffraction and optical measurements. Review of Scientific Instruments, 83(12), p.125102.

Kaneshima, S., T. Okamoto, & H. Takenaka (2007), Evidence for a metastable olivine wedge inside the subducted Mariana slab, Earth Planet. Sci. Lett., 258, 219–227.

Katsura, T., Yoneda, A., Yamazaki, D., Yoshino, T., & Ito, E. (2010). Adiabatic temperature profile in the mantle. Physics of the Earth and Planetary Interiors, 183(1-2), 212-218.

Kawakatsu, H., & Yoshioka, S. (2011). Metastable olivine wedge and deep dry cold slab beneath southwest Japan. Earth and Planetary Science Letters, 303(1-2), 1-10.

Kelbert, A., Schultz, A., & Egbert, G. (2009). Global electromagnetic induction constraints on transition-zone water content variations. *Nature*, *460*(7258), 1003-1006.

Kennett, B. L., Engdahl, E. R., & Buland, R. (1995). Constraints on seismic velocities in the Earth from traveltimes. Geophysical Journal International, 122(1), 108-124.

Lai, X., Zhu, F., Zhang, J. S., Zhang, D., Tkachev, S., Prakapenka, V. B., Chen, B. (2020). An Externally-Heated Diamond Anvil Cell for Synthesis and Single-Crystal Elasticity Determination of Ice-VII at High Pressure-Temperature Conditions. J. Vis. Exp. (160), e61389.

Lebedev, S., Chevrot, S., & Van der Hilst, R. D. (2003). Correlation between the shear-speed structure and thickness of the mantle transition zone. Physics of the Earth and Planetary Interiors, 136(1-2), 25-40.

Li, L., Weidner, D.J., Brodholt, J., Alfe, D., & Price, G.D., 2006. Elasticity of Mg2SiO4 ringwoodite at mantle conditions. Physics of the Earth and Planetary Interiors, 157(3-4), pp.181-187.

Li, Z.-H., Gerya, T. & Connolly, J. A. Variability of subducting slab morphologies in the mantle transition zone: Insight from petrological-thermomechanical modeling. Earth-Science Reviews 196, 102874 (2019).

Liu, Z., Park, J., & Karato, S. I. (2018). Seismic evidence for water transport out of the mantle transition zone beneath the European Alps. Earth and Planetary Science Letters, 482, 93-104.

Mao, Z., Lin, J. F., Jacobsen, S. D., Duffy, T. S., Chang, Y. Y., Smyth, J. R., ... & Prakapenka, V. B. (2012). Sound velocities of hydrous ringwoodite to 16 GPa and 673 K. *Earth and Planetary Science Letters*, *331*, 112-119.

Nishihara, Y., Takahashi, E., Matsukage, K. N., Iguchi, T., Nakayama, K., & Funakoshi, K. I. (2004). Thermal equation of state of (Mg0. 91Fe0. 09) 2SiO4 ringwoodite. Physics of the Earth and Planetary Interiors, 143, 33-46.

Núñez-Valdez, M., Da Silveira, P., & Wentzcovitch, R. M. (2011). Influence of iron on the elastic properties of wadsleyite and ringwoodite. *Journal of Geophysical Research: Solid Earth*, *116*(B12).

Panero, W. R. (2010). First principles determination of the structure and elasticity of hydrous ringwoodite. Journal of Geophysical Research: Solid Earth, 115(B3).

Ringwood, A. E. (1991). Phase transformations and their bearing on the constitution and dynamics of the mantle. Geochimica et Cosmochimica Acta, 55(8), 2083-2110.

Schulze, K., Marquardt, H., Kawazoe, T., Ballaran, T. B., McCammon, C., Koch-Müller, M., ... & Marquardt, K. (2018). Seismically invisible water in Earth's transition zone?. *Earth and Planetary Science Letters*, *498*, 9-16.

Shearer, P.M., 1990. Seismic imaging of upper-mantle structure with new evidence for a 520-km discontinuity. Nature344, 121–126.

Shen, G., Wang, Y., Dewaele, A., Wu, C., Fratanduono, D.E., Eggert, J., Klotz, S., Dziubek, K.F., Loubeyre, P., Fat'yanov, O.V., & Asimow, P.D., 2020. Toward an international practical pressure scale: A proposal for an IPPS ruby gauge (IPPS-Ruby2020). High Pressure Research, 40(3), pp.299-314.

Shen, Z., & Zhan, Z. (2020). Metastable olivine wedge beneath the Japan Sea imaged by seismic interferometry. *Geophysical Research Letters*, *47*(6), e2019GL085665.

Sinogeikin, S. V., Bass, J. D., & Katsura, T. (2003). Single-crystal elasticity of ringwoodite to high pressures and high temperatures: implications for 520 km seismic discontinuity. *Physics of the Earth and Planetary Interiors*, *136*(1-2), 41-66.

Tao K., Grand S. P., & Niu F. N. (2018), Seismic structure of the upper mantle beneath Eastern Asia from full waveform seismic tomography, Geochemistry, Geophysics, Geosystems.

Tian, D., Lv, M., Wei, S. S., Dorfman, S. M., & Shearer, P. M. (2020). Global variations of Earth's 520- and 560-km discontinuities. Earth and Planetary Science Letters, 552, 116600.

Tsujino, N., Yoshino, T., Yamazaki, D., Sakurai, M., Sun, W., Xu, F., Tange, Y., & Higo, Y., 2019. Phase transition of wadsleyite-ringwoodite in the Mg2SiO4-Fe2SiO4 system. American Mineralogist: Journal of Earth and Planetary Materials, 104(4), pp.588-594.588-594.

Wang, J., Sinogeikin, S. V., Inoue, T., & Bass, J. D. (2006). Elastic properties of hydrous ringwoodite at high-pressure conditions. Geophysical Research Letters, 33(14).

Wang, W., Zhang, H., Brodholt, J. P. & Wu, Z. Elasticity of hydrous ringwoodite at mantle conditions: Implication for water distribution in the lowermost mantle transition zone. Earth and Planetary Science Letters 554, 116626 (2021).

Yonggang, G. Y., Wu, Z., & Wentzcovitch, R. M. (2008). α–β–γ transformations in Mg2SiO4 in Earth's transition zone. Earth and Planetary Science Letters, 273(1-2), 115-122.

Zhang, J. S., & Bass, J. D. (2016). Sound velocities of olivine at high pressures and temperatures and the composition of Earth's upper mantle. Geophysical Research Letters, 43(18), 9611-9618.

Zhang, J. S., Bass, J. D. & Zhu, G. (2015). Single-crystal Brillouin spectroscopy with CO2 laser heating and variable q. *Review of Scientific Instruments* **86**, 063905.

Zhang, H., Schmandt, B., & Zhang, J. S. (2021). Localized anisotropy in the mantle transition zone due to flow through slab gaps. Geophysical Research Letters, 48(10), e2021GL092712.

Zhou, W.Y., Hao, M., Ohuchi, T., Chen, B., Miyagi, L. M., Schmandt, B., & Zhang, J.S. (2020). Anisotropy of the Upper Mantle Transition Zone constrained from the first experimentally determined high temperature-pressure single-crystal elasticity data of wadsleyite. In AGU Fall Meeting Abstracts (Vol. 2020, pp. DI030-07).

Zhou, W.Y., Ren, Z., Zhang, J.S., Chen, B., Hao, M., Ohuchi, T., Miyagi, L., Zhang, D., Alp, E.E., Lavina, B., & Schmandt, B., 2021. The Water-Fe-Pressure dependent single-crystal elastic properties of wadsleyite: Implications for the seismic anisotropy in the upper Mantle Transition Zone. Earth and Planetary Science Letters, 565, p.116955.

Supplementary Information

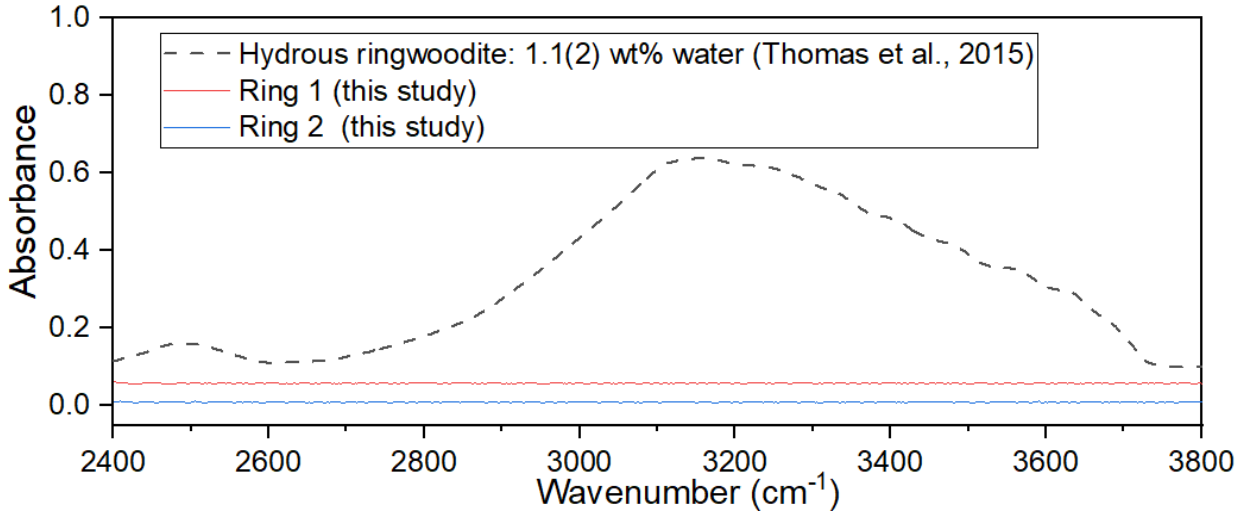

Fig. IV.S1. *Typical FTIR spectra of the synthetic anhydrous ringwoodite samples in this study. Another unpolarized FTIR spectrum for hydrous ringwoodite was also shown for comparison (Thomas et al., 2015). Absorbance is normalized to 50 μm thickness and curves are shifted vertically for clarity.*

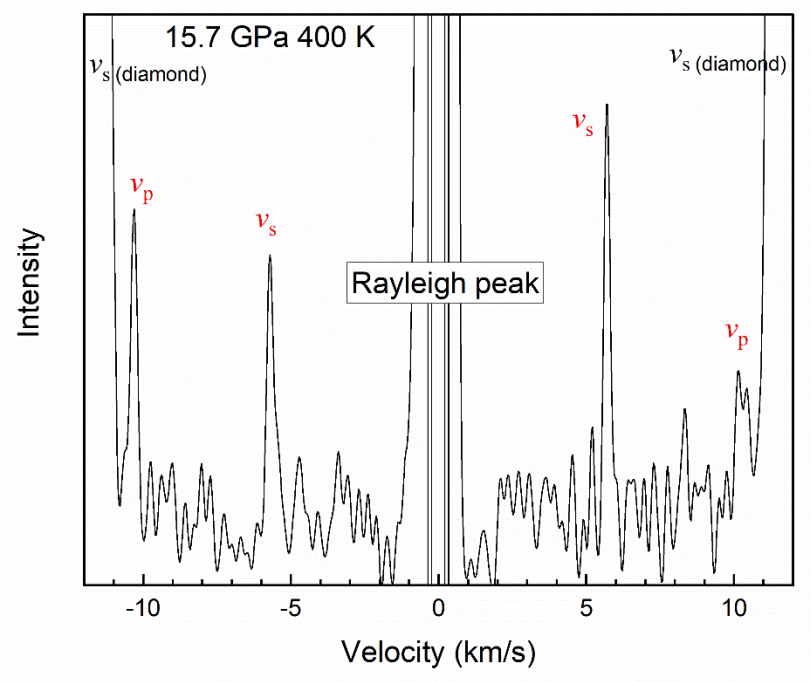

Fig. IV.S2. *A typical Brillouin spectrum collected at 15.7 (4) GPa and 400K for ~15 minutes. Ne peaks are not visible at this P-T condition.*

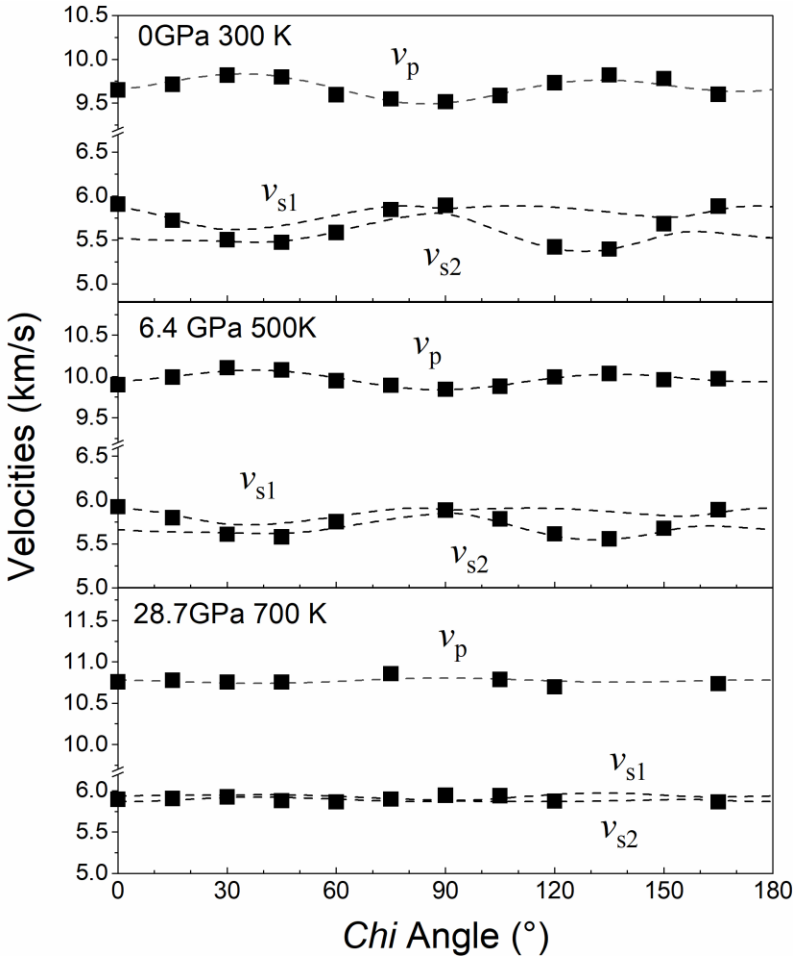

Fig. IV.S3. *Measured acoustic velocities of ringwoodite as a function of laboratory Chi angles under 3 different P-T conditions. Dashed lines are the acoustic velocities calculated from the best-fit single-crystal elasticity model; squares are the experimentally determined velocities. Errors are within the size of the symbols.*

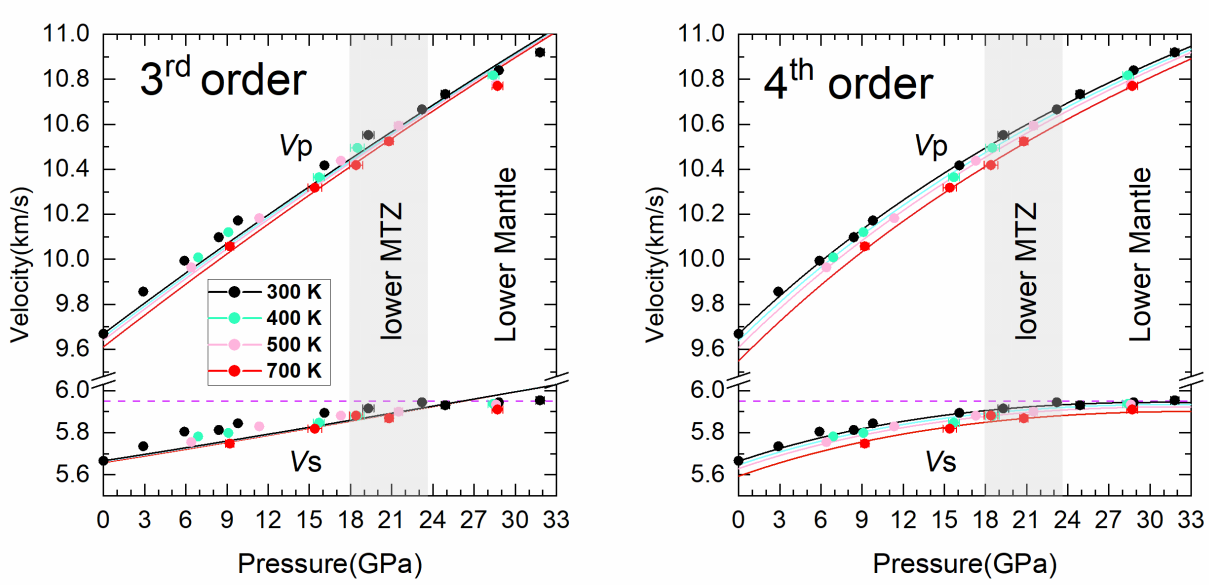

Fig. IV.S4. *3rd and 4th order finite strain EOS fitting results for isotropic aggregate elastic properties of ringwoodite. The RMS error is 12 m/s when using the 4th order finite strain EOS, and 44 m/s when using the 3rd order finite strain EOS. Lines: best-fit model; symbols: experimental data collected in this study.*

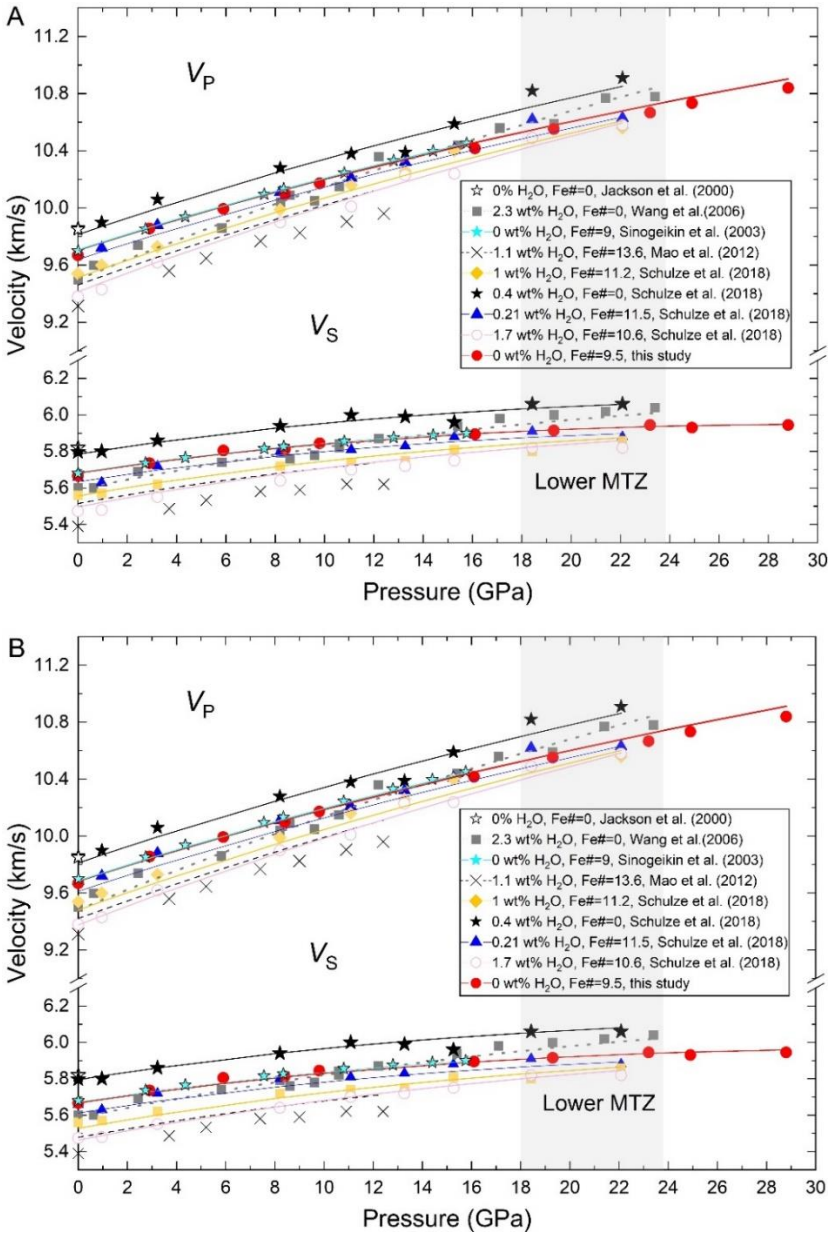

Fig. IV.S5. *Vp and Vs of ringwoodite at high-pressure room-temperature conditions in this and previous studies. Symbols represent sound velocities of different ringwoodite samples measured at 300 K in previous studies and this study. A) Lines represent the modeling results without data from Mao et al. (2012). B) Lines represent the modeling results based on all previous Brillouin spectroscopy data after 2000 including Mao et al. (2012).*

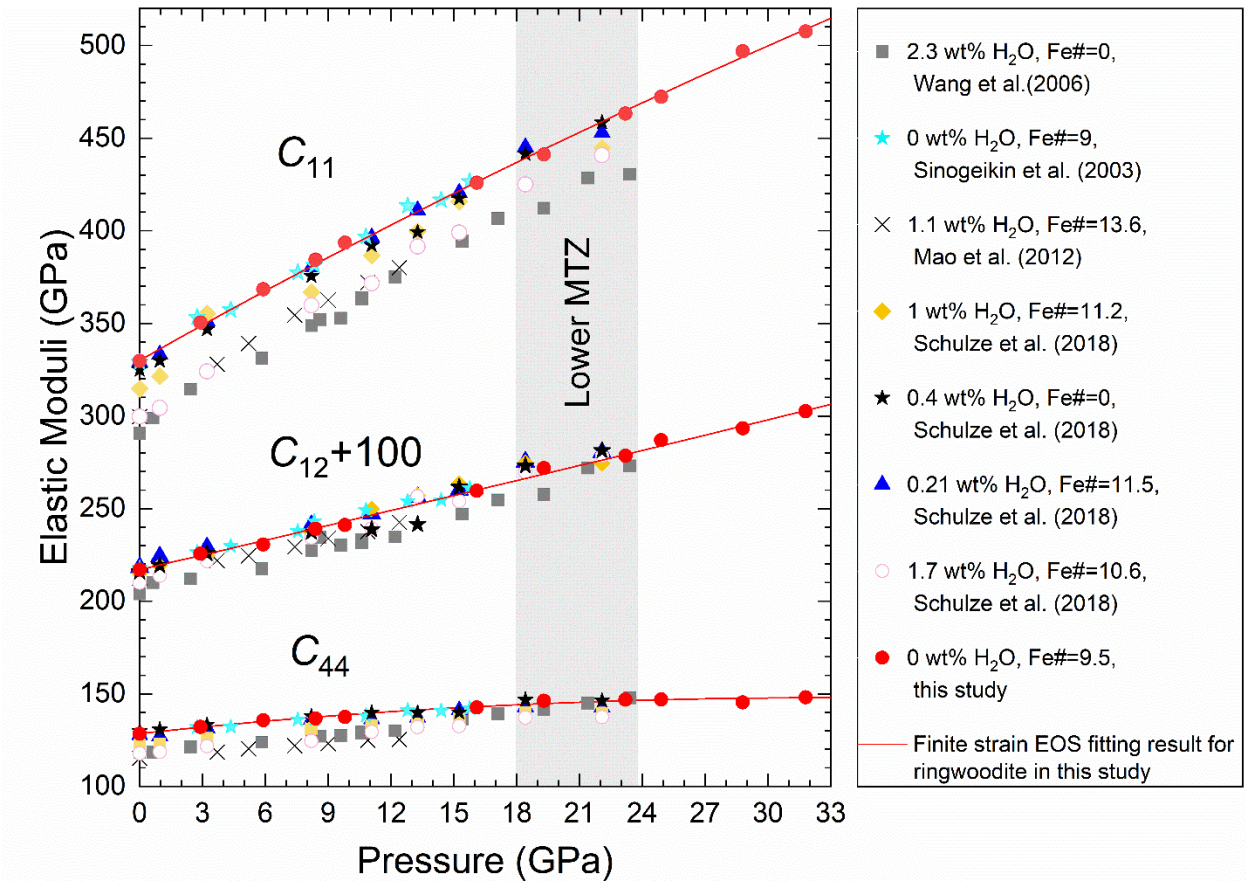

Fig. IV.S6. *C_{ij}s of ringwoodite in this and previous studies at 300K. C_{11} is most sensitive to pressure while C_{44} is least sensitive to pressure.*

Table IV.S1. *EPMA results for the synthetic ringwoodite sample measured in this study.*

Na_2O	MgO	Al_2O_3	SiO_2	CaO	FeO	TOTAL
wt(%)	wt(%)	wt(%)	wt(%)	wt(%)	wt(%)	wt(%)
0.01(1)	49.48(2)	0.13(1)	40.39(11)	0.02(1)	9.36(1)	99.40(8)

Table IV.S2. *Pressure and temperature dependence of C_{11}, C_{44}, C_{12} for the ringwoodite sample measured in this study.*

	C_{11}	C_{44}	C_{12}
C_{ij0} (GPa)	330(1)	128.5(6)	117(1)
$(\partial C_{ij}/\partial P)_{T0}$	6.5(1)	1.27(2)	2.66(3)
$(\partial^2 C_{ij}/\partial P^2)_{T0}$ (GPa^{-1})	-0.068(4)	-0.05(2)	0
$(\partial C_{ij}/\partial T)_{P0}$ (GPa/K)	-0.030(3)	-0.013(2)	-0.010(3)

Table IV.S3. *The water-Fe dependent elastic properties of single-crystal ringwoodite described by the empirical relationship of* $\boldsymbol{B = B_0 + B_1 \times}$ *water (wt%)* $\boldsymbol{+ B_2 \times}$ *Fe#.*

	$\boldsymbol{B_0}$	**B1**	$\boldsymbol{B_2}$
$\boldsymbol{\rho_0}$ (g/cm^3)	3.569(9)	-0.060(6)	0.0132(9)
$\boldsymbol{K_{S0}}$ (GPa)	187(1)	-8.8(7)	0.23(15)
$\boldsymbol{G_0}$ (GPa)	121.1(5)	-6.0 (3)	-0.18(5)
$\boldsymbol{(\partial K_S/\partial P)_{T0}}$	3.8(1)	0.18(9)	0
$\boldsymbol{(\partial K_S^2/\partial P^2)_{T0}}$ (GPa^{-1})	0	0	0
$\boldsymbol{(\partial K_S/\partial T)_{P0}}$ (GPa/K)	-0.014 (3)	0	0
$\boldsymbol{(\partial G/\partial P)_{T0}}$	1.5(1)	0.10(5)	0
$\boldsymbol{(\partial G^2/\partial P^2)_{T0}}$ (GPa^{-1})	-0.046 (14)	0	0
$\boldsymbol{(\partial G/\partial T)_{P0}}$ (GPa/K)	-0.012 (3)	0	0

Table IV.S4. *Summary of previous elasticity measurements of ringwoodite.*

Water wt%	Fe#	Ks_0 GPa	G_0 GPa	$(\partial Ks/\partial P)_{T0}$	$(\partial^2 Ks/\partial P^2)_{T0}$ GPa^{-1}	$(\partial G/\partial P)_{T0}$	$(\partial^2 G/\partial P^2)_{T0}$ GPa^{-1}	$(\partial Ks/\partial T)_{P0}$ GPa/K	$(\partial G/\partial T)_{P0}$ GPa/K	Experiments	References
0	0	185(3)	120(2)	\	\	\	\	−0.024(3)	−0.015(2)	873K,BS	Jackson et al., 2000
0	9	188(3)	120(2)	\	\	\	\	−0.021(2)	−0.016(2)	923K,BS	Sinogeikin et al., 2003
0	9	188(3)	120(2)	4.1(3)	\	1.3(2)	\	\	\	16GPa,BS	Sinogeikin et al., 2003
≤0.01	9	185.1(2)	118.2(1)	\	\	\	\	-0.0193(9)	-0.0148(3)	473K, RUS	Mayama et al., 2005
1	11.5	177(4)	103.1(9)	5.3(4)	\	2.0(2)	\	\	\	9.2GPa, GHz-UI	Jacobsen and Smyth, 2006
0	0	185(2)	127(1)	4.4(2)	\	1.3(1)	\	\	\	14GPa,UI	Higo et al., 2006
0	20	187(2)	116(1)	4.4(2)	\	1.4(1)	\	\	\	14GPa,UI	Higo et al., 2006
0	50	191(2)	102(1)	4.4(2)	\	1.0(1)	\	\	\	14GPa,UI	Higo et al., 2006
0	9	186.2(7)	118.5(4)	4.33(6)	\	1.20(3)	\	-0.0181(8)	-0.0150(4)	18GPa,1673K,UI	Higo et al., 2008
1.1	13.6	175(1)	106(1)	4.0(1)	\	1.98(20)	-0.11(5)	-0.038(7)	-0.017(4)	16GPa,673K,BS	Mao et al., 2012
0.2(1)	11.5	189(1)	118.3(6)	4.06(8)	\	1.59(5)	\	\	\	22GPa,BS	Schulze et al., 2018
1.0(1)	11.2	181.5(6)	112.7(3)	4.3(1)	\	1.71(4)	\	\	\	22GPa,BS	Schulze et al., 2018
1.7(2)	10.6	173(1)	108.1(7)	4.5(1)	\	1.89(6)	\	\	\	22GPa,BS	Schulze et al., 2018
0.4(5)	0	186(1)	119.1(9)	3.9(2)	\	1.72(9)	\	\	\	22GPa,BS	Schulze et al., 2018
0	9.6	188(1)	119(1)	4.0(2)	-0.03(2)	1.56(7)	-0.049(6)	-0.017(4)	-0.011(2)	32GPa, 700K,BS	This study
				3.7(1)	\	1.63 (7)	-0.053(8)	-0.014(3)	-0.012(3)	32GPa, 700K,BS	This study by fixing $(\partial^2 Ks/\partial P^2)_{T0}$ =0
0	9	189.5	\	4.0 (1)	\	\	\	-0.008(5)	\	21GPa,1273K, XRD	Nishihara et al. (2004) with Au pressure calibration standard by Shim et al. (2002)

UI: Ultrasonic Interferometry.
RUS: Resonant Ultrasound Spectroscopy
BS: Brillouin Spectroscopy
XRD: X-ray diffraction: Adiabatic values are calculated using Equations S22-S24.

Table IV.S5. *The maximum and minimum v_p and v_s and their associated polarization directions (19-30GPa, 300 K).*

Pressure	v_p propagation direction = polarization direction				Max v_s splitting propagation direction [011]			
	v_p max	v_p max	v_p min	v_p min	v_s max	v_s max	v_s min	v_s min
GPa	km/s	Polarization	km/s	Polarization	km/s	Polarization	km/s	Polarization
19	11.39	[111]	11.27	[001]	6.44	[100]	6.28	[01-1]
20	11.44	[111]	11.34	[001]	6.45	[100]	6.31	[01-1]
21	11.50	[111]	11.40	[001]	6.46	[100]	6.34	[01-1]
22	11.55	[111]	11.47	[001]	6.47	[100]	6.37	[01-1]
23	11.60	[111]	11.54	[001]	6.48	[100]	6.40	[01-1]
24	11.65	[111]	11.60	[001]	6.48	[100]	6.42	[01-1]
25	11.70	[111]	11.67	[001]	6.49	[100]	6.45	[01-1]
26	11.74	[111]	11.73	[001]	6.50	[100]	6.48	[01-1]
27	11.79	[001]	11.79	[111]	6.51	[01-1]	6.50	[100]
28	11.85	[001]	11.84	[111]	6.53	[01-1]	6.51	[100]
29	11.92	[001]	11.88	[111]	6.56	[01-1]	6.51	[100]
30	11.98	[001]	11.93	[111]	6.58	[01-1]	6.51	[100]

The 4th order finite strain EOS we utilized for high pressure extrapolation (Davies, 1974; Davies and Dzieonski, 1975):

$$\varepsilon = \frac{1}{2}[1 - (\frac{\rho}{\rho_0})^{\frac{2}{3}}] \quad \text{(S1)}$$

$$\rho Vs^2 = (1 - 2\varepsilon)^{\frac{5}{2}}(M_1 + M_2 \cdot \varepsilon + \frac{1}{2}M_3 \cdot \varepsilon^2) \quad \text{(S2)}$$

$$\rho Vp^2 = (1 - 2\varepsilon)^{\frac{5}{2}}(L_1 + L_2 \cdot \varepsilon + \frac{1}{2}L_3 \cdot \varepsilon^2) \quad \text{(S3)}$$

$$P = -(1 - 2\varepsilon)^{\frac{5}{2}}(C_1 \cdot \varepsilon + \frac{1}{2}C_2 \cdot \varepsilon^2 + \frac{1}{6}C_3 \cdot \varepsilon^3) \quad \text{(S4)}$$

where ε is strain, ρ is density, ρ_0 is ambient density, P is pressure. M_1, M_2, M_3, L_1, L_2, L_3, C_1, C_2, and C_3 are defined as:

$$M_1 = G_0 \quad \text{(S5)}$$

$$M_2 = 5M_1 - 3K_{S0} \cdot G_0' \quad \text{(S6)}$$

$$M_3 = 9G_0'' \cdot K_{S0}{}^2 - 3(K_{S0}' - 4)M_2 + 5(3K_{S0}' - 5)M_1 \quad \text{(S7)}$$

$$L_1 = K_0 + \frac{4}{3}M_1 \quad \text{(S8)}$$

$$L_2 = 5L_1 - 3K_{S0}(K_{S0}' + \frac{4}{3}G_0') \quad \text{(S9)}$$

$$L_3 = 9K_{S0}'' \cdot K_{S0}{}^2 + 12G_0'' \cdot K_{S0}{}^2 - 3(K_{S0}' - 4)L_2 + 5(3K_{S0}' - 5)L_1 \quad \text{(S10)}$$

Where G_0', G_0'', K_{S0}', and K_{S0}'' represent $(\partial G/\partial P)_{T0}$, $(\partial^2 G/\partial P^2)_{T0}$, $(\partial Ks/\partial P)_{T0}$, and $(\partial^2 Ks/\partial P^2)_{T0}$ shown in the main text, respectively.

$$C_1 = 3L_1 - 4M_1 \quad \text{(S11)}$$

$$C_2 = 3L_2 - 4M_2 + 7C_1 \quad \text{(S12)}$$

$$C_3 = 3L_3 - 4M_3 + 9C_2 \quad \text{(S13)}$$

$$G = \rho \cdot Vs^2 \quad \text{(S14)}$$

$$K_S = \rho \cdot Vp^2 - \frac{4}{3}G \quad \text{(S15)}$$

$$a_1 = -3K_{S0} \cdot (C_{ij,0}{}' + a_3) + 7C_{ij,0} \quad \text{(S16)}$$

$$a_2 = 9K_{S0}{}^2 \cdot C_{ij,0}{}'' - 3K_{S0}{}'(a_1 - 7C_{ij,0}) + 16a_1 - 49C_{ij,0}$$

(S17)

$$C_{ij} = (1 - 2\varepsilon)^{\frac{7}{2}}(C_{ij,0} + a_1 \cdot \varepsilon + \frac{1}{2}a_2 \cdot \varepsilon^2) - P \cdot a_3$$

(S18)

where a_3 is -3 for C_{11}, a_3 is -1 for C_{44} and C_{12}.

The equations used for high temperature extrapolation are (Duffy and Anderson, 1989):

$$\rho_0(T) = \rho_0(300\text{K}) \cdot \exp\left(-\int_{300}^{T} \alpha(T)dT\right)$$

(S19)

$$M_0(T) = M_0(300\text{K}) + \left(\frac{\partial M}{\partial T}\right)_P (T - 300) \quad \text{(S20)}$$

$$M_0{}'(T) = M_0{}'(300\text{K})\exp\left(\int_{300}^{T} \alpha(T)dT\right) \quad \text{(S21)}$$

Where $\rho_0(300K)$represents density under ambient pressure and temperature (300K). $\rho_0(T)$ represents density under ambient pressure and high temperature. α refers to thermal expansion shown in the main text. $M_0(300\text{K})$ represents the elastic moduli *K*s and *G* under ambient

pressure and temperature (300K). $M_0(T)$ represents the elastic moduli *K*s and *G* under ambient pressure and high temperature. $(\frac{\partial M}{\partial T})_P$ is the temperature derivative of elastic moduli under isobaric condition. $M_0{}'$(T) represents the pressure derivative of elastic moduli *K*s and *G* under ambient pressure and high temperature.

Relationships between isothermal and adiabatic elastic properties.

$$K_{S0} = K_{T0}\,(1 + 300\alpha\gamma) \quad \text{S22}$$

$$\partial K_{S0}/\partial P = (\partial K_{T0}/\partial P)(1 + 300\alpha\gamma) + \frac{300\gamma}{(\partial K_{T0}/\partial T)K_{T0}} \quad \text{S23}$$

$$\partial K_{S0}/\partial T = (1 + 300\alpha\gamma)(\partial K_{T0}/\partial T + K_{S0}\frac{\alpha\gamma + 300(\partial\alpha/\partial T)\gamma}{(1+300\alpha\gamma)^2}) \quad \text{S24}$$

Where α and γ are the thermal expansion coefficient and Grüneisen parameter, respectively. To transfer $\partial K_{S0}/\partial T$ from $\partial K_{T0}/\partial T$ of ringwoodite yielded by Nishihara et al. (2004) (See Table IV.S4), the thermal expansion coefficient α of ringwoodite used in Equations S22-S24 is 2.31×10^{-5} K^{-1} which is yielded by Nishihara et al. (2004). The Grüneisen parameter γ of ringwoodite used in Equations S22-S24 is 1.93 (Katsura, 2004).

Anisotropy indices

Universal Anisotropy (A^{U}), a universal index to quantify the overall elastic anisotropy of single crystals (Ranganathan and Ostoja-Starzewski, 2008), is defined as:

$$A^{\mathrm{U}} = (5\frac{G^{\mathrm{V}}}{G^{\mathrm{R}}} + \frac{{K_s}^{\mathrm{V}}}{{K_s}^{\mathrm{R}}} - 6) * 100\ (\%) \quad \text{S25}$$

The superscripts R denotes Reuss bound and V denotes Voigt bound for the homogeneous isotropic aggregate (Hill, 1963).

Zener anisotropy (A^{Z}), measuring anisotropy of cubic crystals, is defined as (Zener, 1948):

$$A^{\mathrm{Z}} = \frac{2C_{44}}{C_{11}-2C_{12}} * 200\ (\%) \quad \text{S26}$$

V_{P} azimuthal anisotropy (A^{Vp}), which represents the largest velocity difference caused by any 2 v_{p} propagating along different directions, is defined as:

$$A^{\mathrm{Vp}} = \frac{\mathrm{Vp}_{max}-\mathrm{Vp}_{min}}{\mathrm{Vp}_{max}+\mathrm{Vp}_{min}} * 200\ (\%) \quad \text{S27}$$

V_{S} azimuthal anisotropy (A^{Vs}), which refers to the largest difference caused by any 2 v_{s} propagating along different directions, is defined as:

$$A^{\mathrm{Vs}} = \frac{\mathrm{Vs}_{max}-\mathrm{Vs}_{min}}{\mathrm{Vs}_{max}+\mathrm{Vs}_{min}} * 200\ (\%) \quad \text{S28}$$

V_{S} radial anisotropy (D^{Vs}), which represents the maximum velocity difference between v_{s1} (fast S-wave velocity) and v_{s2} (slow S-wave velocity) propagating along the same direction but with different polarizations, is defined as:

$$D^{\mathrm{Vs}} = (\frac{|\mathrm{Vs}_1-\mathrm{Vs}_2|}{\mathrm{Vs}_1+\mathrm{Vs}_2})_{max} * 200\ (\%) \quad \text{S29}$$

For cubic crystals, due to their high symmetry, A^{Vs} is the same as D^{Vs}. For elastically isotropic material, A^{U}, A^{Vp}, A^{Vs}, and D^{Vs} are 0, A^{Z} is equal to 1.

Supplementary References

Davies, G. Effective elastic moduli under hydrostatic stress—I. quasi-harmonic theory. Journal of Physics and Chemistry of Solids 35, 1513-1520 (1974).

Davies, G. & Dziewonski, A. Homogeneity and constitution of the Earth's lower mantle and outer core. Physics of the Earth and Planetary Interiors 10, 336-343 (1975).

Duffy, T. S. & Anderson, D. L. Seismic velocities in mantle minerals and the mineralogy of the upper mantle. Journal of Geophysical Research: Solid Earth 94, 1895-1912 (1989).

Higo, Y., Inoue, T., Irifune, T., Funakoshi, K. I., & Li, B. (2008). Elastic wave velocities of (Mg0. 91Fe0. 09) 2SiO4 ringwoodite under P–T conditions of the mantle transition region. *Physics of the Earth and Planetary Interiors*, *166*(3-4), 167-174.

Higo, Y., Inoue, T., Li, B., Irifune, T., & Liebermann, R. C. (2006). The effect of iron on the elastic properties of ringwoodite at high pressure. Physics of the Earth and Planetary Interiors, 159(3-4), 276-285.

Hill, R. Elastic properties of reinforced solids: some theoretical principles. Journal of the Mechanics and Physics of Solids 11, 357-372 (1963).

Jackson, J. M., Sinogeikin, S. V., & Bass, J. D. (2000). Sound velocities and elastic properties of γ-Mg2SiO4 to 873 K by Brillouin spectroscopy. *American Mineralogist*, *85*(2), 296-303.

Jacobsen, S.D., & Smyth, J.R., 2006. Effect of water on the sound velocities of ringwoodite in the transition zone. In: Jacobsen, S.D., Lee, S.V.D. (Eds.), Earth's Deep Water Cycle. American Geophysical Union, pp.131–145.

Katsura, T., Yokoshi, S., Song, M., Kawabe, K., Tsujimura, T., Kubo, A., ... & Funakoshi, K. I. (2004). Thermal expansion of Mg2SiO4 ringwoodite at high pressures. Journal of Geophysical Research: Solid Earth, 109(B12).

Mao, Z., Lin, J. F., Jacobsen, S. D., Duffy, T. S., Chang, Y. Y., Smyth, J. R., ... & Prakapenka, V. B. (2012). Sound velocities of hydrous ringwoodite to 16 GPa and 673 K. *Earth and Planetary Science Letters*, *331*, 112-119.

Mayama, N., Suzuki, I., Saito, T., Ohno, I., Katsura, T., & Yoneda, A. (2005). Temperature dependence of the elastic moduli of ringwoodite. Physics of the Earth and Planetary Interiors, 148(2-4), 353-359.

Nishihara, Y., Takahashi, E., Matsukage, K. N., Iguchi, T., Nakayama, K., & Funakoshi, K. I. (2004). Thermal equation of state of (Mg0. 91Fe0. 09) 2SiO4 ringwoodite. Physics of the Earth and Planetary Interiors, 143, 33-46.

Thomas, S. M., Jacobsen, S. D., Bina, C. R., Reichart, P., Moser, M., Hauri, E. H., ... & Dollinger, G. (2015). Quantification of water in hydrous ringwoodite. Frontiers in Earth Science, 2, 38.

Ranganathan, S.I., Ostoja-Starzewski, M., 2008. Universal elastic anisotropy index. Phys. Rev. Lett.101 (5), 055504.

Schulze, K., Marquardt, H., Kawazoe, T., Ballaran, T. B., McCammon, C., Koch-Müller, M., ... & Marquardt, K. (2018). Seismically invisible water in Earth's transition zone?. *Earth and Planetary Science Letters*, *498*, 9-16.

Shim, S. H., Duffy, T. S., & Takemura, K. (2002). Equation of state of gold and its application to the phase boundaries near 660 km depth in Earth's mantle. Earth and Planetary Science Letters, 203(2), 729-739.

Sinogeikin, S. V., Bass, J. D., & Katsura, T. (2003). Single-crystal elasticity of ringwoodite to high pressures and high temperatures: implications for 520 km seismic discontinuity. *Physics of the Earth and Planetary Interiors*, *136*(1-2), 41-66.

Wang, J., Sinogeikin, S. V., Inoue, T., & Bass, J. D. (2006). Elastic properties of hydrous ringwoodite at high-pressure conditions. Geophysical Research Letters, 33(14).

Zener, C. M., & Siegel, S. (1949). Elasticity and Anelasticity of Metals. The Journal of Physical Chemistry, 53(9), 1468-1468.

Chapter V

High pressure-temperature phase equilibrium studies on Martian basalts: Implications for the failure of plate tectonics on Mars

Abstract

Mars lacks ongoing tectonic activities such as volcanism and mountain-building processes. Modern plate tectonic movements on the Earth's surface are driven primarily by the descent of subducted slabs into the mantle. Slab crust made of dense eclogite metamorphosed from the Mid-Ocean Ridge Basalt provides an important driving force for slab subduction. Thus, mantle convection inside Mars can be hindered if the density contrast between Martian slab crust and the ambient Martian mantle is sufficiently smaller than that of Earth. To evaluate this hypothesis, we carried out high pressure-temperature phase equilibrium experiments on three different Martian basalts: Yamato 980459, NWA 8159, and GUSEV basalt (Humphrey). The GUSEV basalt and NWA 8159 undergo partial or complete melting along the Martian areotherm due to their high Fe content, suggesting that both compositions are geochemically evolved. Yamato 980459, the nearly primitive Martian basalt, on the other hand, would transform to a low-density eclogite at a depth of ~250 km. The density contrast between a Martian crustal slab made of Yamato 980459, and the ambient Martian mantle is much smaller than that for Earth's mantle. Calculated slab sinking torques and velocities further suggest that sustained buoyancy-driven subduction of thin slabs was unlikely early in Martian history. Additional experiments exploring wider composition and pressure-temperature ranges are needed to fully understand the consequences of Martian mantle compositions and cooling history for the tectonic history of Mars.

1. Introduction

Present-day Mars is dominated by stagnant lid convection, with an intact and immobile lithosphere lid covering the mantle (Tosi and Padovan, 2021), whereas Earth operates with mobile plate tectonics, in which dense oceanic lithosphere subducts into the mantle. The primary driving forces of slab subduction include the negative buoyancy produced by low temperatures (*Ts)* in slabs compared to the ambient mantle, and in addition, the much higher intrinsic density of the oceanic crust after the Mid-Ocean Ridge Basalt (MORB) transforms into eclogite (Coltice et al., 2019). Additional forces from plume and ridge push are an order of magnitude weaker in powering plate motion on Earth (Coltice et al., 2019).

A fundamental unanswered question is why a similar style of plate tectonics has failed to develop (or be sustained) on Mars. Hypotheses are many and varied. For example, Sleep (1994) has proposed that an ultra-fast spreading Martian seafloor would be too young to subduct into the Martian interior, whereas Lenardic et al. (2004) proposed that the growth of buoyant lithosphere in the southern hemisphere stopped plate tectonics on Mars. The role of water can be critical as well. For example, Yoshizaki and McDonough (2021) proposed that the lack of a core dynamo would prevent a protective magnetosphere, allowing loss of water on the Martian surface, thereby increasing lithosphere strength and inhibiting subduction, as previously suggested by Azuma and Katayama (2017).

These hypotheses rely on some anomalous mechanical properties of the Martian lithosphere, caused by different physical processes operating on the Martian surface compared to Earth (e.g., rate at which lithosphere is made) or dramatically different physical conditions (e.g., temperature) in the Martian mantle. For example, Scheinberg et al. (2014) proposed that

a mantle overturn at the last stage of magma ocean crystallization would result in a density stratified Mars mantle, favoring stagnant lid convection. However, as pointed out by Schaefer and Elkins-Tanton (2018), many parameters (e.g., mantle potential temperature and heat flux) in the Martian magma ocean models are unconstrained, and the nature of buoyancy driven convection in the ancient Martian interior remains obscure. It is therefore important to determine the densities of relevant Martian mantle candidate rocks at simultaneously high pressure (*P*) and temperature (*T*) conditions.

Recently, Semprich and Filiberto (2020) calculated the mineral compositions, phase proportions, and densities of three different Martian basaltic crustal materials, including GUSEV basalt (Humphrey), Yamato 980459, and the average Martian crust according to Taylor (2013), in a *P*-*T* space with *P* ranging from 0.1 GPa to 3 GPa and *T* ranging from 773 K to 1373 K, using the Perple_X software package (Connolly, 2005). They found that the eclogites transformed from these basalts are all denser than the ambient Martian mantle. In particular, the GUSEV basalt is significantly denser than the Martian mantle and could easily sink into the mantle through delamination. The Fe#, defined as $100*Fe_{mol}/(Fe_{mol}+Mg_{mol})$, in the Martian mantle (Fe# ~25) is significantly higher than those in Earth's mantle (Fe# ~10) (Taylor, 2013). However, the thermoelastic properties of the (pseudo) Fe-end member minerals in the Holland and Powell (2011) thermodynamic database, which is used in the Perple_X calculations conducted by Semprich and Filiberto (2020), are poorly constrained, especially under high temperatures (Thio et al., 2016). Thus, both the calculated thermodynamic stability fields and the high *P*-*T* densities of the Fe-rich Martian mantle minerals may not be reliable. Perple_X is a powerful tool, but for the Martian interior, experiments are needed to verify the

computational results, as well as directly constrain the mineral compositions and densities of crustal materials at high *P-T* conditions.

The Martian crust is likely dominated by olivine (Ol)-rich basalts, based on orbital and rover spectroscopy measurements (McSween et al., 2006; Mandon et al., 2020). SNC (Shergottites-Nakhlites-Chassignites) meteorites also provide valuable insights into the Martian crustal composition, due to their possibly wider and deeper sampling locations. A large proportion of the Martian shergottites (Ol-phyric shergottites) are thought to represent primary melts (Collinet et al., 2021; Filiberto and Dasgupta, 2011; Gross et al., 2013; Peslier et al., 2010; White et al., 2006). In addition, many Martian basalts exposed on the surface and analyzed by rover spectroscopy measurements (e.g., Golumbia Hills alkali basalts) are thought to have been produced with very minor fractional crystallization (Collinet et al., 2015). Assuming the bulk Martian crust primarily originated from the partial melting of the mantle, and considering the limited magmatic differentiation on Mars (Collinet et al., 2021; Filiberto and Dasgupta, 2011; McSween et al., 2009), the nearly primitive basaltic melts derived from the Martian mantle likely represent a significant fraction of the Martian crust. For example, Yamato 980459, a nearly primitive Martian basalt with a bulk composition similar to the average composition of all Ol-phyric shergottites (White et al., 2006), may be representative of the early Martian crust, although it is chronologically young (Lagain et al., 2021). In addition to Yamato 980459, several more evolved compositions could be important in the Martian crust. For example, NWA 8159 (~2370 Ma), one of the oldest Martian meteorites, is significantly Fe-enriched (~21 wt% FeO) and may represent an evolved part of the crust formed early in Mars history (Herd et al., 2017). The GUSEV basalt (Humphrey) is the least weathered picritic basalt in the GUSEV crater. Its chemical composition on the Martian surface has been

measured by the Spirit Rover (McSween et al., 2006). As shown in Table V.1, GUSEV basalt (Humphrey), Yamato 98049, and NWA 8159 represent 3 different potential Martian crustal compositions, which are all Al-poor compared to MORB. Consequently, eclogites metamorphosed from Martian crustal basalts carry lesser amounts of garnet (Gt), making them less dense than eclogite transformed from MORB.

Table V.1. *Chemical composition (wt%) of 3 Martian basalts, 2 Martian mantle models, Earth's MORB and Pyrolite model.*

	Martian crust			Martian mantle		Earth's oceanic crust	Earth's mantle
name	GUSEV basalt (Humphrey)	NWA 8159	Yamato 980459	DW model	Taylor 2013	MORB	Pyrolite
Type	Picrite basalt	Augite basalt	Olivine Shergottite	Peridotite	Peridotite	Tholeiitic basalt	Peridotite
Age	~3650 Ma	2370±250 Ma	472±47 Ma	\	\	\	\
SiO2 (wt%)	45.9*	48	50.31	44.40	43.7	49.51	44.71
Al_2O_3	10.68*	10.74	5.59	3.02	3.04	16.75	3.98
FeO	18.6*	20.86	17.56	17.90	18.1	8.05	8.18
CaO	7.84*	11.98	6.70	2.45	2.43	12.50	3.17
MgO	10.41*	4.35	19.18	30.20	30.5	9.74	38.73
Na_2O	2.5*	2.46	0.67	0.50	0.53	2.18	0.13
Fe/Si	0.34	0.36	0.29	0.34	0.35	0.14	0.15
Al/Si	0.27	0.26	0.13	0.08	0.08	0.40	0.10
Ca/Si	0.18	0.27	0.14	0.06	0.06	0.27	0.08
References	(Greeley et al., 2005; McSween et al., 2006)	(Herd et al., 2017)	(Dreibus et al., 2003; Greshake et al., 2004; Misawa, 2003; Shih et al., 2005; Shirai and Ebihara, 2004)	(Bertka and Fei, 1997)	(Taylor, 2013)	(Workman and Hart, 2005)	

*denotes measurements made by the Spirit Rover on the surface of Mars.

The classic Martian mantle composition model, the DW (Dreibus and Wänke) model, is derived from the element ratios of the SNC meteorites and based on a bulk CI carbonaceous chondrite composition (Wänke and Dreibus, 1994). Subsequently, Taylor (2013) presented an updated composition model, based on additional Martian surface, orbital, and meteorite data. But as shown in Table V.1, the Taylor (2013) model is nearly identical to the classic DW model, so we adopt the DW model in this study for the composition of the average Martian mantle. The Fe/Si ratio (0.34) of the DW model is more than two times higher than the Fe/Si ratio

(0.15) of the pyrolitic Earth (Workman and Hart, 2005), likely resulting in a much denser Martian mantle compared with Earth's mantle. Due to this compositional difference, it is plausible that the Martian upper mantle is denser than Earth's upper mantle, whereas a Martian slab with a crust made of the Al-poor Martian basalt, such as Yamato 980459, is less dense than a subducting slab with a crust made of MORB. Because subduction on the Earth is partly driven by the negative buoyancy of subducted crust, and the density relationship between the slab crust and the mantle may be different on Mars, careful comparison of the densities of subducted material and ambient mantle at the relevant *P-T* conditions can shed light on the prospects for Martian plate tectonics.

To make this comparison, we have carried out high *P-T* phase equilibrium experiments for 3 different basalts with the compositions of Yamato 980459, GUSEV basalt (Humphrey), and NWA 8159 (Tables V.1, V.2) along a typical Martian areotherm (temperature change as a function of depth inside Mars, similar to the geotherm for Earth) (Longhi et al., 1992). We also compare seismic velocities of one Martian primitive basalt (Yamato 980459) to the ambient Martian mantle along the same areotherm, based on this and previous studies (Bertka and Fei, 1997; Xu et al., 2021).

2. Methods

2.1 High *P-T* Experiments

We conducted the phase equilibrium experiments for three different compositions (Yamato 980459, NWA 8159, and GUSEV basalt (Humphrey)) up to 16 GPa using the 2000-ton and 600-ton Multi-Anvil presses at the Experimental Petrology Laboratory at the University of New Mexico (Tables V.1, V.2). The experimental *P-T* conditions along the typical Martian areotherm are shown in Fig. V.2A. Electron Probe Microanalysis (EPMA)

point analysis and mapping experiments were later conducted for all 15 run products with the Yamato 980459 composition using the JEOL 8200 Electron Microprobe at the Institute of Meteoritics at UNM. Based on the EPMA results, we calculated phase proportions, densities, and sound velocities (V_P, V_S) for all the run products with Yamato 980459 composition using high *P-T* finite strain equations of state (Table V.3). The technical details of the experiments and data analysis methods are described in Supplementary Text 1.

Table V.2. *Experimental conditions in this study.*

Starting material	Pressure (GPa)	Temperature (K)	Capsule	Method
Yamato 980459	1	1223	Mo	Heat to 1523 K, then cool down to the target *P T* and stay at the target *P T* for 6 h
Yamato 980459	2	1353	Mo	Heat to 1623 K, then cool down to the target *P T* and stay at the target *P T* for 3 h
Yamato 980459	3	1473	Mo	Heat to 1723 K, then cool down to the target *P T* and stay at the target *P T* for 10 min
Yamato 980459	4	1543	Mo	Heat to 1873 K, then cool down to the target *P T* and stay at the target *P T* for 2 h
Yamato 980459	4.5	1523	Mo	Heat to 1873 K, then cool down to the target *P T* and stay at the target *P T* for 1.5 h
Yamato 980459	6	1673	Mo	Heat to 1973 K, then cool down to the target *P T* and stay at the target *P T* for 1 h
Yamato 980459	9	1823	Mo	Heat to 2123 K, then cool down to the target *P T* and stay at the target *P T* for 1 h
Yamato 980459	12	1923	Mo	Heat to 2073 K, then cool down to the target *P T* and stay at the target *P T* for 6 hours
Yamato 980459	13	1943	Mo	Heat to 2073 K, then cool down to the target *P T* and stay at the target *P T* for 0.5 h
Yamato 980459	14	1973	Mo	Heat to 2073 K, then cool down to the target *P T* and stay at the target *P T* for 6 hours
Yamato 980459	16	2003	Mo	Heat to 2123 K, then cool down to the target *P T* and stay at the target *P T* for 6 hours
NWA 8159	1	1223	Mo	Heat to 1523 K, then cool down to the target *P T* and stay at the target *P T* for 6 h
NWA 8159	2.5	1403	Mo	Heat to 1703 K, then cool down to the target *P T* and stay at the target *P T* for 6 h
GUSEV basalt (Humphrey)	1	1223	Mo	Heat to 1523 K, then cool down to the target *P T* and stay at the target *P T* for 6 h

Table V.3. *Experimentally determined mineral proportions, compositions and calculated aggregate densities and sound velocities for Yamato 980459 under high P-T conditions.*

	Vol %	Wt %	Composition	Aggregate ρ^{VRH} g/cm^3	Aggregate Vp^{VRH} km/s	Aggregate Vs^{VRH} km/s
1GPa 1223K						
Ol	20	22	$Mg_{3.81(81)}Ca_{0.04(2)}Fe_{2.17(52)}Si_{2.97(10)}O_{12.0(16)}$			
Opx	3	3	$Mg_{3.15(17)}Ca_{0.13(5)}Fe_{0.77(8)}Al_{0.07(2)}Si_{3.92(6)}O_{12.0(5)}$			
Cpx	58	59	$Na_{0.02(1)}Mg_{2.22(22)}Ca_{0.67(14)}Fe_{1.01(5)}Al_{0.27(10)}Si_{3.84(7)}O_{12.0(7}$	3.25(1)	7.24(3)	4.09(4)
Pl	19	16	$Na_{0.71(7)}Mg_{0.07(6)}Ca_{0.83(5)}Fe_{0.14(6)}Al_{1.97(5)}Si_{3.83(7)}O_{12.0(4)}$			
2GPa 1353K						
Ol	4	4	$Mg_{3.31(5)}Ca_{0.03(1)}Fe_{2.66(3)}Al_{0.03(2)}Si_{2.97(13)}O_{12.0(4)}$			
Opx	51	51	$Mg_{2.48(24)}Ca_{0.21(5)}Fe_{1.13(15)}Al_{0.36(10)}Si_{3.81(9)}O_{12.0(8)}$	3.382(1)	7.32(1)	4.22(1)
Cpx	45	45	$Na_{0.09(4)}Mg_{1.73(40)}Ca_{0.99(23)}Fe_{0.96(5)}Al_{0.59(17)}Si_{3.69(15)}O_{12.0(}$			
3GPa 1473K						
Opx	41	40	$Mg_{2.65(13)}Ca_{0.18(3)}Fe_{0.98(9)}Al_{0.26(5)}Si_{3.90(8)}O_{12.0(5)}$			
Cpx	44	44	$Na_{0.10(1)}Mg_{1.95(16)}Ca_{0.83(12)}Fe_{0.93(6)}Al_{0.33(3)}Si_{3.87(8)}O_{12.0(6)}$	3.431(3)	7.56(4)	4.31(1)
Gt	15	16	$Mg_{1.31(15)}Ca_{0.52(3)}Fe_{1.26(10)}Al_{1.94(7)}Si_{3.00(7)}O_{12.0(5)}$			
4GPa 1543K						
Opx	43	42	$Mg_{2.58(7)}Ca_{0.13(3)}Fe_{1.10(8)}Al_{0.12(6)}Si_{4.00(4)}O_{12.0(4)}$			
Cpx	37	36	$Na_{0.13(3)}Mg_{1.84(17)}Ca_{0.89(21)}Fe_{0.96(9)}Al_{0.14(3)}Si_{4.02(3)}O_{12.0(6)}$	3.483(3)	7.66(5)	4.32(2)
Gt	21	22	$Mg_{1.59(14)}Ca_{0.33(3)}Fe_{1.09(9)}Al_{1.91(6)}Si_{3.06(4)}O_{12.0(4)}$			
4.5GPa 1523K						
Opx	42	41	$Mg_{2.60(6)}Ca_{0.13(3)}Fe_{1.13(5)}Al_{0.09(2)}Si_{3.99(2)}O_{12.0(2)}$			
Cpx	39	38	$Na_{0.14(2)}Mg_{1.84(15)}Ca_{0.91(16)}Fe_{0.91(6)}Al_{0.14(2)}Si_{4.00(3)}O_{12.0(5)}$	3.498(3)	7.72(5)	4.34(2)
Gt	20	21	$Mg_{1.47(19)}Ca_{0.36(8)}Fe_{1.19(14)}Al_{1.98(6)}Si_{3.00(5)}O_{12.0(6)}$			
6GPa 1673K						
Ol	7	8	$Mg_{3.23(11)}Ca_{0.03(2)}Fe_{2.67(7)}Si_{3.01(5)}O_{12.0(4)}$			
Cpx	74	72	$Na_{0.12(1)}Mg_{2.14(12)}Ca_{0.62(5)}Fe_{0.98(7)}Al_{0.17(3)}Si_{3.97(6)}O_{12.0(4)}$	3.534(3)	7.82(3)	4.33(2)
Gt	19	20	$Mg_{1.50(14)}Ca_{0.35(9)}Fe_{1.18(6)}Al_{1.93(12)}Si_{3.03(9)}O_{12.0(7)}$			
9GPa 1823K						
Ol	10	10	$Mg_{3.46(18)}Ca_{0.07(6)}Fe_{2.14(10)}Si_{3.11(18)}O_{12.0(9)}$			
Cpx	64	62	$Na_{0.12(1)}Mg_{2.17(11)}Ca_{0.60(6)}Fe_{0.90(5)}Al_{0.12(1)}Si_{4.00(3)}O_{12.0(3)}$	3.62 (3)	8.09(3)	4.39(2)
Gt	26	28	$Mg_{1.62(10)}Ca_{0.38(9)}Fe_{1.22(4)}Al_{1.51(7)}Si_{3.25(5)}O_{12.0(4)}$			
12GPa 1923K						
Cpx	55	52	$Na_{0.13(2)}Mg_{2.16(11)}Ca_{0.73(12)}Fe_{0.90(4)}Al_{0.12(2)}Si_{3.98(2)}O_{12.0(4)}$	3.716(4)	8.43(3)	4.49(1)
Gt	45	48	$Mg_{2.02(6)}Ca_{0.30(3)}Fe_{1.23(3)}Al_{1.03(6)}Si_{3.45(3)}O_{12.0(3)}$			
13GPa 1943K						
Cpx	47	45	$Na_{0.13(2)}Mg_{2.19(8)}Ca_{0.70(8)}Fe_{0.88(4)}Al_{0.11(3)}Si_{4.00(2)}O_{12.0(3)}$	3.754(3)	8.55(3)	4.54 (1)
Gt	53	55	$Mg_{2.10(9)}Ca_{0.30(3)}Fe_{1.15(3)}Al_{0.95(10)}Si_{3.51(6)}O_{12.0(4)}$			
14GPa 1973K						
Cpx	29	27	$Na_{0.16(2)}Mg_{2.03(8)}Ca_{0.88(10)}Fe_{0.82(3)}Al_{0.12(2)}Si_{4.00(2)}O_{12.0(3)}$	3.830(3)	8.78(3)	4.62(1)
Gt	71	73	$Mg_{2.16(7)}Ca_{0.34(3)}Fe_{1.18(4)}Al_{0.66(12)}Si_{3.65(7)}O_{12.0(5)}$			
16GPa 2003K						
Cpx	17	16	$Na_{0.16(2)}Mg_{2.04(7)}Ca_{0.98(8)}Fe_{0.71(4)}Al_{0.13(2)}Si_{4.00(2)}O_{12.0(3)}$	3.890(2)	9.01(2)	4.70(1)
Gt	83	84	$Mg_{2.22(6)}Ca_{0.37(2)}Fe_{1.11(2)}Al_{0.60(14)}Si_{3.69(7)}O_{12.0(5)}$			

8-18 single-point EPMA analyses are conducted for each phase.

2.2 Perple_X calculations

We used the Perple_X software package to calculate mineral proportions and compositions for Yamato 980459 and the DW model along the same Martian areotherm used in our experiments (Connolly, 2005; Longhi et al., 1992). Perple_X results are shown in Fig. V.1B and Fig. V.1D. It is important to note that different thermodynamic databases are available in Perple_X. The Perple_X calculation in this study used the thermodynamic database by Stixrude and Lithgow-Bertelloni (2011), whereas Semprich and Filiberto (2020) adopted the thermodynamic database by Holland and Powell (2011). More calculation details are included in Supplementary Text 2.

2.3 Slab Sinking Torque and Velocity models

As a small rocky planet, secular cooling of Mars results in significant increase of lithosphere thickness over time. For example, the Martian lithosphere thickness is proposed to have been 0-30 km in the Noachian period (4.1-3.7 Ga), increasing to ~110 km during the Hesperian (3.7-3.0 Ga) period and most of the Amazonian period (3000-200 Ma), eventually reaching ~500 km at present (Knapmeyer-Endrun et al., 2021; Grott et al., 2013; Ranalli, 1994, Supplementary Text 3). Over 70% of Martian crust is estimated to have formed by 4.0 Ga ago (Carr and Head III, 2010; Hauck, 2002), and the present Martian crust thickness is estimated to be ~50 km (24-72 km) on average (Knapmeyer-Endrun et al., 2021).

To assess the potential for subduction in the geologic history of Mars, we have calculated sinking torques and subduction velocities of two-dimensional planar subducting slabs under three different settings. For the Noachian period, we assume a thin (30 km thick) crustal slab. For the Hesperian and most of the Amazonian period, the Martian lithosphere thickens over time, and a two-layer Earth-like slab structure (basaltic crust + lithospheric mantle) may be more representative. Thus, we assume the slab has a 50 km thick crust and a

60 km thick lithospheric mantle. In the present day, when the lithosphere is far thicker (Knapmeyer-Endrun et al., 2021), we consider a slab with a 450 km thick lithospheric mantle below the overlying 50 km thick crust.

The density data we use for the slab and mantle are applicable up to 16 GPa, corresponding to the depth Z ≈ 1333 km in the Martian interior. Although the Perple_X calculation results share many similarities with the experimental results in this study (see details in section 3.1), only the mineral compositions and proportions determined from the experiments (Fig. V.1A and V.1C) are used for calculating the density contrast between the slab and the mantle as a function of depth (Fig. V.1E). For calculation purposes, we assume a nominal slab dip angle of θ = 45º, in which case the maximum slab length is approximately 1886 km. We further assume the thermal anomaly in the slab cross-section is conserved during subduction, such that the product of the slab thickness δ and the average temperature anomaly ΔT=T_{mantle}-T_{slab} is uniform with distance along the slab. δc refers to the thickness of the crust, so δ-δc represents the thickness of the lithospheric mantle in the slab. Then the slab sinking torque (per unit distance in the transverse direction) is given by

$$\tau = \int_0^R (\delta c(\rho\alpha\Delta T - \Delta\rho)+(\delta-\delta c)(\rho_{mantle}\alpha\Delta T))g\cos(\theta)rdr \quad (1)$$

where r=z/sin θ is the distance along the slab measured from the surface r=0 to the end of the slab r=R, ρ is the slab isothermal density, $\Delta\rho=\rho_{mantle} - \rho$ is the slab isothermal density anomaly, α is thermal expansion, and g is gravity. Using slab $\alpha=4\times10^{-5}$ K^{-1}, g=372 cm s^{-2} (Justh, 2014) along with ρ and Δρ from Fig. V.1E and V.2D, Fig. V.4 shows the sinking torque calculated from (1) as a function of slab length R for various slab temperature anomalies (ΔT). The equilibrium velocity of the slab during subduction is also obtained by balancing the sinking

torque (1) against the lifting torque applied to the slab by the mantle flow. The calculation details are shown in Supplementary Text 3.

3. Results and Discussion

3.1 Mineralogy and density of Yamato 980459 and Martian mantle

For Yamato 980459, the high *P-T* mineral assemblages determined experimentally agree with the Perple_X calculation results (Fig 1) in terms of the Gt and total pyroxene fractions, although other differences exist. At 1-2 GPa, our experiments suggest plagioclase (Pl) is present, whereas the Perple_X calculations performed in this study and Semprich and Filiberto (2020) both suggest the presence of Gt (Fig. V.1B). The larger stability field of Pl found in our experiments affects the calculated densities of Yamato 980459 at high *P-T* conditions, since Gt is significantly denser than Pl. This discrepancy between the Perple_X calculations and our experiments explains why our results differ from Semprich and Filiberto (2020), who concluded that Yamato 980459 is denser than the Martian mantle at 1-2 GPa. In this study, only our experimental results were used to calculate the density contrast between the Martian eclogite and the ambient mantle. Other small differences include larger stability fields for orthopyroxene (Opx) and Fe-enriched wadsleyite (Wads) in the calculations compared to our experiments (Figs. 1A and 1B). These differences are likely caused by the large uncertainties in the thermodynamic properties of the Fe-end member minerals, such as clinoferrosilite. However, the difference in Opx stability fields is unlikely to significantly affect the calculated density profiles, due to the density similarity between Opx and clinopyroxene (Cpx). Unless otherwise noted, our results below refer to experimental values.

At 1 GPa (~80 km depth), the shergottite basalt (Yamato 980459) is composed of 58 vol% Cpx, 20 vol% Ol, 19 vol% Pl, and 3 vol% Opx. At 2 GPa (~170 km depth), the shergottite

basalt transforms into a pyroxene granulite, which results in a ~2% density increase (Figs. 1A and 1E). The onset of the basalt to eclogite transformation corresponds to the disappearance of Ol at 3 GPa (~250 km), which shows a negligible density jump. From 9 GPa to 16 GPa, Gt grows at the expense of Cpx, as shown in Fig. V.3. Between 13-14 GPa (~1080-1170 km), the density further increases by ~2% with more Fe dissolving into the Gt (Fig. V.1E). It is worth noting that the shergottite basalt-eclogite transformation at 2-3 GPa (~170-250 km) shows no obvious density jump because of the low Al content in Yamato 980459. As the major Al-bearing phase, the Gt content is thus low (~15 vol%) in the Martian eclogite (Fig. V.1) compared to Earth. In Earth's interior, the MORB to pyroxene granulite transformation at ~1 GPa (~30 km) results in a larger density increase of ~5%; the subsequent pyroxene granulite to eclogite transformation at ~2 GPa (~60 km) further increases the density by another 5% (Ito and Kennedy, 1971). Phase equilibrium calculations suggest that the eclogitization of MORB results in a total of ~13% density jump at 60-100 km along the 1600 K adiabatic geotherm (Xu et al., 2008). The Gt content in the eclogite transformed from MORB increases quickly from ~20-40 vol% at 150 km to ~80-90 vol% at 450 km (e.g., Aoki and Takahashi, 2004). These values are significantly higher than the Gt content in the Martian eclogite (15-26 vol%) from 250 km to 750 km. As a result, the density of Martian eclogite made of Yamato 980459 is on average ~0.7 % less than eclogite transformed from MORB on Earth (Fig. V.2B).

The experimentally determined high *P*-*T* phase diagram for the ambient Martian mantle is shown in Fig. V.1C, and the Perple_X computational results are shown in Fig. V.1D. According to previous experimental results (Bertka and Fei, 1997) (Fig. V.1C), the ambient Martian mantle is composed of ~60 vol% Ol, ~30 vol% pyroxene, and ~10 vol% Gt from ~2-13 GPa (~170-1080 km), which is similar to the Earth's ambient mantle. However, the Ol in

the Martian mantle (Fe# ~ 21-25) is significantly more enriched in Fe than the Ol in the Earth's pyrolitic mantle (Fe# ~10). As a result, the ambient Martian mantle is on average ~3 % denser than the ambient Earth's mantle at similar *P*-*T* conditions (Fig. V.2C). We also show the density profile of an oxidized ambient Martian mantle in Fig. V.1E, based on Xu et al. (2021). The densities of the oxidized and reduced ambient Martian mantle (Bertka and Fei, 1997) are similar. Considering the wider *P* range reached in Bertka and Fei (1997), we used the densities calculated from their experimental results in the following discussion. The amount of ferric Fe in the starting materials and run products is negligible, therefore we do not consider the effect of oxygen fugacity in this study.

We found that the relative buoyancy of eclogite and ambient upper mantle is different between Mars and Earth (Fig. V.2D), primarily due to the differences in their chemical compositions. On Earth, a crustal slab made of MORB remains denser than the pyrolitic ambient mantle from ~60-100 km down to ~660 km depth (Xu et al., 2008). This is one of the most important driving forces for the subduction-induced plate tectonics on Earth. In contrast, Martian shergottite basalt Yamato 980459 is found to be less dense than ambient Martian mantle, even after it transforms into eclogite at ~250 km depth. This positive buoyancy persists down to ~300 km depth, after which the eclogite remains neutrally buoyant compared to ambient Martian mantle down to ~500 km depth. Accordingly, dynamics of Mars crust is expected to have been markedly different from that on Earth. For example, the fact that the average crustal thickness is less than 72 km (including beneath Tharsis, Knapmeyer-Endrun et al., 2021), Earth-like delamination is unlikely to have occurred on Mars.

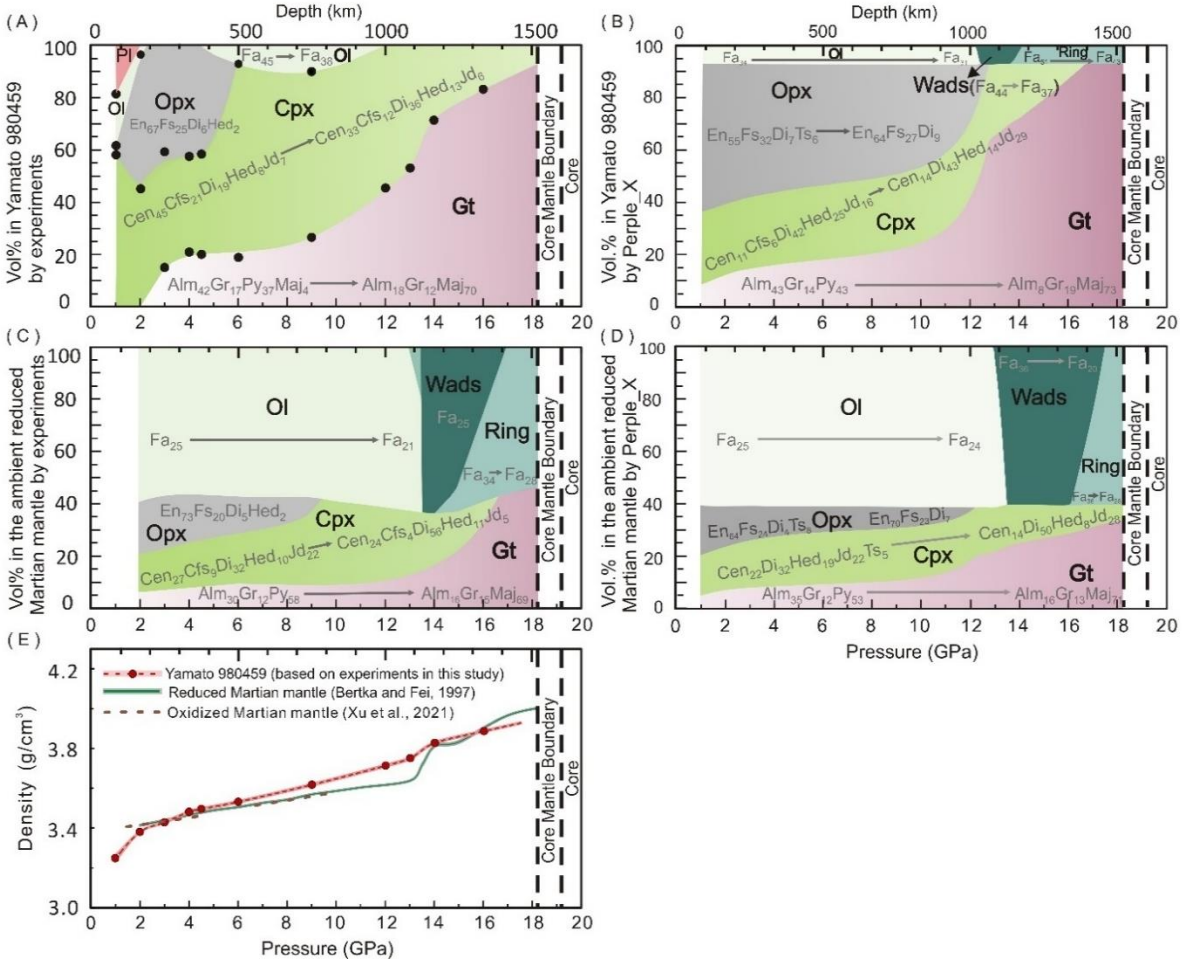

Fig. V.1. (**A**) Experimental phase diagram of Yamato 980459, the black dots representing experimental data points. (**B**) Phase diagram of Yamato 980459 calculated using Perple_X; (**C**) Phase diagram of the ambient Martian mantle under reducing conditions from the DW model (Bertka and Fei, 1997). (**D**) Phase diagram of the ambient Martian mantle calculated using Perple_X with the DW model. (**E**) Densities of Yamato 980459 and the DW model versus pressure; the red dots are the experimental results; the shaded regions are bounded by Voigt and Reuss bounds. (Pl: plagioclase; Opx: orthopyroxene; Cpx: clinopyroxene; Wads: wadsleyite; Ring: ringwoodite; Fa: fayalite; Fo: forsterite; En: enstatite; Fs: ferrosilite; Cen: clinoenstatite; Cfs: clinoferrosilite; Di: diopside; Hed: hedenbergite; Jd: jadeite; Alm: almandine; Gr: grossular; Py: pyrope; Maj: majorite).

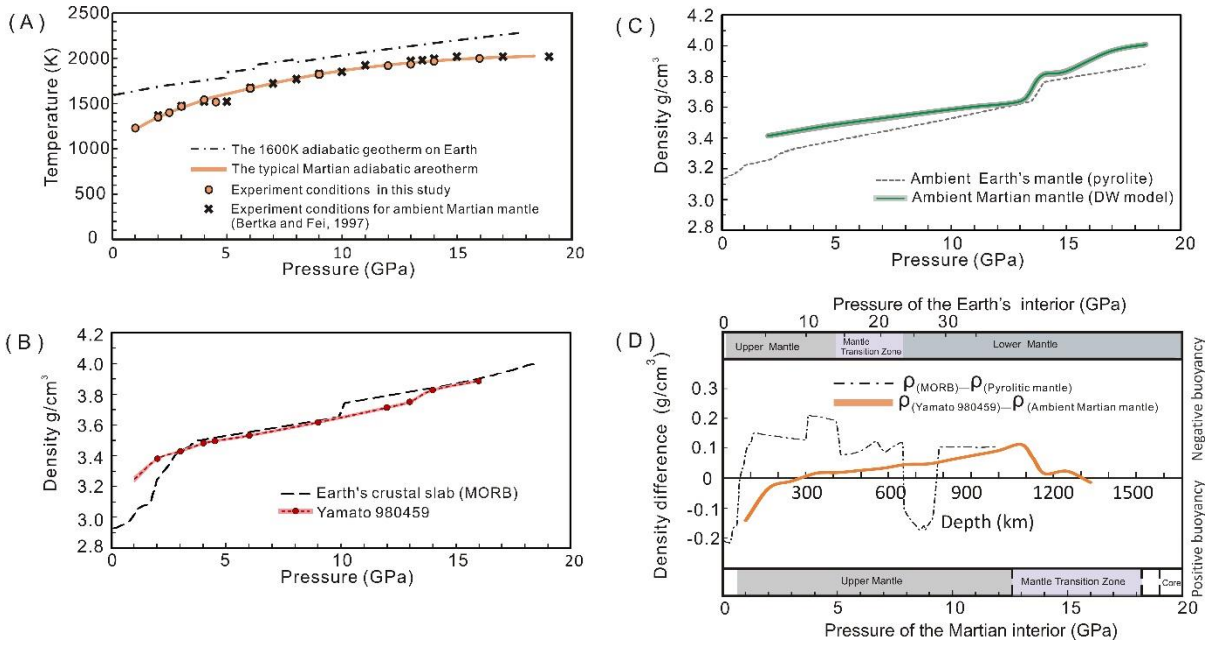

Fig. V.2. *(**A**) Dotted line: Typical 1600 K adiabat for Earth (Katsura et al., 2010); Solid line: typical Martian areotherm (Longhi et al., 1992). (**B**) Density of MORB (Xu et al., 2008) and Yamato 980459 as a function of pressure along the Martian areotherm and Earth's geotherm shown in Fig. V.2A. (**C**) Density of pyrolite (Xu et al., 2008) and the DW model (Bertka and Fei, 1997) as a function of pressure along the Martian areotherm and Earth's geotherm shown in Fig. V.2A. (**D**) Dotted line: density difference between a MORB crustal slab and the ambient (pyrolite) mantle along the Earth's geotherm shown in Fig. V.2A (Katsura et al., 2010; Xu et al., 2008); Solid line: density difference between a Martian crustal slab (Yamato 980459, this study) and the ambient Martian mantle (the DW model, Bertka and Fei, 1997) along the Martian areotherm shown in Fig. V.2A.*

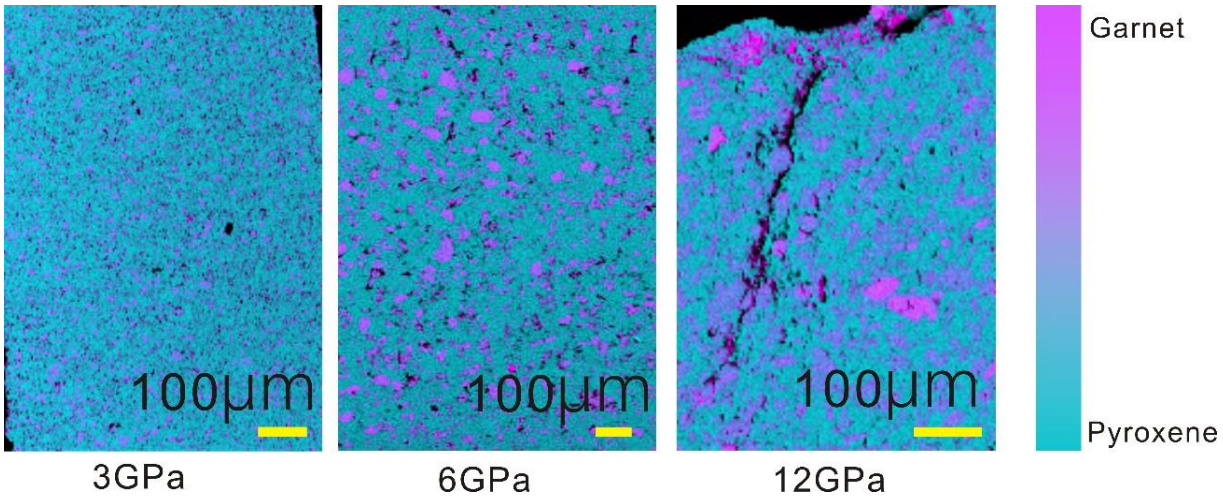

Fig. V.3. *Increasing garnet content with pressure in Yamato 980459, shown by merging Al and Si composition maps measured by EPMA.*

3.2 Melting of GUSEV basalt (Humphrey) and NWA 8159 along the adiabatic areotherm

Unlike Yamato 980459, the GUSEV basalt (Humphrey) composition undergoes partial melting along the adiabatic areotherm of Mars, whereas the basalts with NWA 8159 composition completely melt at 1 GPa and partially melt at 2.5 GPa along the same areotherm. For example, the quenched run products from 1 GPa and 1223 K, with starting compositions of NWA 8159 and GUSEV basalt (Humphrey), both show the spinifex texture of melt (Fig. V.S3), suggesting that 1223 K is well-above solidus of GUSEV basalt (Humphrey) and above liquidus of NWA 8159. In contrast, the phase diagrams of GUSEV basalt (Humphrey) calculated by Semprich and Filiberto (2020) using Perple_X did not show any melt phase between 0.1-3 GPa up to 1373 K, which is again possibly due to the poorly constrained thermodynamic properties of the (pseudo) Fe-end member mantle minerals.

Compared with GUSEV basalt (Humphrey) and NWA 8159, MORB has a much higher solidus. For example, the solidus of MORB is ~1600 K at 1 GPa (Yang and Faccenda, 2020),

at least 377 K higher than that of NWA 8159 and GUSEV basalt (Humphrey). This is explained by the lower Fe content of MORB (~8 wt%) versus NWA 8159 (~21 wt%) and GUSEV basalt (Humphrey) (~19 wt%). The lower liquidus temperature of NWA 8159 compared with GUSEV basalt (Humphrey) at 1 GPa is also consistent with higher FeO content and much lower MgO content in NWA 8159. Similarly, Collinet et al. (2015) reported that the solidus of the terrestrial peridotite is 50 K higher than that of the more Fe-rich ambient Martian mantle.

Due to their low solidus temperatures, crustal slabs made of NWA 8159 or GUSEV basalt (Humphrey) would melt along the Martian adiabatic areotherm. This implies that the compositions of NWA 8159 or GUSEV basalt (Humphrey) are evolved. A previous experimental study also suggested that GUSEV basalt (Humphrey) represents an evolved melt produced by melt/mineral fractionation (Filiberto et al., 2008). As such, they are unlikely to be representative of the Martian crust, due to the limited magmatic differentiation and fractional crystallization on Mars (Collinet et al., 2015; Filiberto and Dasgupta, 2011; McSween et al., 2009). Future experiments are needed to constrain the basalt-eclogite transitions in these evolved Martian basalts along slightly colder Martian areotherms.

3.3 Difficulties to develop buoyancy-driven subduction in the Martian history

To quantitatively evaluate the effect of Martian eclogite on the buoyancy of the slab, we calculated the sinking torques and equilibrium velocities for three different model slabs with 45^{o} dipping angles in the ambient Martian mantle (Fig. V.4). As described in the Method section 2.3, these represent idealized lithosphere structures at different periods in Martian history. We assume the model crusts have the same composition as Yamato 980459 and the model lithosphere mantle has a DW composition. As shown in Fig. V.4, a positive torque/subduction velocity indicates that the slab is dense enough to sink in the mantle (i.e.,

the slab is negatively buoyant with respect to the mantle) whereas negative torque/subduction velocity indicates that the slab would tend to float.

Assuming zero temperature difference between the slab and the ambient Martian mantle, the torque and subduction velocity remain negative for all three slab structures shorter than 650 km in length, thereby prohibiting slabs of this length or less from sinking. However, if the slab is colder than the ambient Martian mantle, the results are somewhat different. In model A, the 30-km thick crustal slab needs to be longer than 300 km to sink even if the slab is on average 400 K colder than the ambient mantle. Therefore, buoyancy-driven continuous subduction cannot be sustained in early Mars unless Martian slabs were somehow forced into the Martian mantle to depth of at least a few hundred kms. The development of slab subduction in model B strongly depends on the temperature anomaly of the 110 km thick composite slab. For example, the slab needs to be longer than 300 km to sink if the slab is 200 K colder than the ambient mantle. This critical length decreases to 150 km if the slab is 400 K colder. On the other hand, the present-day composite slab with 500 km thickness (Fig. V.4C) could easily sink into the mantle due to its much thicker (450 km) and strongly negative buoyant lithospheric mantle. However, fracture and the subsequent formation of plates would be extremely difficult for such an ultra-thick lithosphere in a relatively small planet (e.g., Mars ~ radius 3396 km; Tang et al., 2020).

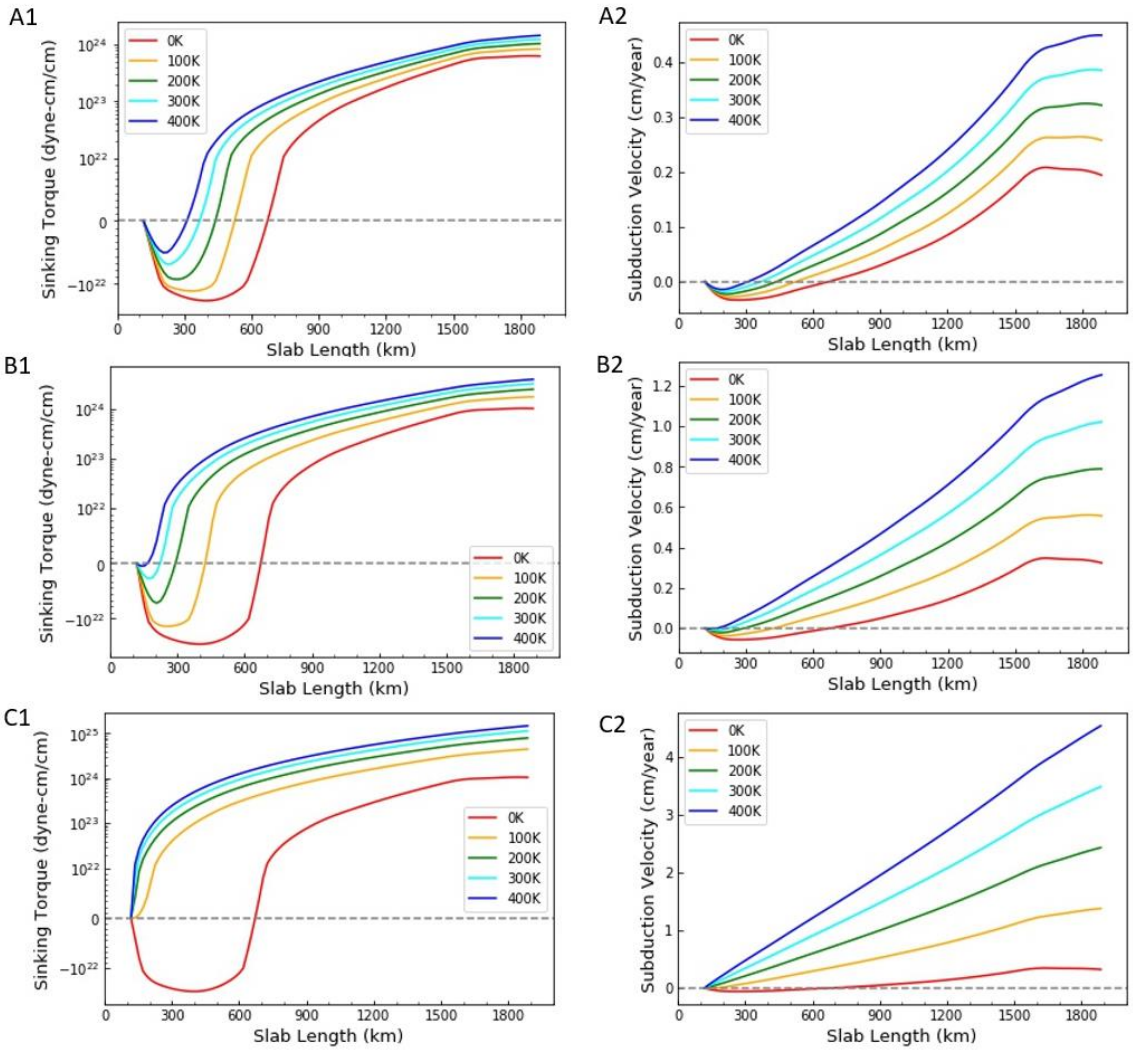

Fig. V.4. *Calculated Martian slab sinking torques (A1, B1, C1) and velocities (A2, B2, C2) for model A, B and C at different temperature anomalies (ΔT =T_{mantle}-T_{slab}). Model A: a 30 km thick crustal slab formed in early Mars. Model B: a 110 km thick composite slab made of a 50 km thick crust and a 60 km thick lithospheric mantle. Model C: a 500 km thick composite slab with a 450 km thick lithospheric mantle below the overlying 50 km thick crust.*

In short, when Mars was young, its thin lithosphere primarily made of basaltic crust was probably easier to fracture and form a multi-plate network (Tang et al., 2020).

Nevertheless, we find that the low density of Martian eclogites made subduction unlikely at that time (Fig. V.5B). Due to secular cooling, the Martian lithosphere thickens and becomes more negatively buoyant over time, eventually allowing it to sink. But it also becomes harder to fracture, thereby inhibiting formation of the plate boundary structures needed to initiate subduction (Fig. V.5C). Nevertheless, we cannot rule out the possibility that at some intermediate stage in Martian history the lithosphere structure allowed for both plate boundary formation as well as negative slab buoyancy. Additional constraints on slab structure and petrology and better resolution of Martian history are needed to address this possibility.

4 Implications

4.1 Geodynamic implications of the buoyant Martian eclogite

The positive buoyancy of eclogite transformed from the nearly primary shergottite basalt has far-reaching implications for the chemical and thermal evolution of Mars. With little Martian crustal material recycled back into the mantle, the crust and the deep mantle tend to separate into distinct geochemical reservoirs, evolving separately through geologic time. Insufficient heat transfer between the deep interior and surface on Mars possibly depressed the heat flux at the core-mantle boundary and resulted in the demise of the Martian dynamo (Breuer et al., 2010). This scenario is also consistent with an early magma ocean and subsequent overturn that may lead to a stably stratified mantle density structure, with generally negative consequences for plate tectonics (Schaefer and Elkins-Tanton, 2018). It is important to note that the compositions of the average Martian crust and mantle as well as their temperature profiles in Martian history are uncertain, and the Martian mantle could be heterogeneous and less enriched in Fe than the classic DW model (Khan et al., 2018; Khan et

al., 2022; Marchi et al., 2020; Wu et al., 2021; Yoshizaki and McDonough, 2020). If so, the conclusions from our dynamic modeling will need to be adjusted.

For example, Semprich and Filiberto (2020) suggested that basalt-eclogite transition can be shifted to lower pressures thus shallower depth along colder areotherms. However, early experiments reported that, due to slow diffusion of ions at temperature less than 873–1073 K, the basalt to eclogite transformation is delayed in the Earth's upper mantle (Ahrens and Schubert, 1975). Delays of this type are supported by metastable gabbro and mafic granulites survival in some ultra-high-*P* and low-*T* metamorphic environments (Faccenda and Dal Zilio, 2017). Therefore, the basalt-eclogite transition on Mars may not take place at lower temperatures due to the kinetic barrier. Interestingly, water is found to increase the reaction rate of basalt-eclogite transition even under lower temperatures and thus can promote the formation of garnet (Ahrens and Schubert, 1975), whereas it can also decrease the density of subducted oceanic crust due to the potential formation of low-density hydrous minerals (e.g., lawsonite) (Chen et al., 2013). Unfortunately, the water contents of the Martian crust and Martian mantle are both highly uncertain (350-6600 ppm for crust and 0.1-250 ppm for mantle, Filiberto et al., 2019; Hu et al., 2020), so that more work is needed to understand the complex effect of water on the buoyancy of Martian eclogite.

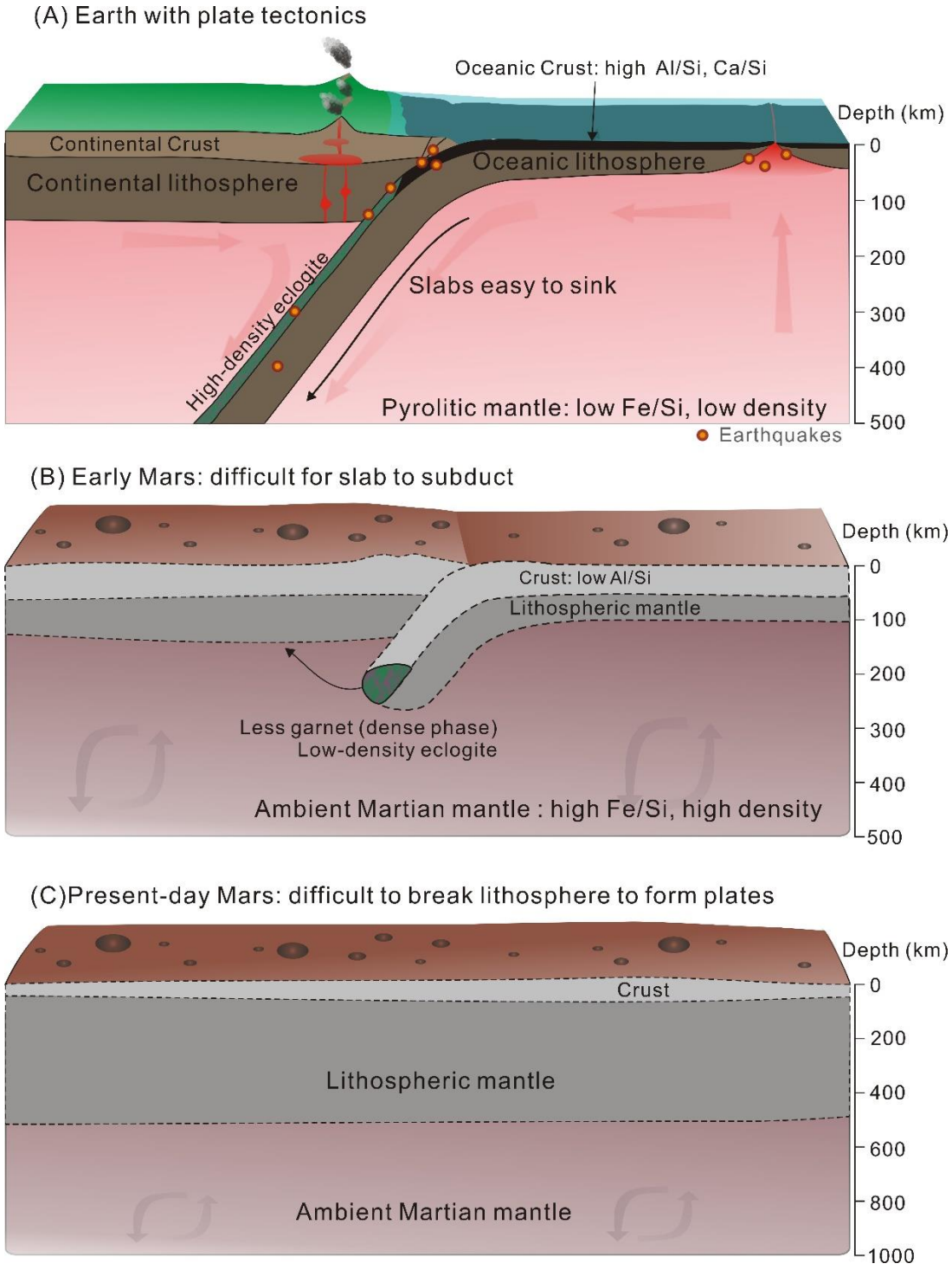

Fig. V.5. *(**A**) Earth with plate tectonics driven by dense subducting slabs; (**B**) Early Mars with no plate tectonics, possibly resulting from the positive buoyancy of eclogite in the ambient Martian mantle; (**C**) Present-day Mars; strength of its thick lithosphere inhibits plate tectonics.*

Future experiments exploring wider crustal composition ranges along colder Martian areotherms can help us understand the possible consequences of the compositions and thermal history on the development of plate tectonics of Mars. Nevertheless, our hypothesis sheds some new lights on understanding the failure of the plate tectonics on Mars (Fig. V.5B). In particular, compared with the Perple_X computational results shown in Semprich and Filiberto (2020) which suggest Martian eclogites transformed from basalts (e.g., GUSEV basalt (Humphrey), Yamato 980459) are denser than the Martian mantle and thus can be easily recycled into the mantle through delamination, our study suggests the opposite: recycling of the Martian crust into the Martian interior is difficult. Moreover, we also found that the failure of plate tectonics on Mars is related to not only the density of Martian eclogite but also the thicknesses of Martian crust and lithosphere (Figs. 5B, 5C). And finally, the evolved high-Fe Martian basalts (GUSEV basalt (Humphrey), NWA 8159) would melt along the Martian adiabatic areotherm, suggesting they are unlikely the representative chemical compositions of the Martian crust due to the limited magmatic differentiation and fractional crystallization history on Mars (Collinet et al., 2015; Filiberto and Dasgupta, 2011; McSween et al., 2009; Filiberto et al., 2008).

4.2 Martian basalt is seismically most distinguishable at transition zone depths

Based on the recent geophysical data obtained from the InSight Mission, Stähler et al. (2021) inverted the *V*p profiles inside Mars down to 800 km depth and the *V*s profiles down to the core-mantle boundary (1520-1600 km) using three different inversion approaches (seismic inversion, geophysical inversion, and geodynamic inversion). Their results indicate that *V*s remains almost constant with depth between 50 km to 1050 km depth in the Martian upper mantle. The abrupt *V*s increase at ~1050 km depth marks the boundary between the Martian upper mantle and transition zone (Stähler et al., 2021). Interpreting these interesting seismic

observations requires our knowledge of the geophysical properties of the Martian crust and mantle rock candidates.

A number of studies have calculated seismic velocity profiles of different Martian crust and mantle rock candidates along Martian areotherms (Plesa et al., 2021; Semprich and Filiberto, 2020; Smrekar et al., 2018). Smrekar et al. (2019) used both Perple_X and Vacher softwares to calculate *V*p and *V*s of the Martian interior assuming the DW model along a hot end-member areotherm. Plesa et al. (2021) used 3D thermal evolution models to constrain the *V*p and *V*s profiles assuming different Martian mantle composition models.

In contrast, there is only one experiment-based determination of *V*p and *V*s profiles for the ambient Martian mantle (Xu et al., 2021), but it was limited to 10.6 GPa (~900 km depth) and relatively oxidizing conditions. Bertka and Fei (1997) conducted phase equilibrium experiments on the ambient Martian mantle DW composition under reducing conditions. It is important to also determine the seismic velocities of ambient Martian mantle under reducing conditions, for comparison with Xu et al. (2021) and for their detection in the Martian mantle. We have used our experimental results to calculate *V*p and *V*s along a typical Martian areotherm down to the core-mantle boundary, for a basalt with Yamato 980459 composition and for ambient Martian mantle with DW composition. These are compared with recent velocity models of Stähler et al. (2021) and the experimental study by Xu et al. (2021). We adopted the experimentally-determined mineral proportions and compositions from this study and from Bertka and Fei (1997), and utilized experimentally determined thermoelastic parameters of relevant mineral phases (Table V.S1, Equations S2-S39). The resulting *V*p and *V*s profiles are shown in Fig. V.6.

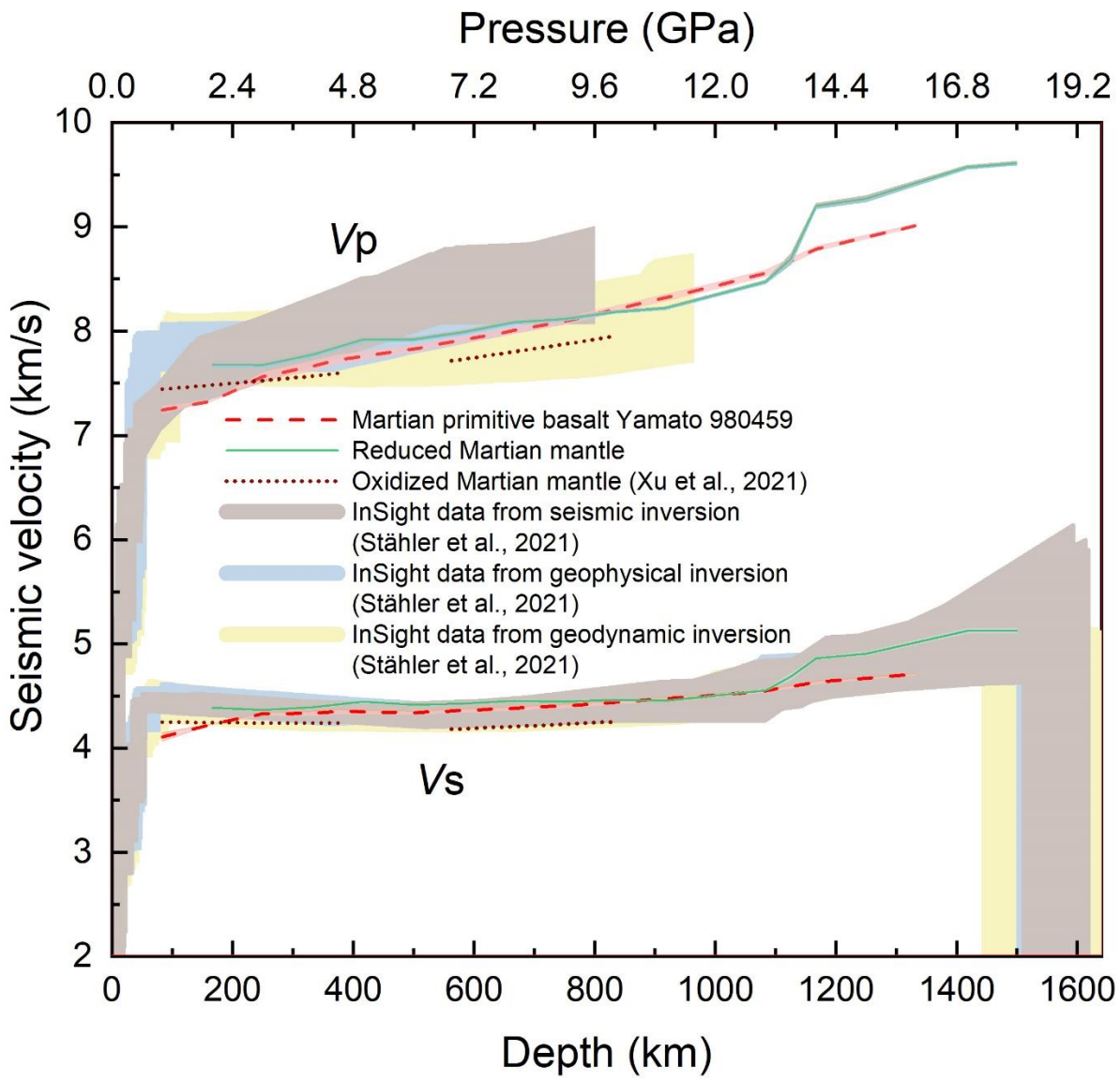

Fig. V.6. *Vp and Vs of Yamato 980459, for a reduced Martian mantle (calculated based on experiments in Bertka and Fei, 1997), and for an oxidized Martian mantle (Xu et al., 2021) along the Martian adiabatic areotherm, compared to seismic velocity profiles (95% credible intervals) from the recent InSight Mission (Stähler et al., 2021). The shaded regions for Yamato 980459 and the reduced Martian mantle are constrained by Voigt and Reuss bounds.*

The *V*p and *V*s profiles of the reduced and oxidized Martian mantle and Yamato 980459 are all in basic agreement with the Martian mantle 1D seismic models constrained from the InSight data (Fig. V.6). The reduced Martian mantle is faster than the oxidized Martian mantle due to the higher Opx content in the oxidized Martian mantle (Xu et al., 2021). Opx is seismically slow among different major mineral phases in the Martian mantle. Yamato 980459 becomes seismically faster than the oxidized Martian mantle below 250 km due to the basalt-eclogite transition. On the other hand, at depths shallower than ~833km (~10 GPa), Yamato 980459 exhibits lower *V*p and *V*s compared with the reduced Martian mantle. At depths greater than ~833 km, *V*p of Yamato 980459 is higher than the reduced Martian mantle down to the base of the upper mantle (~1150 km depth), whereas the *V*s remains similar. Both the *V*p and *V*s of the reduced Martian mantle show an abrupt increase between ~1080-1167 km because of the Ol to Ringwoodite and Wads transformations as found in Bertka and Fei (1997) (Fig. V.1C). The best depth range for detecting the Martian basalt in the Martian interior is between 1150 km and 1400 km in the transition zone, where the *V*s of Yamato 980459 is about 5% lower than that of the reduced Martian mantle.

5. Conclusions

1) High *P-T* phase relationships for a nearly primitive Martian shergottite (Yamato 980459) are determined experimentally up to 16 GPa 2000 K using two Multi-Anvil Presses. The Martian eclogite transformed from this primitive Martian basalt is less dense than the ambient Martian mantle at depths shallower than ~300 km, possibly hindering the subduction of thin slabs into the interior of the young Mars. Although the lithosphere on present-day Mars could

be dense enough to subduct, fracture of this cold thick lithosphere to form mobile plates would require unrealistically large stresses (Tang et al., 2020).

2) GUSEV basalt (Humphrey) and NWA 8159 have much lower solidus *T*s than MORB, due to their Fe-rich compositions. Because they are subject to partial or complete melting along the Martian adiabatic areotherm, they are probably evolved basalts (Filiberto et al., 2008). As such, they are unlikely representative chemical composition of the Martian crust.

3) *V*p and *V*s calculated for the reduced ambient Martian mantle and the Martian primitive basalt (Yamato 980459) along a typical Martian mantle areotherm indicate that the seismic velocity contrast between Martian basalt and ambient Martian mantle reaches a maximum value of 5% between 1150 km and 1400 km depth, within the mantle transition zone.

Acknowledgments We thank Bin Chen, Xiaojing Lai, and Yoshiyuki Okuda for their tutorial in the COMPRES 10/5 assembly, Sibo Chen and Zhiyuan Ren for suggestions and help in the Multi-Anvil experiments, and Mike Spilde for his help with the EPMA experiments. Sandia National Laboratories is a multi-mission laboratory managed and operated by National Technology & Engineering Solutions of Sandia, LLC, a wholly owned subsidiary of Honeywell International Inc., for the U.S. Department of Energy's National Nuclear Security Administration under contract DE-NA0003525. This project is supported by the Startup funding (J.S.Z.) and the Woman in STEM award from the UNM (J.S.Z.).

References

Azuma, S., Katayama, I., 2017. Evolution of the rheological structure of Mars. Earth, Planets and Space 69.

Bertka, C.M., Fei, Y., 1997. Mineralogy of the Martian interior up to core-mantle boundary pressures. Journal of Geophysical Research: Solid Earth 102, 5251-5264.

Breuer, D., Labrosse, S., Spohn, T., 2010. Thermal Evolution and Magnetic Field Generation in Terrestrial Planets and Satellites. Space Science Reviews 152, 449-500.

Carr, M.H., Head III, J.W., 2010. Geologic history of Mars. Earth and Planetary Science Letters 294, 185-203.

Collinet, M., Médard, E., Charlier, B., Vander Auwera, J., Grove, T.L., 2015. Melting of the primitive martian mantle at 0.5–2.2 GPa and the origin of basalts and alkaline rocks on Mars. Earth and Planetary Science Letters 427, 83-94.

Collinet, M., Plesa, A.C., Grove, T.L., Schwinger, S., Ruedas, T., Breuer, D., 2021. MAGMARS: A Melting Model for the Martian Mantle and FeO-Rich Peridotite. Journal of Geophysical Research: Planets 126, e2021JE006985.

Coltice, N., Husson, L., Faccenna, C., Arnould, M., 2019. What drives tectonic plates? Science advances 5, eaax4295.

Connolly, J.A.D., 2005. Computation of phase equilibria by linear programming: A tool for geodynamic modeling and its application to subduction zone decarbonation. Earth and Planetary Science Letters 236, 524-541.

Dreibus, G., Haubold, R., Huisl, W., Spettel, B., 2003. Comparison of the chemistry of Yamato 980459 with DaG 476 and SaU 005, Evolution of Solar System Materials: A new Perspective from Antarctic Meteorites. National Institute of Polar Research (NIPR), pp. 19-20.

Faccenda, M., Dal Zilio, L., 2017. The role of solid–solid phase transitions in mantle convection. Lithos 268, 198-224.

Filiberto, J., Dasgupta, R., 2011. Fe2+–Mg partitioning between olivine and basaltic melts: Applications to genesis of olivine-phyric shergottites and conditions of melting in the Martian interior. Earth and Planetary Science Letters 304, 527-537.

Filiberto, J., Treiman, A., Le, L., 2008. Crystallization experiments on a Gusev Adirondack basalt composition. Meteoritics & Planetary Science 43, 1137-1146.

Greeley, R., Foing, B.H., McSween Jr, H.Y., Neukum, G., Pinet, P., van Kan, M., Werner, S.C., Williams, D.A., Zegers, T.E., 2005. Fluid lava flows in Gusev crater, Mars. Journal of Geophysical Research: Planets 110.

Greshake, A., Fritz, J., Stöffler, D., 2004. Petrology and shock metamorphism of the olivine-phyric shergottite Yamato 980459: Evidence for a two-stage cooling and a single-stage ejection history. Geochimica et Cosmochimica Acta 68, 2359-2377.

Gross, J., Filiberto, J., Herd, C.D., Daswani, M.M., Schwenzer, S.P., Treiman, A.H., 2013. Petrography, mineral chemistry, and crystallization history of olivine-phyric shergottite NWA 6234: A new melt composition. Meteoritics & Planetary Science 48, 854-871.

Hauck, S.A., 2002. Thermal and crustal evolution of Mars. Journal of Geophysical Research 107.

Herd, C.D., Walton, E.L., Agee, C.B., Muttik, N., Ziegler, K., Shearer, C.K., Bell, A.S., Santos, A.R., Burger, P.V., Simon, J.I., 2017. The Northwest Africa 8159 martian meteorite: Expanding the martian sample suite to the early Amazonian. Geochimica et Cosmochimica Acta 218, 1-26.

Holland, T.J.B., Powell, R., 2011. An improved and extended internally consistent thermodynamic dataset for phases of petrological interest, involving a new equation of state for solids. Journal of Metamorphic Geology 29, 333-383.

Ito, K., Kennedy, G.C., 1971. An experimental study of the basalt-garnet granulite-eclogite transition. The structure and physical properties of the Earth's crust 14, 303-314.

Justh, H., 2014. Mars Global Reference Atmospheric Model 2010 Version: Users Guide.

Katsura, T., Yoneda, A., Yamazaki, D., Yoshino, T., Ito, E., 2010. Adiabatic temperature profile in the mantle. Physics of the Earth and Planetary Interiors 183, 212-218.

Khan, A., Liebske, C., Rozel, A., Rivoldini, A., Nimmo, F., Connolly, J., Plesa, A.C., Giardini, D., 2018. A geophysical perspective on the bulk composition of Mars. Journal of Geophysical Research: Planets 123, 575-611.

Khan, A., Sossi, P., Liebske, C., Rivoldini, A., Giardini, D., 2022. Geophysical and cosmochemical evidence for a volatile-rich Mars. Earth and Planetary Science Letters 578, 117330.

Knapmeyer-Endrun, B., Panning, M.P., Bissig, F., Joshi, R., Khan, A., Kim, D., Lekić, V., Tauzin, B., Tharimena, S., Plasman, M., 2021. Thickness and structure of the martian crust from InSight seismic data. Science 373, 438-443.

Lagain, A., Benedix, G., Servis, K., Baratoux, D., Doucet, L., Rajšic, A., Devillepoix, H., Bland, P., Towner, M., Sansom, E., 2021. The Tharsis mantle source of depleted shergottites revealed by 90 million impact craters. Nature communications 12, 1-9.

Lenardic, A., Nimmo, F., Moresi, L., 2004. Growth of the hemispheric dichotomy and the cessation of plate tectonics on Mars. Journal of Geophysical Research: Planets 109, n/a-n/a.

Longhi, J., Knittle, E., Holloway, J.R., Waenke, H., 1992. The bulk composition, mineralogy and internal structure of Mars. Mars, 184-208.

Marchi, S., Walker, R.J., Canup, R.M., 2020. A compositionally heterogeneous martian mantle due to late accretion. Science advances 6, eaay2338.

McSween, H.Y., Taylor, G.J., Wyatt, M.B., 2009. Elemental composition of the Martian crust. Science 324, 736-739.

McSween, H.Y., Wyatt, M.B., Gellert, R., Bell, J., Morris, R.V., Herkenhoff, K.E., Crumpler, L.S., Milam, K.A., Stockstill, K.R., Tornabene, L.L., 2006. Characterization and petrologic interpretation of olivine-rich basalts at Gusev Crater, Mars. Journal of Geophysical Research: Planets 111.

Misawa, K., 2003. The Yamato 980459 shergottite consortium. International SymposiumEvolution of Solar System Materials: A New Perspective from Antarctic Meteorites. Tokyo, Natl Inst. Polar Res 8485.

Peslier, A., Hnatyshin, D., Herd, C., Walton, E., Brandon, A., Lapen, T., Shafer, J., 2010. Crystallization, melt inclusion, and redox history of a Martian meteorite: Olivine-phyric shergottite Larkman Nunatak 06319. Geochimica et Cosmochimica Acta 74, 4543-4576.

Plesa, A.C., Bozdağ, E., Rivoldini, A., Knapmeyer, M., McLennan, S.M., Padovan, S., Tosi, N., Breuer, D., Peter, D., Staehler, S., 2021. Seismic velocity variations in a 3D Martian mantle: implications for the InSight measurements. Journal of Geophysical Research: Planets 126, e2020JE006755.

Schaefer, L., Elkins-Tanton, L.T., 2018. Magma oceans as a critical stage in the tectonic development of rocky planets. Philos Trans A Math Phys Eng Sci 376.

Semprich, J., Filiberto, J., 2020. High-pressure metamorphic mineralogy of the Martian crust with implications for density and seismic profiles. Meteoritics & Planetary Science 55, 1600-1614.

Shih, C.-Y., Nyquist, L.E., Wiesmann, H., Reese, Y., Misawa, K., 2005. Rb-Sr and Sm-Nd dating of olivine-phyric shergottite Yamato 980459: Petrogenesis of depleted shergottites. Antarctic Meteorite Research 18, 46.

Shirai, N., Ebihara, M., 2004. Chemical characteristics of a Martian meteorite, Yamato 980459. Antarctic Meteorite Research 17, 55.

Smrekar, S.E., Lognonné, P., Spohn, T., Banerdt, W.B., Breuer, D., Christensen, U., Dehant, V., Drilleau, M., Folkner, W., Fuji, N., Garcia, R.F., Giardini, D., Golombek, M., Grott, M., Gudkova, T., Johnson, C., Khan, A., Langlais, B., Mittelholz, A., Mocquet, A., Myhill, R., Panning, M., Perrin, C., Pike, T., Plesa, A.-C., Rivoldini, A., Samuel, H., Stähler, S.C., van Driel, M., Van Hoolst, T., Verhoeven, O., Weber, R., Wieczorek, M., 2018. Pre-mission InSights on the Interior of Mars. Space Science Reviews 215.

Tang, C., Webb, A., Moore, W., Wang, Y., Ma, T., Chen, T., 2020. Breaking Earth's shell into a global plate network. Nature communications 11, 1-6.

Taylor, G.J., 2013. The bulk composition of Mars. Geochemistry 73, 401-420.

Thio, V., Cobden, L., Trampert, J., 2016. Seismic signature of a hydrous mantle transition zone. Physics of the Earth and Planetary Interiors 250, 46-63.

Tosi, N., Padovan, S., 2021. Mercury, Moon, Mars: Surface Expressions of Mantle Convection and Interior Evolution of Stagnant-Lid Bodies. Mantle convection and surface expressions, 455-489.

Wänke, H., Dreibus, G., 1994. Chemistry and accretion history of Mars. Philosophical Transactions of the Royal Society of London. Series A: Physical and Engineering Sciences 349, 285-293.

White, D.S.M., Dalton, H.A., Kiefer, W.S., Treiman, A.H., 2006. Experimental petrology of the basaltic shergottite Yamato-980459: Implications for the thermal structure of the Martian mantle. Meteoritics & Planetary Science 41, 1271-1290.

Workman, R.K., Hart, S.R., 2005. Major and trace element composition of the depleted MORB mantle (DMM). Earth and Planetary Science Letters 231, 53-72.

Wu, Y., Li, Q.-L., Che, X., Liao, S., 2021. Heterogeneous martian mantle: Evidence from petrology, mineral chemistry, and in situ U-Pb chronology of the basaltic shergottite Northwest Africa 8653. Geochimica et Cosmochimica Acta 309, 352-365.

Xu, F., Siersch, N., Greaux, S., Rivoldini, A., Kuwahara, H., Kondo, N., Wehr, N., Menguy, N., Kono, Y., Higo, Y., 2021. Low velocity zones in the Martian upper mantle highlighted by sound velocity measurements. Geophysical Research Letters 48, e2021GL093977.

Xu, W., Lithgow-Bertelloni, C., Stixrude, L., Ritsema, J., 2008. The effect of bulk composition and temperature on mantle seismic structure. Earth and Planetary Science Letters 275, 70-79.

Yang, J., Faccenda, M., 2020. Intraplate volcanism originating from upwelling hydrous mantle transition zone. Nature 579, 88-91.

Yoshizaki, T., McDonough, W.F., 2020. The composition of Mars. Geochimica et Cosmochimica Acta 273, 137-162.

Yoshizaki, T., McDonough, W.F., 2021. Earth and Mars–distinct inner solar system products. Geochemistry 81, 125746.

Supplementary Information

Experimental methods

We grounded the starting materials in an agate mortar for 6 h to ensure well mixing. The starting materials were then kept in a vacuum oven at 110 ℃ before use. The experimental *P-T* conditions for all successful runs are shown in Table V.2 in main text. Experiments at 1-9 GPa were performed using the UNM 14/8 assemblies and experiments at 12-16 GPa were performed using the COMPRES 10/5 assemblies (Fig. V.S1). In those experimental runs with Mo capsule, all the run products showed even elemental distribution and little absorption of Al, Ca, Mg, Fe and Si (Fig. V.S2). We also conducted high-pressure (12-16 GPa) phase equilibrium experiments with BN capsules using the 1000-ton Press located at the University of Hawai‘i at Mānoa. However, in the runs with BN capsules, strong absorption of Ca, Mg, and Si was observed (Fig. V.S2). Therefore, we used only the results obtained from the experimental runs conducted with Mo capsules.

All run products were polished, initially with coarse silicon carbide sandpapers and finally with 1 μm alumina powder, to expose a smooth surface of mineral assemblages for optical examination under the microscope and carbon coating for later Electron Probe Microanalysis (EPMA). The element standards for EPMA measurements were albite for Na, olivine for Mg, diopside for Si and Ca, and almandine for Al and Fe. The accelerating voltage was 15 kV and the beam current was 20 nA during operation. Mineral grain sizes were larger than 5 μm and beam size was smaller than 1 μm. To obtain the average chemical composition of each mineral phase, we performed measurements on multiple grains within the same run product. We avoided analyzing the chemical compositions of mineral grains located close to the sample capsule. Based on the average chemical composition of each phase and the starting

material composition, we calculated the weight percent (wt.%) of each mineral phase using the Least Square Mass Balance method(Bertka and Fei, 1997). Using elastic properties of the individual minerals (Table V.S1), we applied third-order (e.g., Gt, pyroxene) or fourth-order finite strain EOS (e.g., Ol) to obtain the density, bulk modulus, and shear modulus of each mineral phase in each run product (Equations S7-S39), along with the volume proportion of each mineral (vol%). We then calculated the bulk densities, V_P, and V_S for the mineral aggregates using Voigt-Reuss-Hill averaging scheme (see Supplementary Equations S2-S6). We applied the same method to calculate the density, V_P, and V_S for the ambient Martian mantle with DW composition, based on the experimental results from Bertka and Fei (1997) (Table V.3 in the main text).

Perple_X calculation

Perple_X is a thermodynamic calculation software package based on Gibbs free energy minimization in a multi-component system(Connolly, 2005). In this study, we used the thermodynamic database by Stixrude and Lithgow-Bertelloni(Stixrude and Lithgow-Bertelloni, 2011). We firstly used the program BUILD to establish the parameter space that would be used for the calculation (e.g., bulk composition, *P-T* conditions), and then ran the program VERTEX to conduct the calculation, and finally utilized the program WERAMI to extract the information we needed at each *P-T* condition (e.g., mineral proportions and compositions). The computational results are shown in Fig. V.1 in the main text.

Martian lithosphere thickness

The Martian lithosphere elastic thicknesses were estimated to be 0-20 km during the Noachian period, increase to >50 km during the Hesperian period, and are 40-150 km spanning most of the Amazonian period(Grott et al., 2012; Grott and Breuer, 2008). The lithosphere mechanical thickness (above the asthenosphere) is 1-2 times the elastic thickness on Earth(McNutt, 1984; Ranalli, 1994), so we adopt the same relationship (1.5) to calculate mechanical lithosphere thicknesses on Mars (see Method 2.2 in the Main Text).

The equilibrium velocity of the slab U is calculated by balancing the sinking torque against the lifting torque by the mantle flow. A corner flow model(Turcotte and Schubert, 2002) with uniform mantle viscosity μ and 45º slab dip yields a lifting torque of approximately $9\mu UR$; equating this with Equation 1 in the main text yields

$$U \approx \frac{\tau}{9\mu R} \quad \text{(S1)}$$

Fig. V.4A2, V.4B2, and V.4C2 in the main text show the equilibrium velocity U for the same set of conditions as in Fig. V.4A1, V.4B1, and V.4C1, respectively. The mantle viscosity used in the Equation S1 is 6×10^{21} Pa-s, which is the average viscosity of the Martian mantle in the *P* range 4-8 GPa(Ruedas et al., 2013). Positive equilibrium velocities correspond to situations in which the dipping angle of the slab can remain constant in time during subduction, whereas negative velocities indicate excess lifting torques, positive slab buoyancy, or both. The slab sinking torque and velocity models are both written in Interactive Data Language.

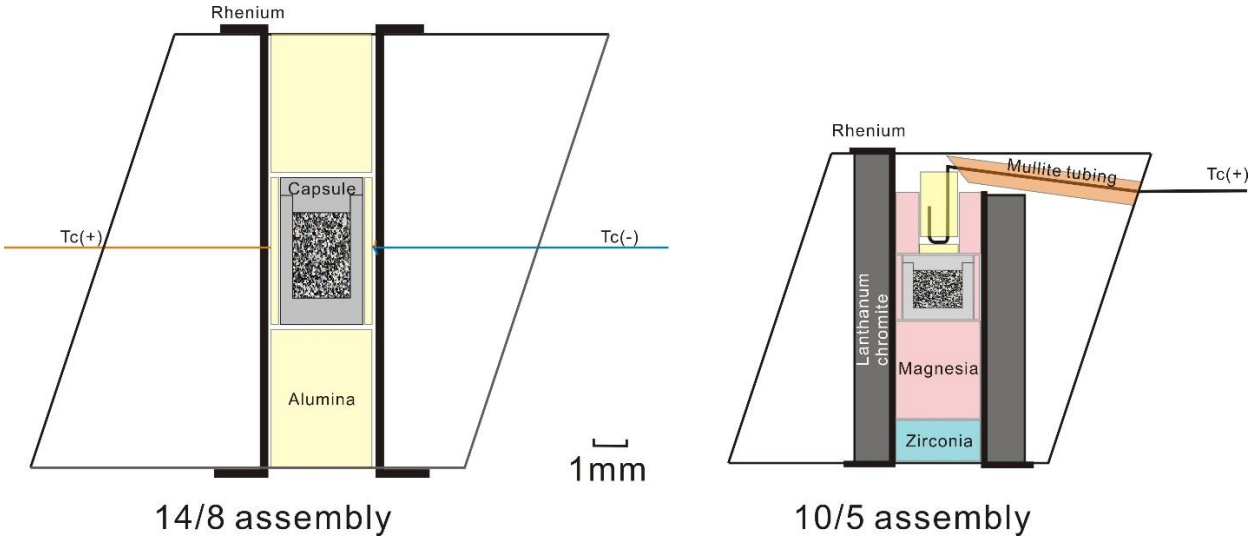

Fig. V.S1. *Schematic cross sections of the UNM 14/8 assembly (Agee et al., 1995) and the COMPRES 10/5 assembly (Leinenweber et al., 2012).*

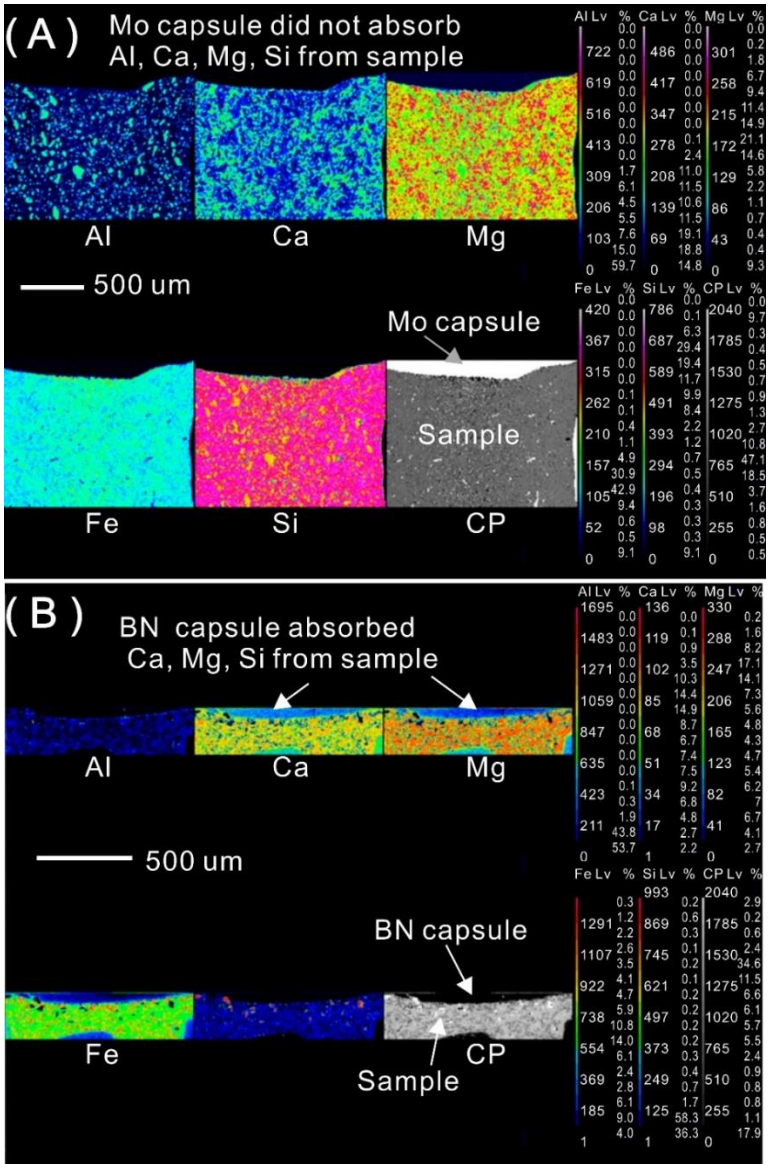

Fig. V.S2. *The run products in Mo capsule and BN capsules. (A) Chemical composition maps for the 4.5 GPa experiment with Mo capsule (capsule is shown as white color in the CP image); the Mo capsule does not absorb Al, Ca, Mg, Fe and Si.* ***(B)*** *Chemical composition maps for the 18 GPa experiment with BN capsule; The BN capsule absorbs a significant amount of Ca, Mg and Si from the sample, so the experiments performed with BN capsules are not used in this study. These compositional maps suggest that Mo capsule is better than BN capsule for high P-T experiments in the Ca-Mg-Si system.*

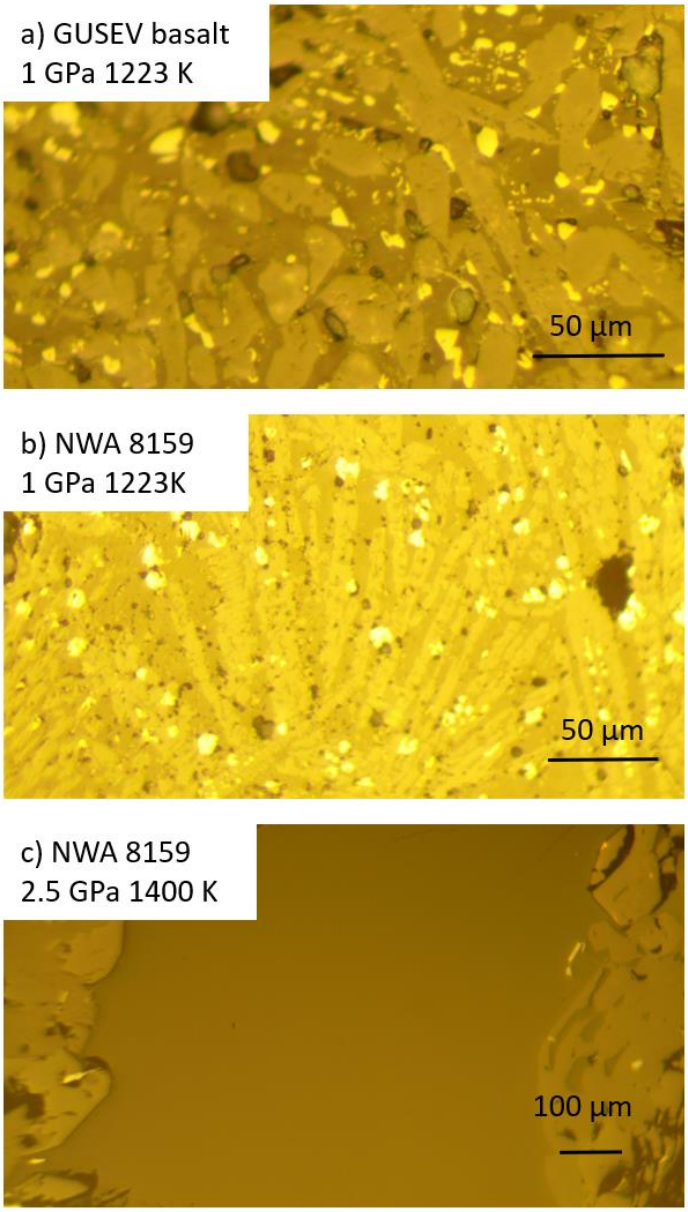

Fig. V.S3. *High P-T run products with NWA8159 and GUSEV basalt (Humphrey) compositions. Run products are polished and examined under the microscope under reflected light illumination. All 3 run products are partially or completely melted.*

Table V.S1. *The thermoelastic properties of different endmember mineral phases for calculating density, Vp and Vs of Yamato 980459 and the DW model at high pressure-temperature (P-T) conditions (bulk modulus: Ks; shear modulus: G).*

Mineral	Endmember	*Ks*	*G*	density0	d*Ks*/d*P*	d^2Ks/d^2P	d*Ks*/d*T*	d*G*/d*P*	d^2G/d^2P	d*G*/d*T*	a_0 ($10^{-4}K^{-1}$)	a_1 ($10^{-8}K^{-2}$)	a_2(K)
Ol	Fo[Mao et al., 2015; Meng et al., 1993]	128.8	81.6	3.227	4.47	0	-0.02	1.8	-0.1	-0.01	0.306	0.796	-0.5782
	Fa[Fei, 1995; Speziale, 2004; Suzuki et al., 1981]	136.3(2)	51.2(2)	4.388(9)	4.9(1)	0	-0.027	1.8(1)	-0.11	-0.017	0.2386	1.153	-0.0518
Pyroxene	En[Jackson et al., 2007; Kung, 2005]	108.5(15)	77.9(7)	3.210	7.2(7)	0	-0.0263(3)	1.7(1)	0	-0.0136(3)	0.297(2)	0.57(1)	0
	Fs[Bass and Weidner, 1984; de Vries et al., 2013; Hugh-Jones, 1997; Kung, 2005]	101(4)	52(2)	4.002(5)	7.2(7)	0	-0.0263(3)	1.7(1)	0	-0.0136(3)	0.57	0	0
	Di[Finger and Ohashi, 1976; Hao et al., 2021; Li and Neuville, 2010]	116.4(7)	73.0(4)	3.272(6)	4.9(1)	0	-0.012(1)	1.6(1)	0	-0.011(1)	0.19	2.08	0
	Hed[Fei, 1995; Kandelin and Weidner, 1988; Li and Neuville, 2010]	120(4)	62(2)	3.657(1)	4	0	-0.012(1)	1.6(1)	0	-0.011(1)	0.298	0	0
	Jd[Hao et al., 2020; Hao et al., 2021]	138(3)	84(2)	3.302	3.9(1)	0	-0.012(1)	1.09(4)	0	-0.011(1)	0.34(5)	0.9	0
Gt	Py[Fei, 1995; Irifune et al., 2008a; Liu et al., 2000; Sinogeikin, 2002; SUZUKI and ANDERSON, 1983]	171.0(5)	94.9(2)	3.560(20)	4.4(1)	0	-0.014(3)	1.15(6)	0	-0.011(2)	0.288	0.2787	-0.5521
	Alm[Arimoto et al., 2015; Fei, 1995]	174.2(12)	94.9(7)	4.319(2)	4.61(14)	0	-0.0267(7)	1.06(6)	0	-0.0131(8)	0.26(5)	2.3(14)	0
	Gr[Fei, 1995; Gwanmesia et al., 2014]	171.2(8)	107.4(2)	3.605(2)	4.47(2)	0	-0.0138(3)	1.29(5)	0	-0.0128(2)	0.1951	0.8089	-0.4972
	Mg-Maj[Fei, 1995; Hao et al., 2020; Irifune et al., 2008a; Liu et al., 2000; Sinogeikin, 2002; SUZUKI and ANDERSON, 1983]	162.0(5)	86.2(2)	3.560(2)	4.4(1)	0	-0.014 (3)	1.15(6)	0	-0.011(2)	0.288	0.2787	-0.5521
	Fe-Maj[Fei, 1995; Ismailova et al., 2017; Murakami et al., 2008; SUZUKI and ANDERSON, 1983]	180.24	88.7(7)	4.409	4.2(2)	0	-0.014(3)	1.28(8)	0	-0.011(2)	0.288	0.2787	-0.5521
Wads	$Fo_{75}Fa_{25}$[Fei et al., 1992; Finger et al., 1993; Zhou et al., 2021]	169(1)	97(2)	3.808(2)	6(1)	-0.16(2)	−0.018(2)	1.8(1)	-0.076(7)	−0.014 (1)	0.2711	0.6885	-0.5767
Ring	Fo[Fei, 1995; Higo et al., 2008; Schulze et al., 2018; SUZUKI et al., 1979]	187(1)	121.1(5)	3.569	3.8(1)	0	-0.014(3)	1.5(1)	-0.046(14)	-0.012(2)	0.2497	0.3639	-0.6531
	Fa[Armentrout and Kavner, 2011; Schulze et al., 2018; Yamanaka, 1986]	204(5)	103(5)	4.848	4	0	-0.014(3)	1.5(1)	-0.046(14)	-0.012(2)	0.2697	0	0

The *V*p and *V*s of plagioclase ($Albite_{46}Anorthite_{54}$) in this study is from the velocity of plagioclase ($Albite_{46}Anorthite_{51}$)(Kono et al., 2008), the density of plagioclase is calculated from data in ref. (Fei, 1995). Ol: olivine; Fa: fayalite; Fo: forsterite; En: enstatite; Fs, ferrosilite; Di: diopside; Hed: hedenbergite; Jd: jadeite; Gt: garnet; Py: pyrope; Alm: almandine; Gr: grossular; Maj: majorite; Wads: wadsleyite; Ring: ringwoodite.

Voigt-Reuss-Hill average of the physical properties of multi-phase mineral aggregates

The Reuss bound represents a uniform stress scenario whereas Voigt bound stands for a uniform strain scenario. In a multi-phase aggregate:

Reuss (R) bound:

$$E^R = \left(\frac{f_a}{E_a} + \frac{f_b}{E_b} + \frac{f_c}{E_c} + \cdots\right)^{-1} \quad \text{(S2)}$$

Voigt (V) bound:

$$E^V = f_a E_a + f_b E_b + f_c E_c + \cdots \quad \text{(S3)}$$

$$\text{Voigt} - \text{Ruess} - \text{Hill (VRH) Average: } E^{VRH} = \frac{E^V + E^R}{2} \quad \text{(S4)}$$

where E^V, E^R, and E^{VRH} represents aggregate properties (*K*s, *G*, ρ) of Voigt bound, Reuss bound, and Hill average (Hill, 1963), respectively; E_a, E_b, E_c … etc. represent these properties of mineral *a*, *b*, c… etc. respectively; f_a, f_b , f_c … etc. represent the volume proportions of mineral *a*, *b*, c… etc. respectively.

$$V_P{}^2 = \frac{K}{\rho} + 4/3\frac{G}{\rho} \quad \text{(S5)}$$

$$V_S{}^2 = \frac{G}{\rho} \quad \text{(S6)}$$

where *V*p and *V*s of Voigt bound, Reuss bound, and Hill average are then derived. The actual properties (*K*, *G*, ρ, *V*p, *V*s) of the multi-phase aggregate should lie in between the Reuss and Voigt bounds. We used Voigt-Reuss-Hill average for our calculations. The Voigt and Reuss bounds are both plotted in Fig. V.1 and V.6.

Using finite strain EOS to calculate the *V*p, *V*s, and ρ of Yamato 980459 and the DW model at high *P-T* conditions

We used the following finite strain EOS to calculate *Ks*, *G*, and ρ of minerals in Yamato 980459 run products and the DW model run products. The choice of using 3rd or 4th order finite strain EOS for each mineral depends on previous studies as shown in Table V.S1. We finally used equations S1-S5 to calculate the *V*p, *V*s, and ρ of mineral aggregates for Yamato 980459 and the DW model under each *P-T* condition.

The 3rd order finite strain EOS(Davies, 1974; Davies and Dziewonski, 1975; Duffy and Anderson, 1989) :

$$\varepsilon = \frac{1}{2}[1 - (\frac{\rho}{\rho_0})^{\frac{2}{3}}] \quad \text{(S7)}$$

$$\rho Vs^2 = (1 - 2\varepsilon)^{\frac{5}{2}}(M_1 + M_2 \cdot \varepsilon) \quad \text{(S8)}$$

$$\rho Vp^2 = (1 - 2\varepsilon)^{\frac{5}{2}}(L_1 + L_2 \cdot \varepsilon) \quad \text{(S9)}$$

$$P = -(1 - 2\varepsilon)^{\frac{5}{2}}(C_1 \cdot \varepsilon + \frac{1}{2}C_2 \cdot \varepsilon^2) \quad \text{(S10)}$$

where ε is strain, ρ is density, ρ_0 is ambient density. M_1, M_2, L_1, L_2, C_1, and C_2 are defined as:

$$M_1 = G_0 \quad \text{(S11)}$$

$$M_2 = 5M_1 - 3K_{S0} \cdot G_0{}' \quad \text{(S12)}$$

$$L_1 = K_0 + \frac{4}{3}M_1 \quad \text{(S13)}$$

$$L_2 = 5L_1 - 3K_{S0}(K_{S0}{}' + \frac{4}{3}G_0{}') \quad \text{(S14)}$$

Where G_0' and $K_{S0}{}'$ represent $(\partial G/\partial P)_{T0}$ and $(\partial Ks/\partial P)_{T0}$ shown in the main text, respectively.

$$C_1 = 3L_1 - 4M_1 \quad \text{(S15)}$$

$$C_2 = 3L_2 - 4M_2 + 7C_1 \quad \text{(S16)}$$

$$G = \rho \cdot Vs^2 \quad \text{(S17)}$$

$$K_S = \rho \cdot Vp^2 - \frac{4}{3}G \quad \text{(S18)}$$

$$\rho_0(T) = \rho_0(300\text{K}) \cdot \exp\left(-\int_{300}^{T} \alpha(T)dT\right) \quad \text{(S19)}$$

$$M_0(T) = M_0(300\text{K}) + \left(\frac{\partial M}{\partial T}\right)_P (T - 300) \quad \text{(S20)}$$

$$M_0'(T) = M_0'(300\text{K})\exp\left(\int_{300}^{T} \alpha(T)dT\right) \quad \text{(S21)}$$

Where $\rho_0(300K)$represents density under ambient *P* and *T* (300K). $\rho_0(T)$ represents density under ambient *P* and high *T*. α refers to thermal expansion shown in the main text. $M_0(300\text{K})$ represents the elastic moduli *K*s and *G* under ambient *P* and *T* (300K). $M_0(T)$ represents the elastic moduli *K*s and *G* under ambient *P* and high *T*. $\left(\frac{\partial M}{\partial T}\right)_P$ is the *T* derivative of elastic moduli under isobaric condition. $M_0'(T)$ represents the *P* derivative of elastic moduli *K*s and *G* under ambient *P* and high *T*.

The 4th order finite strain EOS(Davies, 1974; Davies and Dziewonski, 1975; Duffy and Anderson, 1989):

$$\varepsilon = \frac{1}{2}\left[1 - \left(\frac{\rho}{\rho_0}\right)^{\frac{2}{3}}\right] \quad \text{(S22)}$$

$$\rho Vs^2 = (1 - 2\varepsilon)^{\frac{5}{2}}\left(M_1 + M_2 \cdot \varepsilon + \frac{1}{2}M_3 \cdot \varepsilon^2\right) \quad \text{(S23)}$$

$$\rho Vp^2 = (1 - 2\varepsilon)^{\frac{5}{2}}\left(L_1 + L_2 \cdot \varepsilon + \frac{1}{2}L_3 \cdot \varepsilon^2\right) \quad \text{(S24)}$$

$$P = -(1 - 2\varepsilon)^{\frac{5}{2}}\left(C_1 \cdot \varepsilon + \frac{1}{2}C_2 \cdot \varepsilon^2 + \frac{1}{6}C_3 \cdot \varepsilon^3\right) \quad \text{(S25)}$$

where ε is strain, ρ is density, ρ_0 is ambient density. M_1, M_2, M_3, L_1, L_2, L_3, C_1, C_2, and C_3 are defined as:

$$M_1 = G_0 \quad \text{(S26)}$$

$$M_2 = 5M_1 - 3K_{S0} \cdot G_0' \quad \text{(S27)}$$

$$M_3 = 9G_0'' \cdot {K_{S0}}^2 - 3(K_{S0}' - 4)M_2 + 5(3K_{S0}' - 5)M_1 \quad \text{(S28)}$$

$$L_1 = K_0 + \frac{4}{3}M_1 \quad \text{(S29)}$$

$$L_2 = 5L_1 - 3K_{S0}(K_{S0}' + \frac{4}{3}G_0') \quad \text{(S30)}$$

$$L_3 = 9K_{S0}'' \cdot K_{S0}{}^2 + 12G_0'' \cdot K_{S0}{}^2 - 3(K_{S0}' - 4)L_2 + 5(3K_{S0}' - 5)L_1 \quad \text{(S31)}$$

Where G_0', G_0'', K_{S0}', and K_{S0}'' represent $(\partial G/\partial P)_{T0}$, $(\partial^2 G/\partial P^2)_{T0}$, $(\partial Ks/\partial P)_{T0}$, and $(\partial^2 Ks/\partial P^2)_{T0}$ shown in the main text, respectively.

$$C_1 = 3L_1 - 4M_1 \quad \text{(S32)}$$

$$C_2 = 3L_2 - 4M_2 + 7C_1 \quad \text{(S33)}$$

$$C_3 = 3L_3 - 4M_3 + 9C_2 \quad \text{(S34)}$$

$$G = \rho \cdot Vs^2 \quad \text{(S35)}$$

$$K_S = \rho \cdot Vp^2 - \frac{4}{3}G \quad \text{(S36)}$$

$$\rho_0(T) = \rho_0(300\text{K}) \cdot \exp\left(-\int_{300}^{T} \alpha(T)dT\right) \quad \text{(S37)}$$

$$M_0(T) = M_0(300\text{K}) + \left(\frac{\partial M}{\partial T}\right)_P (T - 300) \quad \text{(S38)}$$

$$M_0'(T) = M_0'(300\text{K})\exp\left(\int_{300}^{T} \alpha(T)dT\right) \quad \text{(S39)}$$

Where $\rho_0(300K)$represents density under ambient *P* and *T* (300K). $\rho_0(T)$ represents density under ambient *P* and high *T*. α refers to thermal expansion shown in the main text. $M_0(300\text{K})$ represents the elastic moduli *K*s and *G* under ambient *P* and *T* (300K). $M_0(T)$ represents the elastic moduli *K*s and *G* under ambient *P* and high *T*. $\left(\frac{\partial M}{\partial T}\right)_P$ is the *T* derivative of elastic moduli under isobaric condition. $M_0'(\text{T})$ represents the *P* derivative of elastic moduli *K*s and *G* under ambient *P* and high *T*.

Supplementary References

Agee, C.B., Li, J., Shannon, M.C., Circone, S., 1995. Pressure-temperature phase diagram for the Allende meteorite. Journal of Geophysical Research: Solid Earth 100, 17725-17740.
Anderson, D.L., Bass, J.D., 1986. Transition region of the Earth's upper mantle. Nature 320, 321-328.
Arimoto, T., Gréaux, S., Irifune, T., Zhou, C., Higo, Y., 2015. Sound velocities of Fe3Al2Si3O12 almandine up to 19 GPa and 1700 K. Physics of the Earth and Planetary Interiors 246, 1-8.
Armentrout, M., Kavner, A., 2011. High pressure, high temperature equation of state for Fe2SiO4 ringwoodite and implications for the Earth's transition zone. Geophysical Research Letters 38.
Azuma, S., Katayama, I., 2017. Evolution of the rheological structure of Mars. Earth, Planets and Space 69.
Bass, J.D., Weidner, D.J., 1984. Elasticity of single-crystal orthoferrosilite. Journal of Geophysical Research: Solid Earth 89, 4359-4371.
Bertka, C.M., Fei, Y., 1997. Mineralogy of the Martian interior up to core-mantle boundary pressures. Journal of Geophysical Research: Solid Earth 102, 5251-5264.
Blum, J., Shen, Y., 2004. Thermal, hydrous, and mechanical states of the mantle transition zone beneath southern Africa. Earth and Planetary Science Letters 217, 367-378.
Breuer, D., Labrosse, S., Spohn, T., 2010. Thermal Evolution and Magnetic Field Generation in Terrestrial Planets and Satellites. Space Science Reviews 152, 449-500.
Buchen, J., Marquardt, H., Speziale, S., Kawazoe, T., Boffa Ballaran, T., Kurnosov, A., 2018. High-pressure single-crystal elasticity of wadsleyite and the seismic signature of water in the shallow transition zone. Earth and Planetary Science Letters 498, 77-87.
Burdick, S., Lekić, V., 2017. Velocity variations and uncertainty from transdimensional P-wave tomography of North America. Geophysical Journal International 209, 1337-1351.
Canales, J.P., Carbotte, S.M., Nedimović, M., Carton, H., 2017. Dry Juan de Fuca slab revealed by quantification of water entering Cascadia subduction zone. Nature Geoscience 10, 864-870.
Carr, M.H., Head III, J.W., 2010. Geologic history of Mars. Earth and Planetary Science Letters 294, 185-203.
Collinet, M., Médard, E., Charlier, B., Vander Auwera, J., Grove, T.L., 2015. Melting of the primitive martian mantle at 0.5–2.2 GPa and the origin of basalts and alkaline rocks on Mars. Earth and Planetary Science Letters 427, 83-94.
Collinet, M., Plesa, A.C., Grove, T.L., Schwinger, S., Ruedas, T., Breuer, D., 2021. MAGMARS: A Melting Model for the Martian Mantle and FeO-Rich Peridotite. Journal of Geophysical Research: Planets 126, e2021JE006985.
Coltice, N., Husson, L., Faccenna, C., Arnould, M., 2019. What drives tectonic plates? Science advances 5, eaax4295.
Connolly, J.A.D., 2005. Computation of phase equilibria by linear programming: A tool for geodynamic modeling and its application to subduction zone decarbonation. Earth and Planetary Science Letters 236, 524-541.
Courtillot, V., Davaille, A., Besse, J., Stock, J., 2003. Three distinct types of hotspots in the Earth’s mantle. Earth and Planetary Science Letters 205, 295-308.
Dannberg, J., Sobolev, S.V., 2015. Low-buoyancy thermochemical plumes resolve controversy of classical mantle plume concept. Nat Commun 6, 6960.
Davies, G., 1974. Effective elastic moduli under hydrostatic stress—I. quasi-harmonic theory. Journal of Physics and Chemistry of Solids 35, 1513-1520.
Davies, G., Dziewonski, A., 1975. Homogeneity and constitution of the Earth's lower mantle and outer core. Physics of the Earth and Planetary Interiors 10, 336-343.
de Vries, J., Jacobs, M.H.G., van den Berg, A.P., Wehber, M., Lathe, C., McCammon, C.A., van Westrenen, W., 2013. Thermal equation of state of synthetic orthoferrosilite at lunar pressures and temperatures. Physics and Chemistry of Minerals 40, 691-703.

Deon, F., Koch-Müller, M., Rhede, D., Wirth, R., 2010. Water and Iron effect on the P-T-x coordinates of the 410-km discontinuity in the Earth upper mantle. Contributions to Mineralogy and Petrology 161, 653-666.
Dreibus, G., Haubold, R., Huisl, W., Spettel, B., 2003. Comparison of the chemistry of Yamato 980459 with DaG 476 and SaU 005, Evolution of Solar System Materials: A new Perspective from Antarctic Meteorites. National Institute of Polar Research (NIPR), pp. 19-20.
Duffy, T.S., Anderson, D.L., 1989. Seismic velocities in mantle minerals and the mineralogy of the upper mantle. Journal of Geophysical Research: Solid Earth 94, 1895-1912.
Faccenda, M., Dal Zilio, L., 2017. The role of solid–solid phase transitions in mantle convection. Lithos 268, 198-224.
Fei, H., Katsura, T., 2020. High water solubility of ringwoodite at mantle transition zone temperature. Earth and Planetary Science Letters 531, 115987.
Fei, Y., 1995. Thermal expansion. Mineral physics and crystallography: a handbook of physical constants 2, 29-44.
Fei, Y., Mao, H.-k., Shu, J., Parthasarathy, G., Bassett, W.A., Ko, J., 1992. Simultaneous high-P, high-TX ray diffraction study of β-(Mg,Fe)2SiO4to 26 GPa and 900 K. Journal of Geophysical Research 97.
Filiberto, J., Dasgupta, R., 2011. Fe2+–Mg partitioning between olivine and basaltic melts: Applications to genesis of olivine-phyric shergottites and conditions of melting in the Martian interior. Earth and Planetary Science Letters 304, 527-537.
Filiberto, J., Treiman, A., Le, L., 2008. Crystallization experiments on a Gusev Adirondack basalt composition. Meteoritics & Planetary Science 43, 1137-1146.
Finger, L.W., Hazen, R.M., Zhang, J., Ko, J., Navrotsky, A., 1993. The effect of Fe on the crystal structure of wadsleyite β-(Mg 1− x Fe x) 2 SiO 4, 0.00≤ x≤ 0.40. Physics and Chemistry of Minerals 19, 361-368.
Finger, L.W., Ohashi, Y., 1976. The thermal expansion of diopside to 800 degrees C and a refinement of the crystal structure at 700 degrees C. American Mineralogist 61, 303-310.
Frost, D.J., Dolejš, D., 2007. Experimental determination of the effect of H2O on the 410-km seismic discontinuity. Earth and Planetary Science Letters 256, 182-195.
Fukao, Y., Obayashi, M., 2013. Subducted slabs stagnant above, penetrating through, and trapped below the 660 km discontinuity. Journal of Geophysical Research: Solid Earth 118, 5920-5938.
Goes, S., Capitanio, F.A., Morra, G., 2008. Evidence of lower-mantle slab penetration phases in plate motions. Nature 451, 981-984.
Greeley, R., Foing, B.H., McSween Jr, H.Y., Neukum, G., Pinet, P., van Kan, M., Werner, S.C., Williams, D.A., Zegers, T.E., 2005. Fluid lava flows in Gusev crater, Mars. Journal of Geophysical Research: Planets 110.
Greshake, A., Fritz, J., Stöffler, D., 2004. Petrology and shock metamorphism of the olivine-phyric shergottite Yamato 980459: Evidence for a two-stage cooling and a single-stage ejection history. Geochimica et Cosmochimica Acta 68, 2359-2377.
Gross, J., Filiberto, J., Herd, C.D., Daswani, M.M., Schwenzer, S.P., Treiman, A.H., 2013. Petrography, mineral chemistry, and crystallization history of olivine-phyric shergottite NWA 6234: A new melt composition. Meteoritics & Planetary Science 48, 854-871.
Grott, M., Baratoux, D., Hauber, E., Sautter, V., Mustard, J., Gasnault, O., Ruff, S.W., Karato, S.I., Debaille, V., Knapmeyer, M., Sohl, F., Van Hoolst, T., Breuer, D., Morschhauser, A., Toplis, M.J., 2012. Long-Term Evolution of the Martian Crust-Mantle System. Space Science Reviews 174, 49-111.
Grott, M., Breuer, D., 2008. The evolution of the Martian elastic lithosphere and implications for crustal and mantle rheology. Icarus 193, 503-515.
Gwanmesia, G.D., Wang, L., Heady, A., Liebermann, R.C., 2014. Elasticity and sound velocities of polycrystalline grossular garnet (Ca3Al2Si3O12) at simultaneous high pressures and high temperatures. Physics of the Earth and Planetary Interiors 228, 80-87.

Gwanmesia, G.D., Whitaker, M.L., Dai, L., James, A., Chen, H., Triplett, R.S., Cai, N., 2020. The Elastic Properties of β-Mg2SiO4 Containing 0.73 wt.% of H2O to 10 GPa and 600 K by Ultrasonic Interferometry with Synchrotron X-Radiation. Minerals 10, 209.
Hao, M., Zhang, J.S., Pierotti, C.E., Zhou, W.-Y., Zhang, D., Dera, P., 2020. The seismically fastest chemical heterogeneity in the Earth's deep upper mantle—implications from the single-crystal thermoelastic properties of jadeite. Earth and Planetary Science Letters 543, 116345.
Hao, M., Zhang, J.S., Zhou, W.Y., Wang, Q., 2021. Seismic Visibility of Eclogite in the Earth's Upper Mantle—Implications From High Pressure-Temperature Single-Crystal Elastic Properties of Omphacite. Journal of Geophysical Research: Solid Earth 126, e2021JB021683.
Hauck, S.A., 2002. Thermal and crustal evolution of Mars. Journal of Geophysical Research 107.
Hayes, G.P., Moore, G.L., Portner, D.E., Hearne, M., Flamme, H., Furtney, M., Smoczyk, G.M., 2018. Slab2, a comprehensive subduction zone geometry model. Science 362, 58-61.
Herd, C.D., Walton, E.L., Agee, C.B., Muttik, N., Ziegler, K., Shearer, C.K., Bell, A.S., Santos, A.R., Burger, P.V., Simon, J.I., 2017. The Northwest Africa 8159 martian meteorite: Expanding the martian sample suite to the early Amazonian. Geochimica et Cosmochimica Acta 218, 1-26.
Higo, Y., Inoue, T., Irifune, T., Funakoshi, K.-i., Li, B., 2008. Elastic wave velocities of (Mg0. 91Fe0. 09) 2SiO4 ringwoodite under P–T conditions of the mantle transition region. Physics of the Earth and Planetary Interiors 166, 167-174.
Hill, R., 1963. Elastic properties of reinforced solids: some theoretical principles. Journal of the Mechanics and Physics of Solids 11, 357-372.
Holland, T.J.B., Powell, R., 2011. An improved and extended internally consistent thermodynamic dataset for phases of petrological interest, involving a new equation of state for solids. Journal of Metamorphic Geology 29, 333-383.
Houser, C., 2016. Global seismic data reveal little water in the mantle transition zone. Earth and Planetary Science Letters 448, 94-101.
Huang, Q., Schmerr, N., Waszek, L., Beghein, C., 2019. Constraints on Seismic Anisotropy in the Mantle Transition Zone From Long-Period SS Precursors. Journal of Geophysical Research: Solid Earth 124, 6779-6800.
Hugh-Jones, D., 1997. Thermal expansion of MgSiO3 and FeSiO3 ortho-and clinopyroxenes. American Mineralogist 82, 689-696.
Hwang, Y.K., Ritsema, J., Goes, S., 2011. Global variation of body-wave attenuation in the upper mantle from teleseismic P wave and S wave spectra. Geophysical research letters 38.
Inoue, T., Yurimoto, H., Kudoh, Y., 1995. Hydrous modified spinel, Mg1. 75SiH0. 5O4: a new water reservoir in the mantle transition region. Geophysical Research Letters 22, 117-120.
Irifune, T., Higo, Y., Inoue, T., Kono, Y., Ohfuji, H., Funakoshi, K., 2008a. Sound velocities of majorite garnet and the composition of the mantle transition region. Nature 451, 814-817.
Irifune, T., Higo, Y., Inoue, T., Kono, Y., Ohfuji, H., Funakoshi, K., 2008b. Sound velocities of majorite garnet and the composition of the mantle transition region. Nature 451, 814-817.
Isaak, D.G., Gwanmesia, G.D., Falde, D., Davis, M.G., Triplett, R.S., Wang, L., 2007a. The elastic properties of β-Mg2SiO4 from 295 to 660 K and implications on the composition of Earth's upper mantle. Physics of the Earth and Planetary Interiors 162, 22-31.
Isaak, D.G., Gwanmesia, G.D., Falde, D., Davis, M.G., Triplett, R.S., Wang, L., 2007b. The elastic properties of β-Mg2SiO4 from 295 to 660K and implications on the composition of Earth's upper mantle. Physics of the Earth and Planetary Interiors 162, 22-31.
Ishii, T., Kojitani, H., Akaogi, M., 2018. Phase relations and mineral chemistry in pyrolitic mantle at 1600–2200 °C under pressures up to the uppermost lower mantle: Phase transitions around the 660-km discontinuity and dynamics of upwelling hot plumes. Physics of the Earth and Planetary Interiors 274, 127-137.
Ishii, T., Kojitani, H., Akaogi, M., 2019. Phase Relations of Harzburgite and MORB up to the Uppermost Lower Mantle Conditions: Precise Comparison With Pyrolite by Multisample Cell High-

Pressure Experiments With Implication to Dynamics of Subducted Slabs. Journal of Geophysical Research: Solid Earth 124, 3491-3507.
Ismailova, L., Bykov, M., Bykova, E., Bobrov, A., Kupenko, I., Cerantola, V., Vasiukov, D., Dubrovinskaia, N., McCammon, C., Hanfland, M., Glazyrin, K., Liermann, H.-P., Chumakov, A., Dubrovinsky, L., 2017. Effect of composition on compressibility of skiagite-Fe-majorite garnet. American Mineralogist 102, 184-191.
Ito, K., Kennedy, G.C., 1971. An experimental study of the basalt-garnet granulite-eclogite transition. The structure and physical properties of the Earth's crust 14, 303-314.
Ivanov, A.V., Litasov, K.D., 2014. The deep water cycle and flood basalt volcanism. International Geology Review 56, 1-14.
Jackson, J.M., Sinogeikin, S.V., Bass, J.D., 2007. Sound velocities and single-crystal elasticity of orthoenstatite to 1073K at ambient pressure. Physics of the Earth and Planetary Interiors 161, 1-12.
Jordan, T.H., 1988. Structure and formation of the continental tectosphere. Journal of Petrology, 11-37.
Justh, H., 2014. Mars Global Reference Atmospheric Model 2010 Version: Users Guide.
Kaminsky, F., 2012. Mineralogy of the lower mantle: A review of 'super-deep'mineral inclusions in diamond. Earth-Science Reviews 110, 127-147.
Kandelin, J., Weidner, D.J., 1988. Elastic properties of hedenbergite. Journal of Geophysical Research 93.
Karato, S.-i., 2011. Water distribution across the mantle transition zone and its implications for global material circulation. Earth and Planetary Science Letters 301, 413-423.
Katsura, T., Mayama, N., Shouno, K., Sakai, M., Yoneda, A., Suzuki, I., 2001. Temperature derivatives of elastic moduli of (Mg0. 91Fe0. 09) 2SiO4 modified spinel. Physics of the Earth and Planetary Interiors 124, 163-166.
Katsura, T., Shatskiy, A., Manthilake, M.A.G.M., Zhai, S., Yamazaki, D., Matsuzaki, T., Yoshino, T., Yoneda, A., Ito, E., Sugita, M., Tomioka, N., Nozawa, A., Funakoshi, K.-i., 2009. P-V-Trelations of wadsleyite determined by in situ X-ray diffraction in a large-volume high-pressure apparatus. Geophysical Research Letters 36.
Katsura, T., Yamada, H., Nishikawa, O., Song, M., Kubo, A., Shinmei, T., Yokoshi, S., Aizawa, Y., Yoshino, T., Walter, M.J., Ito, E., Funakoshi, K.-i., 2004. Olivine-wadsleyite transition in the system (Mg,Fe)2SiO4. Journal of Geophysical Research: Solid Earth 109.
Katsura, T., Yoneda, A., Yamazaki, D., Yoshino, T., Ito, E., 2010. Adiabatic temperature profile in the mantle. Physics of the Earth and Planetary Interiors 183, 212-218.
Kelbert, A., Schultz, A., Egbert, G., 2009. Global electromagnetic induction constraints on transition-zone water content variations. Nature 460, 1003-1006.
Khan, A., Liebske, C., Rozel, A., Rivoldini, A., Nimmo, F., Connolly, J., Plesa, A.C., Giardini, D., 2018. A geophysical perspective on the bulk composition of Mars. Journal of Geophysical Research: Planets 123, 575-611.
Khan, A., Sossi, P., Liebske, C., Rivoldini, A., Giardini, D., 2022. Geophysical and cosmochemical evidence for a volatile-rich Mars. Earth and Planetary Science Letters 578, 117330.
Knapmeyer-Endrun, B., Panning, M.P., Bissig, F., Joshi, R., Khan, A., Kim, D., Lekić, V., Tauzin, B., Tharimena, S., Plasman, M., 2021. Thickness and structure of the martian crust from InSight seismic data. Science 373, 438-443.
Koelemeijer, P., Ritsema, J., Deuss, A., van Heijst, H.J., 2015. SP12RTS: a degree-12 model of shear- and compressional-wave velocity for Earth's mantle. Geophysical Journal International 204, 1024-1039.
Kono, Y., Miyake, A., Ishikawa, M., Arima, M., 2008. Temperature derivatives of elastic wave velocities in plagioclase (An51 1) above and below the order-disorder transition temperature. American Mineralogist 93, 558-564.
Korenaga, J., 2013. Initiation and Evolution of Plate Tectonics on Earth: Theories and Observations. Annual Review of Earth and Planetary Sciences 41, 117-151.

Kung, J., 2005. In-situ elasticity measurement for the unquenchable high-pressure clinopyroxene phase: Implication for the upper mantle. Geophysical Research Letters 32.
Kuritani, T., Xia, Q.-K., Kimura, J.-I., Liu, J., Shimizu, K., Ushikubo, T., Zhao, D., Nakagawa, M., Yoshimura, S., 2019. Buoyant hydrous mantle plume from the mantle transition zone. Scientific reports 9, 1-7.
Lagain, A., Benedix, G., Servis, K., Baratoux, D., Doucet, L., Rajšic, A., Devillepoix, H., Bland, P., Towner, M., Sansom, E., 2021. The Tharsis mantle source of depleted shergottites revealed by 90 million impact craters. Nature communications 12, 1-9.
Lai, X., Zhu, F., Zhang, J.S., Zhang, D., Tkachev, S., Prakapenka, V.B., Chen, B., 2020. An Externally-Heated Diamond Anvil Cell for Synthesis and Single-Crystal Elasticity Determination of Ice-VII at High Pressure-Temperature Conditions. JoVE (Journal of Visualized Experiments), e61389.
Leinenweber, K.D., Tyburczy, J.A., Sharp, T.G., Soignard, E., Diedrich, T., Petuskey, W.B., Wang, Y., Mosenfelder, J.L., 2012. Cell assemblies for reproducible multi-anvil experiments (the COMPRES assemblies). American Mineralogist 97, 353-368.
Lenardic, A., Nimmo, F., Moresi, L., 2004. Growth of the hemispheric dichotomy and the cessation of plate tectonics on Mars. Journal of Geophysical Research: Planets 109, n/a-n/a.
Li, B., Liebermann, R.C., 2014. Study of the Earth's interior using measurements of sound velocities in minerals by ultrasonic interferometry. Physics of the Earth and Planetary Interiors 233, 135-153.
Li, B., Liebermann, R.C., Weidner, D.J., 2001. P-V-Vp-Vs-T measurements on wadsleyite to 7 GPa and 873 K: Implications for the 410-km seismic discontinuity. Journal of Geophysical Research: Solid Earth 106, 30579-30591.
Li, B., Neuville, D.R., 2010. Elasticity of diopside to 8GPa and 1073K and implications for the upper mantle. Physics of the Earth and Planetary Interiors 183, 398-403.
Li, Z.-H., Gerya, T., Connolly, J.A., 2019. Variability of subducting slab morphologies in the mantle transition zone: Insight from petrological-thermomechanical modeling. Earth-Science Reviews 196, 102874.
Libowitzky, E., Rossman, G.R., 1997. An IR absorption calibration for water in minerals. American Mineralogist 82, 1111-1115.
Liu, J., Chen, G., Gwanmesia, G.D., Liebermann, R.C., 2000. Elastic wave velocities of pyrope–majorite garnets (Py62Mj38 and Py50Mj50) to 9 GPa. Physics of the Earth and Planetary Interiors 120, 153-163.
Liu, J., Hu, Q., Kim, D.Y., Wu, Z., Wang, W., Xiao, Y., Chow, P., Meng, Y., Prakapenka, V.B., Mao, H.-K., 2017. Hydrogen-bearing iron peroxide and the origin of ultralow-velocity zones. Nature 551, 494-497.
Liu, W., Kung, J., Li, B., 2005. Elasticity of San Carlos olivine to 8 GPa and 1073 K. Geophysical Research Letters 32.
Liu, W., Kung, J., Li, B., Nishiyama, N., Wang, Y., 2009a. Elasticity of (Mg0.87Fe0.13)2SiO4 wadsleyite to 12GPa and 1073K. Physics of the Earth and Planetary Interiors 174, 98-104.
Liu, W., Kung, J., Li, B., Nishiyama, N., Wang, Y., 2009b. Elasticity of (Mg0. 87Fe0. 13) 2SiO4 wadsleyite to 12 GPa and 1073 K. Physics of the Earth and Planetary Interiors 174, 98-104.
Liu, Z., Gréaux, S., Cai, N., Siersch, N., Ballaran, T.B., Irifune, T., Frost, D.J., 2019. Influence of aluminum on the elasticity of majorite-pyrope garnets. American Mineralogist: Journal of Earth and Planetary Materials 104, 929-935.
Longhi, J., Knittle, E., Holloway, J.R., Waenke, H., 1992. The bulk composition, mineralogy and internal structure of Mars. Mars, 184-208.
Mao, Z., Fan, D., Lin, J.-F., Yang, J., Tkachev, S.N., Zhuravlev, K., Prakapenka, V.B., 2015. Elasticity of single-crystal olivine at high pressures and temperatures. Earth and Planetary Science Letters 426, 204-215.

Mao, Z., Jacobsen, S.D., Frost, D.J., McCammon, C.A., Hauri, E.H., Duffy, T.S., 2011. Effect of hydration on the single-crystal elasticity of Fe-bearing wadsleyite to 12 GPa. American Mineralogist 96, 1606-1612.
Mao, Z., Jacobsen, S.D., Jiang, F., Smyth, J.R., Holl, C.M., Duffy, T.S., 2008a. Elasticity of hydrous wadsleyite to 12 GPa: Implications for Earth's transition zone. Geophysical Research Letters 35.
Mao, Z., Jacobsen, S.D., Jiang, F.M., Smyth, J.R., Holl, C.M., Frost, D.J., Duffy, T.S., 2008b. Single-crystal elasticity of wadsleyites, β-Mg2SiO4, containing 0.37–1.66 wt.% H2O. Earth and Planetary Science Letters 268, 540-549.
Marchi, S., Walker, R.J., Canup, R.M., 2020. A compositionally heterogeneous martian mantle due to late accretion. Science advances 6, eaay2338.
Mashino, I., Murakami, M., Miyajima, N., Petitgirard, S., 2020. Experimental evidence for silica-enriched Earth's lower mantle with ferrous iron dominant bridgmanite. Proceedings of the National Academy of Sciences 117, 27899-27905.
Mattern, E., Matas, J., Ricard, Y., Bass, J., 2005. Lower mantle composition and temperature from mineral physics and thermodynamic modelling. Geophysical Journal International 160, 973-990.
Mayama, N., Suzuki, I., Saito, T., Ohno, I., Katsura, T., Yoneda, A., 2004. Temperature dependence of elastic moduli of β-(Mg, Fe) 2SiO4. Geophysical research letters 31.
McNutt, M.K., 1984. Lithospheric flexure and thermal anomalies. Journal of Geophysical Research: Solid Earth 89, 11180-11194.
McSween, H.Y., Taylor, G.J., Wyatt, M.B., 2009. Elemental composition of the Martian crust. Science 324, 736-739.
McSween, H.Y., Wyatt, M.B., Gellert, R., Bell, J., Morris, R.V., Herkenhoff, K.E., Crumpler, L.S., Milam, K.A., Stockstill, K.R., Tornabene, L.L., 2006. Characterization and petrologic interpretation of olivine-rich basalts at Gusev Crater, Mars. Journal of Geophysical Research: Planets 111.
Meng, Y., Weidner, D., Gwanmesia, G., Liebermann, R., Vaughan, M., Wang, Y., Leinenweber, K., Pacalo, R., Yeganeh-Haeri, A., Zhao, Y., 1993. In situ high P-TX ray diffraction studies on three polymorphs (α, β, γ) of Mg2SiO4. Journal of Geophysical Research: Solid Earth 98, 22199-22207.
Misawa, K., 2003. The Yamato 980459 shergottite consortium. International SymposiumEvolution of Solar System Materials: A New Perspective from Antarctic Meteorites. Tokyo, Natl Inst. Polar Res 8485.
Mohamed, A., Gao, S.S., Elsheikh, A., Liu, K.H., Yu, Y., Fat-Helbary, R., 2014. Seismic imaging of mantle transition zone discontinuities beneath the northern Red Sea and adjacent areas. Geophysical Journal International 199, 648-657.
Murakami, M., Ohishi, Y., Hirao, N., Hirose, K., 2012. A perovskitic lower mantle inferred from high-pressure, high-temperature sound velocity data. Nature 485, 90-94.
Murakami, M., Sinogeikin, S.V., Litasov, K., Ohtani, E., Bass, J.D., 2008. Single-crystal elasticity of iron-bearing majorite to 26 GPa: Implications for seismic velocity structure of the mantle transition zone. Earth and Planetary Science Letters 274, 339-345.
Ohira, I., Jackson, J.M., Sturhahn, W., Finkelstein, G.J., Kawazoe, T., Toellner, T.S., Suzuki, A., Ohtani, E., 2021. The influence of δ-(Al, Fe) OOH on seismic heterogeneities in Earth's lower mantle. Scientific reports 11, 1-9.
Parman, S., Grove, T., Dann, J., 2001. The production of Barberton komatiites in an Archean subduction zone. Geophysical Research Letters 28, 2513-2516.
Peslier, A., Hnatyshin, D., Herd, C., Walton, E., Brandon, A., Lapen, T., Shafer, J., 2010. Crystallization, melt inclusion, and redox history of a Martian meteorite: Olivine-phyric shergottite Larkman Nunatak 06319. Geochimica et Cosmochimica Acta 74, 4543-4576.
Plesa, A.C., Bozdağ, E., Rivoldini, A., Knapmeyer, M., McLennan, S.M., Padovan, S., Tosi, N., Breuer, D., Peter, D., Staehler, S., 2021. Seismic velocity variations in a 3D Martian mantle: implications for the InSight measurements. Journal of Geophysical Research: Planets 126, e2020JE006755.

Price, M.G., Davies, J., Panton, J., 2019. Controls on the Deep-Water Cycle Within Three-Dimensional Mantle Convection Models. Geochemistry, Geophysics, Geosystems 20, 2199-2213.
Ranalli, G., 1994. Nonlinear flexure and equivalent mechanical thickness of the lithosphere. Tectonophysics 240, 107-114.
Ricolleau, A., Fei, Y., Cottrell, E., Watson, H., Deng, L., Zhang, L., Fiquet, G., Auzende, A.L., Roskosz, M., Morard, G., 2009. Density profile of pyrolite under the lower mantle conditions. Geophysical Research Letters 36.
Ritsema, J., Deuss, a.A., Van Heijst, H., Woodhouse, J., 2011. S40RTS: a degree-40 shear-velocity model for the mantle from new Rayleigh wave dispersion, teleseismic traveltime and normal-mode splitting function measurements. Geophysical Journal International 184, 1223-1236.
Ruedas, T., Tackley, P.J., Solomon, S.C., 2013. Thermal and compositional evolution of the martian mantle: Effects of phase transitions and melting. Physics of the Earth and Planetary Interiors 216, 32-58.
Schaefer, L., Elkins-Tanton, L.T., 2018. Magma oceans as a critical stage in the tectonic development of rocky planets. Philos Trans A Math Phys Eng Sci 376.
Schmandt, B., Dueker, K., Hansen, S., Jasbinsek, J.J., Zhang, Z., 2011. A sporadic low-velocity layer atop the western US mantle transition zone and short-wavelength variations in transition zone discontinuities. Geochemistry, Geophysics, Geosystems 12.
Schulze, K., Marquardt, H., Kawazoe, T., Ballaran, T.B., McCammon, C., Koch-Müller, M., Kurnosov, A., Marquardt, K., 2018. Seismically invisible water in Earth's transition zone? Earth and Planetary Science Letters 498, 9-16.
Semprich, J., Filiberto, J., 2020. High-pressure metamorphic mineralogy of the Martian crust with implications for density and seismic profiles. Meteoritics & Planetary Science 55, 1600-1614.
Shih, C.-Y., Nyquist, L.E., Wiesmann, H., Reese, Y., Misawa, K., 2005. Rb-Sr and Sm-Nd dating of olivine-phyric shergottite Yamato 980459: Petrogenesis of depleted shergottites. Antarctic Meteorite Research 18, 46.
Shirai, N., Ebihara, M., 2004. Chemical characteristics of a Martian meteorite, Yamato 980459. Antarctic Meteorite Research 17, 55.
Sinogeikin, S.V., 2002. Elasticity of Majorite and a Majorite-Pyrope solid solution to high pressure: Implications for the Transition Zone. Geophysical Research Letters 29.
Sinogeikin, S.V., Bass, J.D., 2002. Elasticity of pyrope and majorite–pyrope solid solutions to high temperatures. Earth and Planetary Science Letters 203, 549-555.
Smrekar, S.E., Lognonné, P., Spohn, T., Banerdt, W.B., Breuer, D., Christensen, U., Dehant, V., Drilleau, M., Folkner, W., Fuji, N., Garcia, R.F., Giardini, D., Golombek, M., Grott, M., Gudkova, T., Johnson, C., Khan, A., Langlais, B., Mittelholz, A., Mocquet, A., Myhill, R., Panning, M., Perrin, C., Pike, T., Plesa, A.-C., Rivoldini, A., Samuel, H., Stähler, S.C., van Driel, M., Van Hoolst, T., Verhoeven, O., Weber, R., Wieczorek, M., 2018. Pre-mission InSights on the Interior of Mars. Space Science Reviews 215.
Song, T.-R.A., Helmberger, D.V., Grand, S.P., 2004. Low-velocity zone atop the 410-km seismic discontinuity in the northwestern United States. Nature 427, 530-533.
Speziale, S., 2004. Single-crystal elasticity of fayalite to 12 GPa. Journal of Geophysical Research 109.
Stixrude, L., Lithgow-Bertelloni, C., 2011. Thermodynamics of mantle minerals - II. Phase equilibria. Geophysical Journal International 184, 1180-1213.
SUZUKI, I., ANDERSON, O.L., 1983. ELASTICITY AND THERMAL EXPANSION OF A NATURAL GARNET UP TO 1, 000K. Journal of Physics of the Earth 31, 125-138.
SUZUKI, I., OHTANI, E., KUMAZAWA, M., 1979. THERMAL EXPANSION OFγ-Mg2SiO4. Journal of Physics of the Earth 27, 53-61.
Suzuki, I., Seya, K., Takei, H., Sumino, Y., 1981. Thermal expansion of fayalite, Fe 2 SiO 4. Physics and Chemistry of Minerals 7, 60-63.

Tang, C., Webb, A., Moore, W., Wang, Y., Ma, T., Chen, T., 2020. Breaking Earth's shell into a global plate network. Nature communications 11, 1-6.
Taylor, G.J., 2013. The bulk composition of Mars. Geochemistry 73, 401-420.
Thio, V., Cobden, L., Trampert, J., 2016. Seismic signature of a hydrous mantle transition zone. Physics of the Earth and Planetary Interiors 250, 46-63.
Tian, Y., Zhou, Y., Sigloch, K., Nolet, G., Laske, G., 2011. Structure of North American mantle constrained by simultaneous inversion of multiple-frequency SH, SS, and Love waves. Journal of Geophysical Research: Solid Earth 116.
Tosi, N., Padovan, S., 2021. Mercury, Moon, Mars: Surface Expressions of Mantle Convection and Interior Evolution of Stagnant-Lid Bodies. Mantle convection and surface expressions, 455-489.
Turcotte, D.L., Schubert, G., 2002. Geodynamics. Cambridge university press.
Wang, J., Bass, J.D., Kastura, T., 2014. Elastic properties of iron-bearing wadsleyite to 17.7GPa: Implications for mantle mineral models. Physics of the Earth and Planetary Interiors 228, 92-96.
Wang, W., Walter, M.J., Peng, Y., Redfern, S., Wu, Z., 2019. Constraining olivine abundance and water content of the mantle at the 410-km discontinuity from the elasticity of olivine and wadsleyite. Earth and Planetary Science Letters 519, 1-11.
Wang, W., Zhang, H., Brodholt, J.P., Wu, Z., 2021. Elasticity of hydrous ringwoodite at mantle conditions: Implication for water distribution in the lowermost mantle transition zone. Earth and Planetary Science Letters 554, 116626.
Wänke, H., Dreibus, G., 1994. Chemistry and accretion history of Mars. Philosophical Transactions of the Royal Society of London. Series A: Physical and Engineering Sciences 349, 285-293.
Wessel, P., Luis, J., Uieda, L., Scharroo, R., Wobbe, F., Smith, W., Tian, D., 2019. The generic mapping tools version 6. Geochemistry, Geophysics, Geosystems 20, 5556-5564.
Wessel, P., Smith, W.H., 1996. A global, self-consistent, hierarchical, high-resolution shoreline database. Journal of Geophysical Research: Solid Earth 101, 8741-8743.
White, D.S.M., Dalton, H.A., Kiefer, W.S., Treiman, A.H., 2006. Experimental petrology of the basaltic shergottite Yamato-980459: Implications for the thermal structure of the Martian mantle. Meteoritics & Planetary Science 41, 1271-1290.
Workman, R.K., Hart, S.R., 2005. Major and trace element composition of the depleted MORB mantle (DMM). Earth and Planetary Science Letters 231, 53-72.
Wu, Y., Li, Q.-L., Che, X., Liao, S., 2021. Heterogeneous martian mantle: Evidence from petrology, mineral chemistry, and in situ U-Pb chronology of the basaltic shergottite Northwest Africa 8653. Geochimica et Cosmochimica Acta 309, 352-365.
Xie, L., Yoneda, A., Yamazaki, D., Manthilake, G., Higo, Y., Tange, Y., Guignot, N., King, A., Scheel, M., Andrault, D., 2020. Formation of bridgmanite-enriched layer at the top lower-mantle during magma ocean solidification. Nature communications 11, 1-10.
Xu, F., Siersch, N., Greaux, S., Rivoldini, A., Kuwahara, H., Kondo, N., Wehr, N., Menguy, N., Kono, Y., Higo, Y., 2021. Low velocity zones in the Martian upper mantle highlighted by sound velocity measurements. Geophysical Research Letters 48, e2021GL093977.
Xu, W., Lithgow-Bertelloni, C., Stixrude, L., Ritsema, J., 2008. The effect of bulk composition and temperature on mantle seismic structure. Earth and Planetary Science Letters 275, 70-79.
Yamanaka, T., 1986. Crystal structures of Ni 2 SiO 4 and Fe 2 SiO 4 as a function of temperature and heating duration. Physics and Chemistry of Minerals 13, 227-232.
Yang, J., Faccenda, M., 2020. Intraplate volcanism originating from upwelling hydrous mantle transition zone. Nature 579, 88-91.
Ye, L., Li, J., Tseng, T.-L., Yao, Z., 2011. A stagnant slab in a water-bearing mantle transition zone beneath northeast China: implications from regional SH waveform modelling. Geophysical Journal International 186, 706-710.
Yoshizaki, T., McDonough, W.F., 2020. The composition of Mars. Geochimica et Cosmochimica Acta 273, 137-162.

Yoshizaki, T., McDonough, W.F., 2021. Earth and Mars–distinct inner solar system products. Geochemistry 81, 125746.
Zha, C.-s., Duffy, T.S., Mao, H.-k., Downs, R.T., Hemley, R.J., Weidner, D.J., 1997. Single-crystal elasticity of β-Mg2SiO4 to the pressure of the 410 km seismic discontinuity in the earth's mantle. Earth and Planetary Science Letters 147, E9-E15.
Zhang, J.S., Bass, J.D., 2016. Sound velocities of olivine at high pressures and temperatures and the composition of Earth's upper mantle. Geophysical Research Letters 43, 9611-9618.
Zhang, J.S., Bass, J.D., Zhu, G., 2015. Single-crystal Brillouin spectroscopy with CO2 laser heating and variable q. Review of Scientific Instruments 86, 063905.
Zhao, D., Tian, Y., Lei, J., Liu, L., Zheng, S., 2009. Seismic image and origin of the Changbai intraplate volcano in East Asia: role of big mantle wedge above the stagnant Pacific slab. Physics of the Earth and Planetary Interiors 173, 197-206.
Zhou, W.-Y., Ren, Z., Zhang, J.S., Chen, B., Hao, M., Ohuchi, T., Miyagi, L., Zhang, D., Alp, E.E., Lavina, B., 2021. The Water-Fe-Pressure dependent single-crystal elastic properties of wadsleyite: Implications for the seismic anisotropy in the upper Mantle Transition Zone. Earth and Planetary Science Letters 565, 116955.